國立中山大學 物理研究所

博士論文

在 SPring-8/LEPS 中
Λ(1520)來自質子與重氫子的接近閥值光致產生
Near-Threshold Photoproduction of Λ(1520) from Protons and Deuterons at SPring-8/LEPS

研究生：陳家益撰

指導教授：郭啟東教授

章文箴博士

中華民國 九十八 年 七 月

Near-Threshold Photoproduction of $\Lambda(1520)$ from Protons and Deuterons at SPring-8/LEPS

BY

Jia-Ye Chen

Advisers: Prof. Chie-Tong Kuo
Dr. Wen-Chen Chang

THESIS

Submitted as partial fulfillment of the requirements
for the degree of Doctor of Philosophy in Physics
in the Department of Physics of the
National Sun Yat-sen University

July, 2009

Acknowledgments / 致謝

誠心感謝我的指導教授郭啟東教授，在各方面給予我莫大的鼓勵以及明確的指導，尤其以開明的態度讓我可以全心投入喜歡的實驗研究，並且使我能順利完成博士論文，在此致上由衷的感激。

再一次感謝中央研究院物理所的章文箴老師，在我離開實驗組兩年之後，給了我繼續參與 SPring-8/LEPS 實驗的機會。在中央研究院物理所參與研究的期間，不斷的教導我清晰的物理觀念、正確的實驗方式以及實用的研究分析方法，使我受益良多。

I would like to thank Dr. M. Muramatsu from Research Center for Nuclear Physics, Osaka University. Under his instruction, we finished the data analysis and published this result at Physical Review Letter in cooperation with Prof. Wen-Chen Chang and also to fulfill the graduation requirement of National Sun Yat-sen University without delay. I also want to thank all the LEPS colloborators for the great helps both on researches and living at Japan, they are Prof. T. Nakano, Prof. M. Yosoi, Prof. K. Imai, Prof. K. Hicks, Prof. J.K. Ahn, Y. Ohashi, S. Date, T. Hotta, T. Ishikawa, H. Fujimura, H. Kohri, T. Mibe, K. Kino, D.S. Oshuev, Prof. J.L. Tang, J. D. Parker, M. Sumihama, K. Horie, M. Niiyama, M. Uchida, D.S. Ahn, T. Sawada, Y. Nakatsugawa, and Y. Kato.

另外，感謝中央研究院物理研究所中高能實驗組的鄧炳坤老師，在高能物理實驗上的指導以及提供強大的數據分析系統，加速數據分析的進行；同時，感謝謝璨隆在大型數據分析系統以及程式語言上的指導與協助；感謝蘇大順在實驗資料輸出硬體界面上的指導。

再者，感謝中高能實驗組的同事，余岳仲老師、朱明禮老師、許智祐學長、林伯儒、王素音、許軒豪、陳冠銘、張惠珍、賴惠暄、蘇婷婷，以及其他單位的同事，吳喜成、王裕鑫、簡明宏、賴宜瑩、郭惠禎，在諸多實驗與行政事物上的大力幫忙。

也感謝郭榮升老師、周炳榮老師、林盛文學長，中山大學物理系所有其他的老師，系辦公室的徐茹絹小姐以及其他的成員，液晶與奈米光電實驗室的成員，黃宣瑜學長、張志宏、王峻禹、陳玉娉、鄭文碩、吳宜修、彭治杰、康繼中、游凱宇、施景仁、鄭和宜、黃炳堯，在博士班的五年之中給予我的指導與協助。

最後，感謝我的媽媽、妹妹、以及親朋好友，他們給予我精神上最大的支持與鼓勵，以致於完成學業，在此，致上謝意。

摘要

SPring-8/LEPS 實驗設施中，由氫離子雷射光子與 SPring-8 儲存環內 8-GeV 電子束進行背向康卜吞散射而產生的 GeV 級光子束，藉由測量作用後的電子，可標記光子的能量範圍從 1.5 到 2.4 GeV。如此高能量的光子讓我們可以去研究奇異介子與奇異重子的光致產生，例如 ϕ(1020)、Λ(1405) 以及 Λ(1520)。過去 30 年，除了在 NINA/LAMP2 實驗組的高能量 Λ(1520) 光致產生實驗，在接近閥值能量範圍並沒有更進一步的實驗。因此，建立在 NINA/LAMP2 這唯一量測的基礎上，許多理論計算預測，接近閥值能量的 Λ(1520) 光致產生可以被解釋為 *t*-channel K^* 交換模型、*t*-channel K 交換模型；或者是滿足 gauge invariance 的情況下，伴隨著 *t*-channel K 交換的 contact term 模型。藉由 SPring-8/LEPS 實驗設施中前置方向質譜儀與液態氫與液態氘的固定靶在 2002 到 2003 年進行此光致產生實驗；在 JLab/CLAS 所進行的一個質心系統能量與 SPring-8/LEPS 相近的電子產生實驗也被納入本文討論比較。在實驗分析上，我們研究雙軌跡偵測模式去重建 Λ(1520) 共振態分佈以及其他背景反應的共振態與非共振態分佈。我們利用一階段、二階段背景刪減分析方法與數值模擬分析方法，並經由測量反應截面、在 *t*-channel helicity frame 的 K^- 衰變不對稱性以及光子極化方向衰變不對稱性去瞭解 Λ(1520) 的產生機制，而反應截面的量測則是第一次使用液態氘在此低能量的範圍進行。結果，我們觀察到在 $K^{+/0}$ 的背向產生角度上來自質子與中子的反應截面有一個很大的差異，這樣的一個不對稱性可以用滿足 gauge invariance 的條件下，伴隨著 *t*-channel K 交換的 contact term 模型來解釋。相同的解釋，可以用來說明 K^+ 前置產生方向上的反應截面、在 *t*-channel helicity frame 的 K^- 衰變不對稱性，以及光子極化方向衰變不對稱性。另外，新建的時間飄移偵測器則是為了彌補側向與背向接收度的不足，時間飄移偵測器的配置以及基本原理將會在此文章中被討論。

Abstract

GeV photon beams are provided at SPring-8/LEPS facility by backward-Compton scattering (BCS) from Argon laser photon against the 8-GeV electrons inside the SPring-8 storage ring. The energy range of tagged photon by measuring the recoil electron is from 1.5 to 2.4 GeV, and enables us to study the strange meson- and baryon-photoproduction, such as $\phi(1020)$, $\Lambda(1405)$ and $\Lambda(1520)$. In the past 30 years, other than the high-energy $\Lambda(1520)$ photoproduction at NINA/LAMP2 experiment, there is no further study of the $\Lambda(1520)$ photoproduction near the threshold. Based on this exclusive measurement at NINA/LAMP2 experiment, several theoretical calculations predict that the $\Lambda(1520)$ photoproduction near the threshold can be explained by t-channel K^* exchange, t-channel K exchange or the contact term together with the t-channel K exchange under the gauge invariance.

This experiment was performed at SPring-8/LEPS facility with liquid hydrogen and deuterium targets by a forward spectrometer from 2002 to 2003. The electroproduction experiment with similar c.m. energy region performed by JLab/CLAS is included for comparison. We study three two-track detection modes to reconstruct the $\Lambda(1520)$ resonance and other resonant/non-resonant backgrounds by the invariant mass and missing mass spectra. Utilizing the one-/two-step side-band subtraction methods and Monte Carlo simulation method, we measure the differential cross sections, K^- decay asymmetries in t-channel helicity frame and photon beam asymmetries to understand the production mechanism of $\Lambda(1520)$. This is the first time, the differential cross sections were measured at low energies and with a deuterium target. A large asymmetry of the production cross sections from protons and neutrons was observed at backward $K^{+/0}$ angles. It can be explained by the dominance of the contact term along with the t-channel K exchange under the satisfaction of gauge invariance. This interpretation was also compatible with the differential cross sections, K^- decay asymmetry, and the photon beam asymmetry measured in the production from protons in the forward K^+ angles.

A detector upgrade for the acceptance complement is done by introducing a time projection chamber, the configuration and operation principles except for the physics results will also be discussed in this thesis.

Contents

1 Introduction **1**
- 1.1 Physics motivation . . . 1
- 1.2 Previous results . . . 8
- 1.3 SPring-8/LEPS experiment . . . 10

2 Experimental setup **11**
- 2.1 Light source . . . 11
  - 2.1.1 Backward-Compton scattering . . . 11
  - 2.1.2 Synchrotron radiation and SPring-8 . . . 13
  - 2.1.3 Laser system . . . 14
  - 2.1.4 Tagging counter (Tagger) . . . 16
- 2.2 Spectrometer . . . 16
- 2.3 Time Projection Chamber . . . 19
  - 2.3.1 Multi Wire Proportional Chamber . . . 21
  - 2.3.2 From FADC signal to track construction . . . 22

3 Analysis method **26**
- 3.1 Reaction channels . . . 26
- 3.2 Detection modes . . . 26
- 3.3 Analysis scenarios . . . 27
  - 3.3.1 Background non-linearity . . . 27
  - 3.3.2 Side-band subtraction . . . 30
  - 3.3.3 Monte Carlo fitting . . . 30
  - 3.3.4 Non-linearity correction . . . 31
  - 3.3.5 2-step side-band subtraction . . . 32
- 3.4 Event selections . . . 33
  - 3.4.1 Particle identification (PID) . . . 34
  - 3.4.2 Decay-in-flight cuts . . . 35
  - 3.4.3 Vertex cuts . . . 36
  - 3.4.4 Production threshold . . . 37
- 3.5 Data samples . . . 39

4 Results and discussions **40**
- 4.1 Invariant mass and missing mass . . . 40
  - 4.1.1 K^+K^- detection mode from protons . . . 41
  - 4.1.2 K^+K^- detection mode from deuterons . . . 42
  - 4.1.3 K^+p detection mode from protons . . . 42
  - 4.1.4 K^-p detection mode from protons . . . 43

4.1.5 K^-p detection mode from deuterons . . . 43
4.1.6 Mass spectra . . . 44
4.2 Monte Carlo fitting . . . 44
4.2.1 K^+K^- detection mode from protons . . . 45
4.2.2 K^-p detection mode from protons . . . 45
4.2.3 K^-p detection mode from deuterons . . . 46
4.3 The measurement of differential cross section . . . 47
4.3.1 Luminosity . . . 47
4.3.2 Differential cross section . . . 47
4.3.2.1 K^+p detection mode from protons . . . 49
4.3.2.2 K^-p detection mode from protons and deuterons . . . 50
4.3.2.3 Combination of K^+p and K^-p detection mode from protons . . . 52
4.3.2.4 Summarized results . . . 53
4.4 K^- decay asymmetry in $\Lambda(1520)$ t-channel helicity frame . . . 57
4.5 Photon beam asymmetry . . . 63
4.6 Possible interference from ϕ meson events . . . 67
4.7 Effect of AC veto for $\gamma n \to K^0_S \Lambda(1520)$ . . . 68
4.8 Ratio of $\Lambda(1520)$ events between K^+p and single K^+ detection modes . . . 68
4.9 Comparison of acceptance between K^+p and single K^+ detection modes . . . 69

5 Summary **70**

Bibliography **72**

A Differential cross section **74**
A.1 K^+K^- detection mode from protons and deuterons . . . 76
A.1.1 Background non-linearity . . . 76
A.1.2 Differential cross section . . . 77
A.1.3 Background non-linearity and $d\sigma/d\cos\theta_{K^+}$ for $19^o < \theta_{K^+} < 43^o$ . . . 78
A.2 K^+p detection mode from protons . . . 79
A.2.1 Differential cross section I . . . 79
A.2.2 Differential cross section II . . . 83
A.3 K^-p detection mode from protons . . . 87
A.3.1 Background non-linearity . . . 87
A.3.2 Differential cross section . . . 89
A.4 K^-p detection mode from deuterons . . . 91
A.4.1 Background non-linearity . . . 91
A.4.2 Differential cross section . . . 93
A.5 The result of LAMP2 experiment . . . 95
A.6 Total cross sections of LEPS results . . . 96

B K^- decay asymmetry in $\Lambda(1520)$ t-channel helicity frame **97**
B.1 K^-p detection mode from protons . . . 98
B.1.1 Background non-linearity . . . 98
B.1.2 K^- polar angle distribution in $\Lambda(1520)$ t-channel helicity frame . . . 113
B.1.3 Signal-window width dependence of fraction of helicity-3/2 . . . 118
B.2 K^+K^- detection mode from protons . . . 123
B.2.1 Background non-linearity . . . 123

B.2.2 K^- polar angle distribution in $\Lambda(1520)$ t-channel helicity frame 133
B.2.3 Signal-window width dependence of fraction of helicity-3/2 136
B.3 K^+p detection mode from protons 140
B.3.1 Window dependence of K^- polar angle distribution 140
B.3.2 Energy dependence of K^- polar angle distribution 143
B.4 Energy dependence of fraction of helicity-3/2 144

C Photon beam asymmetry **145**
C.1 K^+p detection mode from protons 146
C.1.1 Width dependence in photon energy of 1.9-2.4 GeV 146
C.1.2 Energy dependence in standard 2-step side-band widths 150
C.2 Possible bias in beam asymmetry measurement 151
C.2.1 Filtering between photon polarization and detected K^+ 151
C.2.2 Filtering between photon polarization and detected proton 152
C.2.3 Filtering between detected K^+ and detected proton 153
C.2.4 Reversed filtering between photon polarization and detected proton . . 154

Chapter 1

Introduction

1.1 Physics motivation

In 1947 during an experiment of cosmic ray interactions from proton-nucleus collisions detected by the hydrogen bubble chamber, a "strange" particle which has much longer lifetime (2.63×10^{-10} s) than expected ($\sim 10^{-23}$ s) was discovered and named as Lambda, "Λ". Then, it also led to the discovery of strange quark. Later on, this Λ particle was known as the ground state of Λ baryon families, $\Lambda(1116)$, and possesses the valance quark uds and $I(J^P) = 0(\frac{1}{2}^+)$.

In the study of photoproduction of $\Lambda(1116)$, many possible production diagrams can proceed this reaction. Four most common production candidates and one high-order diagram are shown in Fig. 1.1, five panels are (a) s-, (b) u-, (c) t-/v-, (d) c- channels and (e) loop diagram. As shown in Fig. 1.1, the s-channel corresponds to the photon and nucleon forming an intermediate particle that finally splits into $K^{+/0}$ and $\Lambda(1116)$; the t-channel represents the reaction in which the photon emits the intermediate particle ($K^{-/0}$ or $K^{*-/0}$) and becomes the $K^{+/0}$, while the nucleon absorbs the intermediate particle then becomes the $\Lambda(1116)$ (in order to distinguish the K and K^* exchange in the t channel, an additional symbol "v" is used to specify the t channel through K^* exchange); the u-channel is the t-channel with role interchange of the $K^{+/0}$ and $\Lambda(1116)$; and the c-channel represents the contact term under the satisfaction of gauge invariance, where the gauge invariance which leads to the well-known "conservation of charge" is one kind of charge coupling. The loop diagram will be discussed later.

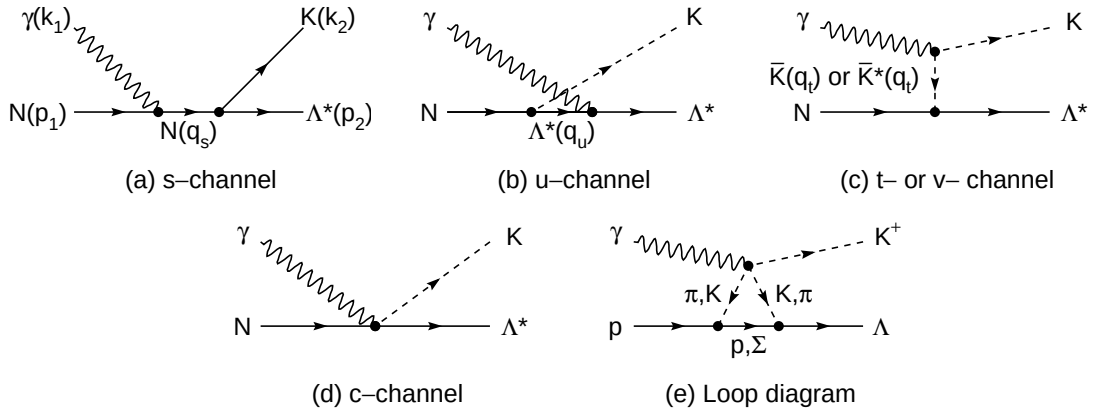

Figure 1.1: Feynman diagrams of reaction channels for $\Lambda(1116)/\Lambda(1520)$ photoproduction [1].

In the past 15 years, the production mechanism of $\Lambda(1116)$ has been well studied through the measurement of differential cross sections and photon-beam asymmetries at ELSA/SAPHIR (photoproduction, $E_\gamma > 2$ GeV), JLab/CLAS (electroproduction, $1.6 < \sqrt{s} < 2.3$ GeV) and SPring-8/LEPS (photoproduction, $1.5 < E_\gamma < 2.4$ GeV), where $\sqrt{s}$ and E_γ means the center-of-mass energy and photon energy respectively. Most recent results were measured by LEPS collaboration and published in 2006 [2].

The photon beam asymmetry is a good method to identify the meson-exchange mechanism in the t-channel. Photon beam asymmetries are measured in the dimension of K^+ azimuthal angle, where the K^+ azimuthal angle ϕ, as shown in Fig. 1.2, is measured relative to the horizontal plane, in each of the vertical and horizontal polarization.

$$\Sigma P_\gamma \cos(2\phi) = \frac{kN_V(\phi) - N_H(\phi)}{kN_V(\phi) + N_H(\phi)}, \tag{1.1}$$

where N_v and N_h are the $\Lambda(1520)$ photoproduction yields with the vertically and horizontally polarized photons respectively, "P_γ" is beam polarization and "k" is a normalization factor determined by photon counts at the tagger. Refer to Nam's calculation at E_γ =2.0 GeV shown in Fig. 1.3 [3], the s, u channels and contact term show weak ϕ dependence in whole angular regions, the photon beam asymmetry from them turns out to be zero, while the photon beam asymmetry from K exchange show that $A(E_\gamma, \theta) = -1$ for whole range of θ, indicated this interaction is dominated by magnetic component. Whereas the $A(E_\gamma, \theta)$ of K^* exchange give the positive contributions other than θ =0° and 180°, shown the dominance of electric component.

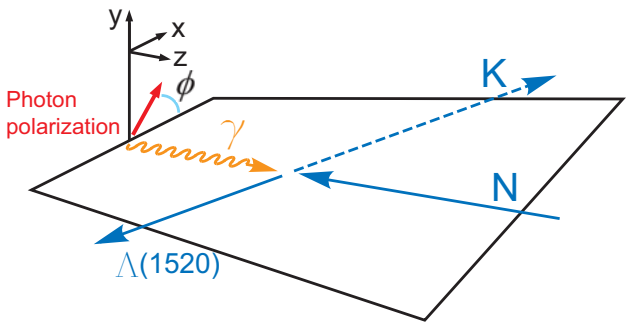

Figure 1.2: Definition of axes on the production plane and azimuthal angle ϕ. The x-, y- and z- axes stand on the production plane instead of Lab. frame, and the ϕ is the azimuthal angle between photon polarization and production plane. [3]

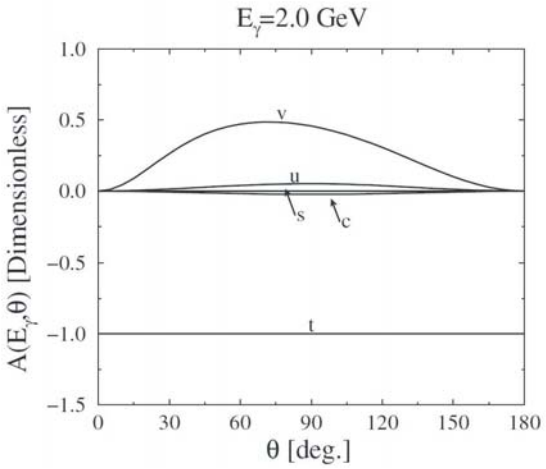

Figure 1.3: Photon beam asymmetries for different contributions.

It can be seen from the left column of Fig. 1.4, based on the measurement of LEPS experiment, the photon beam asymmetries was found to be positive and to increase with the photon energy. It can be explained by Gent isobar model from D.G. Ireland [4] accompany with the mixing model of the Feynman diagram and the Regge model from Mart and Bennhold [5], but not very well.

Owing to a much weaker magnetic interaction provided by much smaller microscopic K^* coupling constants [6] than the phenomenological coupling constants determined by fitting to

the data [7], a further theoretical calculation about Λ(1116) production [8] introduced the one-loop diagram induced by the Wess-Zumino-Witten (WZW) term [9], as shown in Fig. 1.1(e), based on the experimental results from CLAS [10] and LEPS [2], to furnish the leakage of K* exchange. It can be seen from Fig. 1.5, however, both dashed and solid lines including WZW term which contribute the positive photon asymmetries match the LEPS results well. From Fig. 1.6, however, there is no significant difference between theoretical calculations with (solid line) and without (dashed line) the supplement of WZW term.

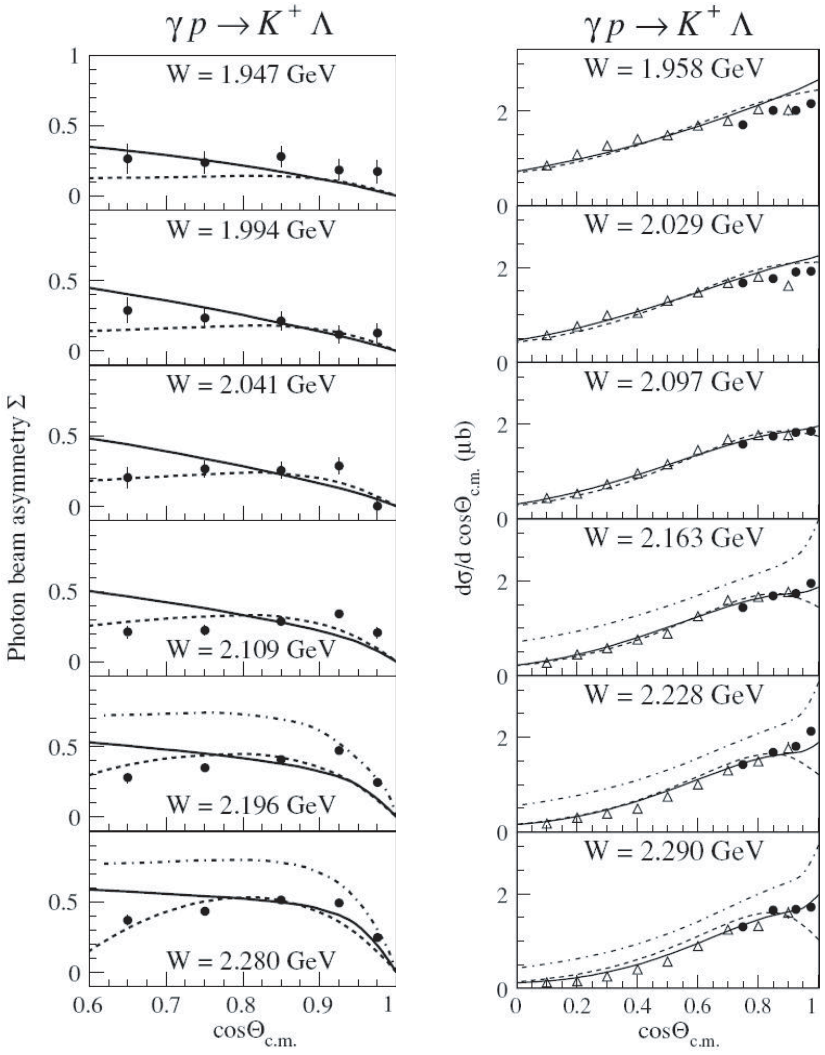

Figure 1.4: Photon beam asymmetries and differential cross sections for the $\gamma p \to K^+\Lambda$ as a function of $\cos\Theta_{c.m.}$ are shown in left and right columns respectively [2]. The closed circles and open triangles are from the LEPS and CLAS respectively. In left column, the dot-dashed, dashed and solid curves are the results of "Regge model with K and K* exchange", "Gent isobar model" and the "mixing model of the Feynman diagram and the Regge model" respectively. In right column, dot-dashed, dashed and solid curves are the theoretical predictions with the Regge model, the Feynman diagram and the mixing model of the Regge model and the Feynman diagram respectively.

Following with the study of Λ(1116) production, we are interested at the photoproduction of Λ(1520) with same diagrams shown in Fig. 1.1(a)-(d), since some theoretical calculations predicted different dominant models for the productions of Λ(1520) which is $I(J^P) = 0(\frac{3}{2}^-)$. The intrinsic difference on spin, J, between Λ(1520) and Λ(1116) might be the reason for different production mechanism. While the experimental results of Λ(1520) photoproduction are available in the photon energy range of 2.8-4.8 GeV from the LAMP2 collaboration, this reaction has not been measured near the threshold.

Other than the study of photon beam asymmetry, as shown in right column of Fig. 1.4 and Fig. 1.6, the differential cross sections of Λ(1116) photoproduction from CLAS and LEPS experiment increase at forward angles. This forward peak resulted from the the significant contribution of K exchange in t-channel, while the contribution from WZW term is minor. Compare

to the Nam's theoretical calculation for $\Lambda(1520)$ photoproduction shown in Fig. 1.7 [3], there is also an obviously forward enhancement contributed by contact-term channel instead of K exchange in the t channel. The contact-term contributions shown in Fig. 1.7 almost dominate overall contributions to the differential cross sections, even though the contributions from K and K* exchange are not negligible, and those from s and u channels are quite small.

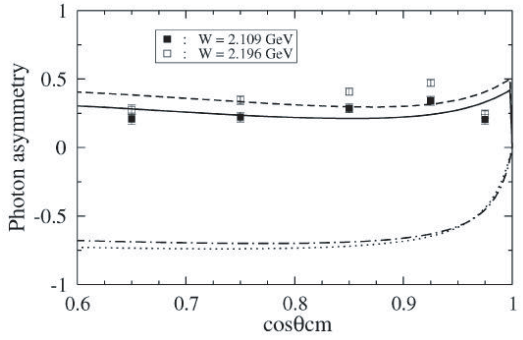

Figure 1.5: Photon asymmetry measurements by LEPS experiment at W=2.109 and 2.196 GeV show as a function of $\cos\theta_{cm}$. The dashed (solid) and dot-dashed (dot) lines show the calculations with and without WZW term at W=2.196 (2.109) GeV.

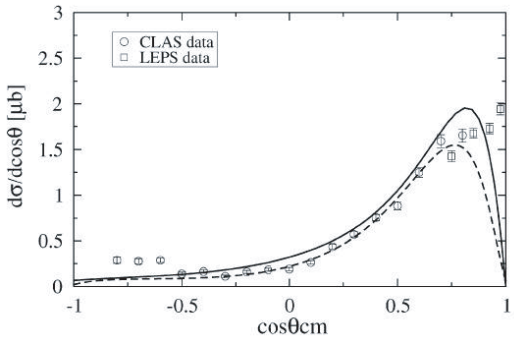

Figure 1.6: Differential cross section at W=2.164 GeV as a function of $\cos\theta_{cm}$. The dashed and solid lines indicates the results of sum of contributions of Fig. 1.1(a)-(d) with and without the contribution of WZW term respectively. The open-circle and open-square data show the results of CLAS and LEPS respectively.

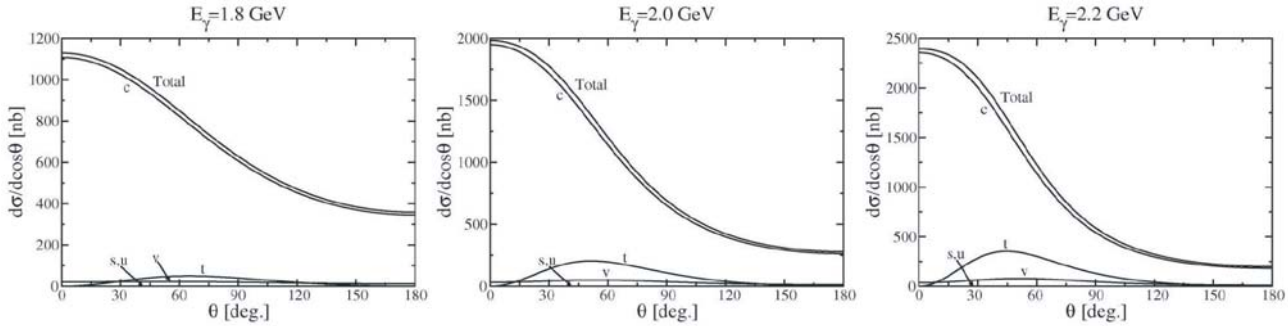

Figure 1.7: Differential cross sections of individual/total contribution as a function of θ at three different photon energies E_γ =1.8, 2.0 and 2.2 GeV.

The LAMP2 results could also be described by a model emphasizing the importance of a contact term, which was necessary to conserve gauge invariance along with t-channel pseudoscalar kaon (K) exchange [11]. In this framework, a strong asymmetry is distinctively predicted in the $\Lambda(1520)$ photoproduction cross sections from protons and neutrons because the dominant contribution from the contact term is absent in the production from neutrons [1, 12]. According to theoretical prediction of total cross section of $\Lambda(1520)$ photoproduction [1], in the process $\gamma p \to K^+\Lambda(1520)$, c-channel (contact term), depicted in Fig. 1.1, dominates this process near the production threshold as shown in the left panel of Fig. 1.8. And, since $\gamma n \to K^0\Lambda(1520)$ is a neutral process, the contact term is absent. This absence caused the total cross section of γn process to become smaller than that for the γp process, the predicted

total cross section was shown in the right panel of Fig. 1.8.

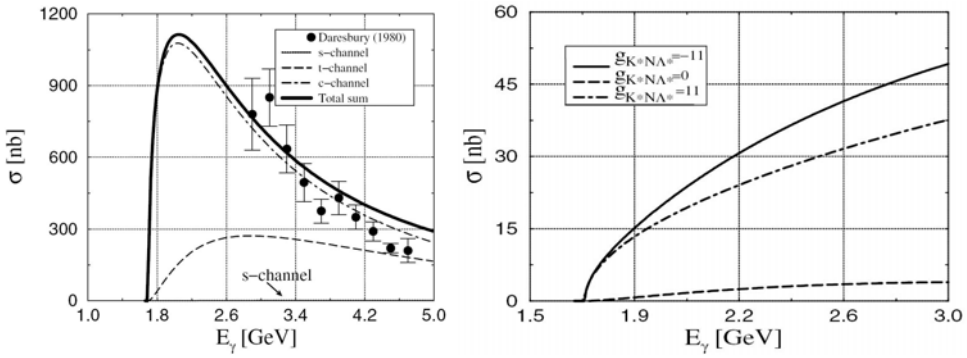

Figure 1.8: The predictions of total cross sections for the proton and neutron target are shown in the left and right panels respectively [1]. In the left panel, the s-, t- and c-channel contributions are drawn separately. The experimental data are taken from LAMP2 experiment [13]. In the right panel, total cross sections with three different coupling constants $g_{K^*N\Lambda^*}$ (11., 0. and -11.) are shown individually.

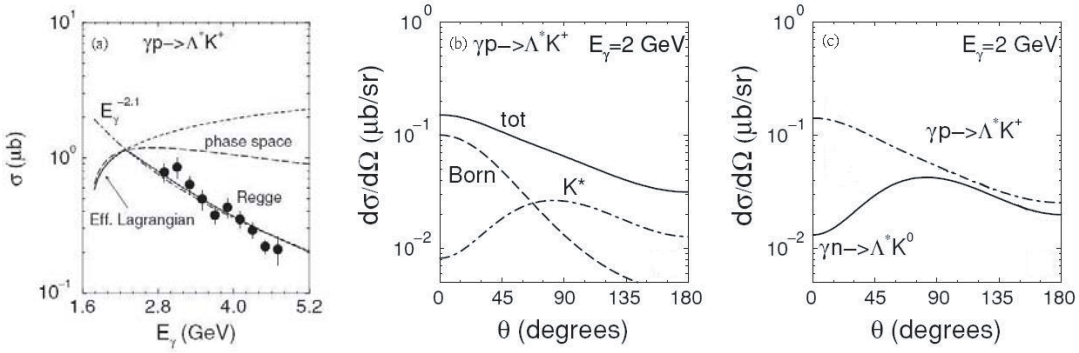

Figure 1.9: (a) The total cross section of the reaction $\gamma p \to \Lambda^* K^+$ as a function of photon energy. The solid circles are the result of LAMP2 experiment. The dot-dashed line shows a fit to LAMP2 data by $\sigma \simeq 0.7(\mu b)[2.9(GeV)/E_\gamma]^{2.1}$. The long-dashed line shows the cross sections from the phase space. The dashed line shows the assumption of the amplitude of $\Lambda(1520)$ photoproduction at low- and high-energy regions. The short-dashed line is the extrapolation of effective Lagrangian model to the high-energy region. (b) The differential cross section of the reaction $\gamma p \to \Lambda^* K^+$ at $E_\gamma = 2$GeV as a function of θ in c.m. frame, where the "Bonn" term represent the sum of contribution of s-, t- and c-channel in Fig. 1.1(a, c, d). (c) The differential cross section of the reactions $\gamma p \to \Lambda^* K^+$ (dot-dashed) and $\gamma n \to \Lambda^* K^0$ (solid) at $E_\gamma = 2$GeV as a function of θ in c.m. frame.

Another theoretical calculation about the $\Lambda(1520)$ photoproduction, based on the quark-gluon string model, was done by Titov *et al.* [14]. Assuming that the cross sections of $\Lambda(1520)$ production at photon energies close to the production threshold can be described by the effective Lagrangian formalism, nevertheless at high energies, vector meson K* exchange and Regge model dominated, as shown in Fig. 1.9(a). It can be seen from Fig. 1.9(b) and (c), the main difference of differential cross sections at the forward region came from the contribution of Bonn term in the γp reaction; at backward production, the shapes and values of differential cross sections of two reactions are similar to each other.

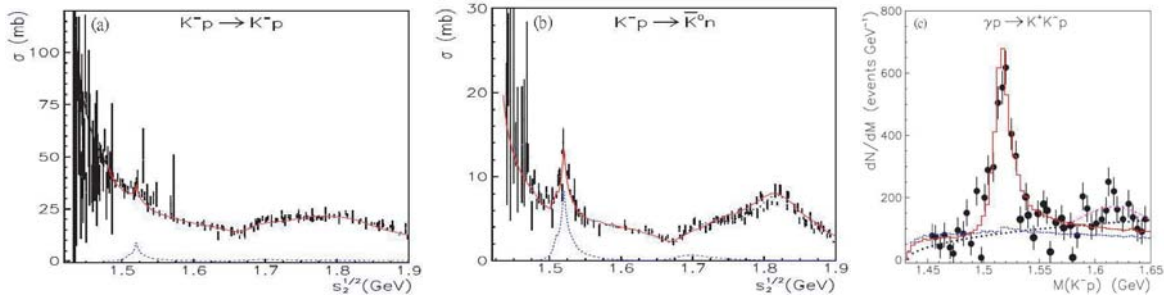

Figure 1.10: The total cross sections of reactions (a) $K^-p \to K^-p$ and (b) $K^-p \to \bar{K}^0n$ as a function of the invariant collision energy. The data came from ref. [15]. The red-solid lines represent the results including full reaction amplitudes, while the blue-dashed lines show the contribution from D_{03} partial wave only. (c) The invariant mass spectrum of K^-p for the reaction $\gamma p \to K^+K^-p$, where the red-solid and blue-dashed lines show the results of Drell mechanism with and without the inclusion of K^* exchange respectively; the dot line indicates the result from phase space with a constant amplitude at $E\gamma$ =3.8 GeV; and the dot-dashed line represents the contribution of a $\Lambda(1600)$ P_{01}-resonance.

There is also a theoretical calculation from Sibirtsev *et al.* which claimed that Drell mechanism can not describe the $\Lambda(1520)$ photoproduction from protons of LAMP2 data well alone, the discrepancy can be explained by the K^* exchange in the t-channel [16]. Drell mechanism (namely pseudoscalar K exchange) means that the incoming photon virtually decays into a K^+K^- pairs, the K^- penetrates into proton initiating the reactions to various final states, such as quasi-elastic scattering $K^-p \to K^-p$ or charge-exchange rescattering $K^-p \to \bar{K}^0n$, while the K^+ emerges directly [17]. Making a comparison between (a) and (b) in Fig. 1.10, it shows that the $\Lambda(1520)$ signal mainly came from the reaction $\gamma p \to K^+\bar{K}^0n$ instead of $\gamma p \to K^+K^-p$. If the $\Lambda(1520)$ resonance does produce from the intermediate reaction $\gamma p \to K^+K^-p$, there will be another mechanism dominate in this step rather than the Drell mechanism. Therefore, the K^* exchange was considered as a dominant mechanism and demonstrated a good agreement with the invariant mass spectrum of LAMP2 experiment, as shown in Fig. 1.10(c).

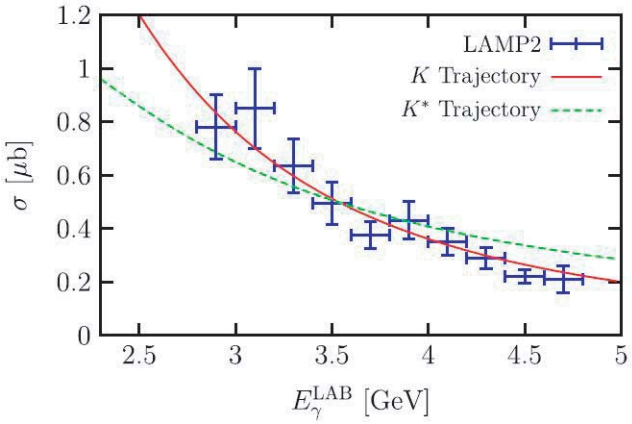

Figure 1.11: The total cross section of the reaction $\gamma p \to K^+\Lambda(1520)$ as a function of photon energy at Lab. frame. The red-solid and green-dashed lines indicates the results of K- and K^*-exchange trajectories respectively.

Furthermore, the other theoretical calculation utilizing the chiral unitary model based on the same LAMP2 data was performed by Toki *et al.* [18]. It turns out that the contribution of K* exchange at low energies was small, so that the pseudoscalar K exchange dominates in the reaction $\gamma p \to K^+\Lambda(1520)$, as shown in Fig. 1.11. An extrapolation including the K and Reggeon exchange models predicts the total cross section to be around 2 μb at the E_γ ~2GeV.

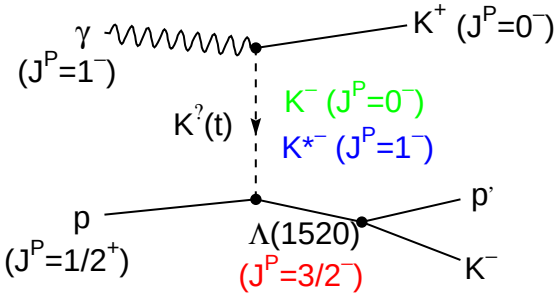

Figure 1.12: Feynman diagram of $\Lambda(1520)$ photoproduction.

Except for the measurement of differential cross sections and photon beam asymmetries, the decay angular distribution of K^- at the t-channel helicity frame (Gottfried-Jackson frame) [19] of the $\Lambda(1520)$ is related to its helicity state, which differs depending on reaction mechanisms including K^- or K^{*-} exchange in the t-channel [14, 18] and contact-term channel [1]. As seen from Fig. 1.12, the dominant exchange particle of K^{*-} or K^- in this reaction is unclear. This information can be obtained by the determination of helicity state of $\Lambda(1520)$.

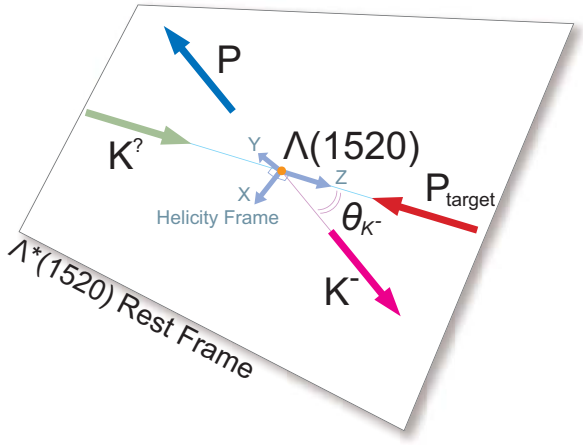

Figure 1.13: The schema of the $\Lambda(1520)$ t-channel helicity frame, z-axis is assigned to be anti-parallel to the direction of the incident proton and the y-axis is perpendicular to the production plane.

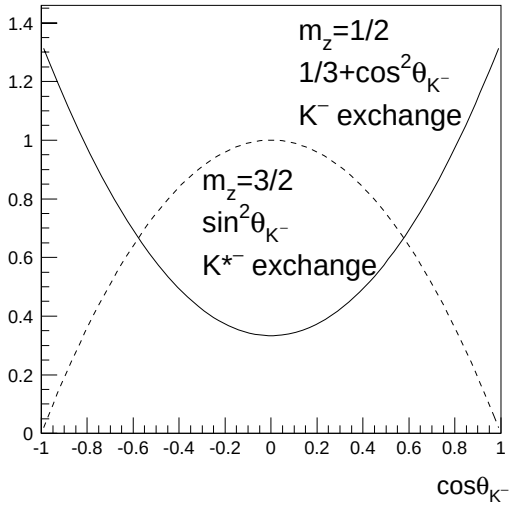

Figure 1.14: The expected K^- decay angular distribution in $\Lambda(1520)$ t-channel helicity frame.

$$I(\cos\theta,\phi) = \frac{3}{4\pi}\{\rho_{33}\sin^2\theta + \rho_{11}(\frac{1}{3}+\cos^2\theta) - \frac{2}{\sqrt{3}}Re\rho_{31}\sin 2\theta\cos\phi - \frac{2}{\sqrt{3}}Re\rho_{3-1}\sin^2\theta\cos 2\phi\} \tag{1.2}$$

Referring to the spin density matrix ρ_{2M2M} within the density matrix function $I(\cos\theta,\phi)$ [13] listed in Eq. 1.2, where M and M' are spin projection quantum numbers, we measure the decay angle θ_{K^-} in the $\Lambda(1520)$ t-channel helicity frame shown in Fig. 1.13. Here is an assumption that there is no ϕ dependence in the decay angular distribution of K^-. Therefore, to integrate the $I(\cos\theta,\phi)$ with ϕ in whole range ($0\sim2\pi$), we obtain

$$I(\cos\theta) = \frac{3}{4\pi}\{\rho_{33}\sin^2\theta + \rho_{11}(\frac{1}{3}+\cos^2\theta)\} \tag{1.3}$$

In Fig. 1.13, the z-axis is defined to be anti-parallel to the direction of the incident proton in the $\Lambda(1520)$ rest frame and the y-axis is the normal to the production plane.

The intensity of K^{*-} exchange forms a $\sin^2\theta_{K^-}$ distribution and K^- behaves as a $\frac{1}{3}+\cos^2\theta_{K^-}$ distribution, shown in Fig. 1.14. If the $\Lambda(1520)$ spin projection is only spinless kaon, $K^-(m_z = \pm\frac{1}{2})$, exchange, the ratio of $m_z = \pm\frac{3}{2}$ to $m_z = \pm\frac{1}{2}$ population is zero. On the other hand, if this reaction was dominated by vector kaon, $K^{*-}(m_z = \pm\frac{3}{2})$, exchange exclusively by the ratio of $m_z = \pm\frac{3}{2}$ to $m_z = \pm\frac{1}{2}$ is $3:1$. In LAMP2 experiment [13], they assumed a trace condition, $\rho_{33}+\rho_{11} = \frac{1}{2}$, in the evolution of density matrix function $I(\cos\theta,\phi)$ given in Eq. 1.2, but this trace condition didn't include the contributions from the last 2 terms of Eq. 1.2.

In addition, the $\Lambda(1520)$ hyperon recently has received great interest since its mass is close to that of the claimed pentaquark Θ^+ [20] with an opposite strangeness, as shown in Eq. 1.4 and 1.5.

$$\gamma + p(uud) \rightarrow K^+(u\bar{s}) + \Lambda^*(uds) \rightarrow K^+ + p + K^- \tag{1.4}$$
$$\gamma + n(udd) \rightarrow K^-(\bar{u}s) + \Theta^+(uudd\bar{s}) \rightarrow K^- + n + K^+ \tag{1.5}$$

Because of these features, photoproduction of $\Lambda(1520)$ from protons bears a close resemblance to that of Θ^+ from neutrons.

$$\gamma + d \rightarrow \Lambda(1520) \ + \Theta^+ \tag{1.6}$$

An associated photoproduction of $\Lambda(1520)$ and Θ^+ might be performed from the deuterons, as shown in Eq.1.6. One possible Feynman diagram is shown in Fig. 1.15.

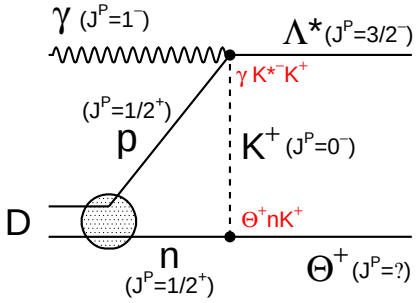

Figure 1.15: Feynman diagram of $\Lambda(1520)$ and Θ^+ associated photoproduction from deuterons. [14]

1.2 Previous results

In order to determine the contributions to $\Lambda(1520)$ production quantitatively, we use same fitting function, Eq. 1.7, as that of CLAS experiment [21] to fit the $\cos\theta_{K^-}$ decay angular

distribution by assuming only K^{*-} and K^- exchanges dominate $\Lambda(1520)$ production.

$$f(\theta_{K^-}) = \alpha(\frac{1}{3} + \cos^2\theta_{K^-}) + \beta \sin^2\theta_{K^-} + \gamma \cos\theta_{K^-}, \tag{1.7}$$

and

$$\alpha + \beta = 1 \tag{1.8}$$

α and β indicate the fraction of helicity-1/2 and helicity-3/2 respectively. The last term, "$\gamma \cos\theta_{K^-}$", in Eq. 1.7 describes an asymmetric distribution represented the interference with spin-$\frac{1}{2}$ background hyperons.

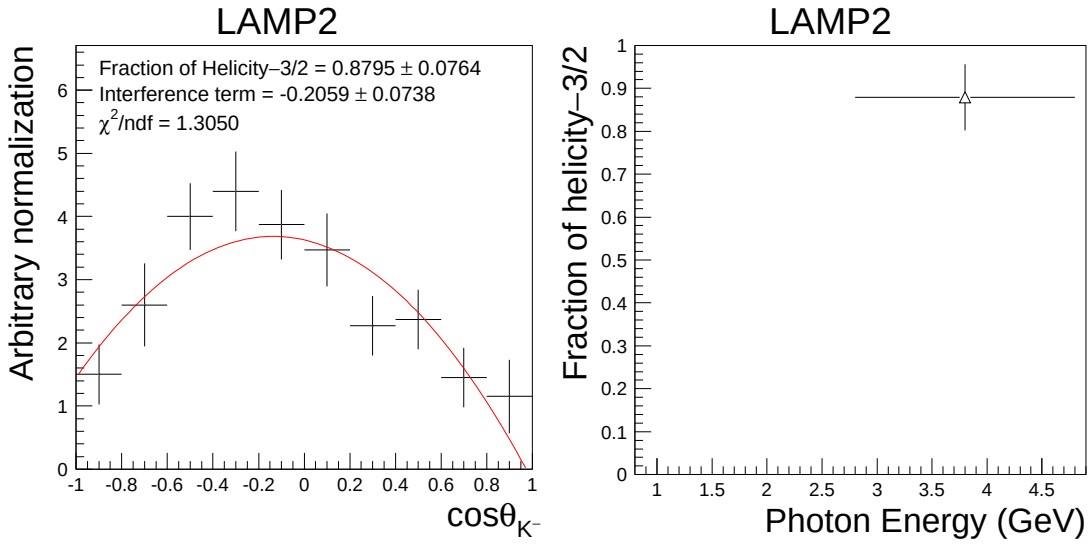

Figure 1.16: The $\cos\theta_{K^-}$ distribution in t-channel helicity frame and fitting result of LAMP2 experiments.

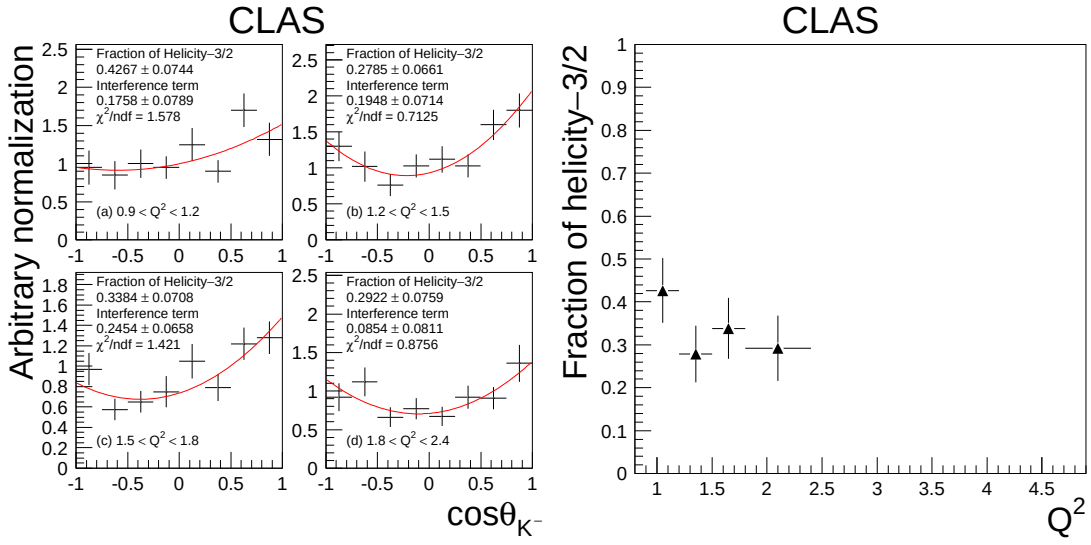

Figure 1.17: Four $\cos\theta_{K^-}$ distribution in t-channel helicity frame and fitting results of CLAS experiments.

By utilizing Eq. 1.7 and the constrain Eq. 1.8, the fitting results of previous 2 experiments, LAMP2 [13] and CLAS [21], are shown in Fig. 1.16 and 1.17 respectively. In LAMP2 exper-

iment, the range of photon energy is from 2.8 to 4.8 GeV. The CLAS facility, however, is an electroproduction experiment, and the data were divided into four regions of Q^2, *virtuality*. It can be seen in the left panel of Fig. 1.16, the $\cos\theta_{K^-}$ distribution of LAMP2 experiment behaves much like the $\sin^2\theta_{K^-}$ as shown in Fig. 1.14. Then, the fitting gives a significant contribution, 88±8%, from helicity-3/2 state. The result of LAMP2 experiment is larger than the upper limit, 75%, of the theoretical prediction of Clebsch-Gordon coefficients in a PURE K^{*-} exchange. On the contrary, four $\cos\theta_{K^-}$ distribution and fitting results of CLAS experiment show a relatively larger contribution from helicity-1/2 state.

The result of LAMP2 experiment indicates a distinct K^{*-}-exchange dominance from photoproduction. On the contrary, the electro-production in CLAS experiment behaves closer to a K^--exchange dominance within the similar energy range as LEPS experiment. There is difference in a dominant component of the helicity state measured by these two experiments. It is unclear whether possible energy, angular or photon-virtuality dependence is the main cause of difference.

1.3 SPring-8/LEPS experiment

In SPring-8/LEPS experiment, a high-intensity polarized photon with an energy range from 1.5 to 2.4 *GeV* provided by the Backward Compton Scattering facility (BCS) was used to interact with protons and deuterons.

Table 1.1: Comparison of experimental conditions between NINA/LAMP2, JLab/CLAS and SPring-8/LEPS

	Reaction	(Virtual) Photon Energy	C.M. Energy
LAMP2	$\gamma p \to K^+\Lambda(1520)$	$2.8 < E_\gamma(\mathrm{GeV}) < 4.8$	$2.48 < \mathrm{W(GeV)} < 3.14$
CLAS	$e^- p \to e'^- K^+\Lambda(1520)$	$0.9 < Q^2(\mathrm{GeV}^2) < 2.4$	$1.95 < \mathrm{W(GeV)} < 2.65$
LEPS	$\gamma p \to K^+\Lambda(1520)$	$1.5 < E_\gamma(\mathrm{GeV}) < 2.4$	$1.92 < \mathrm{W(GeV)} < 2.32$

Making a comparison, as shown in Table 1.1, SPring-8/LEPS experiment covers a relatively lower photon energy around the production threshold. Therefore, it is able to measure cross sections near the production threshold. On the other hand, SPring-8/LEPS experiment has a similar energy range to CLAS experiment with real photon instead of virtual photon of electroproduction. It allows us to clarify the meson exchange dominance in $\Lambda(1520)$ production not only in energy dependence but in the virtuality of photon.

The experimental setup of SPring-8/LEPS will be described in Chapter 2; the scenarios of data analysis including reaction channels, two analytic methods, data samples and event selections will be discussed in Chapter 3. Following with experimental results and discussions including the studies of mass spectrum, background linearity, total/differential cross section from different targets, decay asymmetry and photon beam asymmetry in different detection modes will be presented in Chapter 4. Eventually, we give a summary in Chapter 5.

Chapter 2

Experimental setup

2.1 Light source

2.1.1 Backward-Compton scattering

The production threshold for $\Lambda(1520)$ photoproduction is above 1.75 GeV, thus a GeV photon energy as the incident light source is needed. In 1963, Milburn, Arutyunain and Tumanian purposed the Compton scattering of laser light against high-energy electrons could produce GeV γ ray for the first time, the backward-Compton scattering (BCS) as shown in Fig. 2.1 [22], where the energy of a scattered photon is k_2, E_e is the incident electron energy, k_1 is the laser photon energy, θ_1 and θ_2 are the directions of incoming and outgoing photons respectively.

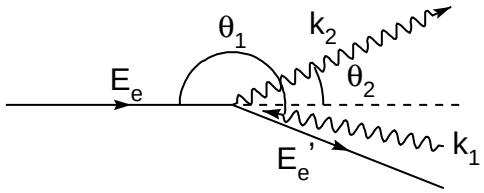

Figure 2.1: Kinematic variables of the backward-Compton-scattering process in the Lab. frame.

Based on the energy-momentum conservation, the energy of a scattered BCS photon energy E_γ is depicted as

$$k_2 = k_1 \frac{1 - \beta \cos\theta_1}{1 - \beta \cos\theta_2 + \frac{k_1(1-\cos\theta)}{E_e}} \tag{2.1}$$

where $\frac{P_e}{E_e} = \beta = \frac{v_e}{c}$ is the velocity of incident electron in unit of the velocity of light, c and $\theta = \theta_2 - \theta_1$. By assuming $\gamma = E_e/m_e \gg 1$, $\beta \simeq 1$, $\theta_1 \simeq 180^\circ$ and $\theta_2 \ll 1$, the Eq. 2.1 can be rewritten as

$$k_2 = \frac{4E_e^2 k_1}{m_e^2 + 4E_e k_1 + \theta_2^2 \gamma^2 m_e^2} \tag{2.2}$$

If the laser photon is anti-parallel to the electron beam and is scattered backward $\theta_2 = 0^\circ$, we would get the highest outgoing photon energy,

$$k_2 = \frac{4k_1 E_e^2}{m_e^2 + 4k_1 E_e}. \tag{2.3}$$

As the incident laser lights are 100% polarized, a backward-Compton scattering photon is polarized at the maximum energy. The polarization drops as the photon energy decreases, as

shown in Fig. 2.2. However, we could change a wavelength of laser lights easily so that the polarization remains reasonably high in the energy region of interest.

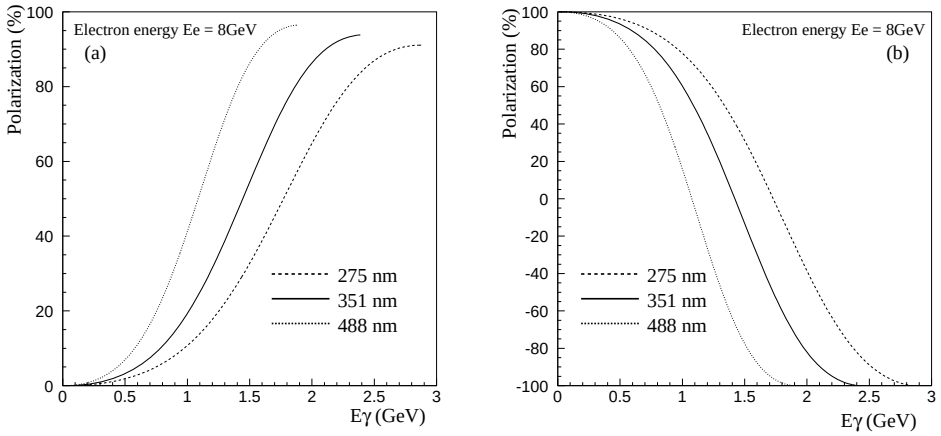

Figure 2.2: While the laser photon is full polarized, the polarization of the BCS photon is a function of E_γ by using the 8 GeV incident electron beam. (a) Linear polarization and (b) Circular polarization.

In Fig. 2.3, the maximum energy E_γ^{max} as a function of incident electron energy E_e is shown with different wavelengths of laser photons. In this experiment, a 351-nm Ar-ion laser (Coherent Sabre) was used to produce BCS photon against the 8-GeV circulating electron bunches in the storage ring of SPring-8, the BCS photon energy is up to 2.4 GeV. The energy spectrum and beam profile of BCS photon beam were measured by a PWO ($PbWO_4$) crystal calorimeter located at 42.8 m far from the center of the straight section inside the laser hutch.

Fig. 2.4 shows the energy spectra of BCS photon beam and Bremsstrahlung beam created in the residual gas in the storage ring. The maximum energy of Bremsstrahlung beam is 8 GeV corresponding to the electron beam energy.

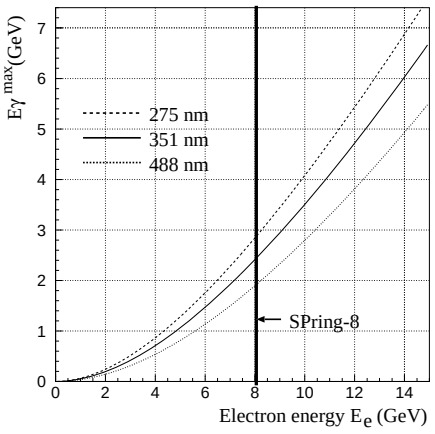

Figure 2.3: Maximum BCS photon energies as a function of energy of the incident electron for laser photons with 275, 351 and 488 nm wavelengths respectively.

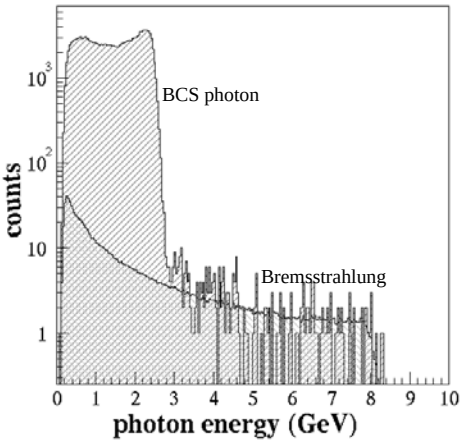

Figure 2.4: Energy spectra of the BCS photon measured by a PWO crystal calorimeter and Bremsstrahlung.

2.1.2 Synchrotron radiation and SPring-8

In October 1988, Japan Atomic Energy Research Institute (JAERI) and the Institute of Physical and Chemical Research (RIKEN) began to plan and to construct a synchrotron radiation facility. In June 1989, Harima Science Garden City was selected as the site for the facility, as shown in Fig. 2.5. In October 1997, SPring-8 opened for research until now. Synchrotron radiation is emitted from an electron traveling at almost the speed of light when its path is bent by a magnetic field. As it was first observed in a synchrotron in 1947 and was named "synchrotron radiation".

Figure 2.5: The location of SPring-8.

SPring-8 (an acronym for Super Photon ring-8 GeV) is a research facility that was built to generate synchrotron radiation, "the light of modern science". Fig. 2.6 is a bird's eye view of SPring-8. Because is has highest electron energy, the largest circumference and advanced insertion devices, SPring-8 is the one of the world's most powerful third-generation synchrotron radiation facility.

Figure 2.6: Bird's Eye View of SPring-8.

SPring-8's main facilities are shown in Fig. 2.7, the accelerator complex is composed of an injector linac (linear accelerator), a booster synchrotron and a low emittance storage ring. It generates electrons with an electron gun, and accelerates them to energy of 1 GeV, The accelerated electron beam is transported to the synchrotron, which then accelerates it to 8 GeV. Finally, the beam is injected into the storage ring and stored with the energy of 8 GeV.

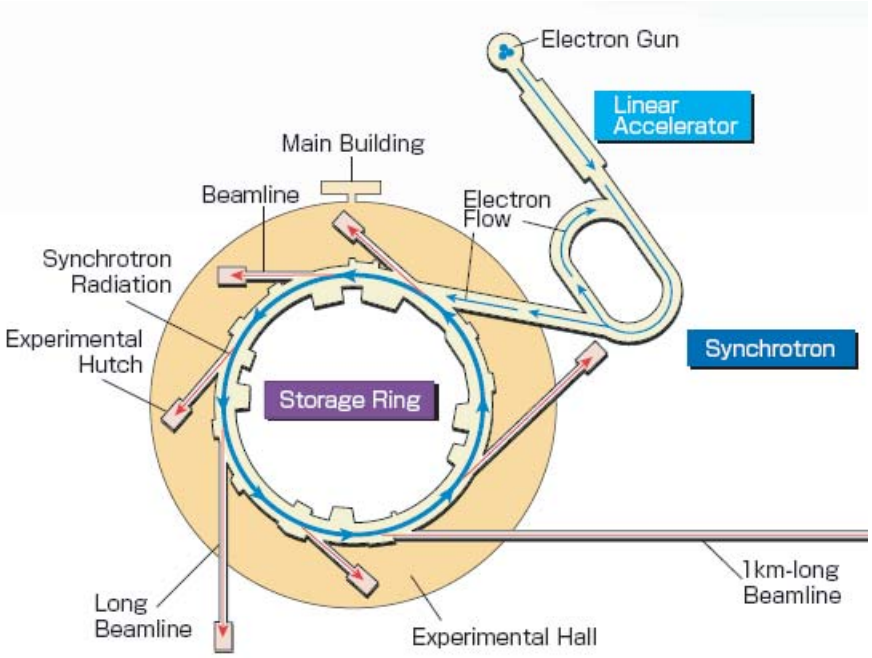

Figure 2.7: SPring-8's main facility.

2.1.3 Laser system

The 100% linear polarized, horizontal or vertical polarization, laser system we used as the light source in the initial stage is an Argon laser. A 5W Argon laser has 2W output power at 351nm (3.5 eV). The GeV photon beam at SPring-8 is produced by backward-Compton scattering of laser photon from 8 GeV electrons with the maximun photon energy of 2.4 GeV. Those high-energy photons were transported through the beam pipe to the experimental hutch where the detector located. If a higher power laser with 5 W output is used, it increases the intensity of BCS photon beam to about 10^7 photons/sec.

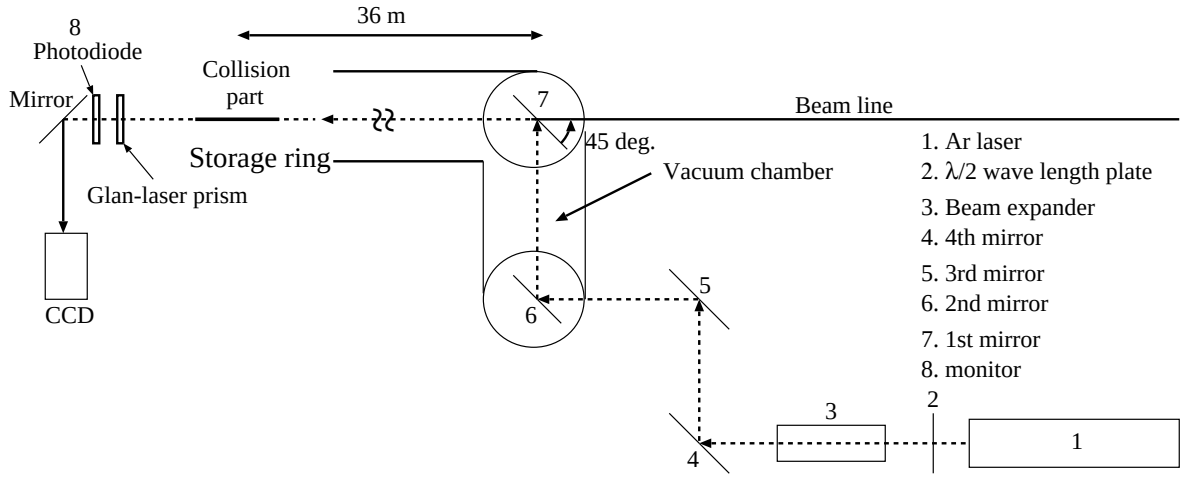

Figure 2.8: Schematic view of the laser operation system.

Fig. 2.8 shows the schematic view of Argon laser operation system. The laser photon passed

through $\lambda/2$-wavelength plate to change its polarization. Beam expander was used to adjust the laser beam profile. After that, the extended laser beam was navigated to the collision part inside the storage ring. At the end of the straight section in the storage ring, we measured the polarization angle and degree by rotating the Glan-laser prism, the intensity of the laser was measured behind the prism with a photodiode as a function of rotation angle. The intensity distribution for laser photon polarization measurement were shown in Fig. 2.9.

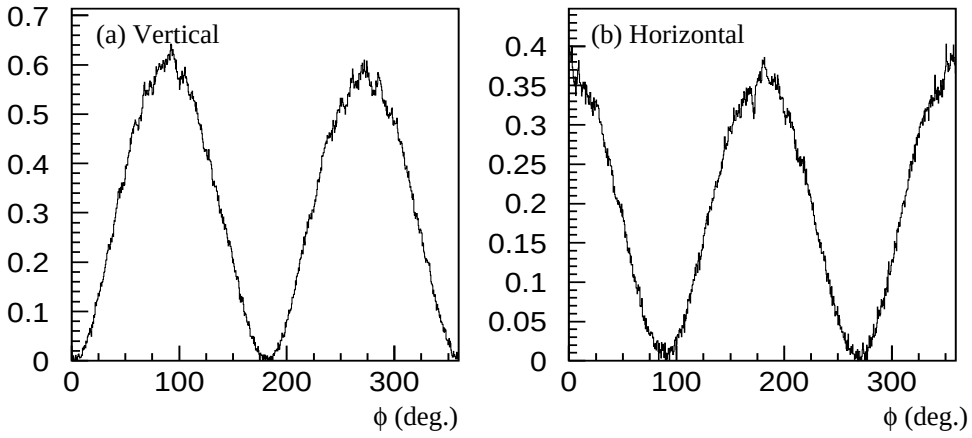

Figure 2.9: Intensity of photodiode output as a function of the angle of Glan-laser prism for (a) vertically polarized laser photons and (b) horizontally polarized laser photons.

Fig. 2.10 shows the overview of our experimental facility, the Laser Electron Photon facility at SPring-8 (LEPS).

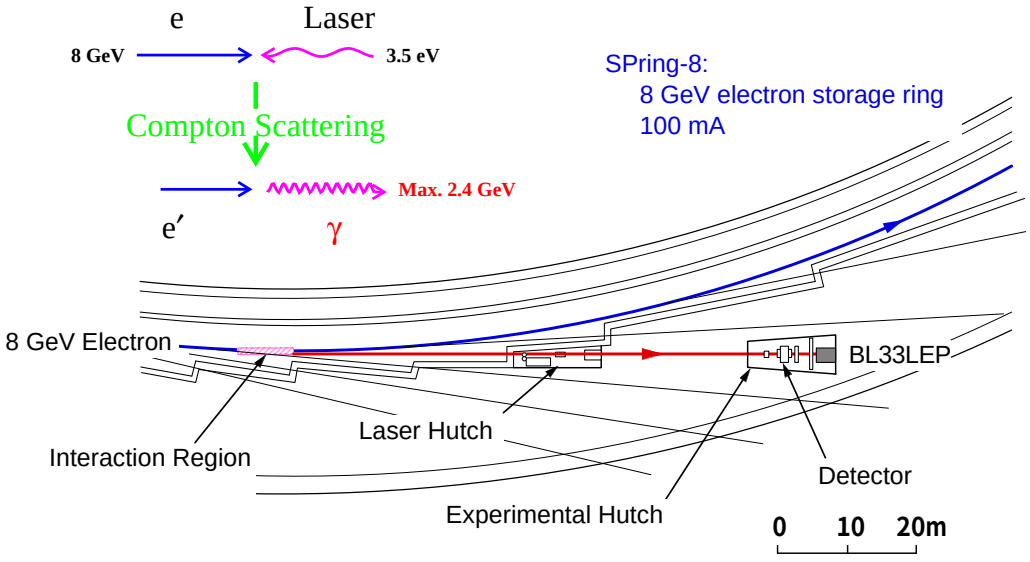

Figure 2.10: Overview of LEPS.

2.1.4 Tagging counter (Tagger)

Based on the energy conservation, the energy of BCS photons, E_γ, was determined by measuring the energy of recoiled electron, $E_{e'}$. $E_\gamma = E_e - E_{e'}$, where E_e is the energy of electron beam inside the storage ring (7.975±0.003 GeV). As shown in Fig. 2.1, an electron scattered by BCS process will lose its energy. After passing through the bending magnet, the scattered electron deviated from its normal orbit in the storage ring and was detected by the tagger counter located at the downstream of bending magnet of the storage ring. The displacement determined by the tagging counter was proportional to the energy of recoiled electron, the scheme of tagging counter is shown in Fig. 2.11. The energy resolution, 15 MeV, was estimated by measuring electron-positron pair production by the BCS photons with the LEPS spectrometer.

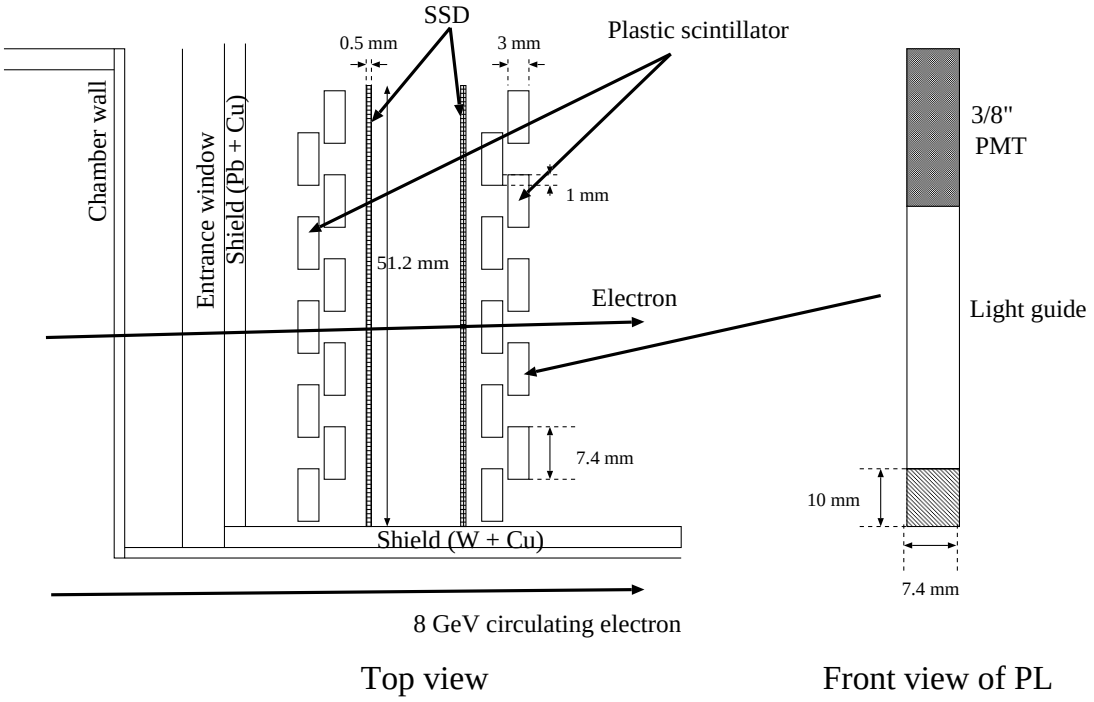

Figure 2.11: Tagging counter.

2.2 Spectrometer

The whole measurement system includes two parts: readout system and detectors system. As shown in Fig. 2.12, the LEPS detectors setup from upstream consists of a upstream-veto counter (UPveto), a Liquid Hydrogen/Deuterium target (LH_2/LD_2), a plastic scintillator (trigger counter), an aerogel Čerenkov counter (AC), a silicon strip detector (SSD), three drift chambers (DCs), a dipole magnet and a time-of-flight wall (TOF). Each part of detectors has connection with the readout system for data-acquisition.

UPveto The UPveto was used to reject the pair-production e^+e^- converted from BCS photons in air, the residual gas or Al window of the beam pipe.

LH_2/LD_2 target A 50mm-long liquid hydrogen/deuterium target were used in this experiment, it was located at the 952 mm upstream of the center of dipole magnet. The shape

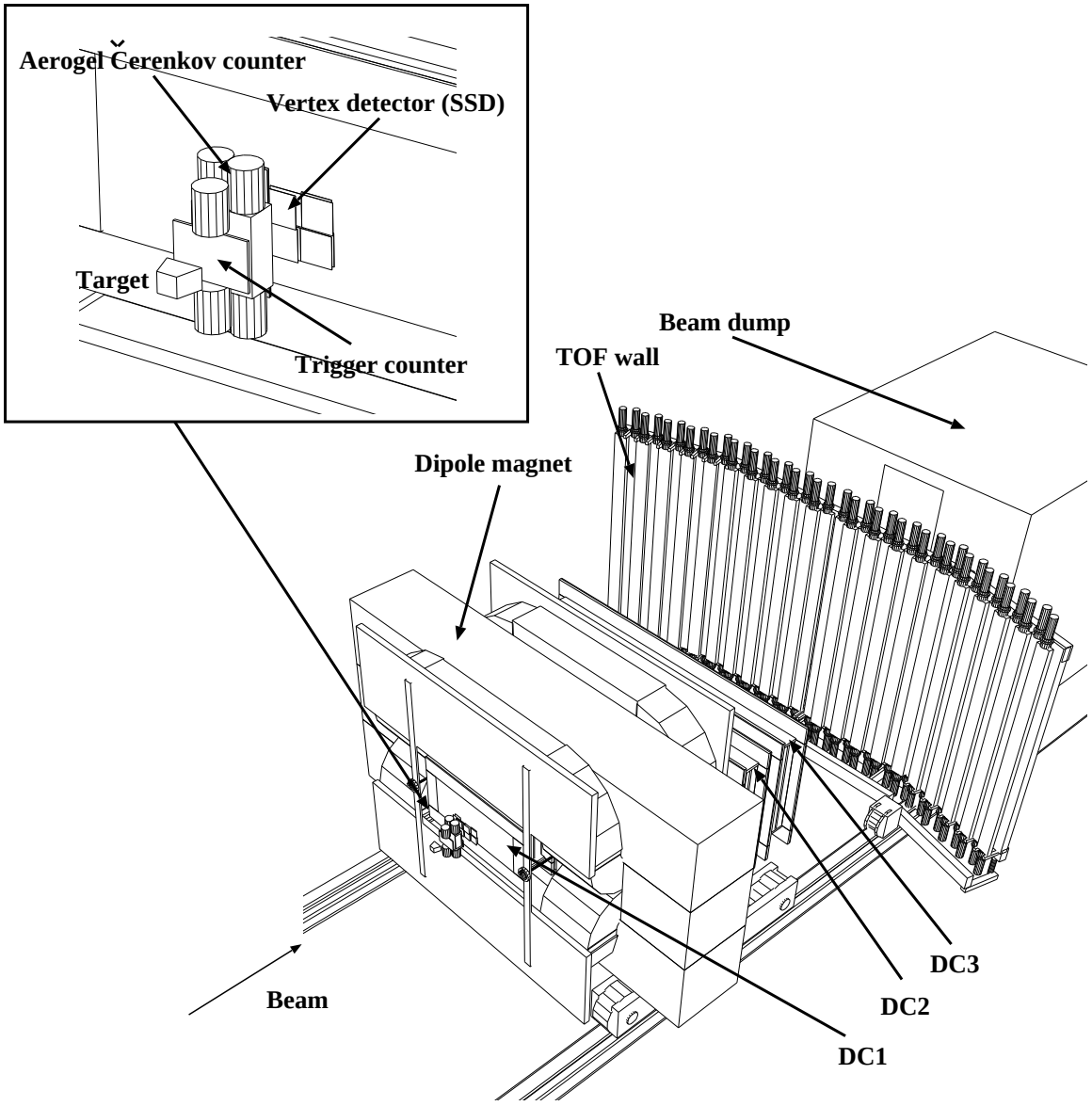

Figure 2.12: The setup of LEPS detectors.

of target cell was designed to avoid the loss of acceptance of charged particles detected by spectrometer.

AC The aerogel Čerenkov counter is just downstream of the plastic scintillator. Based on the Čerenkov radiation theory, the AC counter helps us to do a selection that throws away charged particles whose velocities are very large or are greater than the velocity of photon in a medium.

SSD When a thin and high-resolution detector is required near an interaction region, the silicon strip detector is very useful. As an incident charged particle passed through the silicon, it deposits ionization energy and dislodge electrons. Due to the electric field inside the SSD, the ionization energy causes a separation of the electrons and holes. The SSD collect at the electrode, giving a signal proportional to the deposited ionization energy. In LEPS, the SSD consists of 2 planes (x- and y-) of single-sided silicon strip

with a thickness of 300 μm and a width of 120 μm pitch.

DCs Charged particles passing through the drift chamber liberate electrons that drift toward the anodes. After electrons are collected at the anode, the provide a signal that a particle has passed. This signal is fed into TDC and ADC module. According to the drift time of electrons, we could determine the accurate hit position in the chamber that was traversed by the incident particle in terms of typical resolution. In LEPS, a 5 planes (x, x', y, y', u) multi-wire drift chamber (DC1) is located upstream of the magnet and two sets of multi-wire drift chambers (DC2 and DC3) are located downstream of the magnet. The active area size of DC2 and DC3 is 200 cm (width) $\times$ 80 cm (height). Both of two sets have 5 planes (x, x', y, y', v).

Dipole Magnet The dipole magnet in LEPS is a bending magnet whose size is 135 cm (wide) $\times$ 55 cm (high). The length of the pole is 60 cm, and its field strength at the center is 1 Tesla. With the dipole magnet, we can determine the momentum of charged particle.

TOF wall In this experiment, it needs a clock to measure the time of flight while particles fly through whole detectors. Here, we utilize the scintillator counters to give us a stop signal. As shown in Fig. 2.13, the TOF wall contains 40 2m-long plastic scintillation bars with a cross section of 4 cm (thickness) $\times$ 12 cm (width). The start signal, T_0, for time measurement is provided by a RF signal from 8 GeV storage ring, where electrons are bounded at every 2 nsec (508 MHz) with a width (σ) of 12 psec. Since the speeds of both electron beam and a laser-electron photon are the same, the arrival time of laser-electron photon at the target is synchronized with the RF signal. When a charged particle passes through the trigger counter, an output signal is transported to the readout system. Here is the first stop of time measurement, T_1. Then, the charged particle hits on the TOF wall. This hit gives us the second stop, T_2. Finally, the real time of flight is the difference of 2 stop time, $\Delta T = (T_2 - T_0) - (T_1 - T_0)$.

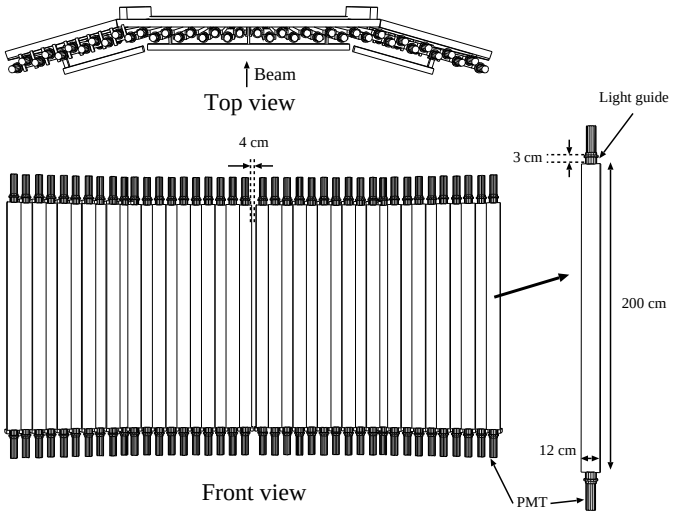

Figure 2.13: Drawing of the TOF wall.

2.3 Time Projection Chamber

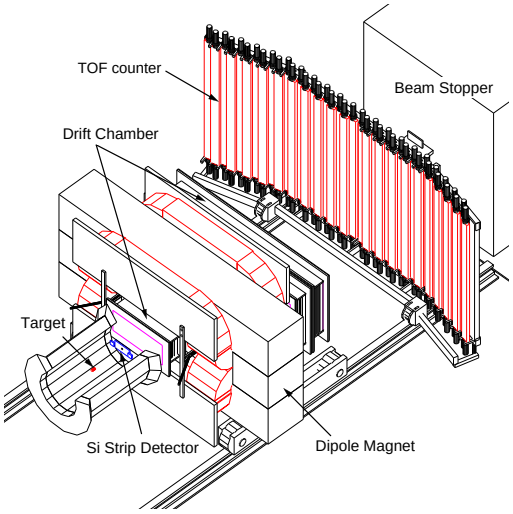

Figure 2.14: LEPS detectors.

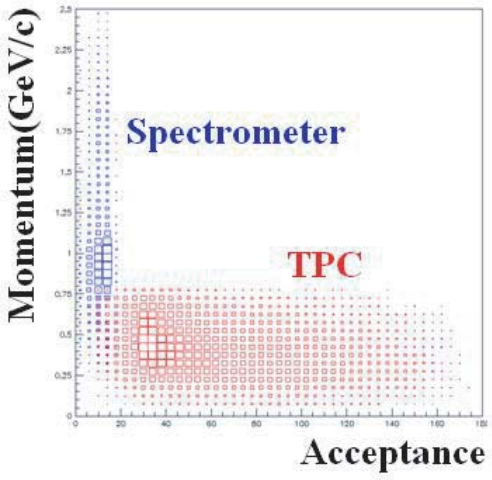

Figure 2.15: Comparison of detection for acceptance and momentum between Spectrometer and TPC.

As described in previous section, the LEPS Spectrometer was designed to detect the charged particle in the very forward region with high momentum. In order to complement the detection for wider acceptance and low-momentum charged particles in LEPS experiment, a 4-π detector, Time Projection Chamber (TPC) embedded inside a 2-Tesla solenoid superconducting magnet, was brought in for this purpose and set in front of Spectrometer, as shown in Fig. 2.14. The comparison of detection for acceptance and momentum between Spectrometer and TPC is shown in Fig. 2.15.

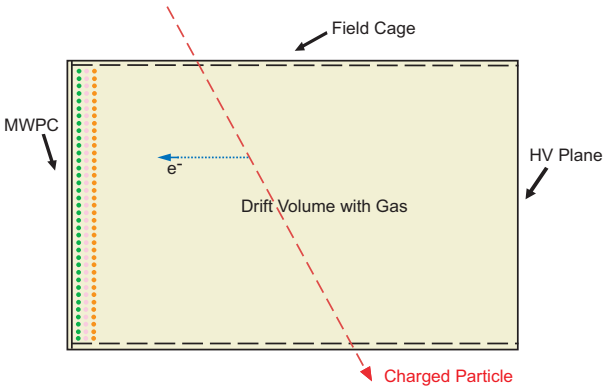

Figure 2.16: The basic elements of a TPC

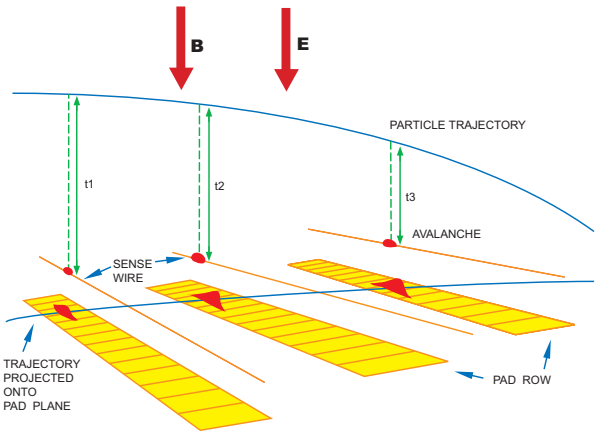

Figure 2.17: The schema of the drift and detection process of electrons on the sense wires.

The TPC [23], as shown in Fig. 2.16, consists of a large drift volume in a uniform electric field provided by High-Voltage plane on one side and the surrounding field cage, terminated by Multi-Wire Proportional Chamber (MWPC) on the other side. The wall of field cage parallel to the direction of drift are installed with electrodes connected by a resistor chain creating a linearly potential.

While the charged particles pass through the drift volume, the energy loss from the traversing charged particles ionizes the gas molecules inside the drift space then produce the ions and ionized electrons. Under the influence of electric field, the ionization electrons drift towards the MWPC. The electrons arriving at MWPC are multiplied by gas amplification then produce the avalanche on the sense wires, as shown in Fig. 2.17. The avalanche on the sense wire then produce the image charges on the some small segmented area of cathode plane underneath, usually called pads. Both signals from sense wires and pads were transferred through the pre-Amplifier, shaper and Flash-Analog-to-Digital converter (FADC) for data acquisition. Combined the drift time for each of the pad signals, the TPC is able to provide three-dimension particle trajectories by electronic means. Typically, the TPC is embedded in a uniform magnetic field whose direction is parallel to the electric field. It does not only allow to measure the momentum of charged particle from the track curvature but also improves the spatial resolution and resolving power by suppressing the transverse diffusion of electrons during the drift process.

In order to make sure that low-momentum charged particles are detected at large dip angle or backward direction, as shown in Fig. 2.18, six trigger scintillators were set to surround the TPC. Furthermore, the wire signal from avalanche or image charge signal on each pad can provide the specific energy loss, dE/dx, of charged particles, helping us to make the particle identification. It can be seen from Fig. 2.19, by requiring two charged particles were detected by forward spectrometer, p, K^+, π^+ and π^- bands can be identified clearly.

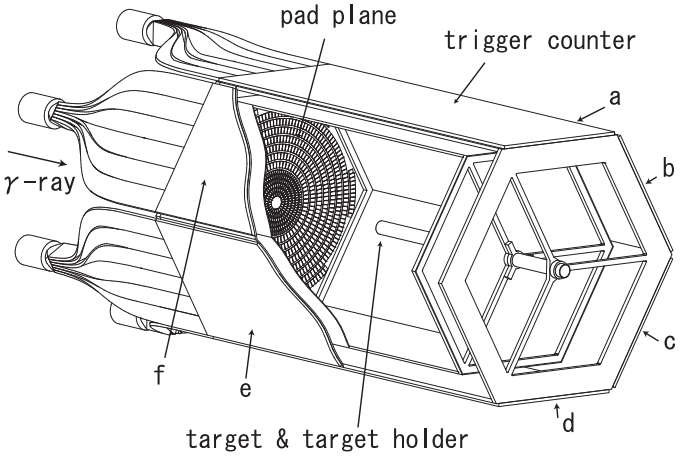

Figure 2.18: The schema of TPC surrounding by six trigger scintillators (a-f).

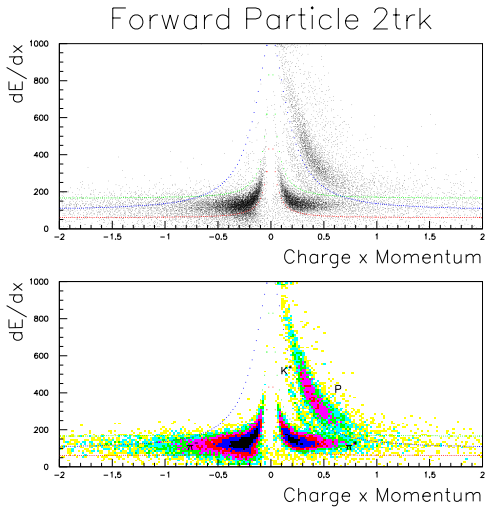

Figure 2.19: Particle identification of TPC by "dE/dx" versus "charge×momentum".

In LEPS experiment, there are two-generation TPCs including circular configuration pads plane with one-dimension wires for nuclei targets (C, Cu and CH_2) and hexagonal configuration pads plane with hexagonal wires for liquid hydrogen and deuterium targets, as shown in Fig. 2.20. Through the first TPC, we are able to study the $\Lambda(1405)$ photoproduction where a kink decay to $\Sigma^{\pm}\pi^{\mp}$ can be obtained within the inner layers; or the medium effect of ϕ photoproduction from different nuclei targets. First result from LEPS first TPC was studies and published by M. Niiyama *et al.* about "Photoproduction of $\Lambda(1405)$ and $\Sigma^0(1385)$ on the proton at E_γ = 1.5-2.4 GeV" [24]. After enlarging the inner space for cooling system, the second-generation TPC allows us to study the claimed Θ^+ photoproduction in the backward direction from liquid hydrogen and deuterium targets.

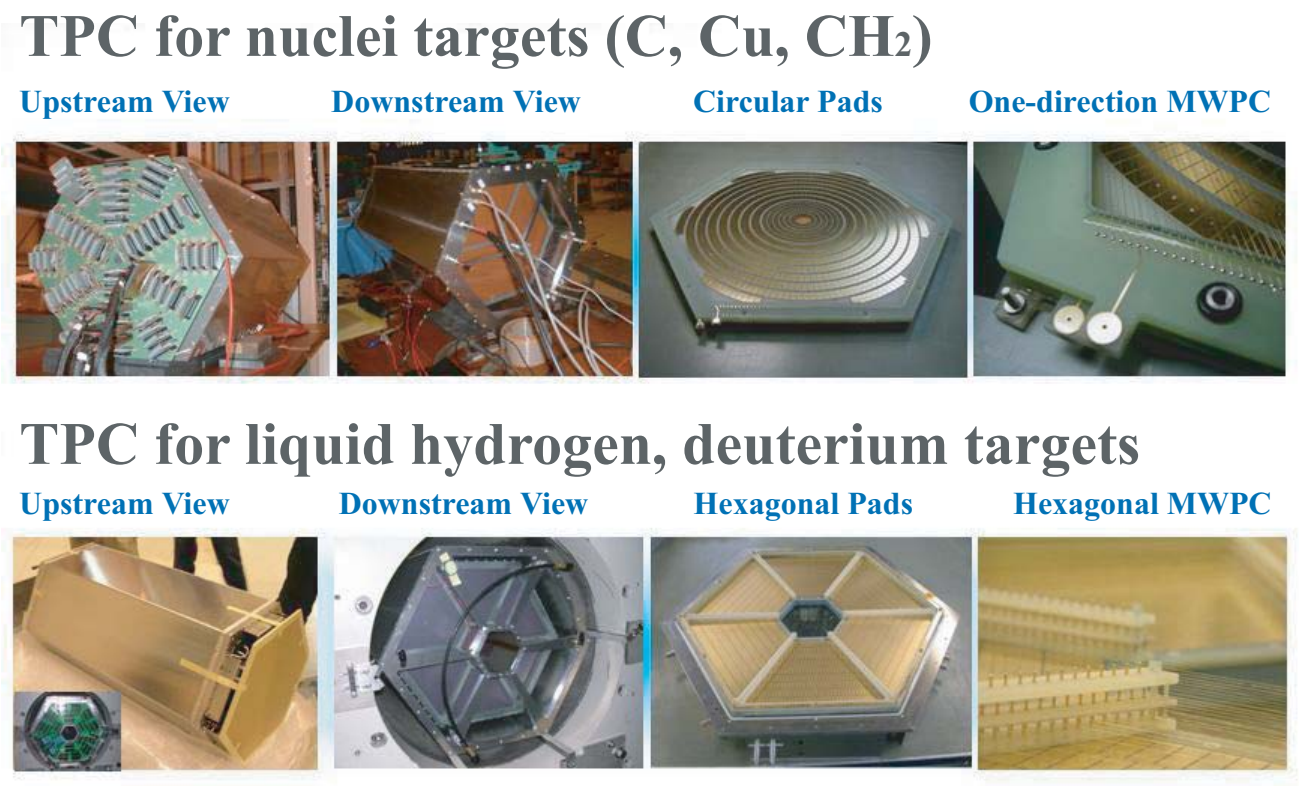

Figure 2.20: Two-generation TPCs in LEPS experiments.

In the following sub-sections, the operational principle and configuration of MWPC and basic concept of data analysis from FADC signal to track construction, based on the first generation TPC, will be discussed briefly.

2.3.1 Multi Wire Proportional Chamber

The MWPC consists of a cathode plane and three wire grids above it: The wire grid containing the sense/field wires, shielding wires closes the volume of the proportional region, and the gating wire, as shown in Fig. 2.21.

Sense Wires The sense wires are the anode wires of the proportional cell and are at positive high voltage with respect to the surroundings. The electrons arrive from the drift volume towards these wires and initiate the avalanche process there.

Field Wires The field wires serve to electrically decouple the sense wires.

Shielding Wires The shielding wires are to hold the same potential as the cathode plane, to align the electric-field lines.

Gating Wires The uniformity of the electric field is of prime importance in a TPC. Even if the field cage creates a homogeneous field, it can be destroyed by the presence of space charge in form of ions in the drift volume. The problem of space charge can be reduced by a gating wire which in its closed state prevents electric charges from traversing the wire. Fig. 2.20 shows the electric field for the two states of a gating grid.

Open State The gating wire is at a potential corresponding to its location, nearly not disturbing the original field.

Closed State A potential difference between the two semi-wires is applied such that a dipole field is created to stop the ions created in the avalanche process from traveling back into the drift volume, and to stop the electrons coming from the drift volume before they enter the proportional region.

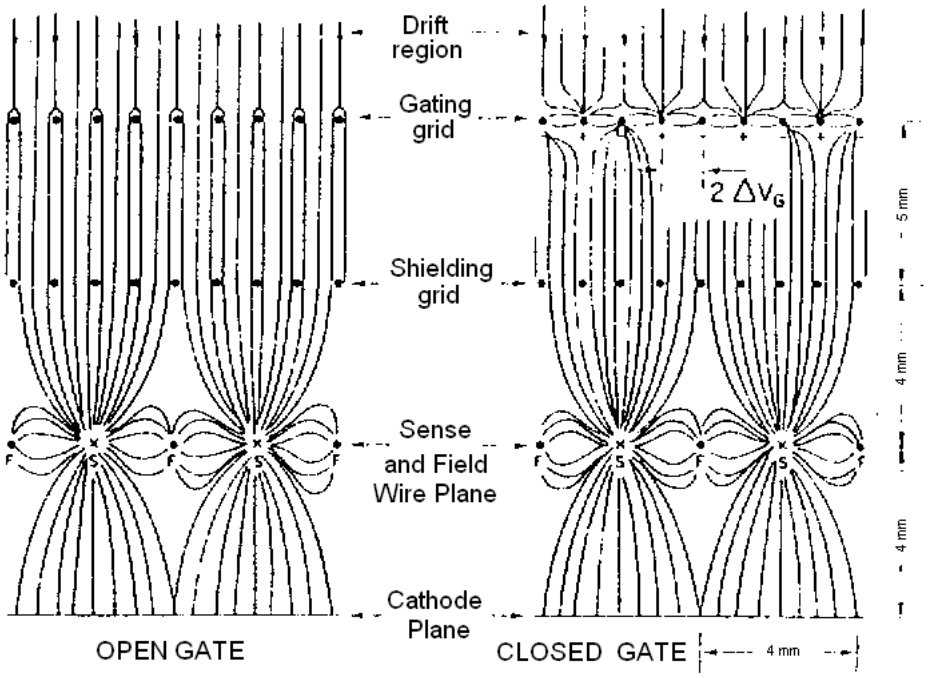

Figure 2.21: Electric field lines with the gate in "open state" and in "closed state". [23]

2.3.2 From FADC signal to track construction

FADC signals For LEPS first TPC, there are totally 1152 FADC channels used for readout, 1056 channels for pads and 96 channels for wires. To scan all the FADC channels, according to the DATAID (ID=1 for ADC, ID=2 for TDC and ID=3 for Trailer), then obtain the pulse profile as shown in Fig. 2.22.

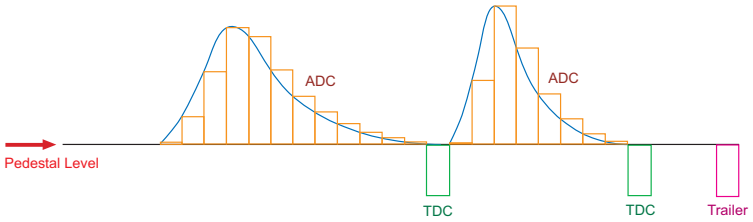

Figure 2.22: The schematic ADC, TDC and Trailer.

Suppress pedestal A real ADC signal should have its limitation. That means that the ADC height must greater then one specific value called pedestal. Therefore, all the ADC heights obtained from scanning FADC channels need to have the pedestal removed. As shown in the Fig. 2.22, a real pulse profile must be higher then the pedestal level. Unfortunately, the pedestal level would vary with time. Even if the variation of the pedestal level is not so large, it is better to measure the pedestal level every 5 or 6 hours.

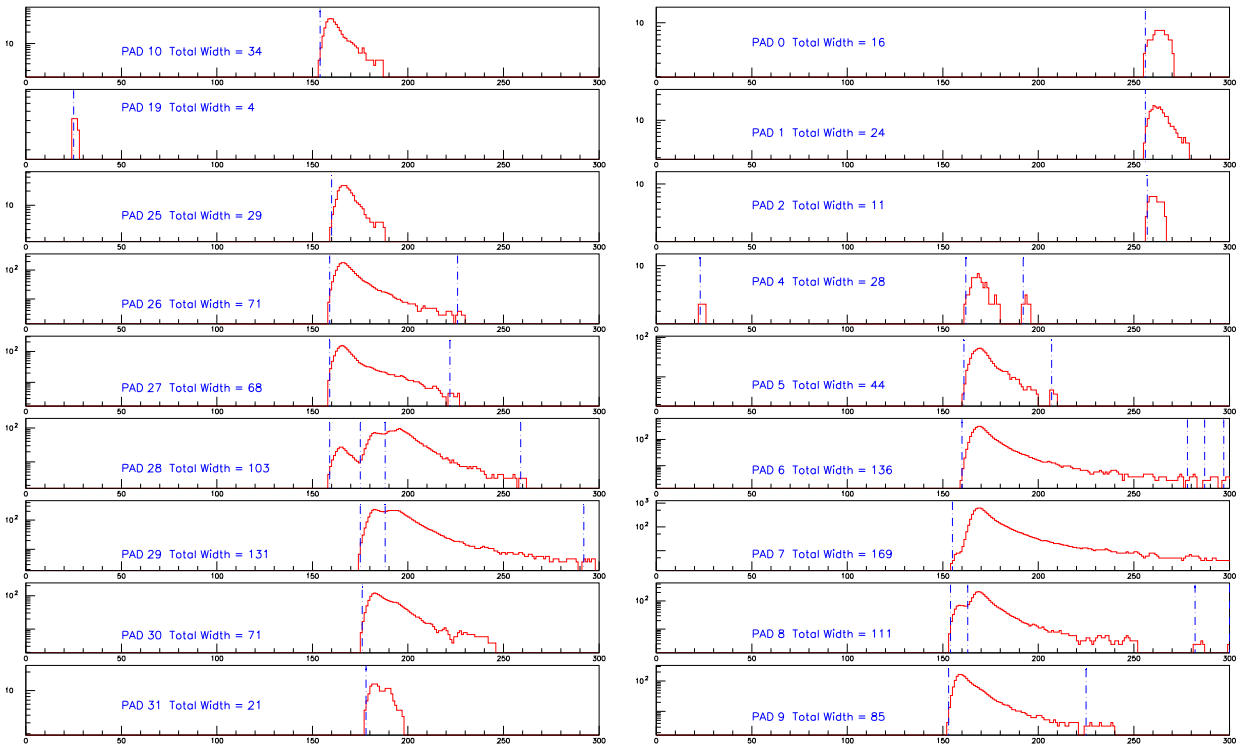

Figure 2.23: Pulse shape on layer 1 of R32338 Event4.

Set pulses To describe a pulse clearly, it includes ADC and TDC of pulse peak bin, width of pulse, sum of ADC value, mean value of TDC (center of gravity of this pulse) and the TDC of final ADC bin. So, to scan whole ADC bins in each channel, the specific pulse configuration could be obtained. Fig. 2.23 is a real-event example about the pulse profile, it is from Layer 1 of 4th event of run 32338. The vertical dashed lines in each small plot show the beginning of this pulse, and the `PAD 0" or "PAD 1" which show the pad number correspond to the position on transverse plane.

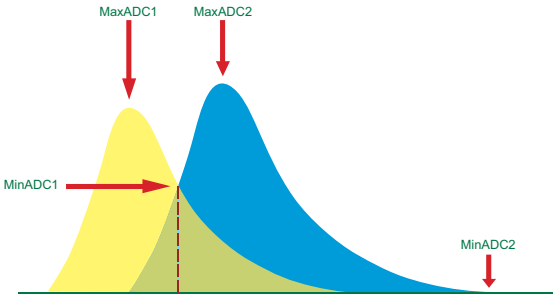

Figure 2.24: Schematic pileup pulses.

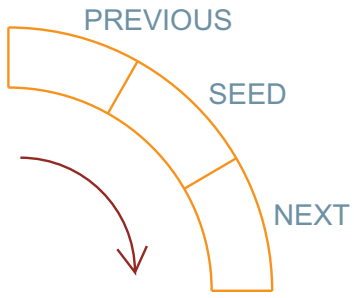

Figure 2.25: Forming cluster on the same layer, using one pad as a seed and then searching the neighboring pads.

Pileup pulse Usually, it would has the pile-up pulse on one pad as shown in Fig. 2.24. Two pulse are overlapped. Current criteria to define a pile-up pulse are listed below.

- There are more then one peak inside the pulse profile.

- The difference between MaxADC1 and MinADC1 is greater then 15.

To separate the pile-up pulse is fitting the pile-up with two individual pulses, and then two separated pulses could be obtained. But, the current analysis is to slice from the TDC value of MinADC1. Therefore, there are two incomplete pulses. This part would be improved by the two-individual-pulse fitting later.

Form clusters After obtaining the pulses in the individual pad, according to the order of pads and layers, to search the pulse on each pad from first pad of the first layer. When there is one pulse or several pulses on one pad, using the first pulse of this pad as a seed, then check the time overlap in the neighboring pads, next one and previous one as shown in Fig. 2.25.

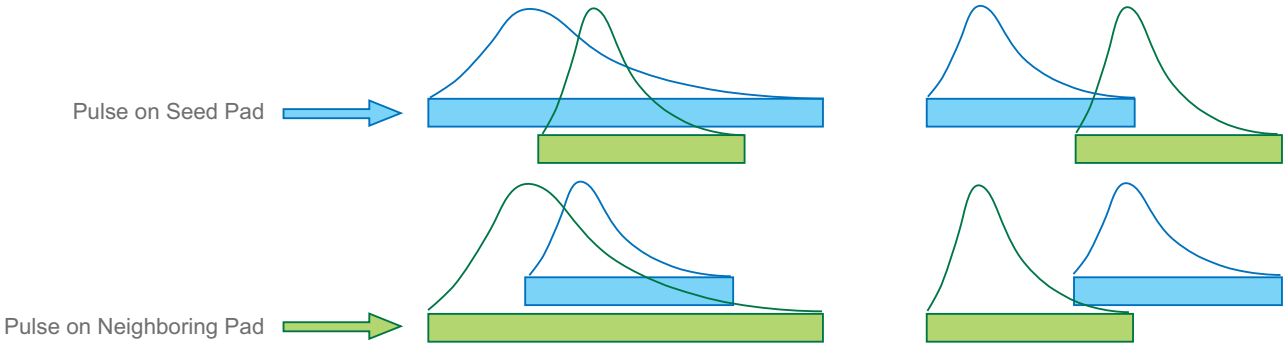

Figure 2.26: Comparing the time overlap between the pulse on seed pad and the one on neighboring pad

To compare the time overlap between the pulse on seed pad and the one on neighboring pad, as shown in Fig. 2.26, if the the neighboring pulse satisfies any one of four types, the neighboring pulse would be involved in the same cluster and then used to be a new seed to search the other pulses on new neighboring pads. Hence, one cluster could involve many pulses on many pads, no matter if those pulses are on the same pad, if and only if those pulses are on the neighboring pads and satisfy the criterion about time overlap.

Set hits Following from clusters, "Hit" could be got by analyzing clusters. The cluster which pulses within could be used to pick out the hits should obey the following criteria.

- A cluster must contains pulses more than two pulses.
- A cluster must have a pulse which its height(peakADC) greater than four channels of ADC.

One hit is composed of three pulses on three neighboring pads on the same layer respectively. However, by some reason, pulses located on three neighboring pads but different layers are suspended now. Currently, to set one hit, it is not allowed that number of pulses are less than or more than three pulses. Pulses located on the same pad is also forbidden.

In order to find the three pulsed on the neighboring pads, the algorithm is as follows.

1. Clusters have to be satisfy the above criteria.

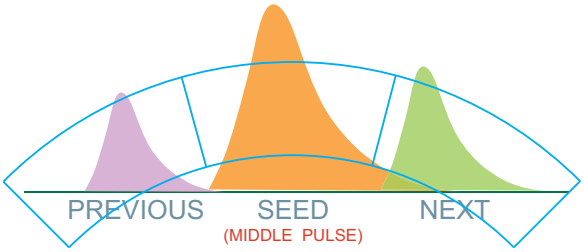

Figure 2.27: One hit is composed of three pulses on the neighboring pads respectively.

2. Sorting the pulses within one cluster by peak ADC from high to low.
3. To choose the pulse with higher peak ADC as a SEED, and then to check the pulse which peak ADC is lower than the seed one, if this pulse is on the neighboring pad(next or previous pad), it would be picked out to set as a member of one hit. As mentioned before, one hit could only contain 3 pulses, the middle pulse should have higher peak ADC than two side ones, as shown in Fig. 2.27. It is the reason to sort the ADC height and utilize the higher ADC one as a seed.

Find track candidates If a hit has a pulse which its height is greater than the threshold of ADC to be selected, it would be used as a selected-hit for track finding. Two real events were shown in Fig. 2.28, a 3-d event display was shown in left plot and a 2-d plot by Runge-Kutta tracking method is shown in the right plot. Eventually, to measure the momentum from trajectory curvature and the energy loss from FADC signal of each track, the particle identification can be obtained as shown in Fig. 2.19 for further studies.

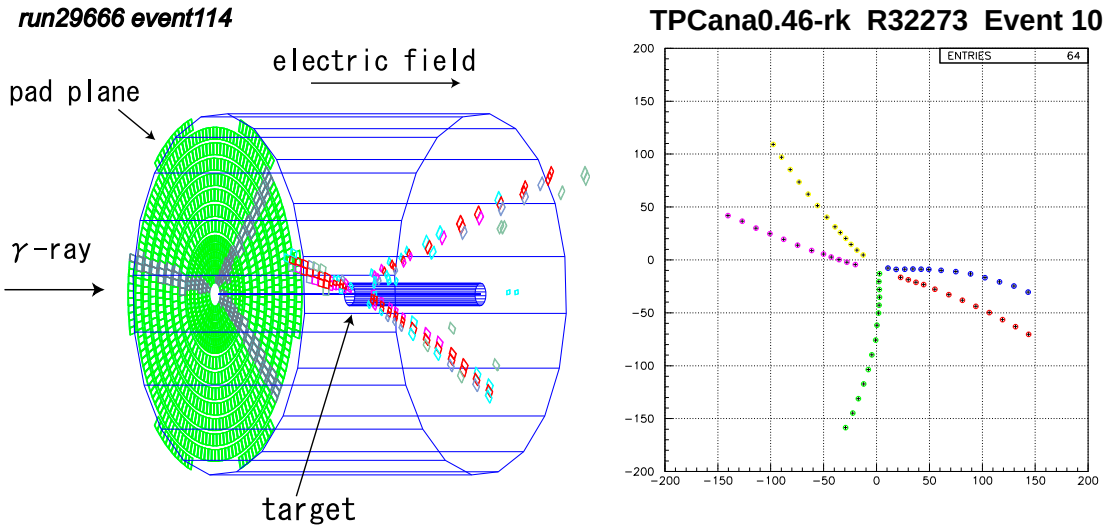

Figure 2.28: Two real events are shown by 3-d event display in the left plot and 2-dimension plot by Runge-Kutta tracking method in the right plot.

Chapter 3

Analysis method

In analysis, the photoproduction of $\Lambda(1520)$ from two targets, hydrogen and deuterium, was studied in K^+K^-, K^+p and K^-p detection modes. The side-band method for background estimation is the main feature of this work, in contrast to Monte-Carlo fitting one [25] and the individual results are compared. The results of production from protons and deuterons enable the study of photoproduction from neutrons. The 3 detection modes, K^+K^-, K^+p and K^-p pairs, are complementary in coverage of acceptance, so that backward (K^+K^- and K^+p) and forward (K^-p) productions of the $\Lambda(1520)$ in the c.m. system can be examined, respectively.

3.1 Reaction channels

In the beginning of data analysis, all the reaction channels will be shown first, and help us to identify the production channels and background channels.

1. Production Channels
   (a) $\gamma + p \rightarrow K^+ + \Lambda^* \rightarrow K^+ + K^- + p$
   (b) $\gamma + d(p) \rightarrow K^+ + \Lambda^* \rightarrow K^+ + K^- + p$
   (c) $\gamma + d(n) \rightarrow K^0 + \Lambda^* \rightarrow \pi^+ + \pi^- + K^- + p$
2. Background Channels
   (a) $\gamma + N \rightarrow \phi + N \rightarrow K^+ + K^- + N$
   (b) $\gamma + N \rightarrow K^+ + K^- + N$
   (c) $\gamma + d \rightarrow \Theta^+ + \Lambda^* \rightarrow n + K^+ + p + K^-$

3.2 Detection modes

According to the production/background channels listed above, what we actually interested are K^- and p generated from the decay of $\Lambda(1520)$ events, mainly focusing on the 3-particle final state (K^+, K^-, p). However, not all the K^- and p come from the decay of $\Lambda(1520)$. They can also be the productions of ϕ photoproduction or some other else. For convenience, we rearrange the three particles K^+, K^- and p into three sets of two-track detection modes, K^+K^-, K^+p and K^-p detection modes. By requiring a missing particle $p/K^-/K^+$ corresponding to its

detection mode $K^+K^-/K^+p/K^-p$ based on the energy momentum conservation, $\Lambda(1520)$ photoproduction can be studied. For example, as shown in Fig. 3.1, K^-p detection mode means that K^- and p are detected by forward spectrometer accompanied a backward missing K^+.

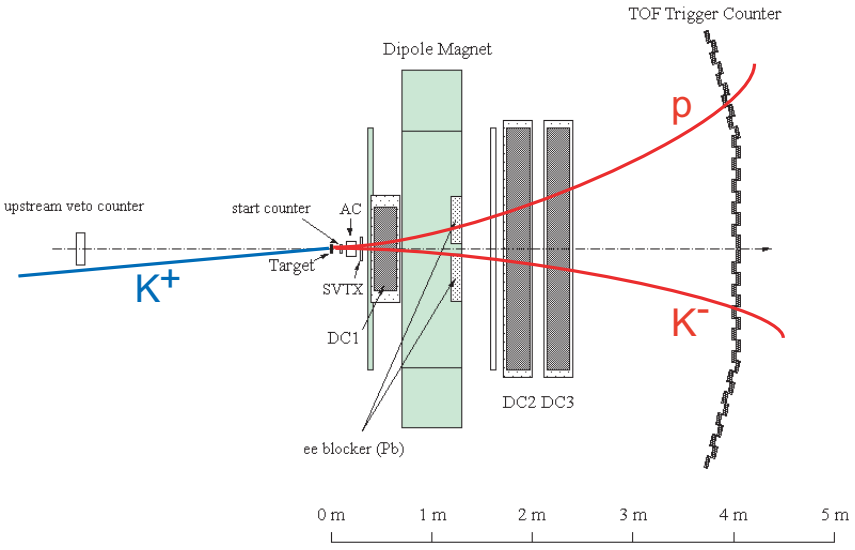

Figure 3.1: The schema of side-band subtraction method.

3.3 Analysis scenarios

In this analysis, it strongly depends on the fitted Monte Carlo ntuples generated by Muramatsu [25]. Not only to evaluate the number of yield by subtracting simulated background from mass spectrum of data, but also to determine a reasonable mass spectrum range over which property of good linearity is shown for side-band subtraction study. It is not always true that good background linearities were found in the interested kinematic region. In such case of bad background linearity, a further non-linearity correction is needed. "Side-Band subtraction", "Monte Carlo Fitting" and "Non-Linearity Correction" will be discussed individually.

3.3.1 Background non-linearity

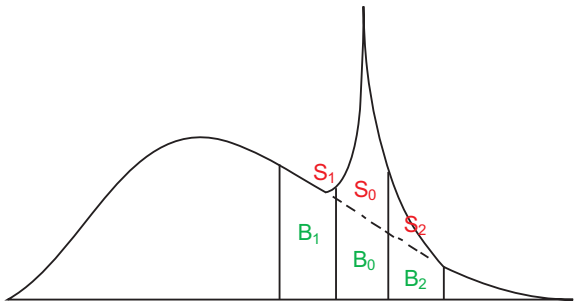

Figure 3.2: The schema of side-band subtraction method.

Before discussing the side-band subtraction method, the most important issue is how to determine the background *linearity* or vice versa *non-linearity* (NL). Therefore, it is better to determine the background non-linearity quantitatively and will help us to determine a reasonable and acceptable mass spectrum range with good linearity for further studies, such as decay angular distribution, differential cross section and so on. As shown in Fig. 3.2, the side-band regions, "$B_1 + S_1$" and "$B_2 + S_2$", are of the equal mass width as the signal window, "$B_0 + S_0$". The definition of non-linearity (NL) and the associated errors are given in Eq. 3.1-3.3 by replace G_x as R_x. One set of relative ratio coefficients in K^-p detection mode of hydrogen target is listed in Table 3.1.

Table 3.1: Global fitting factors and relative ratio coefficients for background linearity study in K^-p detection mode of hydrogen target

	Global Fitting Factors G_x	Relative Ratio Coefficients R_x
KKp	0.0282	1.
$K\Lambda^*$	0.0171	0.60638
ϕ	0.0361	1.28014

However, the non-linearity will be affected strongly by the statistic of denominator, $\sqrt{N_{B_0}}$, in Eq. 3.1. Therefore, a better way to measure the non-linearity is to normalize the Monte Carlo background components to real data spectrum by applying the global fitting factors given in Table 3.1 instead of the relative ratio coefficients. Final definition of non-linearity calculations are listed in Eq. 3.1-3.3.

$$NL \equiv \frac{N_{B_0} - \frac{1}{2}(N_{B_1} + N_{B_2})}{\sqrt{N_{B_0}}} \tag{3.1}$$

$$Error_{B_{(0,1,2)}} = \sqrt{\left(\sqrt{N_{B_{\phi(0,1,2)}}}\right)^2 \times G_\phi + \left(\sqrt{N_{B_{KKp(0,1,2)}}}\right)^2 \times G_{KKp} + ...} \tag{3.2}$$

$$Error_L = \frac{\sqrt{(Error_{B_0})^2 + \frac{1}{2}\left((Error_{B_1})^2 + (Error_{B_2})^2\right)}}{\sqrt{N_{B_0}}} \tag{3.3}$$

where $N_{B_{(0,1,2)}} = N_{B_{\phi(0,1,2)}} \times G_\phi + N_{B_{KKp(0,1,2)}} \times G_{KKp} + ...$ and G_x means the global fitting factors of background components.

One example of background non-linearity studies in K^-p detection mode from proton target by using global fitting factors, G_x, is shown in Fig. 3.3 and 3.4. As shown in Fig. 3.3, we studied the 8-bin K^- polar angle in t-channel helicity frame in the photon energy of 2.25-2.40 GeV. In each plot, the black histogram indicates the mass spectrum from read data and the red one shows the estimated Monte Carlo background component.

Based on the mass spectra of estimated Monte Carlo background components in Fig. 3.3, the evaluations of "Non-Linearity" and "Non-Linearity Factor" are shown in the left and right plots of Fig. 3.4 respectively. In this evaluation, the signal window is $1519 \pm 15 MeV/c^2$, that is, from 1515 to 1534 MeV/c^2, and 2 30-MeV/c^2 side-band regions are neighboring to the signal window in the low-mass and high-mass sides individually. Typically, the acceptable non-linearity is smaller than $1\sigma_{N_{signal}}$.

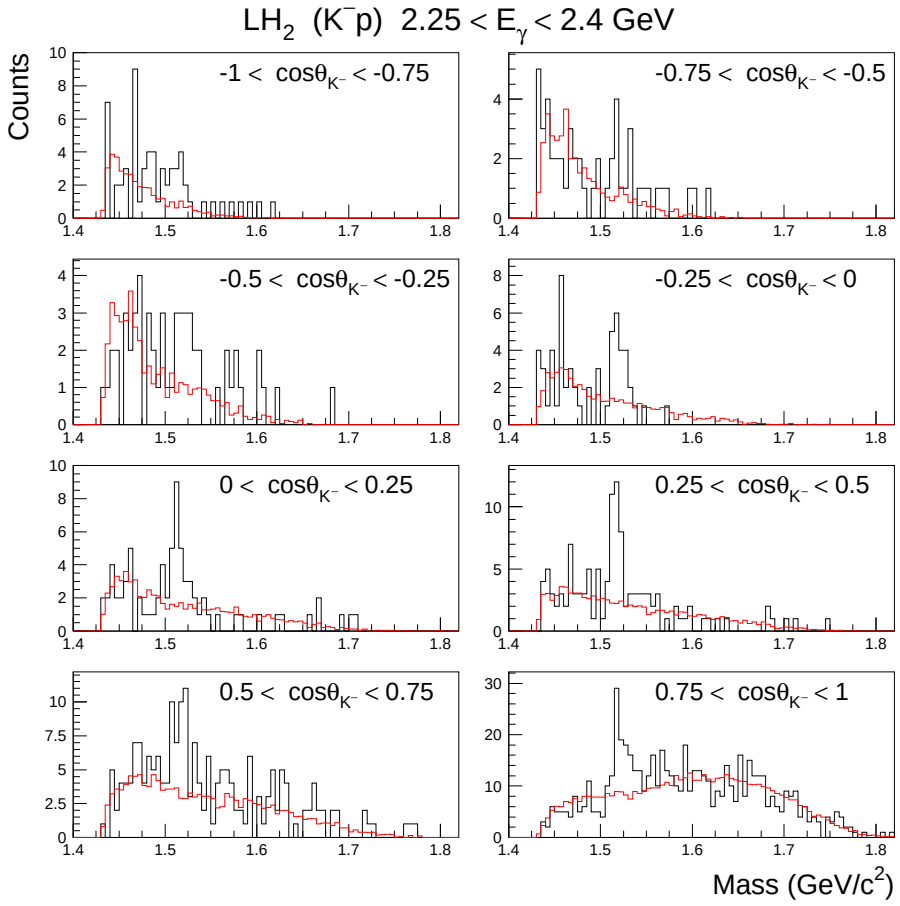

Figure 3.3: 8 plots show the mass spectra of read data (black histogram) and the estimated Monte Carlo background component (red histogram) by K^- polar angle in t-channel helicity frame. In this background linearity study, the photon energy range is from 2.25 and 2.40 *GeV*

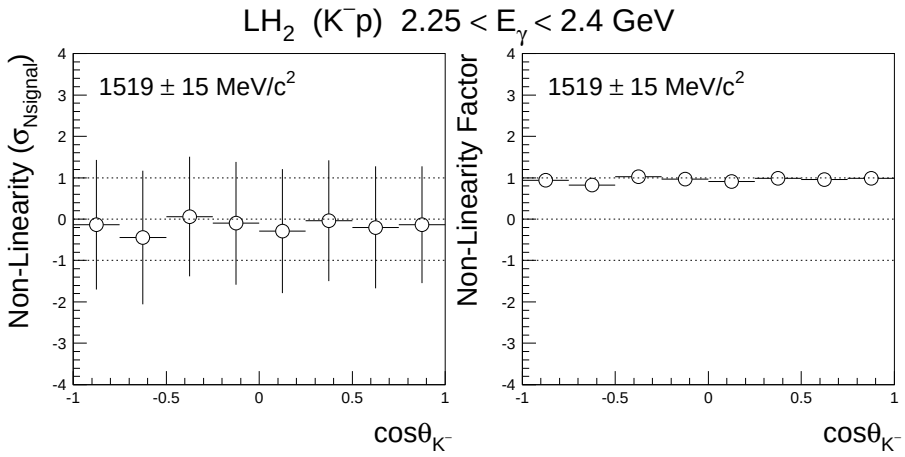

Figure 3.4: The "Non-Linearity" and "Non-Linearity Factor" in the photon energy of 2.25-2.40 GeV in the K^-p detection mode from proton targets are shown in the left and right plots respectively.

3.3.2 Side-band subtraction

Relied on the linearity of Monte Carlo background spectrum, by choosing the mass spectrum range with good background linearity to study the yield of $\Lambda(1520)$ production. According to the Fig. 3.2, the yield can be calculated by side-band method as shown in Eq. 3.4.

$$\begin{aligned} Yield &= (S_0 + B_0) - \frac{1}{2}(S_1 + S_2 + B_1 + B_2) \\ &= (S_0 - \frac{1}{2}(S_1 + S_2)) + (B_0 - \frac{1}{2}(B_1 + B_2)) \end{aligned} \tag{3.4}$$

Refer to Fig. 3.2 and Eq. 3.4, assuming that the background linearity near the mass peak is good, namely $B_0 - \frac{1}{2}(B_1 + B_2) = 0$, the S_0 can be calculated by Eq. 3.4 accompanied with the sneak-in factor ϵ from Monte Carlo simulation, as shown in Eq. 3.5.

$$\begin{aligned} \Delta S \equiv S_0 - \frac{1}{2}(S_1 + S_2) &= S_0 \left[1 - \frac{\frac{1}{2}(S_1 + S_2)}{S_0}\right] \\ \epsilon \equiv \frac{\frac{1}{2}(S_1 + S_2)}{S_0} & \\ \Rightarrow S_0 = \frac{\Delta S}{1 - \epsilon} & \end{aligned} \tag{3.5}$$

3.3.3 Monte Carlo fitting

From Fig. 3.5, subtracting the background components from real data mass spectrum to obtain the yield of $\Lambda(1520)$. Please refer to [25] for details of Monte Carlo background estimation produced by Muramatsu. A brief description about how to generate background spectrum is in the following.

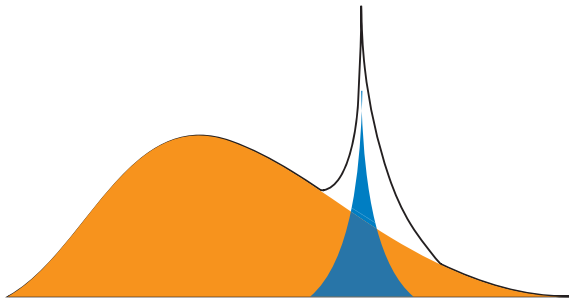

Figure 3.5: The schema of Monte Carlo fitting method.

- Producing background spectra for two major photoproduction processes of ϕp and non-resonant K$\bar{\text{K}}$p final states individually. Small contributions other than $\Lambda(1520)$ and ϕ productions were included in the category of "non-resonant" process. These processes were generated by assuming a constant matrix element in a GEANT3-based MC simulation package [26].

- KΛ(1520) photoproduction was simulated by varying width of the resonance depending on phase space of decay products with Blatt-Weisskopf barrier penetration model [27]. Kinematical dependences of the simulated events, including polar angles and momenta of the detected tracks and c.m. energy, were adjusted by skimming events to reproduce the real hydrogen data.

- The individual photo-reaction was isolated by tagging/untagging $\Lambda(1520)$ and ϕ peaks with subtraction of contaminations from the other processes, so that the event skimming and normalizations were properly done.

- Quasi-free photoproduction spectra in the deuterium data were estimated just by adopting influence of Fermi motion in the MC samples skimmed using the hydrogen data. An off-shell correction was taken into account for a nucleon target inside deuterium. A MC sample only for non-resonant K^0K^-p production from neutrons was additionally prepared based on the deuterium data.

- Sum of all the processes were well consistent with real spectra of invariant and missing masses within slices pf photon energy and polar angle.

3.3.4 Non-linearity correction

As we mentioned before, the mass spectrum did not have good background linearity in all dimensions. A further correction must be taken care, especially in the K^+K^- detection mode from hydrogen target. Therefore, we introduce in a new variable, "scale". It will be multiplied to physics results after the standard side-band subtraction procedure. The evaluation of "scale" is shown in Eq. 3.6-3.11.

Non-Linearity Factor (NLF),

$$NLF \equiv \frac{B_0}{\frac{1}{2}(B_1 + B_2)}. \tag{3.6}$$

Sneak-in Factor ($Factor$),

$$Factor \equiv 1 + \kappa \equiv \frac{MC_0}{MC_0 - \frac{1}{2}(MC_1 + MC_2) \times NLF}. \tag{3.7}$$

$$Yield' \equiv (S_0 + B_0) - \frac{1}{2}(S_1 + B_1 + S_2 + B_2) \times NLF \tag{3.8}$$

$$\rightarrow Factor_{NLF=1} \equiv \frac{MC_0}{MC_0 - \frac{1}{2}(MC_1 + MC_2)}. \tag{3.9}$$

$$\rightarrow Yield'_{NLF=1} = (S_0 + B_0) - \frac{1}{2}(S_1 + B_1 + S_2 + B_2) \tag{3.10}$$

$$scale = \frac{Yield' \times Factor}{Yield'_{NLF=1} \times Factor_{NLF=1}} \tag{3.11}$$

3.3.5 2-step side-band subtraction

Since many possible background processes other than the K^+K^-p final state were involved in the K^+p detection mode, MC simulations were not adopted for background estimation. Different from the standard side-band subtraction described in section 3.3.2, a 2-step side-band subtraction method was implemented to treat complicated background contamination in K^+p detection mode of hydrogen target.

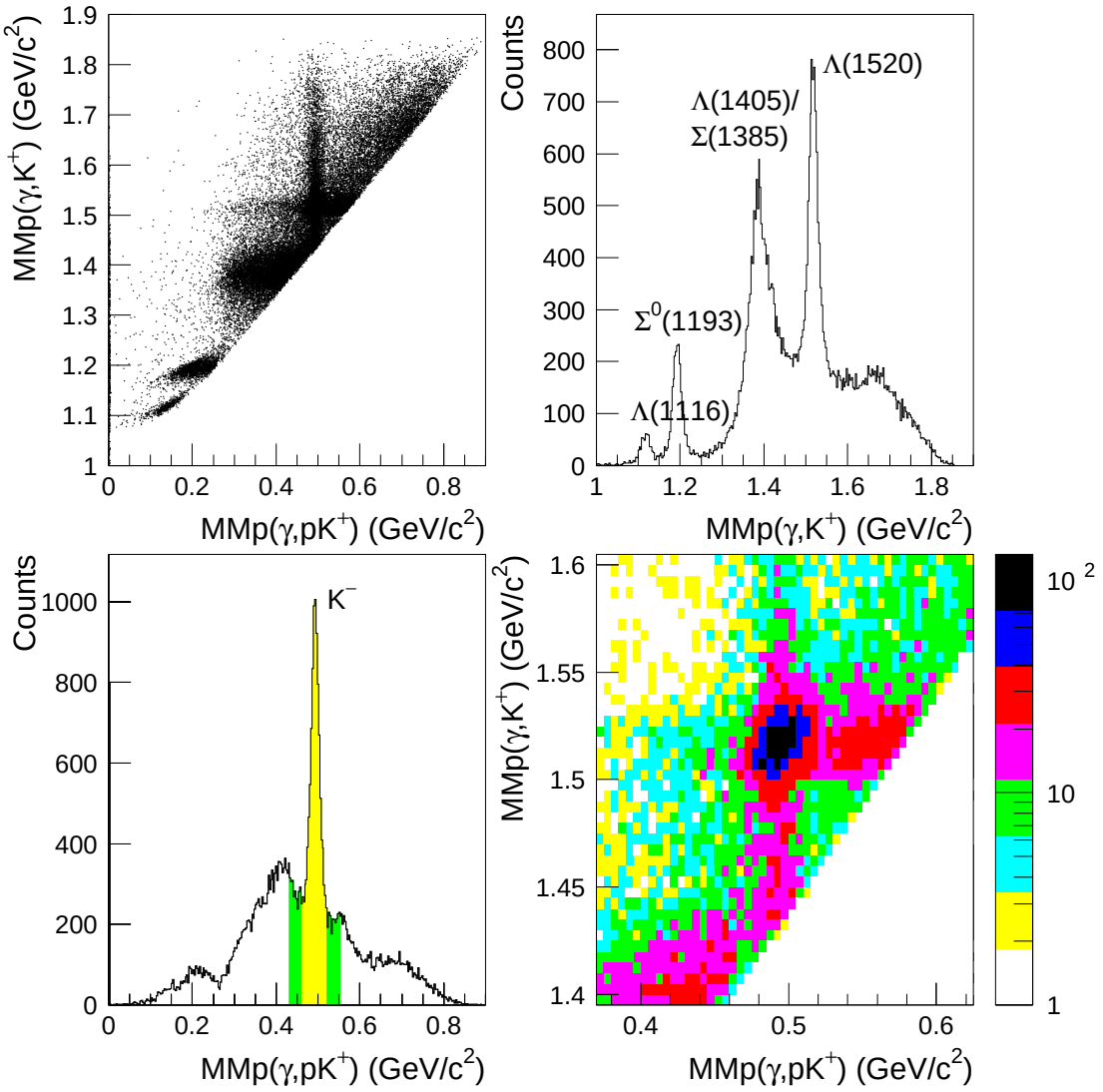

Figure 3.6: Dalitz plot and mass spectra of massing mass of K^+ versus missing mass of pK^+ in K^+p detection mode of hydrogen target. A zoom-in Dalitz plot around the mass range of $\Lambda(1520)$ and K^- was shown in bottom-right panel.

It can be seen from Fig. 3.6, both mass spectra of "missing mass of K^+" (top-right panel) and "missing mass of pK^+" (bottom-left panel) show complicate background contamination. In the case of "missing mass of pK^+", an significant contamination came from the production of $\Lambda(1405)/\Sigma(1385)$ in the low-mass region; simultaneously, an unknown bump structure about 1.7 GeV/c^2 contaminates from high-mass side. On the other hand, the contamination under the peak of K^- in the mass spectrum of "missing mass of pK^+ is totally indistinguishable.

The background includes $\gamma + p \to \Lambda + \pi^+$, $\Sigma + \pi^+$, $\Lambda + \pi^0 + \pi^+$, $\Sigma + \pi^0 + \pi^+$, $\Sigma(1285) + \pi^+$, $K^{*+}(892) + \Lambda$, $K^{*+}(892) + \Sigma$, and so on. Therefore, we use the 2-step side-band subtraction method.

At the first step, three mass spectra of "missing mass of K^+" were selected in the range of "missing mass of pK^+" of 0.433-0.463 (low-mass), 0.463-0.523 (middle-mass, ± 30 MeV/c^2 away from PDG value of Kaon mass) and 0.523-0.553 (high-mass) GeV/c^2, corresponding to the colored histograms (left green, central yellow and right green parts) in bottom-left panel of Fig. 3.6 respectively. Subtracted the sum of low-mass and high-mass "missing mass of K^+" spectra from the middle-mass "missing mass of K^+" spectrum to have the first-step side-band subtracted mass spectrum. Here, there is a linearity problem of "missing mass of pK^+" spectrum".

Following the second-step, side-band subtraction was performed on which was obtained in the previous step. Non-linearity of hyperon backgrounds in "missing mass of pK^+" spectrum is removed assume that the linearity in "missing mass of K^+ is better. Non-linearity of non-resonance KKp background in "missing mass of K^+" spectrum still remains. In summary, the 2-step side-band subtraction method calculates raw signal counts by $(N_5 - N_4 - N_6) - (N_2 - N_1 - N_3) - (N_8 - N_7 - N_9)$, as shown in Fig. 3.7. This is actually consistent with the case where the order of side-band subtractions is reversed : $(N_5 - N_2 - N_8) - (N_4 - N_1 - N_7) - (N_6 - N_3 - N_9)$.

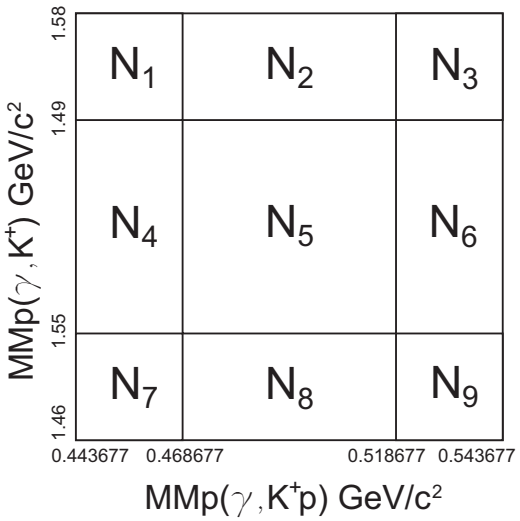

Figure 3.7: Conceptual explanation of 2-step side-band subtraction method.

3.4 Event selections

All the cut conditions in K^-p and K^+K^-/K^+p detection modes were listed in Table 3.2, where the photon energy was re-calculated by utilizing " photonenergy2trk.f "
in " miho:/np1b/v01/sp8lep/OfficialMacro/func/ " provided by Kato [28]. The photon energy cut, $E_\gamma > 1.75$ GeV, in the K^-p detection was set by the production threshold of $\Lambda(1520)$. However, the photon energy cut, $E_\gamma > 1.90$ GeV, in K^+K^- detection mode was due to the acceptance of $\Lambda(1520)$ photoproduction drops drastically below 1.9 GeV. An additional cut condition, "invm(K^+K^-)>1.030 GeV/c^2"/"MMp(γ,p)>1.050 GeV/c^2", was applied to exclude

the significant contamination of ϕ events in the K^+K^-/K^+p detection mode. All the other event selection conditions were discussed in the following subsections.

Table 3.2: Cut conditions for K^-p and K^+K^-/K^+p detection modes

K^-p mode	K^+K^-/K^+p mode
ntrk > 1	ntrk > 1
3σ PID	4σ PID
ikm/ipr $\neq 0$	ikm/ikp $\neq 0$
ithtofhit(ikm/ipr) > 0	ithtofhit(ikm/ikp) > 0
prbchi2(ikm/ipr) ≥ 0.02	prbchi2(ikm/ikp) ≥ 0.02
abs(ytof(ikm/ipr)-tofdiff(ikm/ipr)) ≤ 80	abs(ytof(ikm/ikp)-tofdiff(ikm/ikp)) ≤ 80
abs(itof(ikm/ipr)-tofid(ikm/ipr)) < 2	abs(itof(ikm/ikp)-tofid(ikm/ikp)) < 2
nuotl(ikm/ipr) ≤ 6	nuotl(ikm/ikp) ≤ 6
-1100 $\leq$ vtz $\leq$ -900	-1100 $\leq$ vtz $\leq$ -900
abs(vtx) ≤ 15	abs(vtx) ≤ 25
$0.40 \leq$ MMp(γ,K^-p)$-M_K \leq 0.62$ GeV/c^2	$\lvert$MMp(γ,K^+K^-)$-M_P\rvert \leq 0.050$ GeV/c^2
photon energy ≥ 1.75 GeV	photon energy ≥ 1.9 GeV
	invm(K^+K^-) > 1.030 GeV/c^2 (K^+K^- only)
	MMp(γ,p) > 1.050 GeV/c^2 (K^+p only)

3.4.1 Particle identification (PID)

Since the $\Lambda(1520) \rightarrow K^- + p$ is the main detected decay mode in this analysis, therefore how to identify K^- and p from experimental data is the main issue. One of the ways to distinguish different particles is by mass. From experimental data, we could get the momentum (p) of the particle from the bending angle as it passed the magnet and the velocity (β) from the path length and time of flight. Then the mass of particle is

$$m = \left(p^2 \frac{1-\beta^2}{\beta^2} \right)^{\frac{1}{2}} \tag{3.12}$$

, where β is the velocity of particle.

Usually we use some selection criteria to identify particles and suppress background tracks. In order to define particles' boundaries more quantitatively, instead of m distribution, we bring in a m^2-distribution boundary as shown in Fig. 3.8, a 2-D distribution of momentum versus mass square. It can can be seen from Fig. 3.8, some band structures can be seen. From Eq. 3.12, we can derive the resolution of m^2, $\sigma^2_{m^2}$, as

$$\sigma^2_{m^2} = 4m^2 \left(\frac{\sigma_p}{p} \right)^2 + \frac{4p^4}{\beta^2} \left(\frac{\sigma_{TOF}}{L} \right)^2 \tag{3.13}$$

, where m is the particle's mass peak position; L is the length of flight path; σ_p is the momentum resolution and σ_{TOF} is the TOF resolution.

Depending on Eq. 3.13, we studied the momentum dependence of mass-square resolution, $\sigma^2_{m^2}$, we eventually determined the particle identification boundary for proton and Kaon and shown in Fig. 3.8. In Fig. 3.8, 2 inner solid lines defined the 3σ PID boundaries and 2 outer dashed lines indicated the 4σ PID boundaries for proton, $K^{+/-}$ and $\pi^{+/-}$. In our study, 3-σ boundary was used for K^-p detection mode. A wider PID boundary, 4σ, was utilized to collect more events in $\Lambda(1520)$ production of K^+K^- and K^+p detection mode since the acceptance of K^+K^- and K^+p detection modes are relatively small.

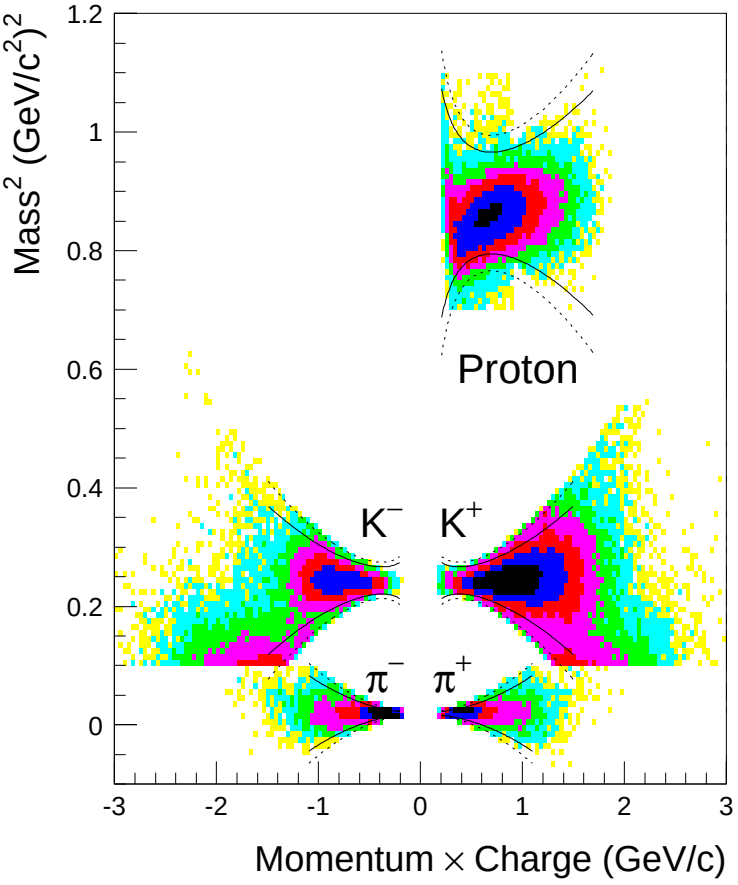

Figure 3.8: Particle Identification Boundaries.

3.4.2 Decay-in-flight cuts

- At least one hit must be accepted by the TOF counter (Fig. 3.9).
- We make cuts on the difference of transverse positions between reconstructed hit position at the TOF counter and the measured positions by the TOF counter itself. If the difference of the TOF slat number, $abs(itof - tofid)$, was greater than 1 (Fig. 3.10) or the difference of y coordinate, $abs(ytof - tofdiff)$, was greater than 80 mm (Fig. 3.11), those tracks will be rejected.
- The reconstructed hit position of tracking chamber away from the expected trajectory more than the resolution was considered as a outlier and removed from the tracking.

While the number of outliers of one track was greater than 6, this track will be rejected (Fig. 3.12).

- If the χ^2 probability of a fitting of the track reconstruction was greater than 0.2, this track will be rejected (Fig. 3.13).

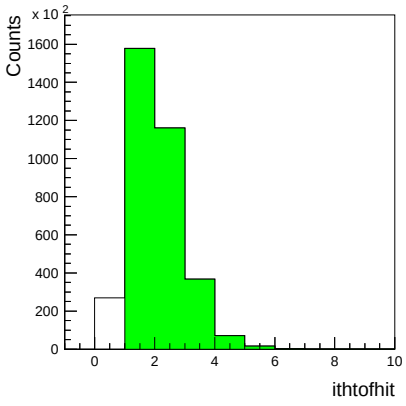

Figure 3.9: Number of hits at TOF counters.

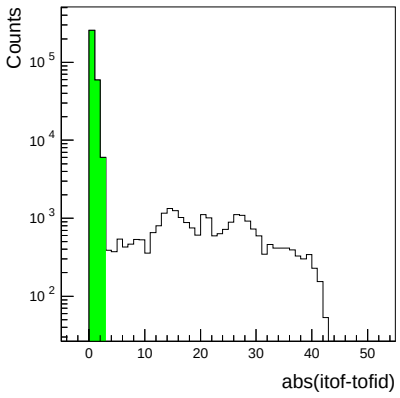

Figure 3.10: Position difference in X coordinate.

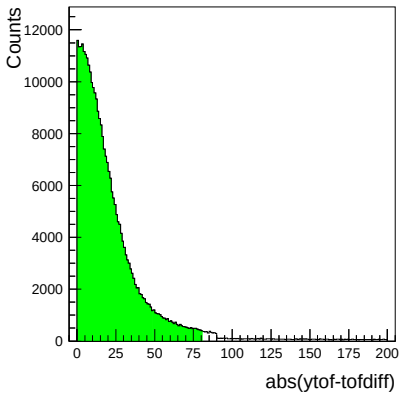

Figure 3.11: Position difference in Y coordinate.

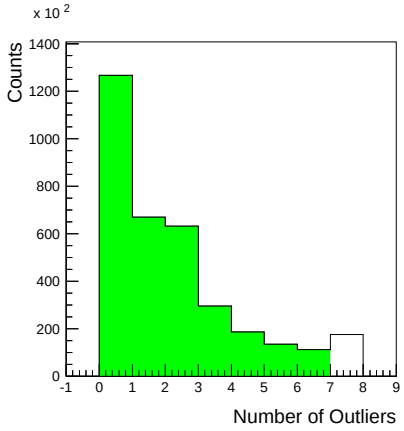

Figure 3.12: Number of outliers hits.

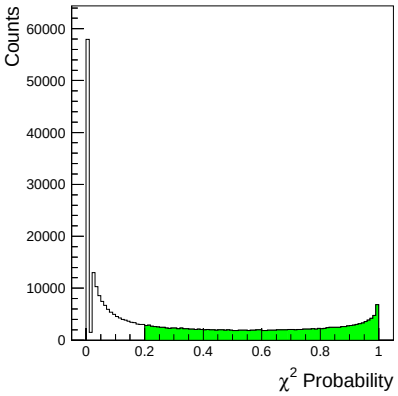

Figure 3.13: χ^2 probability.

3.4.3 Vertex cuts

- The cut condition of vertex position of liquid hydrogen and deuterium targets in x coordinate was chosen as $\pm 15mm$ away from center of target for K^-p detection mode and $\pm 25mm$ away from center of target for K^+K^-/K^+p detection mode (Fig. 3.14).

- Depends on the experimental setup, the positions of liquid hydrogen and deuterium targets in z coordinate are located between -900 mm and -1100 mm (Fig. 3.15).

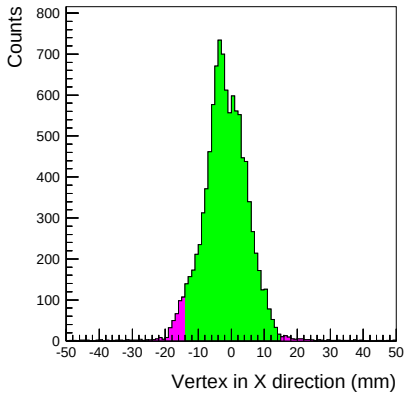

Figure 3.14: Vertex position in x coordinate.

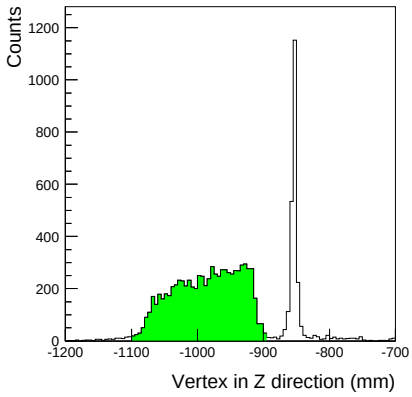

Figure 3.15: Vertex position in z coordinate.

3.4.4 Production threshold

The first thing that needs to be done is to derive the relativistically kinematics invariants, known as the Mandelstam variables s and t. Mandelstam variable s stands for CMS energy squared, $s = (k_1 + k_2)^2 = (k_3 + k_4)^2$; variable t is defined as the 4-momentum transfer squared, $t = q^2 = (k_1 - k_3)^2 = (k_2 - k_4)^2$.

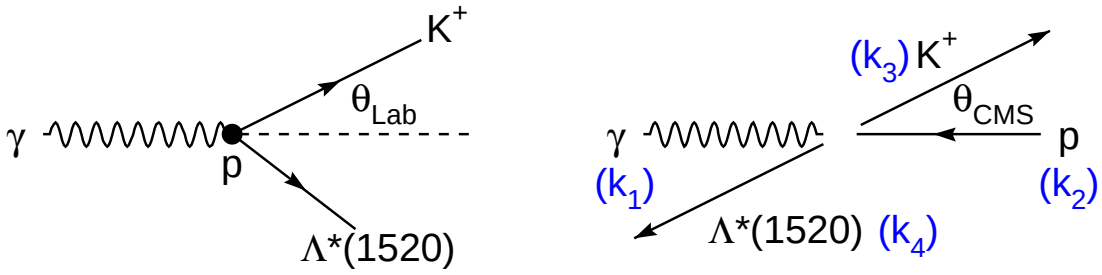

Figure 3.16: $\Lambda(1520)$ photoproduction in Lab.(left diagram) and CMS (right diagram) frames.

Fig. 3.16 shows the reaction of $\gamma + p \rightarrow \Lambda(1520) + K^+$ in Lab. and CMS frames respectively. Referring to the right diagram of Fig. 3.16, $\Lambda(1520)$ photoproduction in CMS frame, k_1, k_2, k_3, k_4 denote the 4-momenta of particles: γ, p, K^+ and $\Lambda(1520)$ and are shown in Eq. 3.14-3.17 respectively.

$$k_1 = \begin{pmatrix} E_{\gamma_{CMS}} \\ 0 \\ 0 \\ P_{\gamma_{CMS}} \end{pmatrix} \quad (3.14) \qquad k_2 = \begin{pmatrix} \sqrt{M_p^2 + P_{p_{CMS}}^2} \\ 0 \\ 0 \\ P_{p_{CMS}} \end{pmatrix} \quad (3.16)$$

$$k_3 = \begin{pmatrix} \sqrt{M_{K^+}^2 + P_{K^+_{CMS}}^2} \\ P_{K^+_{CMS}} \sin\theta_{CMS} \cos\phi_{CMS} \\ P_{K^+_{CMS}} \sin\theta_{CMS} \sin\phi_{CMS} \\ P_{K^+_{CMS}} \cos\theta_{CMS} \end{pmatrix} \quad (3.15) \qquad k_4 = \begin{pmatrix} \sqrt{M_\Lambda^2 + P_{\Lambda_{CMS}}^2} \\ P_{\Lambda_{CMS}} \sin\theta_{CMS} \cos\phi_{CMS} \\ P_{\Lambda_{CMS}} \sin\theta_{CMS} \sin\phi_{CMS} \\ P_{\Lambda_{CMS}} \cos\theta_{CMS} \end{pmatrix} \quad (3.17)$$

, with the notation as:

$E_{\gamma_{CMS}}$	incident photon energy in CMS frame
$P_{\gamma_{CMS}}$	momentum of incident photon in CMS frame
M_p	mass of proton
$P_{p_{CMS}}$	momentum of proton in CMS frame
M_{K^+}	mass of K^+
$P_{K^+_{CMS}}$	momentum of K^+ in CMS frame
θ_{CMS}	polar angle of K^+ in CMS frame
ϕ_{CMS}	azimuthal angle of K^+ in CMS frame
M_Λ	mass of $\Lambda(1520)$
$P_{\Lambda_{CMS}}$	momentum of $\Lambda(1520)$ in CMS frame

Based on Eq. 3.14-3.17, the Mandelstam variable s and t can be evaluated as the following. In LEPS experiment, $m_1 = 0$, namely,

$$s \equiv (k_1+k_2)^2 = (k_3+k_4)^2 = m_1^2 + 2E_1E_2 - 2P_1P_2 + m_2^2 = 2E_\gamma M_p + M_p^2 \quad (3.18)$$

$$t \equiv (k_1-k_3)^2 = (k_2-k_4)^2 = m_1^2 + 2E_1E_3 + 2P_1P_3 + m_3^2 \quad (3.19)$$

$$= (E_{1_{CMS}} - E_{3_{CMS}})^2 - (P_{1_{CMS}} - P_{3_{CMS}})^2 - 4P_{1_{CMS}}P_{3_{CMS}}\sin^2\left(\frac{\theta_{CMS}}{2}\right) \quad (3.20)$$

$$= M_{K^+}^2 - 2E_{1_{CMS}}E_{3_{CMS}} + 2P_{1_{CMS}}P_{3_{CMS}}\cos\theta_{CMS} \quad (3.21)$$

If $\theta_{CMS} = 0$,

$$t = M_{K^+}^2 - 2E_{1_{CMS}}E_{3_{CMS}} + 2P_{1_{CMS}}P_{3_{CMS}}. \quad (3.22)$$

And if $\theta_{CMS} = \pi$,

$$t = M_{K^+}^2 - 2E_{1_{CMS}}E_{3_{CMS}} - 2P_{1_{CMS}}P_{3_{CMS}}, \quad (3.23)$$

where

$$E_{1_{CMS}} = \frac{s + m_1^2 - m_2^2}{2\sqrt{s}} = \frac{s - M_p^2}{2\sqrt{s}} \quad (3.24)$$

$$E_{3_{CMS}} = \frac{s + m_3^2 - m_4^2}{2\sqrt{s}} = \frac{s + M_{K^+}^2 - M_\Lambda^2}{2\sqrt{s}} \quad (3.25)$$

$$P_{1_{CMS}} = \sqrt{E_{1_{CMS}}^2 - m_1^2} = E_{1_{CMS}} \quad (3.26)$$

$$P_{3_{CMS}} = \sqrt{E_{3_{CMS}}^2 - m_3^2} = \sqrt{E_{3_{CMS}}^2 - m_{K^+}^2} \quad (3.27)$$

Utilizing Eq. 3.22-3.23, the production threshold of $\Lambda(1520)$ photoproduction can be evaluated. Simultaneously, the production threshold of $\Theta^+(1540)$ can be derived by utilizing the mass of K^0 (497.648 MeV/c^2) and the mass of Θ^+ (1540 MeV/c^2) instead of the mass of K^+

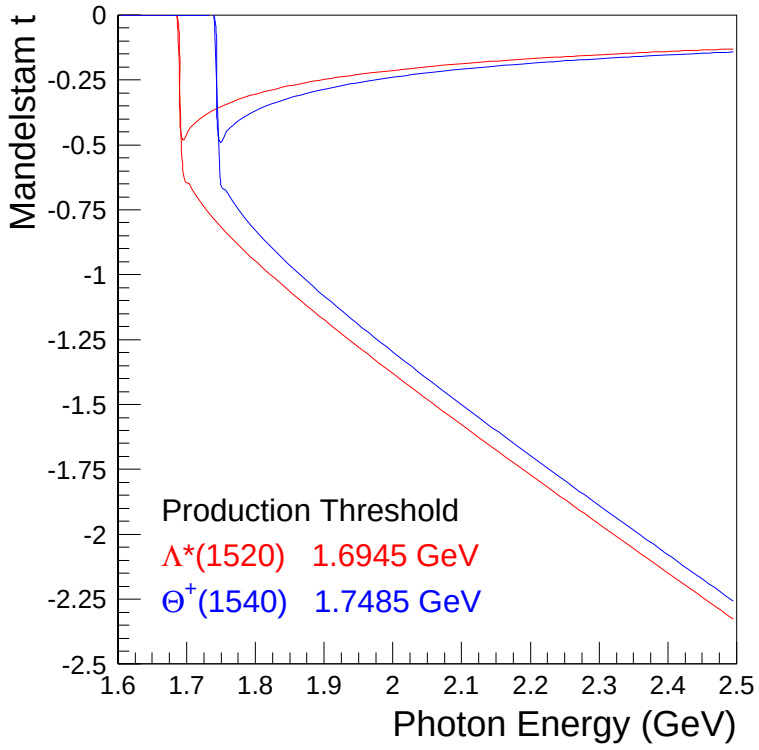

Figure 3.17: Production threshold of $\Lambda(1520)$ and $\Theta^+(1540)$

(493.677 MeV/c^2) and the mass of Λ(1519.5 MeV/c^2) in Eq. 3.16-3.21. Both of them are shown in Fig. 3.17.

From Fig. 3.17 it can be seen that the production threshold of $\Lambda(1520)$ is 1.6945 GeV. Since the $\Lambda(1520)$ production will accompany Θ^+ production, we apply 1.75-GeV cut on $\Lambda(1520)$ photoproduction for further study on Θ^+ photoproduction in K^-p detection mode. On the other hand, because of low statistic at photon energy below 1.9 GeV in K^+K^- detection mode, a 1.9-GeV photon-energy cut was applied in K^+K^- detection mode.

3.5 Data samples

In this experiment, there are 2 kinds of targets, liquid hydrogen and liquid deuteron. For convenience, we used LH_2 and LD_2 as the abbreviations of "liquid hydrogen target" and "liquid deuterium target". All data samples used for analysis are listed below. In hydrogen data analysis, 5 missing runs weren't included in this study since the Monte Carlo estimation did not include these 5 missing runs in the ntuples training.

LH_2 miho:/np1b/v01/sp8lep/OfficialMacro/runinfo/runlistllh2.dat

24011, 24012, 24013, 24014 and 24015 were not included in this study.

LD_2 miho:/np1b/v01/sp8lep/OfficialMacro/runinfo/runlistlld2.dat

Chapter 4

Results and discussions

4.1 Invariant mass and missing mass

The main purpose of this study is to reconstruct the $\Lambda(1520)$ baryon events from two-track events. The invariant mass of $\Lambda(1520)$ baryon and missing mass of different missing particles in 3 detection modes are reconstructed to identify the $\Lambda(1520)$ events. Backward (forward) production of $\Lambda(1520)$ in the c.m. system is examined by detecting a K^+K^- or K^+p (K^-p) pair. Two charged particles are identified by a 3σ or 4σ cut in squared mass depending on their momenta. A particle decaying in flight is removed by required good track fitting qualities. The vertex point of two tracks is required within the target volume and the beam size. Photon energy is required to be greater than 1.90 (1.75) GeV for the K^+K^- and K^+p (K^-p) detection mode because of our acceptance to the $\Lambda(1520)$ photoproduction.

In K^+K^- detection mode, we measured the missing mass of K^+ to identify the $\Lambda(1520)$ baryon. Simultaneously, we reconstructed K^+ and K^- to form the invariant mass of $\phi(1020)$ meson and determine the missing mass of K^+K^- to be proton by energy-momentum conservation. As shown in Fig. 4.1 and Fig. 4.3 for hydrogen and deuterium targets respectively, a clear proton band associated with the momentum and a proton resonance peak can be recognized. Owing to the Fermi motion inside the deuterium target, the width of missing mass of $K^+K^-$from deuterons is obviously larger than that from protons. From Fig. 4.2 and Fig. 4.4, in order to enhance the $\Lambda(1520)$ resonance structure, a $\phi(1020)$ exclusion cut, the invariant mass of K^+K^- greater than 1.03 GeV/c^2 was applied in K^+K^- detection mode. Even we required the 3-particle $K\bar{K}p$ final state, that is to study the missing mass of K^+ while the missing mass of K^+K^- was around the mass of proton, the S/N ratio of $\Lambda(1520)$ resonance structure in K^+K^- detection mode is still very small, especially for that from deuterium targets.

Similar to the K^+K^- detection mode, we measured the missing mass of K^+ to identify the $\Lambda(1520)$ baryon in K^+p detection mode from hydrogen target exclusively. In parallel, we measured the missing mass of proton to identify the $\phi(1020)$ meson and determined the missing mass of pK^+ to be K^-. Similar plots can be seen from Fig. 4.5 and Fig. 4.6. It can be seen from the bottom plot of Fig. 4.5, unlike the missing mass spectra in K^+K^- detection mode shown in the bottom plots of Fig. 4.1 and Fig. 4.3, the background contamination under the K^- resonance peak is complicated and not easy to dig out the K^- event exclusively. That is why we introduce the 2-step side-band subtraction method. A similar $\phi(1020)$ exclusion cut, missing mass of proton is greater than 1.05 GeV/c^2, was also applied in K^+p detection mode, but not shown in plots. The spectrum of missing mass K^+ shown in the right panel of Fig. 4.6 has applied the 3-particle $K\bar{K}p$ final state.

Different from the K^+K^- and K^+p detection modes, we detected K^- and proton to form the

invariant mass of $\Lambda(1520)$ baryon in K^-p detection mode from hydrogen and deuterium targets, and to determine the missing mass of pK^- to be K^+. Meanwhile, we measured the missing mass of proton to identify the main background component, $\phi(1020)$ events, in K^-p detection mode. Similar plots can be seen in Fig. 4.7 and Fig. 4.8 for hydrogen target; Fig. 4.9 and Fig. 4.10 for deuterium target. In K^-p detection mode, no $\phi(1020)$ exclusion cut was applied because $\phi(1020)$ events were kinematically suppressed.

According to Fig. 4.1, 4.3, 4.5, 4.7 and 4.9, in order to determine the 3-particle $K\bar{K}p$ final state, "|missing mass of K^+K^- − M_p| ≤ 0.050 GeV/c^2" was applied in K^+K^- detection mode; "0.468 ≤ missing mass of K^+p ≤ 0.518 GeV/c^2" was applied in K^+p detection mode; "0.40 ≤ missing mass of K^-p ≤ 0.62 GeV/c^2" was applied in K^-p detection mode. 2 dash lines in top-left and bottom-left plots of each figure pointed out the boundaries of event selections.

Mass spectra, other than Fig. 4.1-4.10, with specific photon energy regions and $K^{+/0}$ polar angle ranges in c.m. system are plotted in Fig. 4.11, where the specific polar angle ranges are depending on the measurement of differential cross sections. In comparison with K^+K^-, K^+p and K^-p detection modes, the spectator K^0 which occurs only in the K^-p detection mode of deuterium events means that some of events came from the photoproduction from neutron inside the deuterium target. As shown in Fig. 4.11, the real-data spectra (solid line) and estimated background spectra (all the others) were overlapped, and the hatched area indicated the typical side-band areas. In Fig. 4.11(a), the background contribution which came from ϕN photoproduction is comparable to that of non-resonant KKN photoproduction. Differed from Fig. 4.11(a), the background contribution in Fig. 4.11(c,d) is mainly non-resonant KKN photoproduction. On the other hand, the photoproduction of $\Lambda(1520)$ in K^+K^- and K^+p detection mode are generated mainly in the backward region. In contrast, that in K^-p detection mode is produced in the forward region.

4.1.1 K^+K^- detection mode from protons

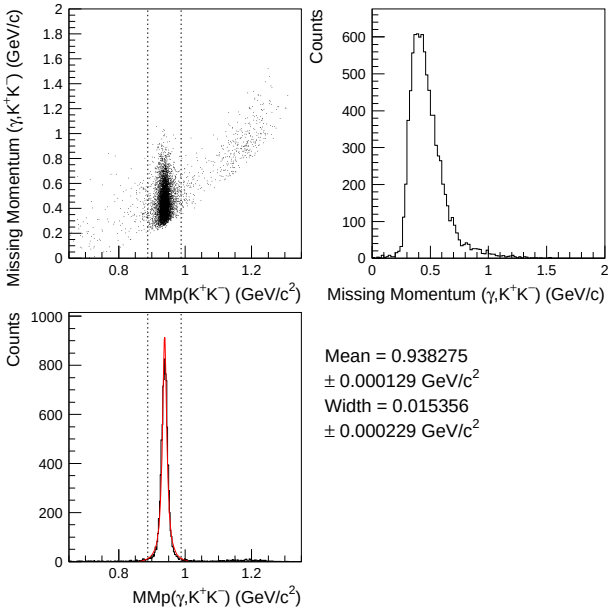

Figure 4.1: Missing mass and momentum of K^+K^- .

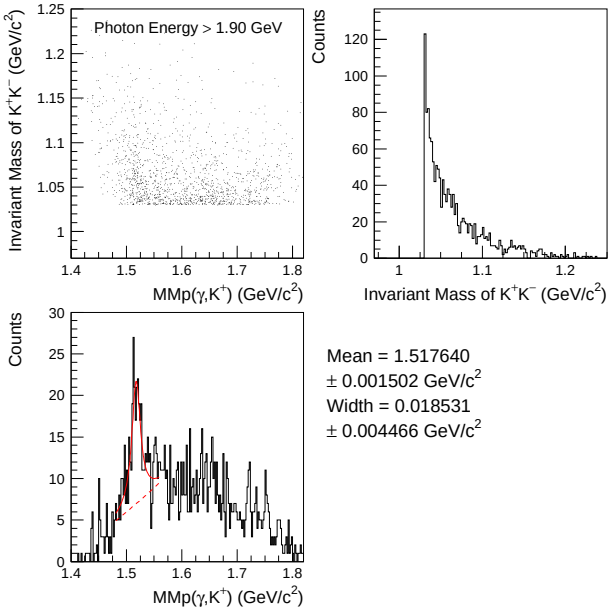

Figure 4.2: Invariant mass of K^+K^- and missing mass of K^+.

4.1.2 K^+K^- detection mode from deuterons

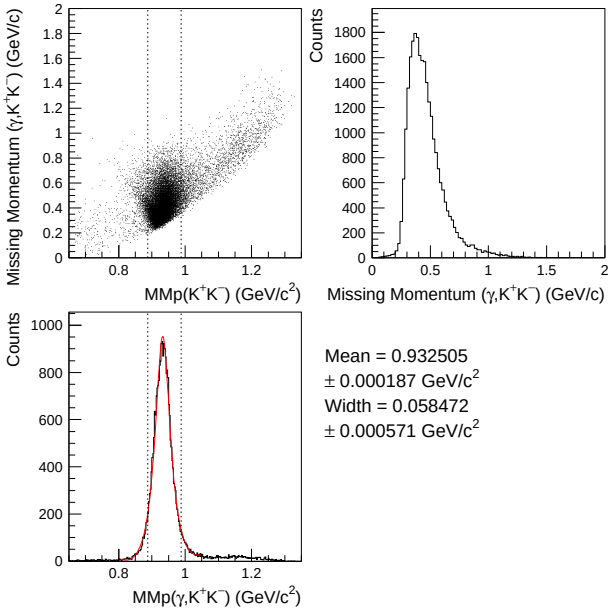

Figure 4.3: Missing mass and missing momentum of K^+K^- .

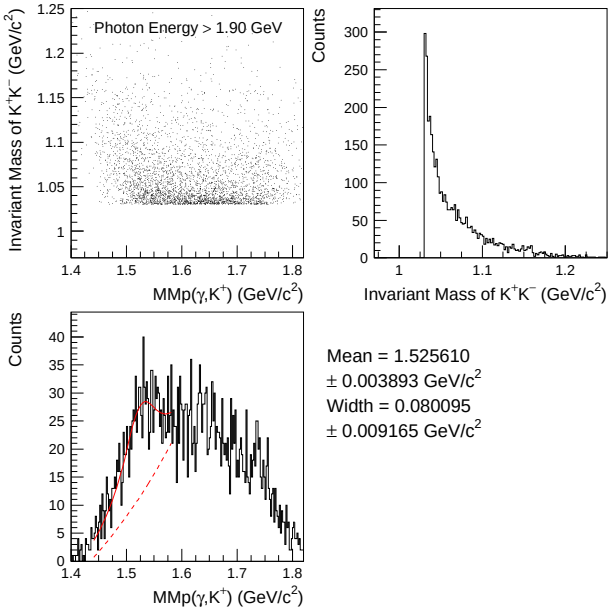

Figure 4.4: Invariant mass of K^+K^- and missing mass of K^+.

4.1.3 K^+p detection mode from protons

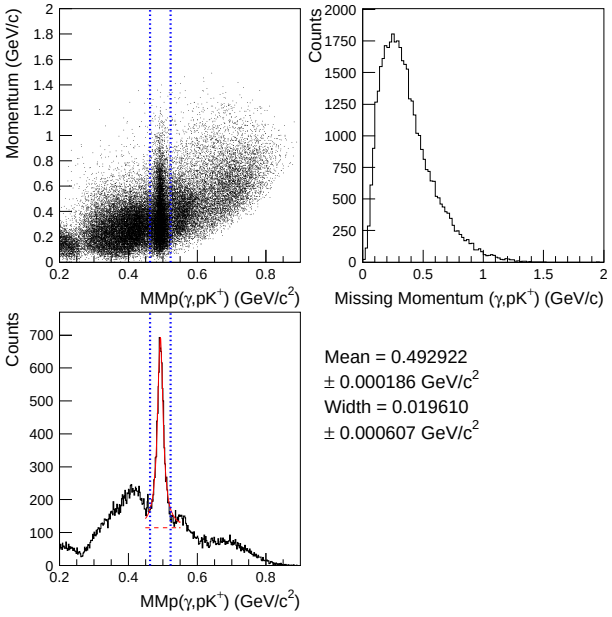

Figure 4.5: "Missing mass and missing momentum of K^+p .

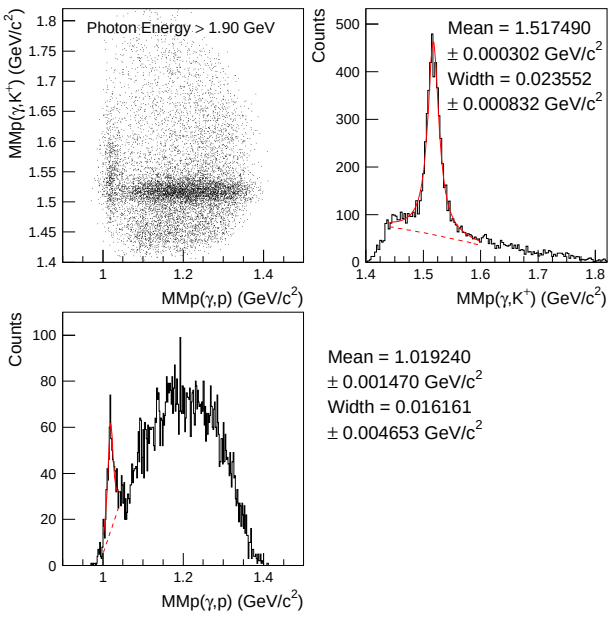

Figure 4.6: Missing mass of proton and missing mass of K^+.

4.1.4 K^-p detection mode from protons

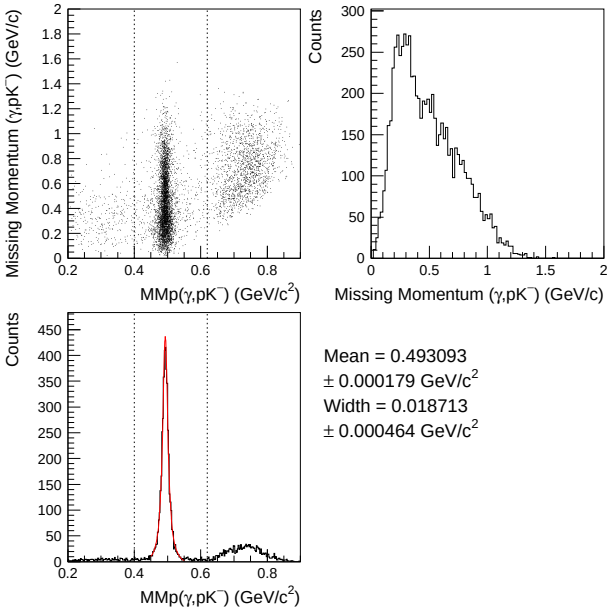

Figure 4.7: Missing mass and missing momentum of pK^-.

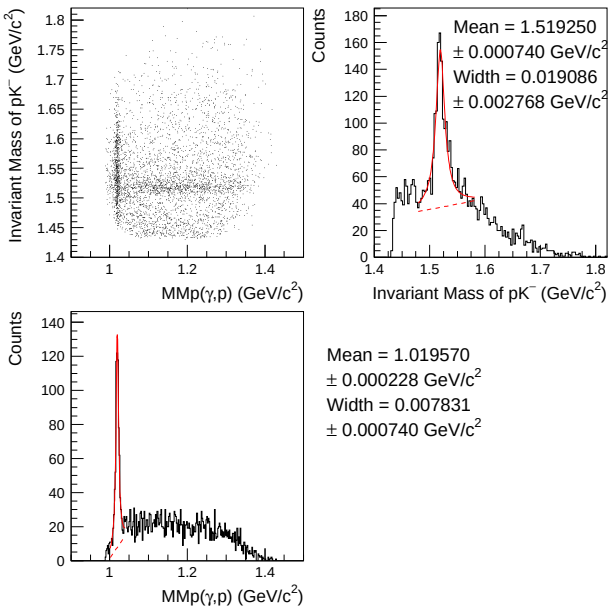

Figure 4.8: Invariant mass of $pK^-$and missing mass of proton.

4.1.5 K^-p detection mode from deuterons

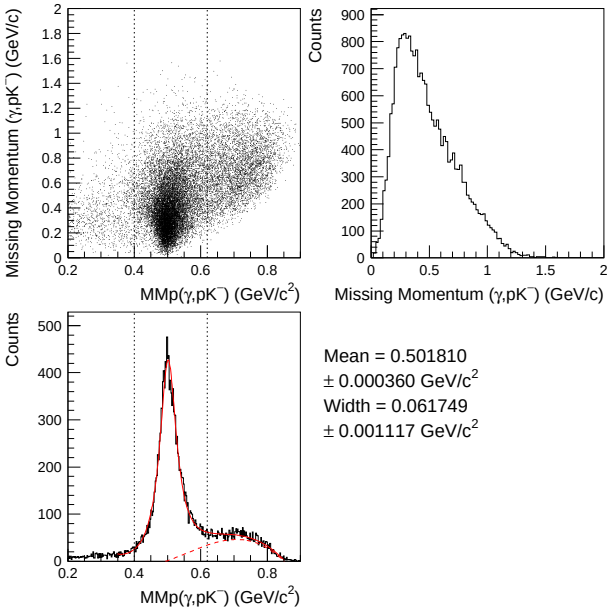

Figure 4.9: Missing mass and momentum of pK^-.

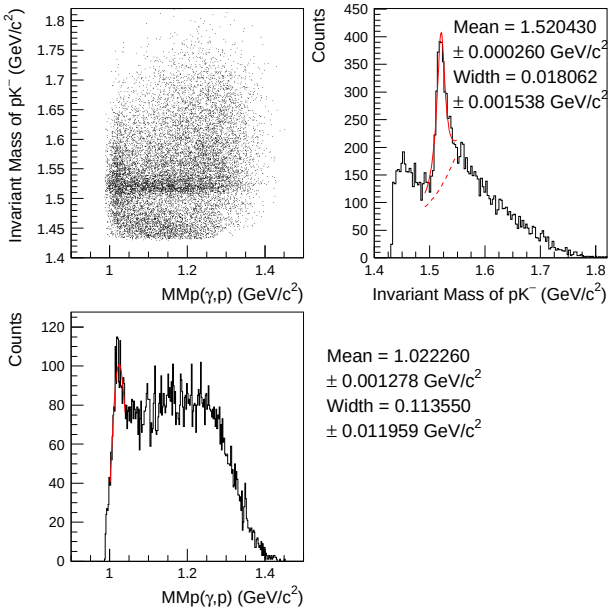

Figure 4.10: Invariant mass of $pK^-$and missing mass of proton.

4.1.6 Mass spectra

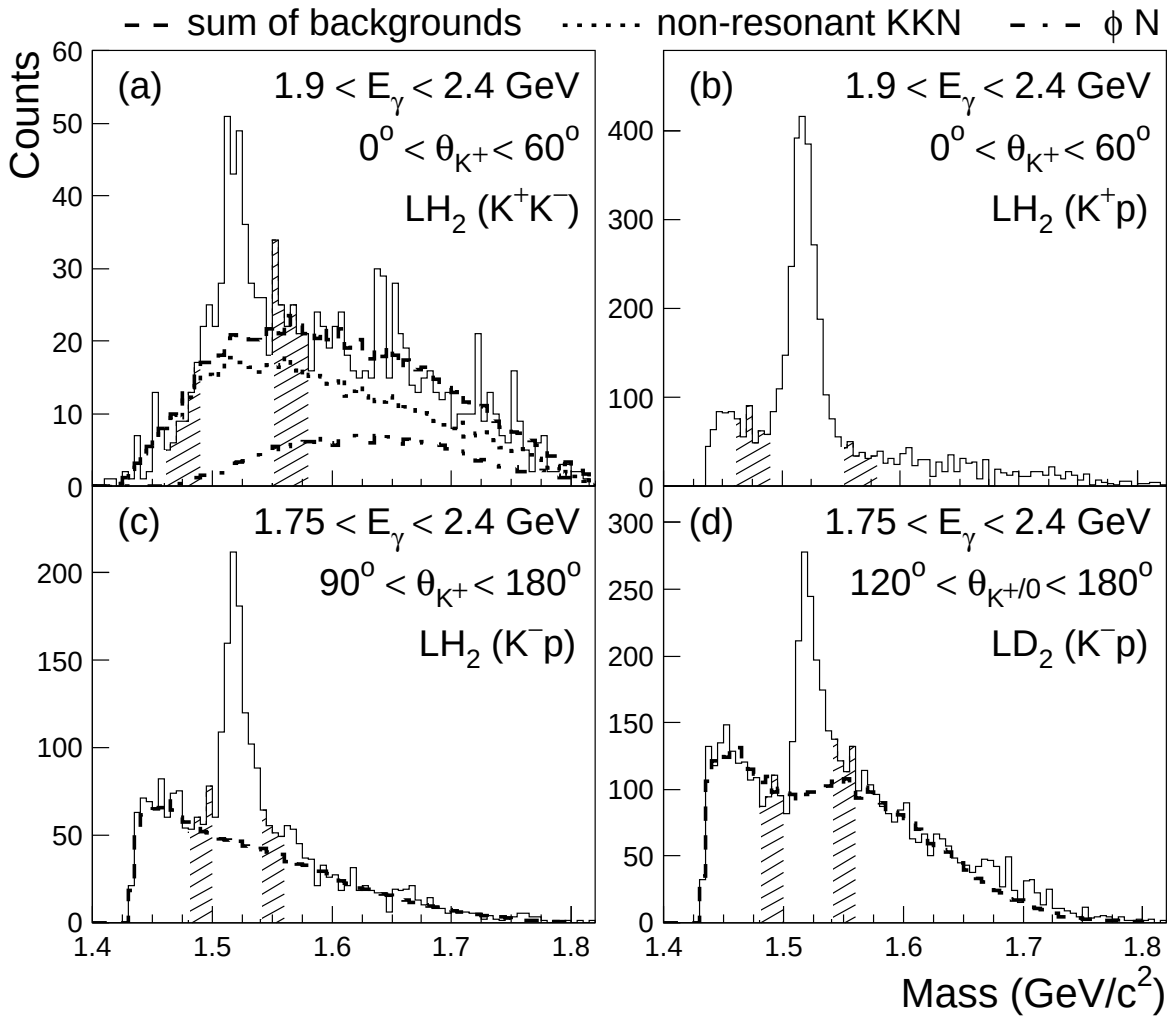

Figure 4.11: (a) and (b) show spectra of K^+ missing mass from the hydrogen data in the K^+K^- and K^+p detection modes, respectively. (c) and (d) show K^-p invariant mass spectra in the K^-p detection mode from hydrogen and deuterium data, respectively. Background estimates based on Monte Carlo simulations are overlaid, while typical side-band selections are indicated by hatched area. The background spectra in (c) and (d) are dominated by non-resonant $K\bar{K}p$ photoproduction.

4.2 Monte Carlo fitting

In K^-p detection mode, not only the invariant mass of pK^- and missing mass of proton, but the plot of missing mass of deuteron will also be shown. On the other hand, the missing mass of K^+ and invariant mass of K^+K^- will be shown in K^+K^- detection mode. In the following plots of Monte Carlo fitting from Fig. 4.12 to 4.14, black histogram shows the spectrum of real data, different production components are shown as overlapped histograms with different colors. Then, the red histogram is the sum of estimated components.

4.2.1 K^+K^- detection mode from protons

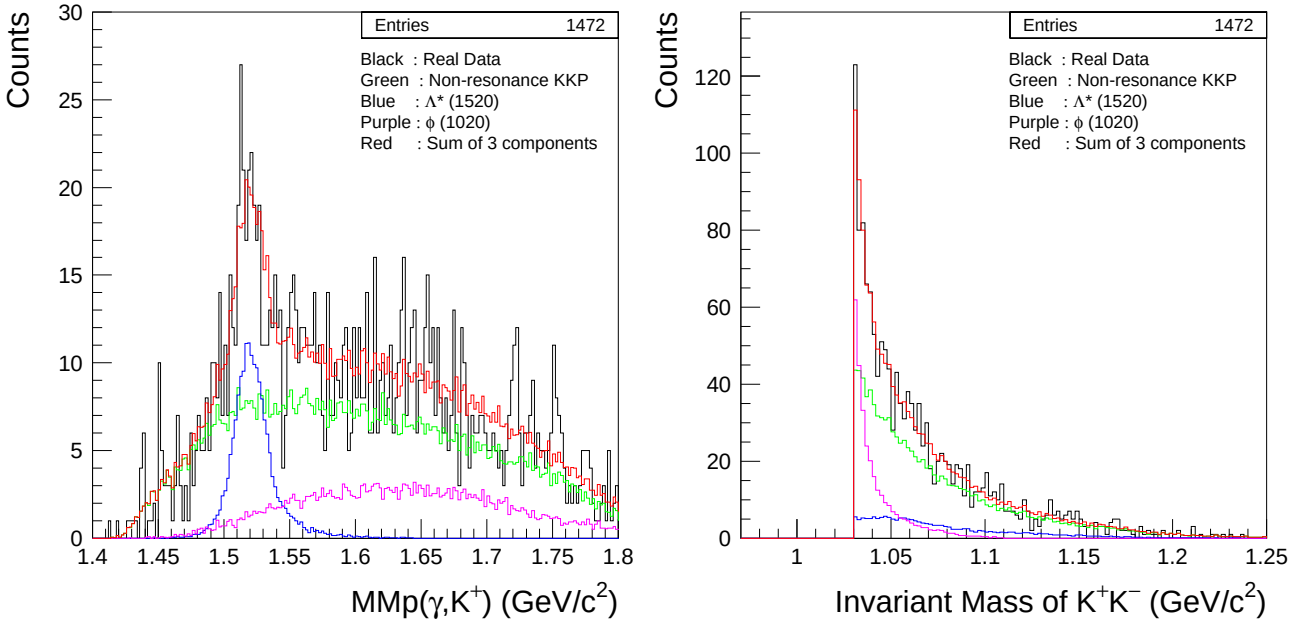

Figure 4.12: The Monte Carlo fitting plots of missing mass of K^+ and invariant mass of K^+K^- from hydrogen data.

4.2.2 K^-p detection mode from protons

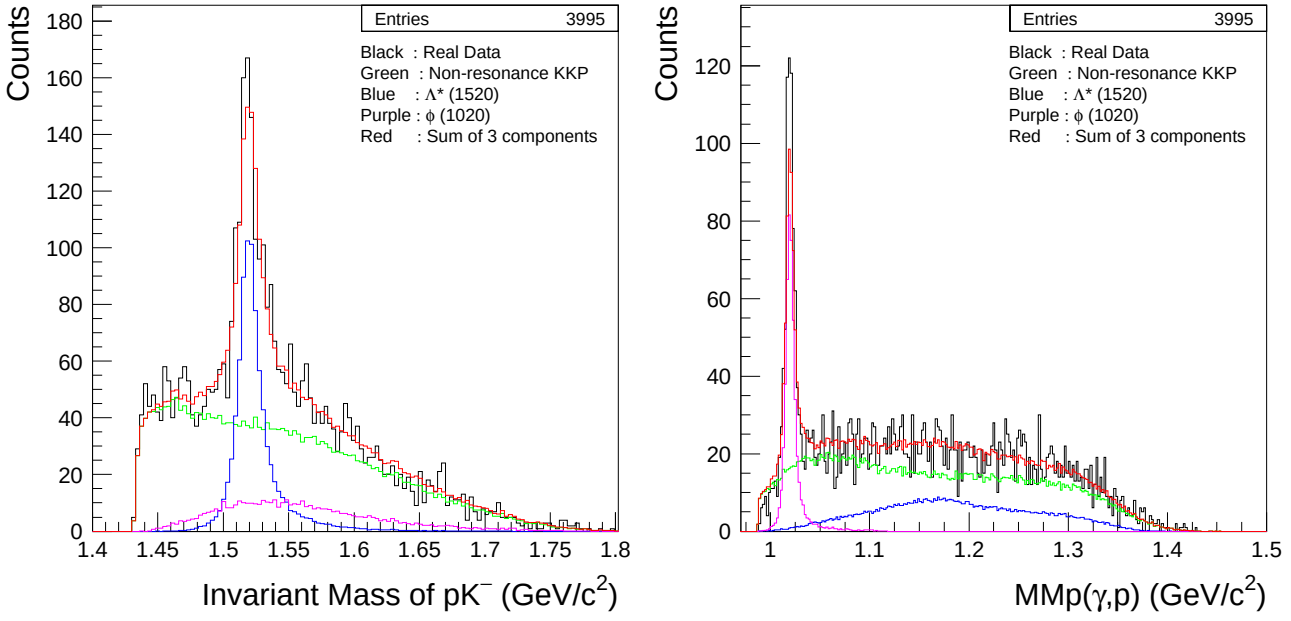

Figure 4.13: The Monte Carlo fitting plots of invariant mass of pK^- and missing mass of proton from hydrogen data.

4.2.3 K^-p detection mode from deuterons

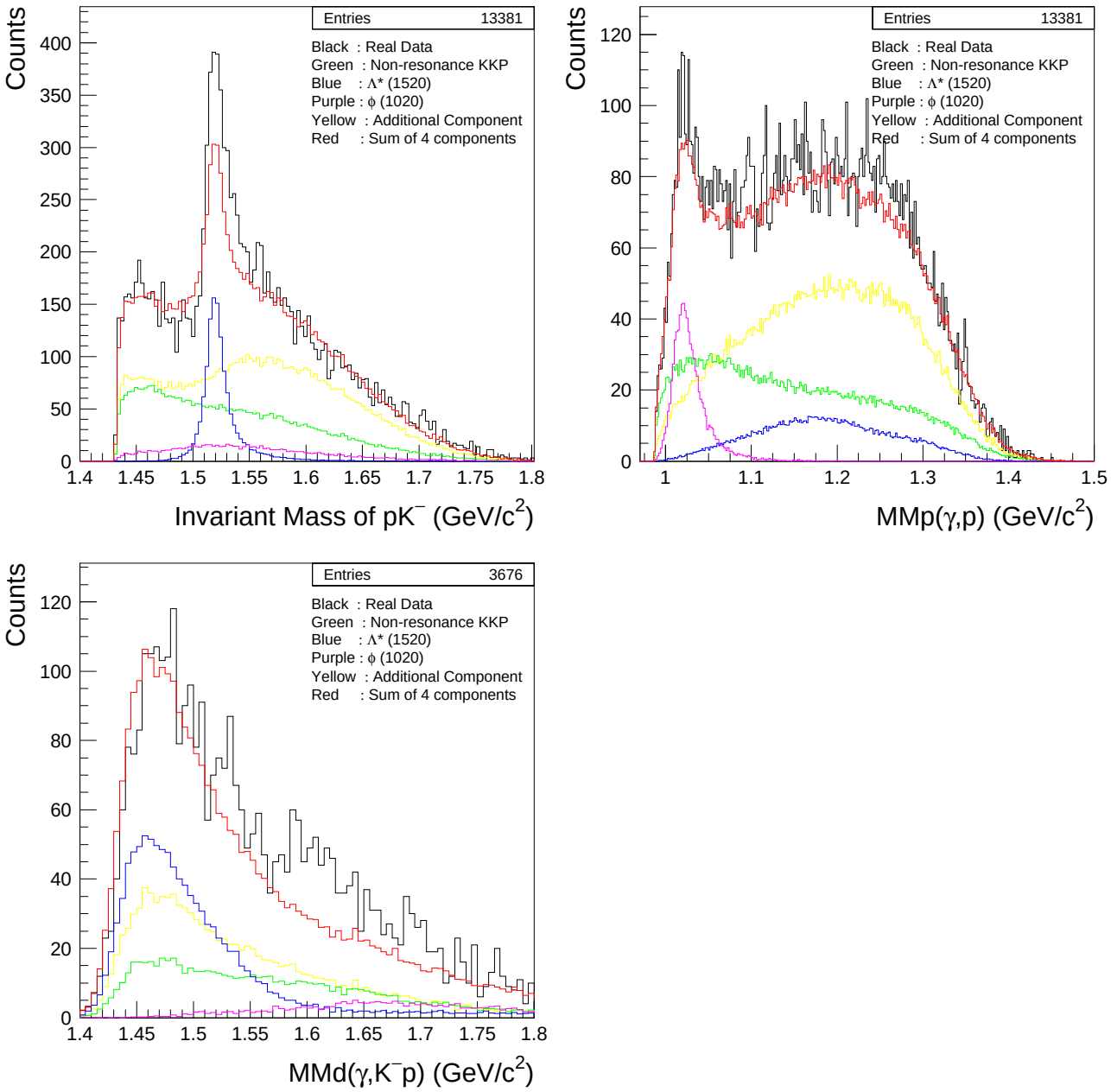

Figure 4.14: The Monte Carlo fitting plots of invariant mass of pK^- , missing mass of proton from deuterium data and missing mass of deuteron from deuterium data.

In cases of K^+K^- and K^-p detection modes from hydrogen data, the simulated components including the $\Lambda(1520)$, $\phi(1020)$ meson and non-resonant KKP events fit well with the real data. As shown in bottom plot of Fig. 4.14 for the K^-p detection mode from deuterium data, however, the claimed Θ^+ photoproduction and the unknown 1.6-GeV bump show in the spectrum of missing mass of deuteron which go beyond our understanding can not be simulated well. Therefore, an additional cut condition "MMd(γ,K^-p) < 1.51 GeV/c^2" was implemented in K^-p detection mode of deuterium target to avoid those contamination. A validity check of cut condition "MMd(γ,K^-p)" will be shown later.

4.3 The measurement of differential cross section

4.3.1 Luminosity

According to the number-of-photon tables provides by Sumihama and Kato, the luminosity can be evaluated as the followings.

(a) Number of Target

N_{target} (LH_2) = 6.76574×10^{23} / cm^2

N_{target} (LD_2) = 8.08427×10^{23} / cm^2

(b) Probability of N_{tag}=1

$P_{ntag=1}$ (LH_2 K^-p mode) = 0.8241

$P_{ntag=1}$ (LD_2 K^-p mode) = 0.8108

$P_{ntag=1}$ (LH_2 K^+K^- mode) = 0.8437

$P_{ntag=1}$ (LD_2 K^+K^- mode) = 0.8302

(c) Branching Ratio = 0.225

(d) Transmission : P_{trans} = 0.526

Luminosity = $N_\gamma \times N_{target} \times P_{ntag=1} \times P_{trans}$

Target	Mode	E_γ (GeV)	N_γ	Luminosity (1/pb)
LH_2	K^+K^-	1.75–1.90	3.72410E+11	0.111822
LH_2	K^+K^-	1.90–2.05	4.34670E+11	0.130517
LH_2	K^+K^-	2.05–2.20	5.00660E+11	0.150331
LH_2	K^+K^-	2.20–2.40	7.66750E+11	0.230229
LH_2	K^-p	1.75–1.90	3.72410E+11	0.109224
LH_2	K^-p	1.90–2.05	4.34670E+11	0.127484
LH_2	K^-p	2.05–2.20	5.00660E+11	0.146839
LH_2	K^-p	2.20–2.40	7.66750E+11	0.224880
LD_2	K^-p	1.75–1.90	5.40230E+11	0.186260
LD_2	K^-p	1.90–2.05	7.04340E+11	0.242841
LD_2	K^-p	2.05–2.20	8.09750E+11	0.279184
LD_2	K^-p	2.20–2.40	1.21205E+12	0.417889

4.3.2 Differential cross section

Due to the limitation of statistics in K^+K^- detection mode from protons, no finer energy dependence of differential cross section was examined as we measured in K^+p or K^-p detection modes. Therefore, the measurement in K^+K^- detection mode from protons was confined in photon energy of 1.9-2.4 GeV in K^+ polar angle of 0-60 degrees. Acceptance factors were estimated in Monte Carlo simulation taking into account the measured decay asymmetry of

$\Lambda(1520)$. We confirmed that the ratio of luminosities estimated for the hydrogen and deuterium runs was consistent with that of $\Lambda(1520)$ signal counts in the two data sets with detection of all three tracks in the K^+K^-p final state, which only arose from the interaction with protons.

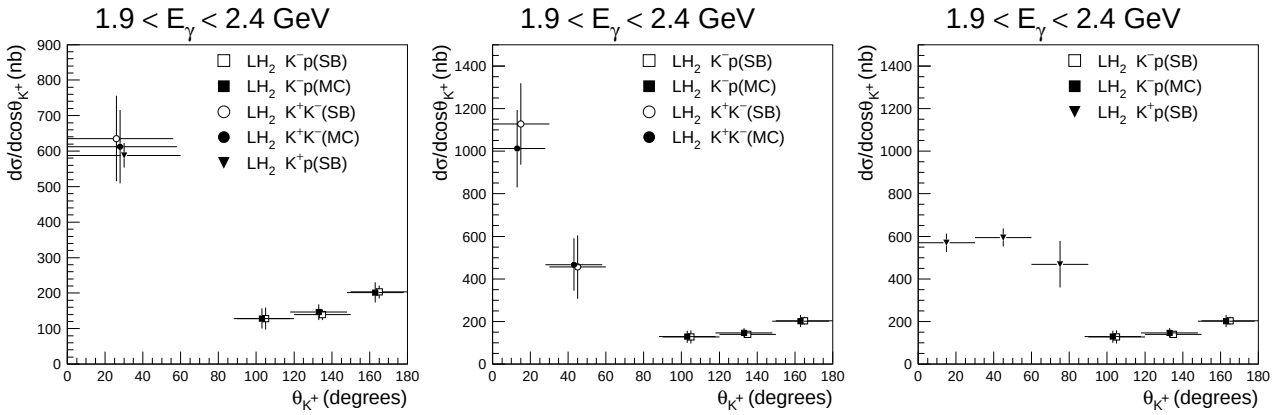

Figure 4.15: The measurement of differential cross sections in K^+K^-, K^+p and K^-p detection mode from protons in photon energy of 1.9-2.4 GeV by Monte Carlo based and side-band subtraction methods.

The left panel of Fig. 4.15 shows that the differential cross sections measured in K^+ polar angle of 0-60 degrees from K^+K^- and K^+p detection modes were consistent with each other. Cross sections at forward K^+ angles are more than three times larger than those at backward angles. This tendency does not contradict the existing theoretical picture [1, 14, 18, 16] which considers the dominance of a contact-term contribution but no contribution from the K^* exchange. While we divided the 0-60 degrees into 0-30 and 30-60 degrees, a significant discrepancy was observed in the range of K^+ polar angle of 0-30 degree by comparing the middle and right panel of Fig. 4.15. We have not resolved the discrepancy of results obtained in the two detection modes, but this may be caused by an interference effect due to different background compositions.

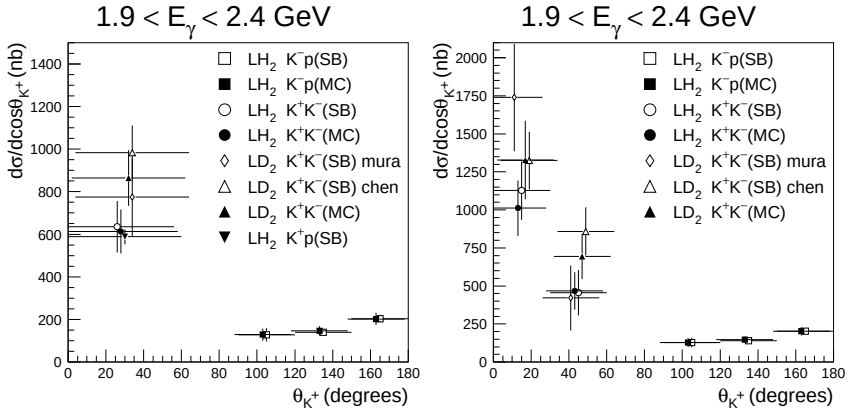

Figure 4.16: The measurement of differential cross sections in K^+K^-, K^+p and K^-p detection mode from protons and deuterons in photon energy of 1.9-2.4 GeV by Monte Carlo based and side-band subtraction methods.

We show differential cross sections of K^+K^- detection mode from deuterons in Fig. 4.15 and

Fig. 4.16 respectively. It can be seen that forward enhancement in K^+ polar angle dependence was confirmed in all the analysis methods even the statistics in K^+K^- detection mode were not large. More information about the measurement of differential cross sections in K^+K^- detection mode from protons are available in Fig. A.1-A.4.

4.3.2.1 K^+p detection mode from protons

In the case of K^+p detection mode from protons, the Fig. 4.17 shows the 2-step windows dependence of differential cross sections in photon energy of 1.9-2.4 GeV in K^+ polar angle of 0-30 and 30-60 degrees, where $\Lambda(1520)$ signal-window widths were examined under the requirement $|\mathrm{MMp}(\gamma,K^+p)-M_K| < 20\sim30$ MeV/c^2. It can be seen that the measurement of $d\sigma/d\cos\theta_{K^+}$ became relatively stable in K^+ polar angle of both 0-30 and 30-60 degrees while the $\Lambda(1520)$ signal-window width is greater than 20 MeV/c^2. Here, we set the "$|\mathrm{MMp}(\gamma,K^+p)-M_K| < 25$ MeV/c^2" and "$|\mathrm{MMp}(\gamma,K^+)-M_{\Lambda(1520)}| < 30$ MeV/c^2" as the standard 2-step windows requirements and as a reference measurement in K^+p detection mode.

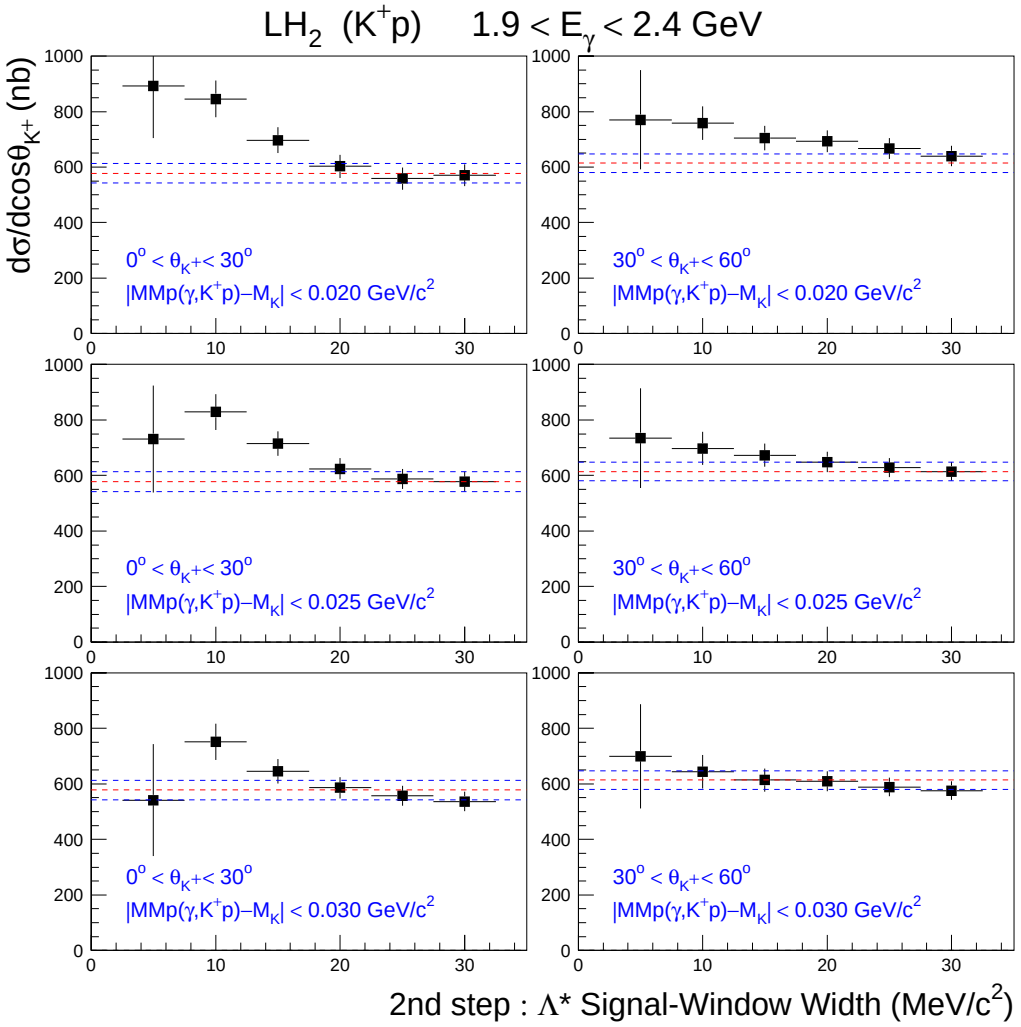

Figure 4.17: 2-step windows dependence of differential cross sections in photon energy of 1.9-2.4 GeV in K^+ polar angle of 0-30 and 30-60 degrees within the K^+p detection mode from protons, where the colored-bashed lines indicate the reference values under standard requirements.

In addition to the case with full energy range, as shown in Fig. A.5-A.8, we measured the window dependence of differential cross sections under the condition "$|MMp(\gamma,K^+p)-M_K| <$ 25 MeV/c^2" in photon energy of 1.75-1.9, 1.9-2.05, 2.05-2.2 and 2.2-2.4 GeV in K^+ polar angle of 0-30, 30-60, 60-90, 90-180, 0-60 and 19.4-43.2 degrees.

In order to make a comparison in differential cross sections between results of two-track K^+p detection mode and single K^+ detection mode in forward region, Fig. A.9-A.12 demonstrate the detail of 6×6 2-step side-band subtraction measurement in K^+p detection mode from protons. A summarized plot under standard requirement is shown in Fig. 4.18, 0∼20% of enhancement was observed in photon energy of 1.9-2.2 GeV in comparison with that in photon energy of 2.2-2.4 GeV. The tendency of a bump structure is consistent with the observation by single K^+ detection mode, but its strength is smaller than that of single K^+ detection mode, where 20∼40% enhancement was reported.

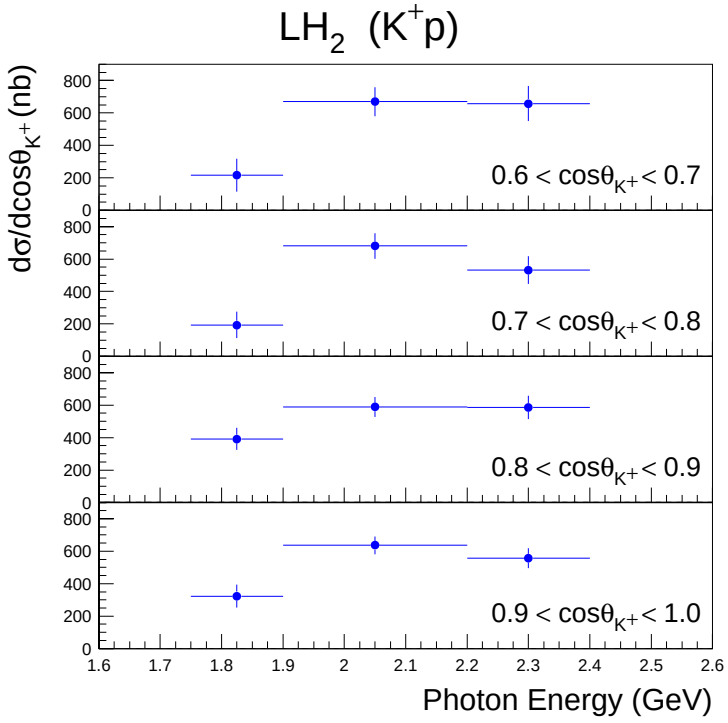

Figure 4.18: The energy dependence of differential cross sections in K^+p detection mode from protons were examined under the condition of $0.6 < \cos\theta_{K^+} < 1.0$.

4.3.2.2 K^-p detection mode from protons and deuterons

Differential cross sections in backward K^+ angles are smaller than 1/3 of those in $0° < \theta_{K^+} < 60°$. This may contradict with the interpretation of s-channel N* resonance around W=2.11 GeV (E_γ=1.9-2.0 GeV) in Λ(1520) photoproduction using single K^+ detection.

In order to investigate this possible contradiction further, we looked into the energy dependence of differential cross sections in backward K^+ angles with K^-p detection mode. The left column of Fig. 4.19 shows the energy dependence both from Monte Carlo based and side-band subtraction methods in 4 regions of backward K^+ angles. In $120° < \theta_{K^+} < 150°$, the differential cross section increases toward lower photon energy, and there is no bump structure. In $150° < \theta_{K^+} < 180°$, an enhancement is observed around E_γ=2.1 GeV, but it does not

correspond to the mass of claimed N* by single K^+ detection. In case we combine these two angle regions, $120° < \theta_{K^+} < 150°$ and $150° < \theta_{K^+} < 180°$, there is no obvious enhancement. At least, no clear bump structure corresponding to W=2.11 GeV is observed in the backward K^+ angles with K^-p detection mode. Same measurement from deuterons shows similar energy dependence of differential cross sections in the K^+ polar angle of 120-180 degrees.

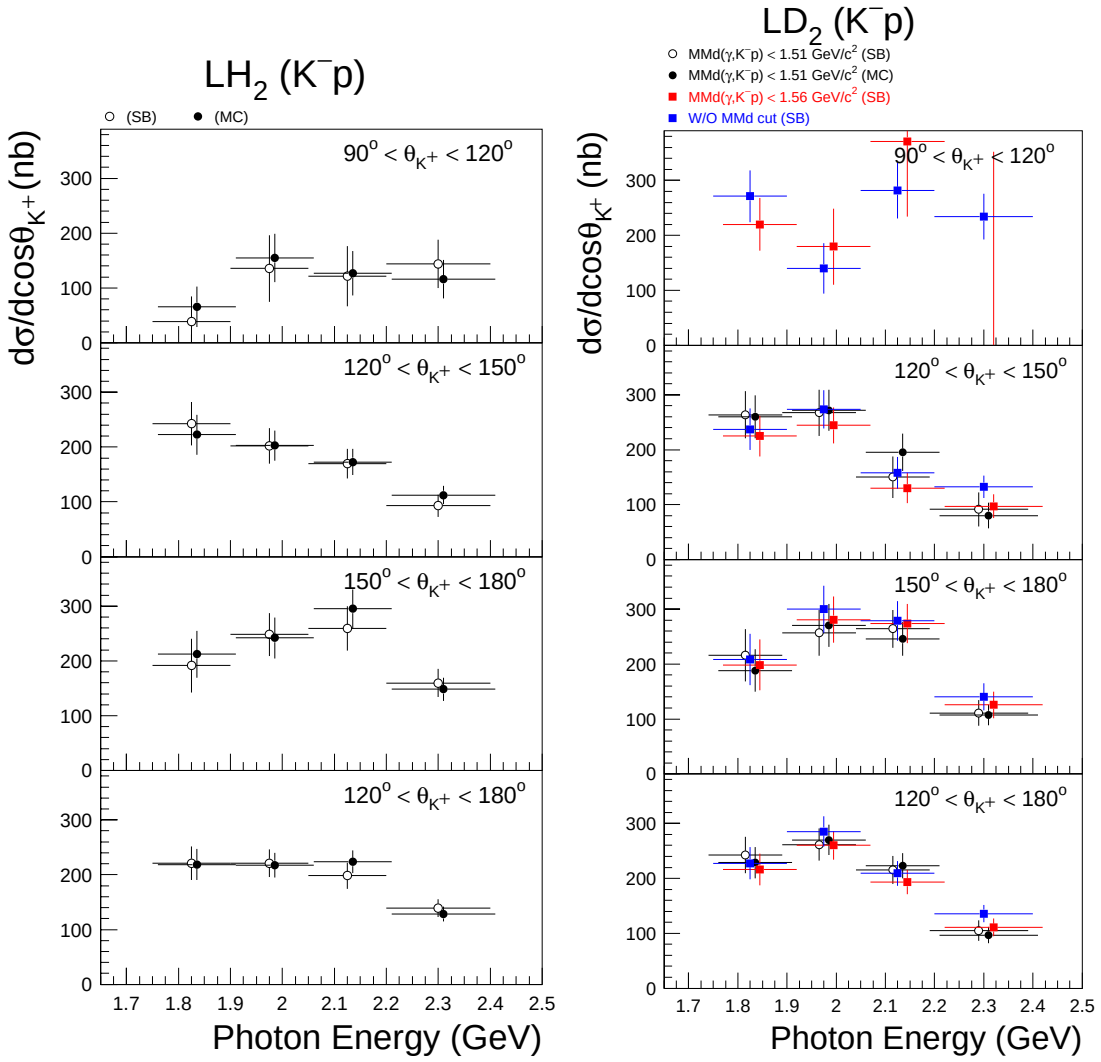

Figure 4.19: The energy dependence of differential cross sections in K^-p detection mode from protons and deuterons in backward K^+ polar angles are shown in left and right columns respectively. A validity check of cut condition "MMd(γ,K^-p)| < 1.510 GeV/c^2" is overlaid in the right column.

An additional study about the validity of cut condition "MMd(γ,K^-p)< 1.510 GeV/c^2" is overlaid in right column of Fig. 4.19. This cut condition was applied to remove the contamination from Θ^+ photoproduction and 1.6-GeV bump, as shown in the bottom-left panel of Fig. 4.14. Therefore, we change to cut boundary to 1.56 GeV/c^2 and without MMd cut, the results are overlaid by red-solid and blue-solid squares in right column of Fig. 4.19 respectively. It turns out to be of no bias with this cut condition. More information about the measurement of differential cross sections in K^-p detection mode from protons and deuterons are available in Fig. A.13-A.20.

4.3.2.3 Combination of K^+p and K^-p detection mode from protons

As we mentioned in Sec. 4.3.2.1, we did the similar studies as the left column of Fig. 4.19 in K^+p detection mode from protons, and show in Fig. A.5-A.8. Combining the measurement in left column of Fig. 4.19 and those from Fig. A.5-A.8 with standard 2-step requirements, the differential cross sections which cover whole K^+ polar angle range in 4 photon energy slices are shown in Fig. 4.20.

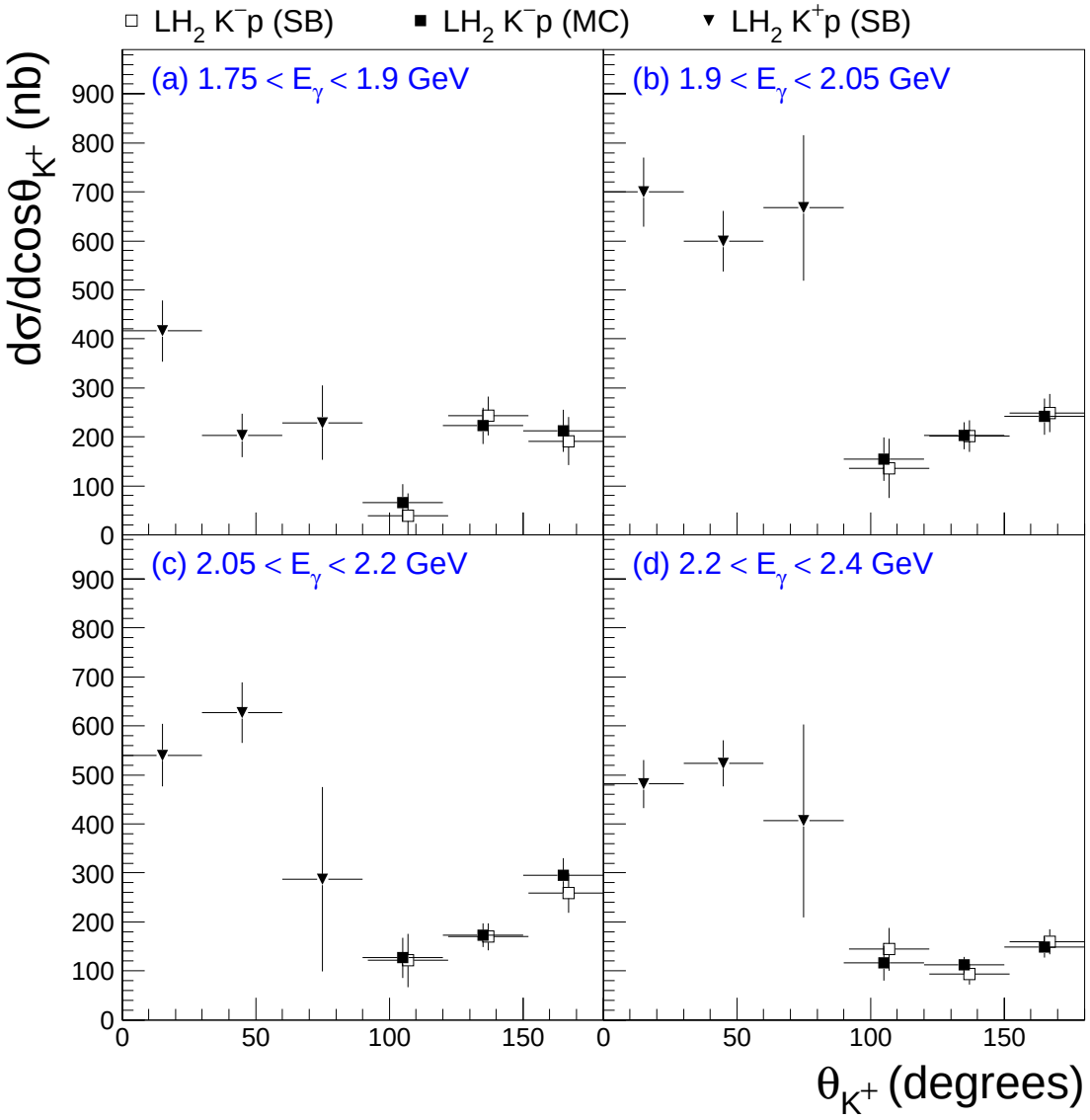

Figure 4.20: By combining the measurement from K^+p and K^-p detection modes, differential cross sections from protons which cover whole K^+ polar angle range in 4 photon energy slices are shown in 4 panels.

By summing up the measurement in Fig. 4.20, even though the error bar in K^+ polar angle of 60°-90° of each panel is huge, where we selected the results in K^-p detection mode from side-band subtraction method, the total cross sections are shown in Fig. 4.21. The results of present measurement and LAMP2 experiment are shown in Fig. 4.21, also the parametrization function from SLAC group was overlaid for comparison. Our cross sections are lower than the theoretical prediction.

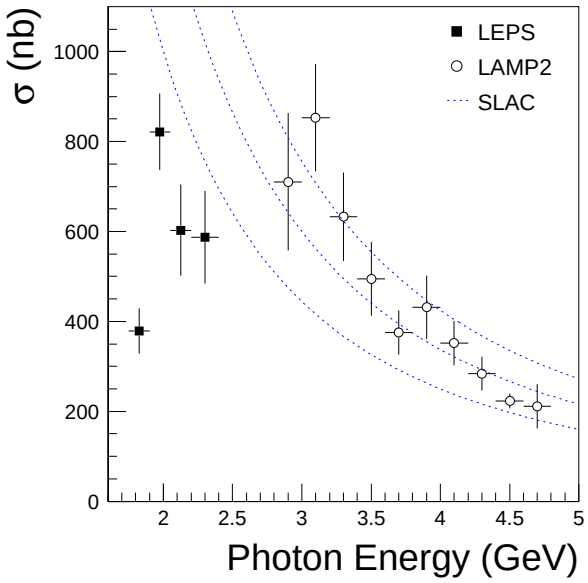

Figure 4.21: Total cross sections (solid squares) of $\Lambda(1520)$ photoproduction in the photon energy of 1.75-1.9, 1.9-2.05, 2.05-2.2 and 2.2-2.4 GeV of LEPS experiment overlaid with the measurement from LAMP2 experiment [13] (open circles), where 3 dashed lines indicated the parametrization function, $\sigma_{tot}(\Lambda(1520)) = (5.4 \pm 1.4)/k^2 \mu b$, from SLAC group [29]. Numerical values of LEPS results are listed in Tab. A.3.

4.3.2.4 Summarized results

As shown in Fig. 4.22, we studied the invariant mass of K^-p in K^+K^-p detection mode from protons and deuteriums. The total luminosity for hydrogen target is 0.608427 $1/\mu b$ and for deuterium target is 1.126174 $1/\mu b$, the luminosity ratio of deuterium target to hydrogen target is 1.851. After applying the luminosity ratio on mass spectra of hydrogen, the mass spectra of invariant mass of K^-p from scaled protons and deuterons were overlaid in the same panel with different cut conditions depicted above the panels. The counting range of $\Lambda(1520)$ events is from 1.50 to 1.54 GeV/c^2. Numbers of $\Lambda(1520)$ events with different cut conditions without background subtraction were listed in the Table 4.1. After applying the luminosity ratio, the raw counts between scaled protons and deuterons from (1,2) to (1,2,3,4) are almost identical on both cases. The non-resonant KKp contaminates in condition (1), therefore the counts of both are different in that.

Table 4.1: Number of $\Lambda(1520)$ events in the range of invariant mass of K^-p of 1.50-1.54 GeV/c^2 with four kinds of cut conditions from protons, scaled protons and deuterons.

Cut conditions	proton	scaled proton	deuteron
(1)	104	192.5	257
(1,2)	89	164.7	163
(1,2,3)	84	155.5	153
(1,2,3,4)	31	57.4	62

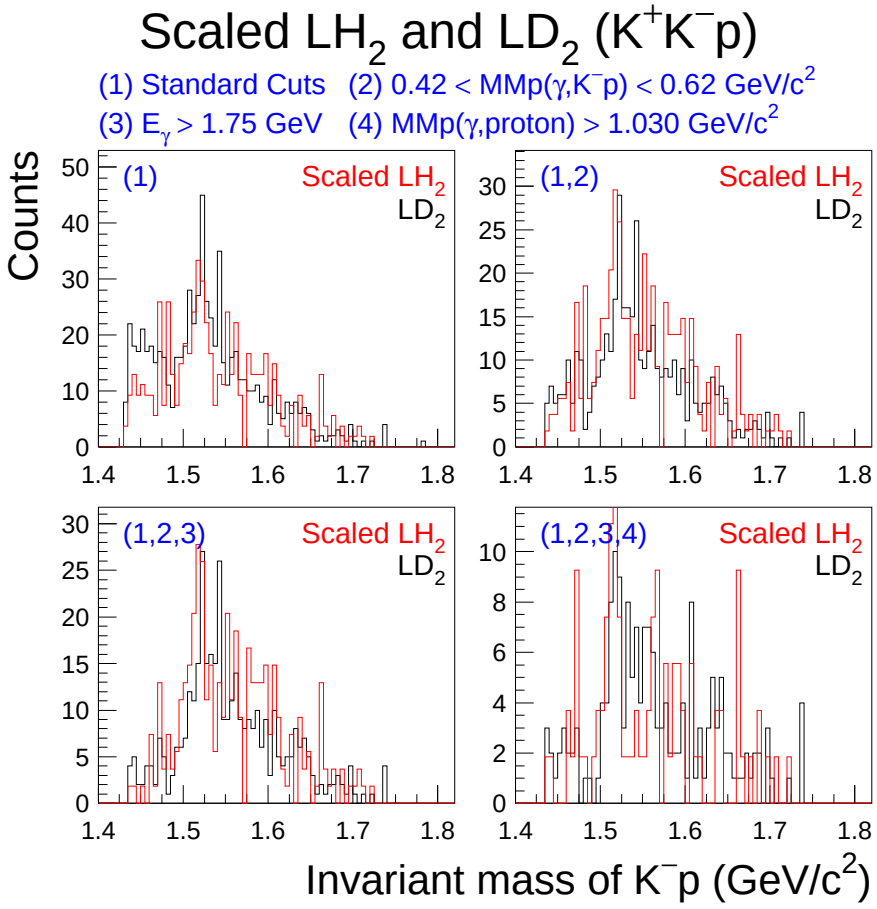

Figure 4.22: Invariant mass spectra of K^-p in the KKp detection mode from scaled protons and deuterons were shown with four kinds of cut conditions, depicted above the panels.

Therefore, we confirmed that the ratio of luminosity estimated for hydrogen and deuterium runs was consistent with that of the $\Lambda(1520)$ signal counts in the two data sets with detection of all three tracks in the K^+K^-p final state, which only arose from the interaction with protons.

From the Fig. 4.23 it can be seen that we studied the K^+ polar angle dependence and photon energy dependence of differential cross from protons in K^+K^-, K^+p and K^-p detection modes, and made a comparison with the result of LAMP2 experiment.

Firstly, in Fig. 4.23(a), we studied the polar angle dependence of differential cross section in photon energy of 1.9-2.4 GeV. As we mentioned in previous section, different detection modes have complementary coverage. The behavior of differential cross section shown a non-monotonic distribution, the increments happened in both most backward and forward ranges. Again, this tendency does not contradict the existing theoretical predictions which considers the dominance of a contact-term contribution but no contribution from K^* exchange under a rescaling by a cut-off mass of 650 MeV [1, 30].

Secondly, in order to make a comparison with the result of LAMP2 experiment, as shown in Fig. 4.23(b), we studied the differential cross section within the same angular region as LAMP2 experiment, where the evaluation of measurement of LAMP2 experiment is shown in appendix A.5. Fig. A.3 shows the mass spectra and the corresponding values of non-linearity and non-linearity factor. It appeared from Fig. A.3 that the events of $\Lambda(1520)$ resonance structure happened on the saddle point of the sum of background spectra. By checking the

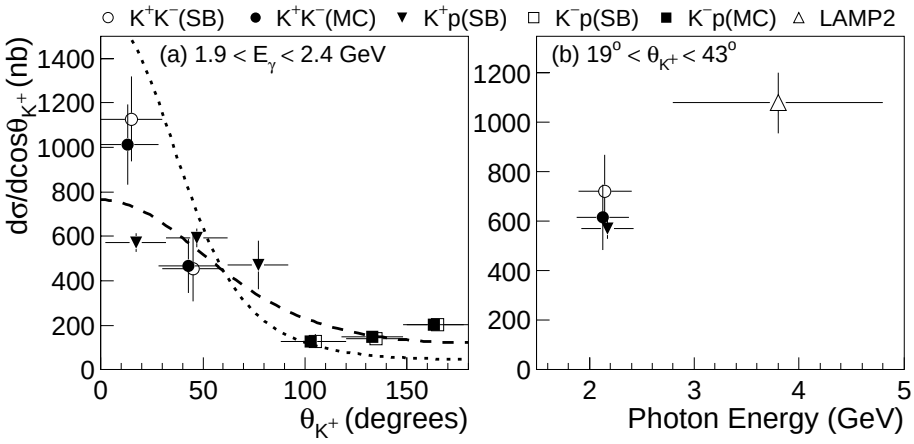

Figure 4.23: (a) Differential cross sections from the hydrogen data in a photon energy of 1.9-2.4 GeV. Data points in forward and backward K6+ angles come from the K^+K^-/K^+p and K^-p detection modes, respectively. Sideband-based (SB) and Monte Carlo-based (MC) estimations are simultaneously plotted. A dashed (dotted) line indicates a theoretical prediction for the photon energy of 1.85 (2.35) GeV with K exchange and a contact term [30]. (b) Differential cross sections from this work and LAMP2 in c.m. K^+ angles of 19-43 degrees.

background linearity in different photon energy slices and different K^+ polar angle slices shown in Fig. A.1, unfortunately, the worst background linearity behaved merely in this particular angle range. An underestimated background contribution might take place in this study, therefore, the non-linearity correction mentioned before is significant in this study. According to Fig. A.4, the measurement of differential cross section with a widest side-band range, 30 MeV/c^2, was chosen as the result shown in the plot of paper because of the smallest uncertainty. In this measurement, theoretical calculations predict $\sim 1\mu$b or more at $E_\gamma \sim 2$ GeV with inputs from the LAMP2 result [1, 14, 18, 16], and the present results are smaller than those predictions. This measurement shall provide new information for theoretical models.

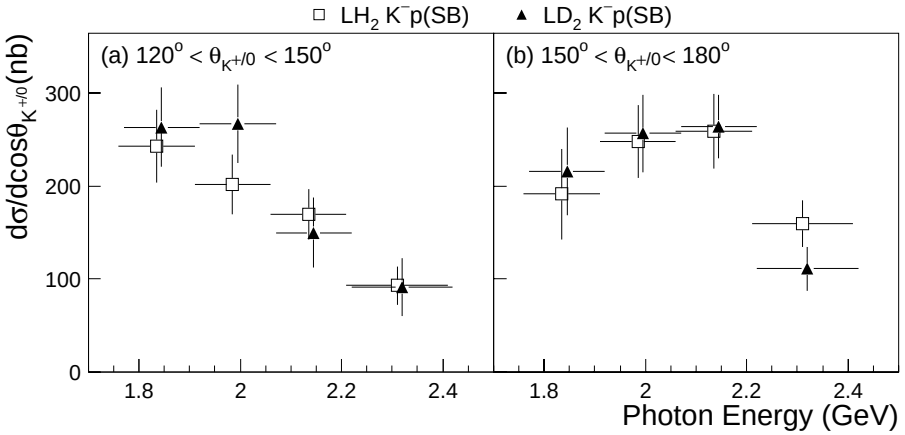

Figure 4.24: Differential cross sections for backward $K^{+/0}$ angles in the K^-p detection mode from the hydrogen and deuterium targets as a function of photon energy in two $K^{+/0}$ angle regions.

Let us now turn to the measurement of differential cross section in K^-p detection mode.

Here only the estimations using side-band subtractions are shown, and their deviations from MC-based results are typically 7%. Fig. 4.24 shows energy dependence of differential cross sections in K^+ polar angle of 120-150 and 150-180 degrees in K^-p detection mode from protons and deuterons. To make a comparison between the results of protons and deuterons in the same photon energy region and polar angle range, the differential cross section from two different targets are close to each other.

Based on the measurement in Fig. 4.24, we calculated the combined differential cross sections in the photon energy of 1.75-2.4 GeV and K^+ polar angle greater than 120 degrees from protons and deuterons, and then evaluated the ratio of deuterons to protons. The calculations were done by side-band subtraction method only, and show in Tab. 4.2, where differential cross sections in K^+ polar angle of 120°-150° and 150°-180° were combined by taking a weighted average with $d\cos\theta_{K^+}$ (0.36603 for 120°-150° and 0.13397 for 150°-180°).

Table 4.2: Differential cross sections in backward K^+ polar angles

K^+ polar angle	Photon Energy (GeV)	$d\sigma/d\cos\theta_{K^+}$ (nb)	
		LH_2	LD_2
120°-150°	1.75-1.9	242.841±39.4075	263.675±43.0377
	1.9-2.05	201.748±32.3878	267.224±41.8693
	2.05-2.2	169.768±27.0854	149.947±37.6471
	2.2-2.4	92.9783±20.3966	91.3669±30.8475
	1.75-2.4	161.205±13.9880	172.309±18.7166
150°-180°	1.75-1.9	191.428±48.7495	215.726±47.4598
	1.9-2.05	248.351±39.0218	256.836±41.4339
	2.05-2.2	259.095±40.3009	264.154±34.2209
	2.2-2.4	159.842±25.2862	110.982±23.5714
	1.75-2.4	208.012±18.0385	197.729±17.0269
120°-180°	1.75-2.4	173.747±11.3233	179.120±14.4411

$$\frac{LD_2}{LH_2} = \frac{179.120 \pm 14.4411}{173.747 \pm 11.3233} = 1.0309 \pm 0.1069 \tag{4.1}$$

According to Eq. 4.1, the ratio of differential cross sections of deuterons to protons is 1.0309±0.1069 in the side-band subtraction method. Accompanied with the study of Table 4.1, the $\Lambda(1520)$ photoproduction from neutrons was found to be strongly suppressed at backward K^0 angles. The observation of a large asymmetry between the productions from protons and neutrons conflicts with the model considering a dominance of t-channel K^* exchange [14], but can be explained by the model where the contact term plays a major role [1]. Larger cross sections were observed at lower energies as shown in Fig. 4.24, and this behavior is qualitatively consistent with a theoretical calculation in Ref. [1]. In the backward K^+ production from protons, cross sections also show an increase toward $\theta_{K^+} = 180°$ as shown in Fig. 4.23(a). This may indicate an additional contribution from u-channel diagrams, which are conventionally considered to be small in the theoretical models [1, 14, 18, 16].

4.4 K^- decay asymmetry in $\Lambda(1520)$ t-channel helicity frame

Decay asymmetry was measured in $\Lambda(1520)$ t-channel helicity frame, which was defined by taking a quantization axis to the direction of a t-channel exchanged particle (or the anti-direction of a target proton).

As we demonstrated the mass spectra of real data and estimated Monte Carlo background and the angular dependence of "Non-Linearity" and "Non-Linearity Factor" in Fig. 3.3 and 3.4, similar studies by signal-window width dependence in different photon energy ranges were shown in appendix B. In this study, 5 kinds of photon energy slices were set to K^-p detection mode, 4 kinds for K^+K^- detection mode and 2 kinds for K^+p detection mode. The photon energy slices of K^-p, K^+K^- and K^+p detection modes are listed in Table 4.3.

Table 4.3: Energy slices of K^-p, K^+K^- and K^+p modes for K^- decay asymmetry study.

Number of Slices	K^-p mode	K^+K^- mode	K^+p mode
1	1.75 - 2.40 GeV	1.90 - 2.40 GeV	1.90 - 2.40 GeV
2	1.75 - 2.20 GeV	1.90 - 2.20 GeV	
	2.20 - 2.40 GeV	2.20 - 2.40 GeV	
3	1.75 - 2.00 GeV	1.90 - 2.10 GeV	1.75 - 1.90 GeV
	2.00 - 2.20 GeV	2.10 - 2.25 GeV	1.90 - 2.20 GeV
	2.20 - 2.40 GeV	2.25 - 2.40 GeV	2.20 - 2.40 GeV
4	1.75 - 1.95 GeV	1.90 - 2.05 GeV	
	1.95 - 2.10 GeV	2.05 - 2.20 GeV	
	2.10 - 2.25 GeV	2.20 - 2.30 GeV	
	2.25 - 2.40 GeV	2.30 - 2.40 GeV	
5	1.75 - 1.90 GeV		
	1.90 - 2.05 GeV		
	2.05 - 2.20 GeV		
	2.20 - 2.30 GeV		
	2.30 - 2.40 GeV		

It can been seen from Fig. B.1, in the photon energy of 1.75-2.4 GeV, we studied the background linearity of 8-bin K^- polar angle in t-channel helicity frame in K^-p detection from protons. The left column shows the mass spectra of real data (black) and estimated Monte Carlo background (red). The middle column shows the non-linearity of signal-window width dependence, the top and bottom dash lines in each panel of middle column indicate the 1-σ deviation away from "Zero", the central dash line. The width of side-band region is greater than or equivalent to the width of $\Lambda(1520)$, 15.6 MeV/c^2, and also the non-linearity is required to be stable with respect to the variation of width, whose typical value is about 15 or 20 MeV/c^2. The non-linearity is checked to be smaller than 1σ. The right column shows the non-linearity factor of signal-window width dependence. Similar studies with different photon energy ranges in K^-p detection mode is shown in Fig. B.2-B.15.

Following the study of background linearity, as shown in middle and bottom parts of Fig. B.16, we studied the energy and width dependence of K^- polar angle distribution in

$\Lambda(1520)$ t-channel helicity frame in K^-p detection mode from protons. Results from side-band subtraction and Monte Carlo based methods are compared simultaneously. In each part, the first row demonstrates the "Counts", "Acceptance" and "Counts/Acceptance" from side-band method; the second one shows the corresponding plots from Monte Carlo method.

The last term of Eq. 1.7, $\gamma \cos\theta_{K^-}$, introduces the asymmetry composition into K^- polar angle distribution. While we investigate the K^- polar angle distribution in both K^-p and K^+K^- detection modes from protons, they behaved symmetry distribution. In the beginning, therefore, we neglected the last term in Eq. 1.7 to fit the K^- polar angle distribution, namely the $f'(\theta_{K^-})$ shown in Eq. 4.2.

$$f'(\theta_{K^-}) = \alpha(\frac{1}{3} + \cos^2\theta_{K^-}) + \beta \sin^2\theta_{K^-}, \tag{4.2}$$

Instead of fitting "Counts/Acceptance" by Eq. 4.2, we used "$f'(\theta_{K^-}) \times$ *Acceptance*" to fit the distribution of "Counts". That helped us to minimize the fitting errors. And, the corresponding distribution of $f(\theta_{K^-})$ accompanied with the fitting parameters from "$f'(\theta_{K^-}) \times$ *Acceptance*" were overlaid on "Counts/Acceptance".

The signal-window width dependence of "fraction of helicity-3/2" in 2 different photon energy slices were shown top and middle panels of Fig. B.21. It can be seen from them, there is no significant width dependence in both cases while we picked up a reasonable width greater than 15 MeV/c^2. K^+K^- detection mode from protons has parallel studies in appendix B.2.

Based on the reasonable selections of signal-window width, 15-MeV/c^2 and 20-MeV/c^2 signal window of K^-p and K^+K^- modes were chosen in obtaining the results of side-band method respectively to compare with the results of Monte Carlo method of 20-MeV/c^2 signal window. As shown in Fig. 4.25 (Fig. 4.26), we studied the energy dependence of t-channel helicity component without including an interference term in 3 kinds of photon energy slices from K^-p (K^+K^-) detection mode of protons. No significant energy dependences were observed in both K^-p and K^+K^- detection modes. The results of K^- decay asymmetry study with various photon energy slices in K^-p and K^+K^- detection modes from protons were shown in Fig. B.48.

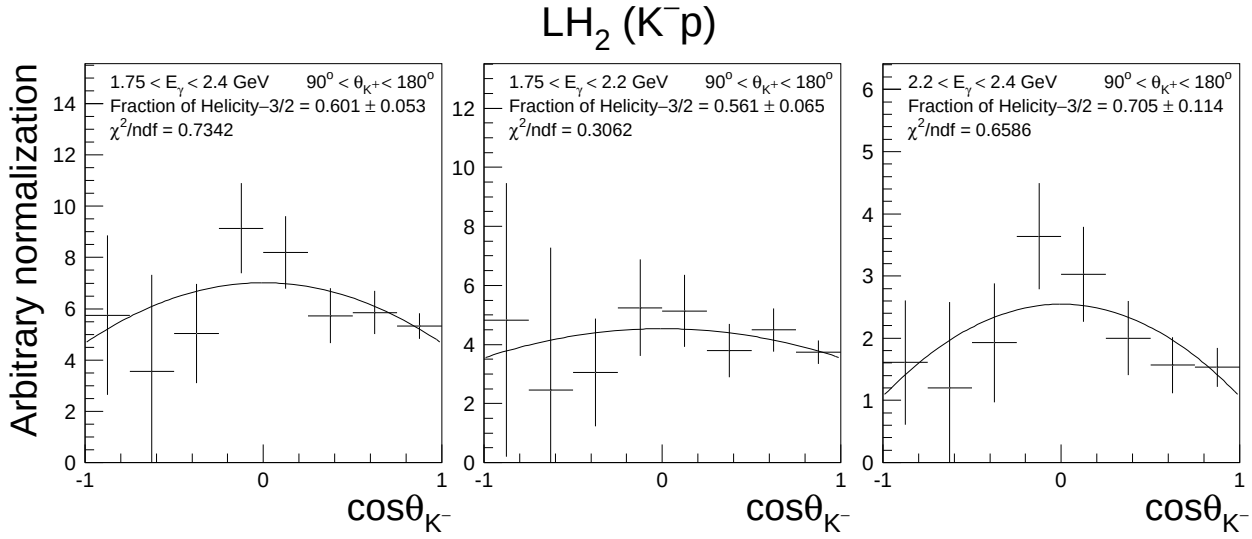

Figure 4.25: K^- polar angle distribution in photon energy of 1.75-2.4, 1.75-2.2 and 2.2-2.4 GeV with fit of t-channel helicity component in K^-p detection mode from protons.

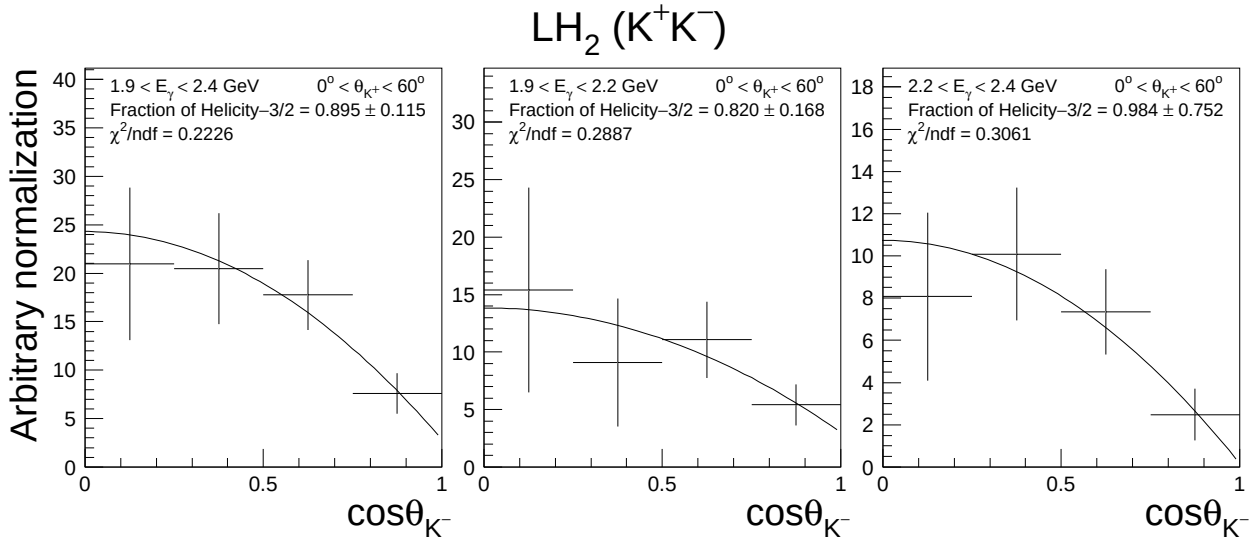

Figure 4.26: K^- polar angle distribution in photon energy of 1.9-2.4, 1.9-2.2 and 2.2-2.4 GeV with fit of t-channel helicity component in K^+K^- detection mode from protons.

In K^+p detection mode, the proton tends to be produced in the forward direction, and statistics of the analyzed sample was therefore enhanced in backward K^- angles, which are opposite directions to the sample in K^+K^- detection mode.

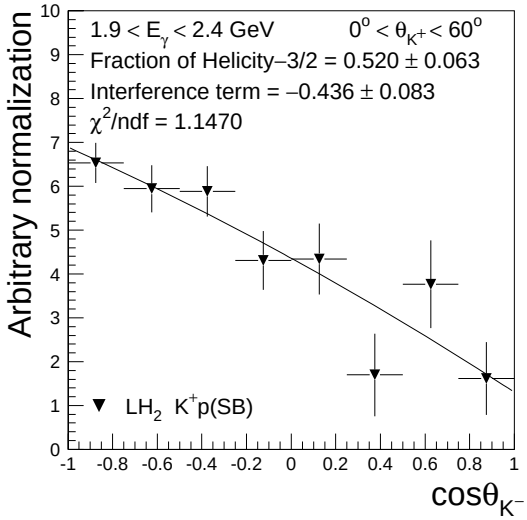

Figure 4.27: Decay asymmetry in $\Lambda(1520)$ t-channel helicity frame from K^+p detection mode of protons.

Fig. 4.27 shows the measured decay asymmetry distribution. Because of larger acceptance, the whole $\cos(\theta_{K^-})$ range was covered in contrast with the K^+K^- detection mode. It can be seen from Fig. 4.27, it turns out that an interference effect is very strong in the photon energy of 1.9-2.4 GeV and forward K^+ angle region. The interference effect has been seen in both LAMP2 and CLAS experiments but their interference were weaker than our result, as shown

in Fig. 1.16 and 1.17.

$$f'(\theta_{K^-}) = (1-\beta)(\frac{1}{3} + \cos^2\theta_{K^-}) + \beta \sin^2\theta_{K^-} + \gamma\cos\theta_{K^-} \quad (4.3)$$

Fitting the K^- polar angle distribution in Fig. 4.27 by Eq. 4.3, replacing α by 1-β in Eq. 1.7, the measured decay asymmetry is also shown in Fig. 4.27.

As shown in Fig. 4.27, the fraction of helicity-3/2 component was comparable with that of helicity-1/2 component. (In the case of K^+K^- detection mode, due to the limitation of acceptance, the fitting was limited to be in the range of "$\cos\theta_{K^-} > 0$" only and without an interference term. Therefore, we claimed that the decay asymmetry was strongly dominated by helicity-3/2 component.) This implies a sizable contribution from K-exchange in t-channel in additional to the contribution from K^*-exchange in t-channel. The result is clearly different from that of both LAMP2 and CLAS experiments.

In order to compare the result of decay asymmetry between K^+p and K^+K^- detection modes, corrected number of $\Lambda(1520) \rightarrow K^-p$ events divided by acceptance were implemented in K^+K^- detection mode with the side-band subtraction method by requiring K^+ polar angle in c.m. system to be smaller that 60 degrees, so that the kinematical conditions became the same as each other. Since the luminosity and solid angle is the same in K^+p and K^+K^- detection mode, a simple comparison can be seen by overlaying the "counts/acceptance" from 2 detection modes, as shown in Fig. 4.28. Results from 2 detection modes are statistically consistent with each other at individual $\cos\theta_{K^-}$ region.

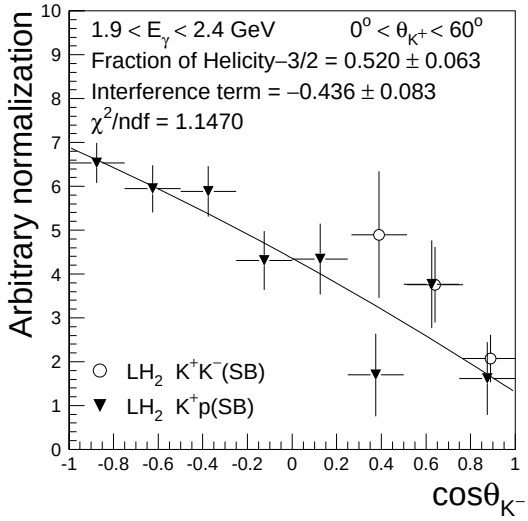

Figure 4.28: Decay asymmetry in $\Lambda(1520)$ t-channel helicity frame from K^+p detection mode of protons along with overlaying the result from K^+K^- detection mode.

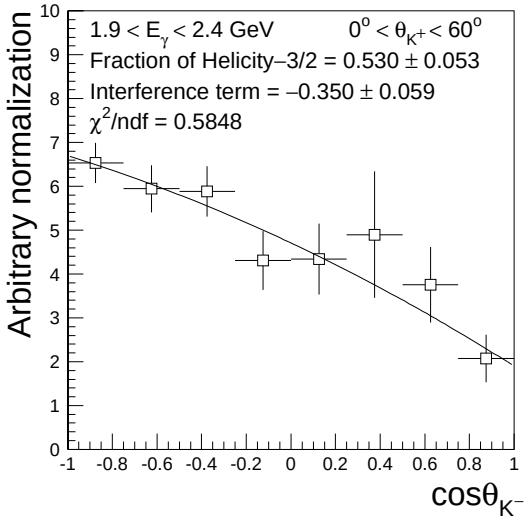

Figure 4.29: Decay asymmetry distribution, which is composed by results from K^+K^- detection mode ($\cos\theta_{K^-}$ >0.25) and K^+p detection mode ($\cos\theta_{K^-}$ <0.25).

Fractions of helicity state must be the same in both K^+p and K^+K^- detection modes, and only strength of interference could differ depending on amount of backgrounds. However, this strength looks also similar to each other in Fig. 4.28. Therefore, it is natural to test the decay asymmetry parameters by combining the K^+p and K^+K^- detection modes. In the forward K^- direction, the statistics of K^+K^- detection mode is better, and S/N ratio in K^+p detection

mode gets worse. So results from K^+K^- mode were plotted in $\cos\theta_{K^-} > 0.25$ while results from K^+p mode were plotted in the other $\cos\theta_{K^-}$ region.

Two kinds of evaluations of decay asymmetry parameters as shown in Fig. 4.28 and Fig. 4.29 gave consistent results, and we choose parameter from Fig. 4.28 as a standard one by considering the possibilities of slight difference of interference amplitude and systematics in signal counting.

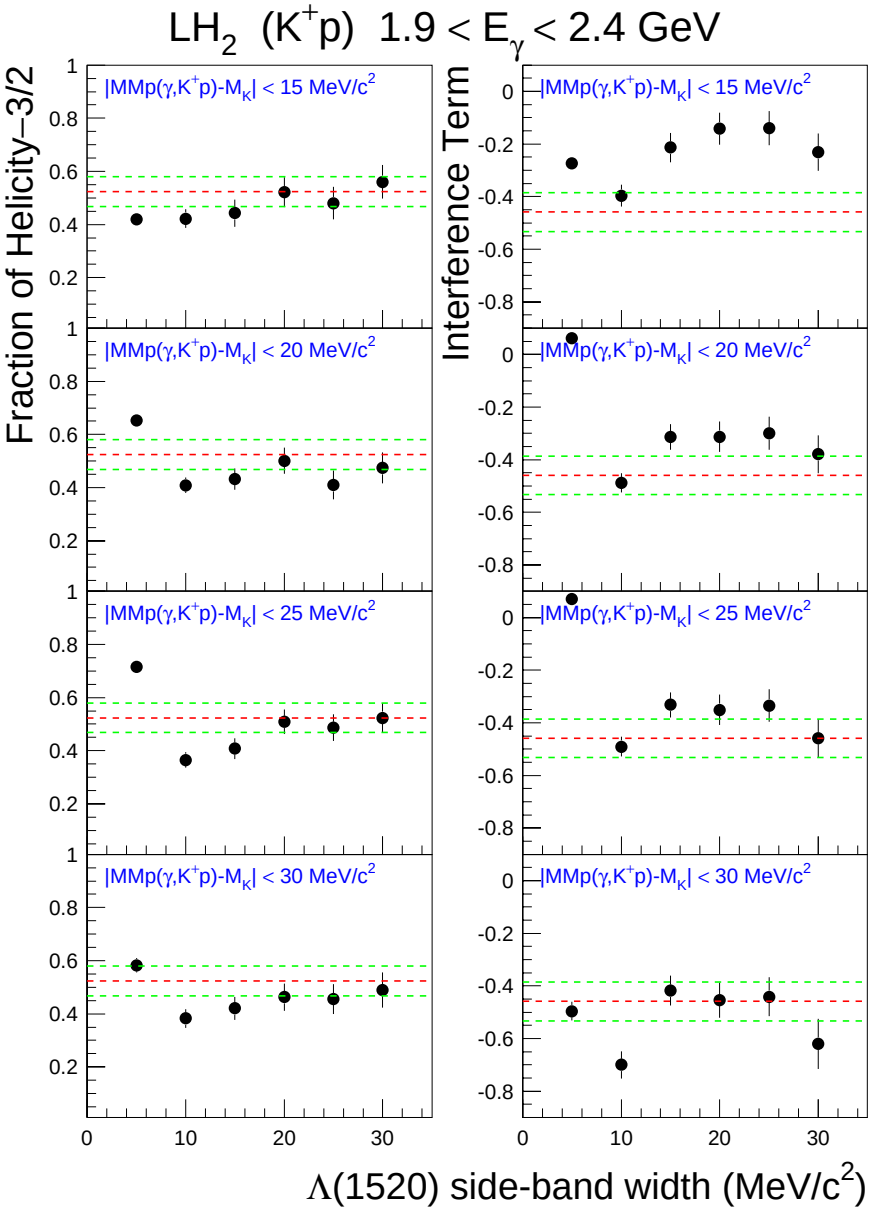

Figure 4.30: Fraction of helicity-3/2 component (left column) and relative strength of interference term (right column) as functions of signal window sizes in MMP(γ,K^+) [horizontal axis] and MMp(γ,K^+p) [four panels from top] distributions.

In Fig. 4.30, we showed the fractions of helicity-3/2 component and coefficients of interference term as functions of signal window widths. The results are stable around the standard window sizes. The effect of uncertainty in background estimations including non-linearity was not large.

After introducing an interference term in the fitting of decay asymmetry in K^+p detection mode, the fits in forward $\Lambda(1520)$ photoproduction, K^-p detection mode of protons, were also updated accordingly. Fig. 4.31 shows new fits to K^- decay angular distributions from side-band subtraction method, whose data points are the same as that in Fig. 4.25. The interference term was not strong as that of backward $\Lambda(1520)$ photoproduction, and new fitting results were not far from the previous results without including interference term.

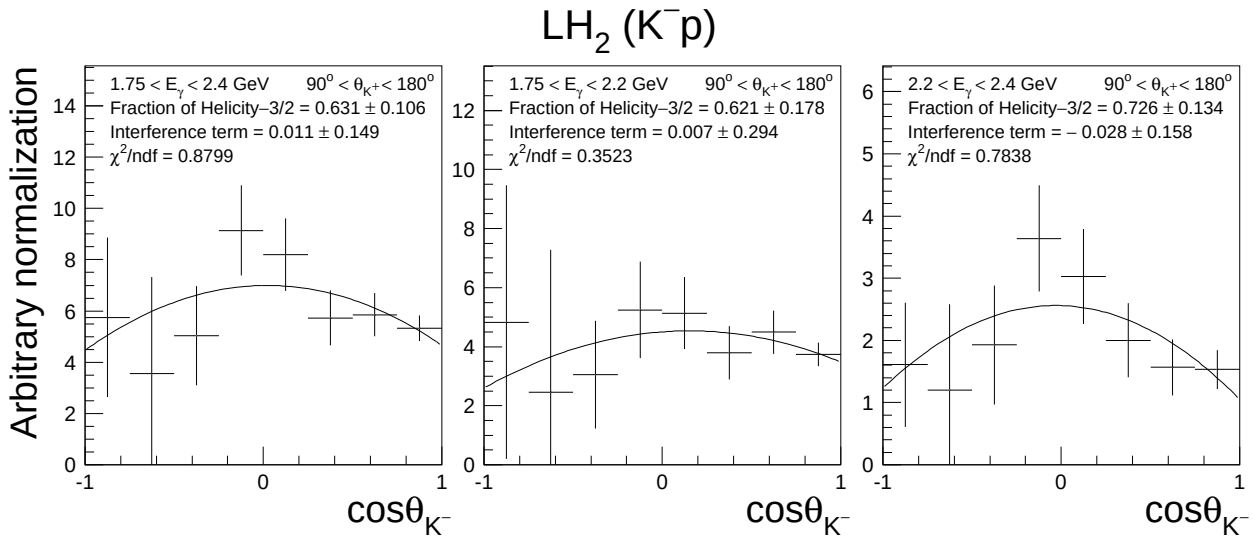

Figure 4.31: K^- polar angle distribution in photon energy of 1.75-2.4, 1.75-2.2 and 2.2-2.4 GeV with fit of t-channel helicity component including an interference term in K^-p detection mode from protons.

It can be seen from middle and right panels of Fig. 4.31, the increase of fraction may be indicated in higher photon energy region. However, the error bar become larger than the previous fits because of the increase of free parameters, and the deviation of helicity-3/2 fractions at the two photon energy is now 0.47σ in side-band subtraction method and 0.26σ in Monte Carlo based method. So, we decided to show a single fitting result with full photon energy range of 1.75-2.4 GeV only, as shown in right panel of Fig. 4.32.

In comparison with the result of LAMP2 experiment, the fraction of helicity-3/2 component was measured to be 0.520±0.063 in photon energy of 1.9-2.4 GeV in K^+p detection mode, and clearly differ from 0.880±0.076 by LAMP2 [13]. The present result was closer to the value from the low-energy electroproduction by CLAS[21], which obtained 0.446±0.069 in $0.9 < Q^2 < 1.2$ GeV^2. One possible way to accommodate the observed ratio of the two spin projections under the dominance of a contact-term contribution is to introduce a small contribution from the K^* exchange with a destructive interference between $S_z = \pm\frac{3}{2}$ components, as shown in Fig. 13 of Ref. [1]. The $K^*N\Lambda(1520)$ coupling constant, which controls the strength of such an interference, is experimentally undetermined, and the theoretical predictions of its absolute value vary in the range of 0-15 [31]. The same fitting procedure was also performed for the K^- angular distribution at backward K^+ angles in K^-p detection mode. As shown in Fig. 4.32(b), while the interference was found to be weak, the fraction of $S_z = \pm\frac{3}{2}$ was measured to be 0.631±0.106 (0.545±0.076) in the side-band subtraction (MC-based) method for the photon energy range of 1.75-2.4 GeV. These fractions were similar to the result in the forward K^+ direction. Accompanying with the result of LAMP2 experiment, the energy dependence of

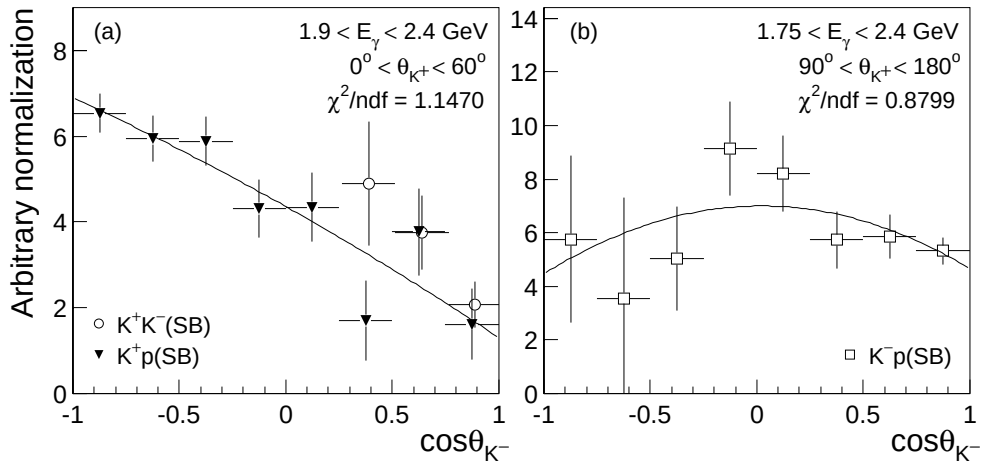

Figure 4.32: K^- polar angle distribution at the t-channel helicity frame of $\Lambda(1520)$, produced from the hydrogen target. (a) shows a result in the K^+K^- detection mode. (b) and (c) show results in the K^-p mode from photon energy of 1.75-2.2 GeV and 2.2-2.4 GeV, respectively. Solid lines indicates fit by a linear combinations of helicity-3/2 and 1/2 components.

"Fraction of helicity-3/2" in one photon energy slice in both K^-p and K^+p detection mode from protons were shown in Fig. 4.33.

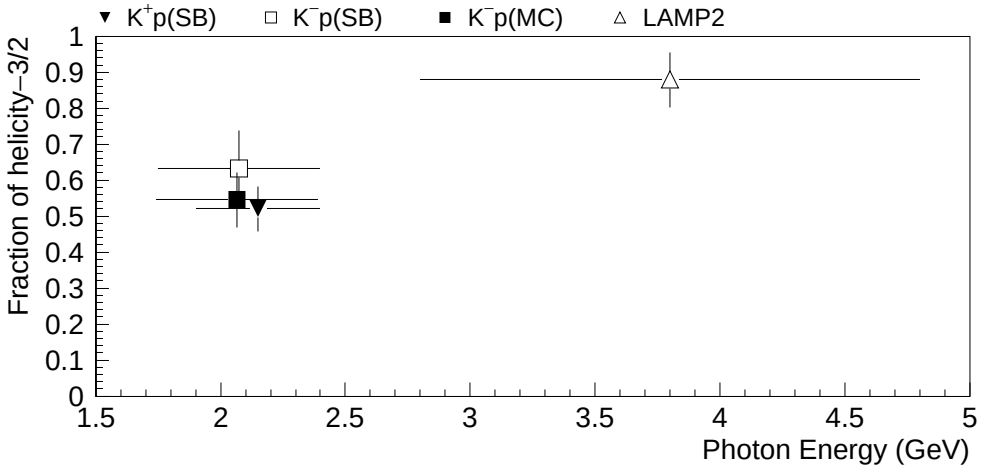

Figure 4.33: Fractions of the helicity-3/2 component as a function of photon energy. Results in the forward K^+ angle (0-60 degree) are shown by circles along with the LAMP2 result (a triangle). Results in the backward K^+ angle (90-180 degree) are shown by squares. Sideband-based (SB) and Monte Carlo-based (MC) estimations are simultaneously plotted.

4.5 Photon beam asymmetry

Photon beam asymmetry was measured in K^+p detection mode from protons for the K^+ polar angles less than 60 degrees by dividing K^+ azimuthal angle into 8 bins. The photon beam asymmetry (Σ) was measured by the fit based on the Eq. 1.1. The beam polarization was

calculated to be 0.87752 by taking weighted average of energy-dependence beam polarization $0.972 \times \left(-1.9563 + 2.434E_\gamma - 0.51219E_\gamma^2\right)$ with $\Lambda(1520)$ production rates in K^+ polar angle less than 60 degrees and every 100 MeV photon energy E_γ interval. The normalization factor of two polarization states was estimated to be

$$k = \frac{N_{hori}}{N_{vert}} = \frac{1.29869 \times 10^{12}}{1.50784 \times 10^{12}} = 0.86129, \tag{4.4}$$

where the photon counts normalized by N_{proton}/N_{photon} were used.

Because of the same acceptances and sneak-in factors for a certain azimuthal direction, the obtained raw signal counts can be inputted directly into the right-hand side of Eq. 1.1, and we obtained the photon beam asymmetry distribution as shown in Fig. 4.34.

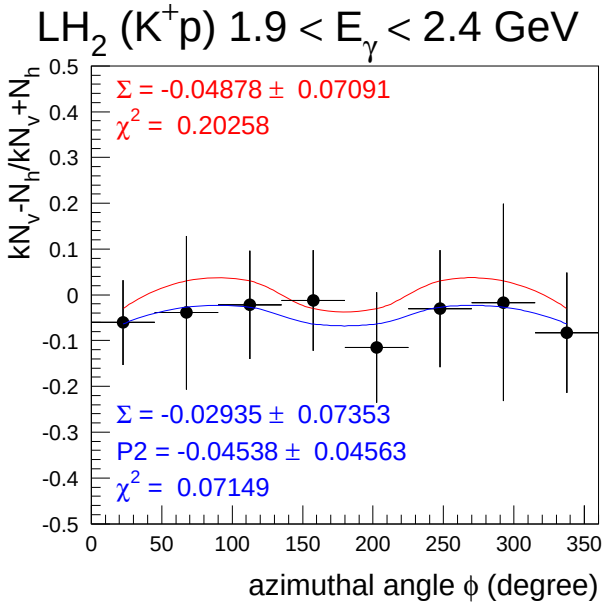

Figure 4.34: Photon beam asymmetry distribution measured in K^+p detection mode from protons for K^+ polar angle less than 60 degrees. Both "$\Sigma P_\gamma \cos(2\phi)$" and "$\Sigma P_\gamma \cos(2\phi)$+ const." were fitted by red and blue curves respectively.

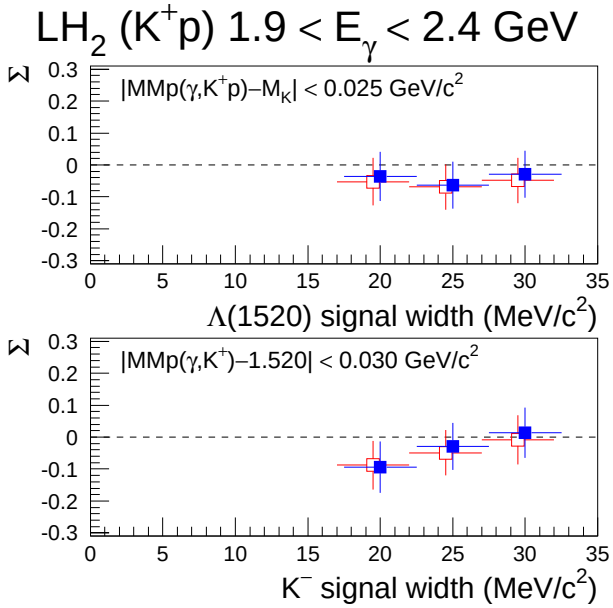

Figure 4.35: 2-dimension window dependence of photon beam asymmetry in photon energy of 1.9-2.4 GeV in K^+p detection mode from protons, where red-empty and blue-solid squares indicated the fitting without and with a vertical offset respectively.

In the beginning, "$\Sigma P_\gamma \cos(2\phi)$" was fitted to the obtained photon beam asymmetry distribution, as shown in the red fitting of Fig. 4.34, the measured photon beam asymmetry was -0.04878±0.07091 with $\chi^2 = 0.20258$. Although the error bars of photon beam asymmetry distribution in Fig. 4.34 are large, the mean of 8 $(kN_V(\phi) - N_H(\phi))/(kN_V(\phi) + N_H(\phi))$ values is shifted downwardly from zero. This is not likely due to systematic errors in 2-step side-band subtraction method because this shift happens even without any side-band subtractions. The reason has not been fully understood, but a systematic error of "k" may partly explain it because this factor increases by 1.3-2.1% without the N_{proton}/N_{photon} normalization and some of correction factors. (Tagger dead time correction was retained.) Owing to such a systematic error, its effect to the photon beam asymmetry Σ must show up as an offset parameter like "$\Sigma P_\gamma \cos(2\phi)$+ const.". Therefore, this function form was fitted to the same photon beam

asymmetry distribution and obtained $\Sigma = -0.02935 \pm 0.07353$ with $\chi^2 = 0.07149$. In both cases, the photon beam asymmetry was consistent with zero, and it was indicated that there was no strong contribution only from K or K* exchanges, although the negative Σ means unnatural parity exchange or K exchange. This small beam asymmetry is consistent with the prediction of the theoretical model where the contact-term contribution is dominant [3], and thus the contribution from the t-channel K* exchange is suggested to be small.

Other than the measured photon beam asymmetry under the standard 2-step side-band subtraction condition shown in Fig. 4.34, according to Fig. C.1-C.4 in App. C.1.1, we studied the window dependences of $|\mathrm{MMp}(\gamma,\mathrm{K}^+\mathrm{p})-\mathrm{M}_K|$ and $|\mathrm{MMp}(\gamma,\mathrm{K}^+)-\mathrm{M}_{\Lambda(1520)}|$ in the range of 15-30 MeV/c^2. Some the measurement were summarized in Fig. 4.35. No obvious window dependence was observed.

Photon beam asymmetry has been measured in photon energy greater than 1.9 GeV for K$^+$ polar angle less than 60 degree with K$^+$p detection. A further study included both 2002-2003 and 2006-2007 data were examined with finer photon energy slices, as shown in Fig. C.5, a few selections of photon energy were performed to measure the photon beam asymmetry in 6 panels. It can be seen from Fig. 4.36, basically the photon beam asymmetries were consistent with zero and no clear structure can be identified. The photon beam asymmetry in photon energy of 1.9-2.0 and 2.3-2.4 GeV may tend to deviate from zero, but it is not conclusive based on a large statistical error.

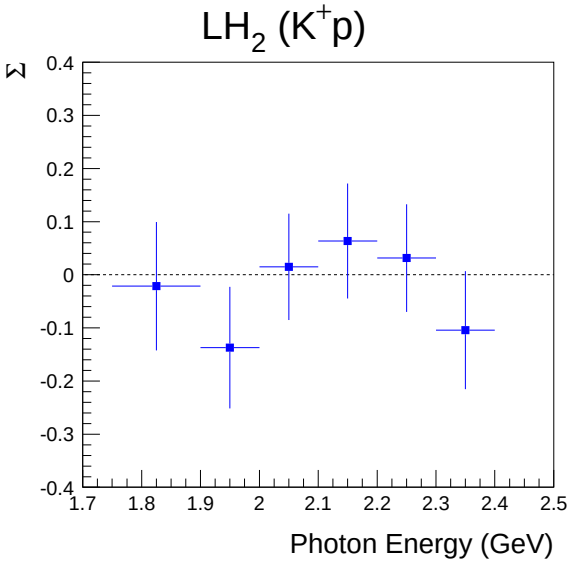

Figure 4.36: The energy dependence of photon beam asymmetry in K$^+$p detection mode from protons.

Raw beam asymmetry for $\Lambda(1520)$ side-band regions (N_2+N_8), K$^-$ side-band regions (N_4+N_6) and "$\Lambda(1520)$ & K$^-$" signal region (N_5) were measured, shown in following lists, where the $N_{1\sim9}$ has same definitions as shown in Fig. 3.7. In this method, possible systematic errors can be checked in an unbiased way by comparing the raw beam asymmetry of neighboring regions. All combined asymmetries are very close to zero, and there is no jump between the signal and side-band region.

- raw beam asymmetry : $\Lambda(1520)$ side-band region (N_2+N_8)

2002-2003 -0.008305±0.050950

2006-2007 0.023194±0.051656

combined 0.007127±0.036231

- raw beam asymmetry : K^- side-band region (N_4+N_6)

2002-2003 0.076765±0.048357

2006-2007 -0.003519±0.047108

combined 0.036621±0.033854

- raw beam asymmetry : $\Lambda(1520)$ & K^- signal region (N_5)

2002-2003 0.017473±0.027906

2006-2007 0.028406±0.028512

combined 0.020123±0.019800

In addition, as shown in Fig. 4.37, we checked the raw counts and measured raw beam asymmetry based on the definition of $N_{1\sim9}$ in Fig. 3.7. Other than the results of N_1 and N_9, most of regions shown the result of photon beam asymmetry around zero.

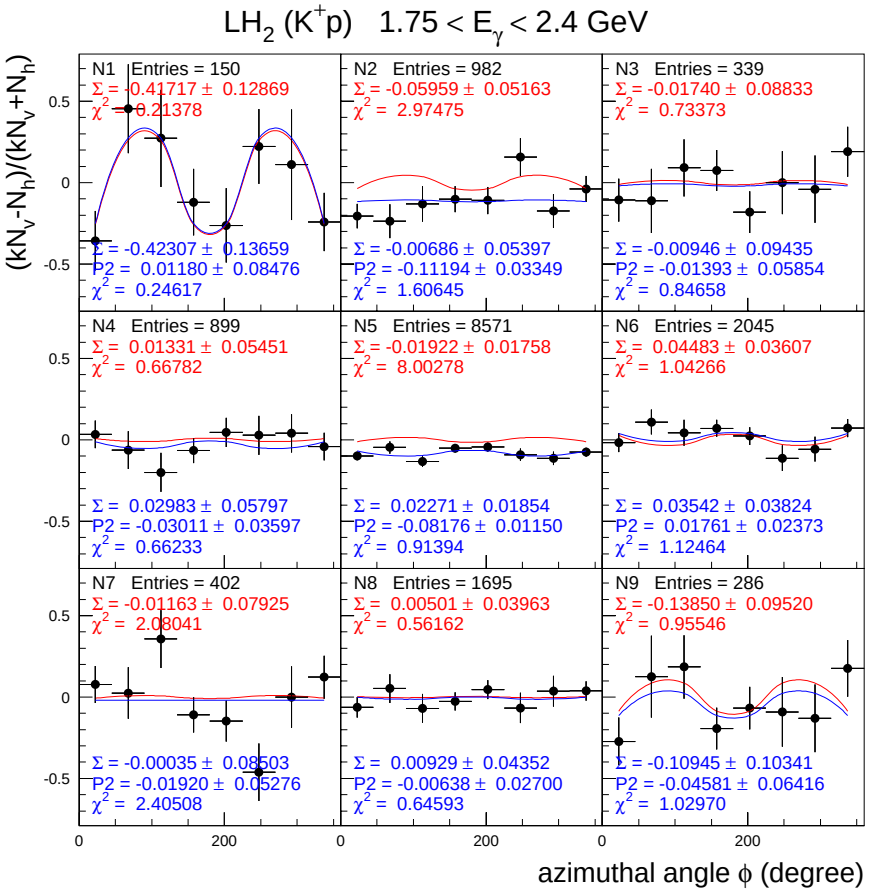

Figure 4.37: Raw counts and raw beam asymmetry measurement based on the definition in Fig. 3.7.

4.6 Possible interference from ϕ meson events

It can be seen from Fig. 4.38, K^+K^- invariant mass distributions were examined in K^+p detection mode by plotting proton missing mass distributions as a function of K^- polar angle in $\Lambda(1520)$ t-channel helicity frame in order to check possible interferences. Simultaneously phase space MC simulation of $\Lambda(1520)$ photoproduction was compared with hydrogen data, and ratios of the real spectra and the MC spectra were plotted as shown in bottom 2×2 panels. These results may not be conclusive because of background contamination in the real data sample and the phase space assumption of the MC simulation, but the calculated ratios were not flat as a function of the K^+K^- mass.

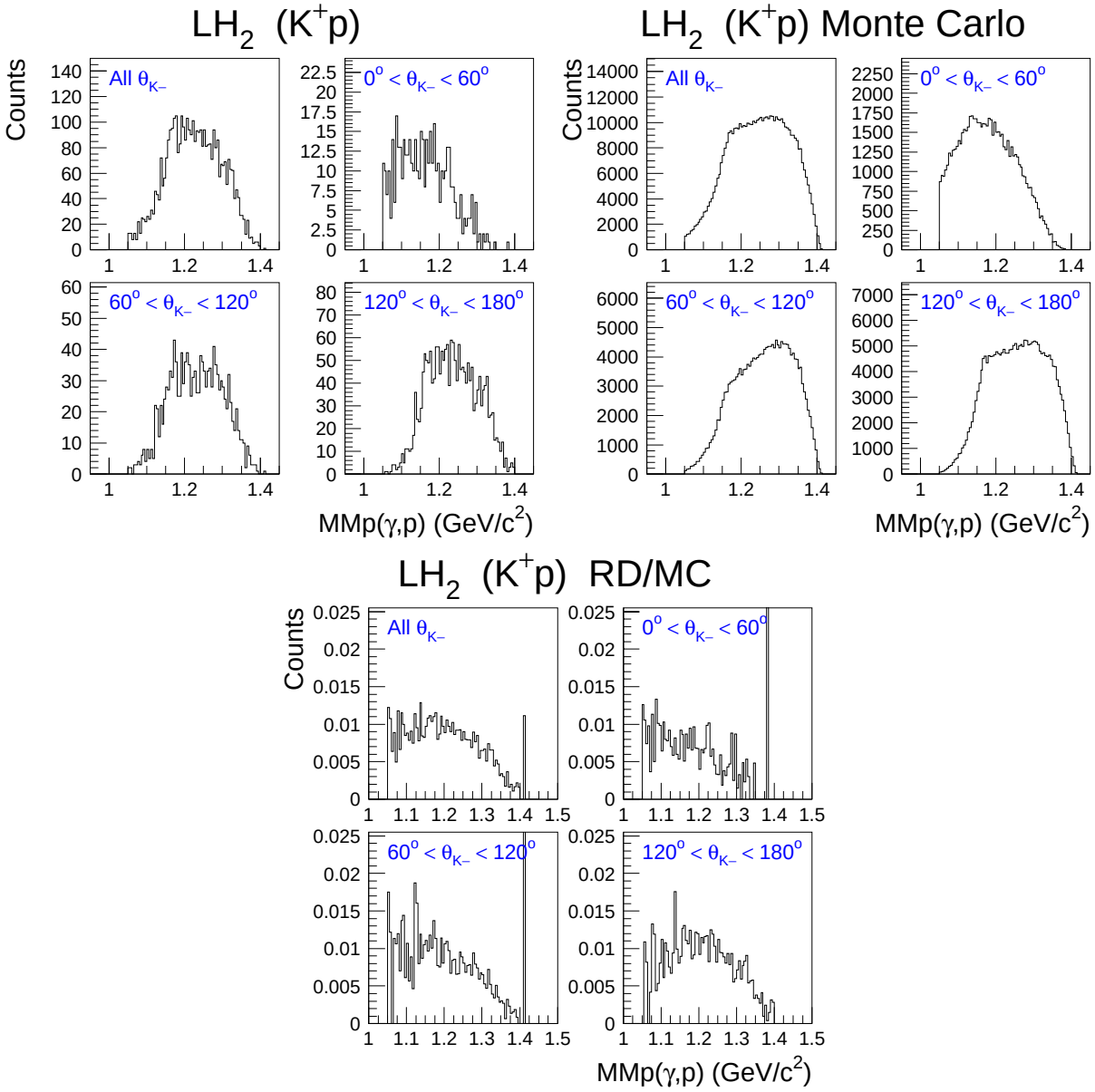

Figure 4.38: K^+K^- invariant mass distributions as a function of K^- polar angle in $\Lambda(1520)$ t-channel helicity frame from K^+p detection mode of protons and phase space Monte Carlo simulation were shown in left and right 2×2 panels. The ratios of real spectra and Monte Carlo spectra were shown in bottom 2×2 panels.

4.7 Effect of AC veto for $\gamma n \rightarrow K^0_S \Lambda(1520)$

In K^-p detection mode of deuterons, $\Lambda(1520)$ photoproduction from both protons and neutrons can be examined. Although the target isospin asymmetry, which suppresses the production from neutrons, has been indicated in Sec. 4.3.2.4, it should be confirmed how aerogel Čerenkov (AC) veto can affect (or reduce) the differential cross sections of "$\gamma n \rightarrow K^0_S \Lambda(1520)$ ", where K^0_S decays to $\pi^+\pi^-$ with BR=0.6861. Therefore, this reaction channel was generated by a Monte Carlo simulation with a constant matrix element, and a probability to be vetoed by AC was measured by using the variable 'vetofac', which was calculated based on Poisson statistics of photoelectrons. We generated 50,000,000 events and applied the same event selections as analysis of deuterons data. The probability that π^+ or π^- pass through the AC radiator was 12.90±0.07% with the detection of K^- and proton at the forward spectrometer and MMd(γ,K^-p)<1.51 GeV/c^2. As shown in Fig. 4.39, momenta of those pions were relatively low. Therefore, the AC veto rate for "$\gamma n \rightarrow K^0_S \Lambda(1520)$ " reaction was measured to be 0.012±0.002%, after separating out the acceptance effect. (This rate was 1.151±0.013% even without the requirement of MMd(γ,K^-p)<1.51 GeV/c^2.) It was confirmed that the effect of AC veto was negligibly small within our analysis conditions.

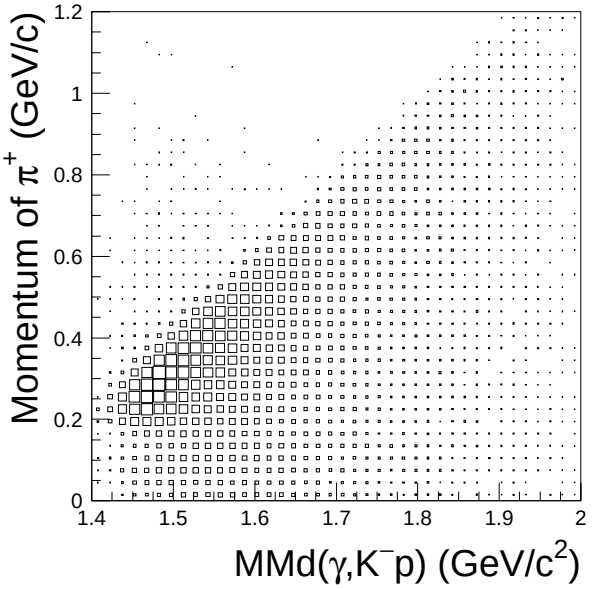

Figure 4.39:

4.8 Ratio of $\Lambda(1520)$ events between K^+p and single K^+ detection modes

We checked the K^+p/single K^+ ratio of raw counts in "|MMp(γ,K^+)-$M_{\Lambda(1520)}$ | < 0.030 GeV/c^2" as a function of azimuthal angle, separately for vertical and horizontal polarizations with requirements of "|MMp(γ,K^+p)-M_K| <0.025 GeV/c^2" and a ϕ exclusion cut for K^+p mode. In addition, We also repeated the same measurement in side-band regions (0.030< |MMp(γ,K^+)-$M_{\Lambda(1520)}$ | <0.060 GeV/c^2). As shown in Fig. 4.40, the results were measured in photon energy of 2.1-2.4 GeV and K^+ polar angle less than 60 degrees. In Fig. 4.40, the upper (lower) panels

correspond to vertical (horizontal) polarization and left (right) panels correspond to the signal (side-band) region. Generally it looks that there is no big difference between vertical and horizontal samples. A general tendency of slight increase in 180 degrees may be caused by proton acceptance because zero degree is defined to horizontal plane here.

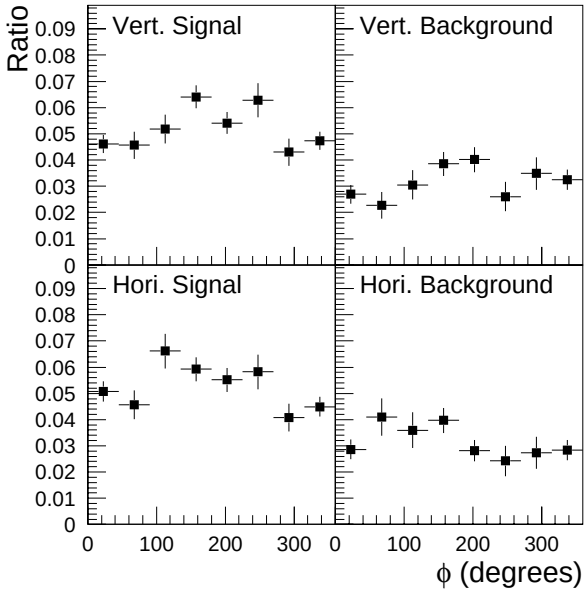

Figure 4.40: Ratio of $\Lambda(1520)$ events between K^+p and single K^+ detection modes, where vertical (horizontal) polarization from signal (side-band) region was examined respectively.

4.9 Comparison of acceptance between K^+p and single K^+ detection modes

An additional check of acceptance with 2-track and single K^+ detections is shown in Fig. 4.41. The energy dependences are not so strong for both detection modes. Slight increase of single K^+ acceptance with photon energy could result in a slightly higher value of beam asymmetry if the asymmetry goes up in higher energy. But this effect would be small because a difference of acceptances between 1.9 and 2.4 GeV is merely 10%.

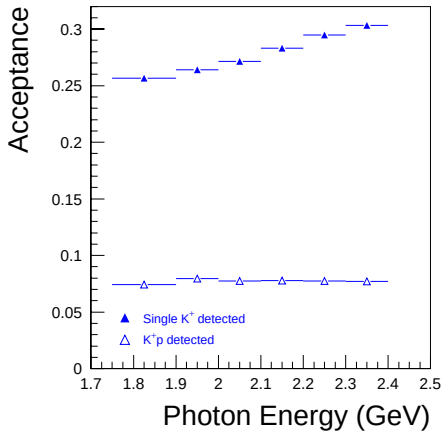

Figure 4.41: Energy dependence of acceptance from K^-p and single K^+ detection modes.

Chapter 5

Summary

Several theoretical calculations, based on the high-energy $\Lambda(1520)$ photoproduction from LAMP2 experiments, predicted possible dominated processes including t-channel K^*exchange , t-channel pseudoscalar K exchange or contact term together with the t-channel K exchange under gauge invariance. In order to realize the real process, SPring-8/LEPS performed the$\Lambda(1520)$ photoproduction near the production threshold from 2002 to 2003.

Almost 100% linearly polarized Argon laser system with λ=351nm was used as the light source in the initial stage. GeV photon beams at SPring-8/LEPS is produced by backward-Compton scattering of laser photon from 8 GeV electrons with maximum photon energy 2.4 GeV. The energy resolution measuring the tagging system located inside the storage ring is about 15 MeV and the flux of tagged photon is about 5×10^5 photons/sec. High-energy photons were transported through the beam pipe to the experimental hutch where the detectors located. LEPS detectors setup from upstream consists of a time projection chamber (TPC) inside a solenoid superconducting magnet, a plastic scintillator, an Aerogel Cerenkov counter (AC), a silicon strip detector (SSD), three drift chambers (DCs), a dipole magnet and a time-of-flight wall (TOF). The time of flight determined by RF signals of accelerator and TOF wall has the resolution about 110 ps. The momentum measured by DCs and the dipole magnet give the resolution around 5 MeV/c roughly.

Following with the $\Lambda(1116)$ photoproduction from protons merely, we studied $\Lambda(1520)$ photoproduction with liquid hydrogen and deuterium targets at E_γ =1.75 $\sim$ 2.4 GeV. We measured the K^-p detection mode in the backward $K^{+/0}$ direction from protons and deuterons; and the K^+K^- and K^-p detection modes in the forward K^+ direction from protons. Except for the study of K^+p detection mode from protons, we performed the standard side-band subtraction method and Monte Carlo simulation method with the estimation of background non-linearity on both K^-p and K^+K^- detection modes. Owing to the complicated and indistinguishable background contamination in K^+p detection mode from protons, a two-step side-band subtraction was used to minimize the background contamination. By studying the invariant mass and missing mass spectra of $\Lambda(1520)$ and all the other resonant/non-resonant backgrounds, we measured the differential cross sections, K^- decay asymmetries in t-channel helicity frame and photon beam asymmetries.

At backward $K^{+/0}$ angles, we compared the cross sections from protons and deuterons. A strong suppression of the production from neutrons was observed as suggested in the theory advocating the importance of the contact term.

Similar to the measurement from $\Lambda(1116)$ production, a peaking behavior of differential cross sections in forward K+ angle was observed from the hydrogen data in addition to dominance of the helicity-3/2 component in the decay asymmetry. This suggested a dominant

contribution either from K^* exchange in the t-channel or contact-term channel, but not K exchange in the t-channel, differed from the dominance of t-channel K exchange in the $\Lambda(1116)$ production. The measured cross sections were smaller than existing theoretical calculations based on the LAMP2 result, and our measurement will provide a new constraint. In the backward K^+ production from protons, slight increase of differential cross sections and weaker strength of the helicity-3/2 component were observed as new information, possibly indicating a u-channel contribution. There also existed energy dependences of the cross sections and the helicity-3/2 fractions in this angular region.

By the decay asymmetry in the production from protons, the contribution from the $S_z = \pm\frac{3}{2}$ component was determined to be nearly 50%. This fact may be explained by the weak K^* exchange along with postulating a destructive interference between the $S_z = \pm\frac{3}{2}$ components.

In the measurement of photon beam asymmetry, the $\Sigma \sim 0$ which is dominated by the contact-term channel is different from the positive behavior measured in the $\Lambda(1116)$ production suggested by the dominance of Gent isobar model accompanied with the mixing model of the Feynman diagram and the Regge model.

The forward enhancement of the differential cross section and the small value of the photon beam asymmetry are also compatible with the interpretation adopting the contact term. Future precision measurements of the decay asymmetry and the photon beam asymmetry shall provide more accurate constraints on the value of $K^*N\Lambda(1520)$ coupling constant as well as details of reaction dynamics. Further theoretical studies will be also desired at a more quantitative level to explain the two asymmetry measurements.

This work is closely related to the possible production of Θ^+. Firstly, the LEPS experiment has reported the possibility of coherent photoproduction of $\gamma d \to \Lambda(1520)\ \Theta^+$ [32], where forward $\Lambda(1520)$ production plays an important role to induce the reaction of $K^+n \to \Theta^+$. The present measurement of elementary cross sections is essential to advance theoretical calculations of this reaction. Secondly, a comparison of the results in the LEPS [33] and CLAS [34] experiments might hints that Θ^+ photoproduction from protons is suppressed relative to that from neutrons. Such a target-isospin asymmetry may originate from the contact term [11] as suggested by the forward $\Lambda(1520)$ photoproduction in the present work.

We don't report the backward photoproduction results from LEPS TPC experiment in this thesis. By Flash ADC module, we can get the pulses information corresponding to each pad due to induced charges produced by electron avalanches. Search the time-overlapped pulses on neighboring and sequential pads to form clusters. In each cluster, looking for pulses on three individually neighboring pads to set hit location. Combining with the drift time, 3-dimension trajectory of the particle can be clearly reconstructed. The momentum of charged particle can be determined from curvature of trajectory. Finally, with the correlation between energy loss and momentum, particle identification can be done, unlike the particle identification of forward spectrometer determined by time-of-flight and momentum measurement.

Bibliography

[1] S.-I. Nam, A. Hosaka and H.-C. Kim, Phys. Rev. D **71**, 114012 (2005).

[2] M. Sumihama *et al.* (LEPS Collaboration), Phys. Rev. C **73**, 035214 (2006).

[3] S.-I. Nam, K.S. Choi, A. Hosaka and H.-C. Kim, Phys. Rev. D **75**, 014027 (2007).

[4] D.G. Ireland, S. Janssen, and J. Ryckebusch, Nucl. Phys. **A740**, 147 (2004).

[5] T. Mart and C. Bennhold, *Kaon Photoproduction in the Feynman and Regge Theories*, arXiv:nucl-th/0412097.

[6] A. Reuber, K. Holinde, J. Speth, Nucl. Phys. A **570**, 543 (1994).

[7] F.X. Lee, T. Mart, C. Bonnhold, L.E. Wright, Nucl. Phys. A **695**, 237 (2001).

[8] S. Ozaki, H. Nagahiro and A. Hosaka, Phys. Lett. B **665**, 178 (2008).

[9] E. Witten, Nucl. Phys. B **223** 422 (1983).

[10] R. Bradford, *et al.* (CLAS Collaboration), Phys. Rev. C **73** 035202 (2006).

[11] S.-I. Nam, A. Hosaka, and H.-C. Kim, Phys. Lett. B **633**, 483 (2006); S.-I. Nam, A. Hosaka, and H.-C. Kim, J. Korean Phys. Soc. **49**, 1928 (2006); S.-I. Nam, A. Hosaka, and H.-C. Kim, Phys. Lett. B **579**, 43 (2004).

[12] M. Karliner and H. J. Lipkin, hep-ph/0506084.

[13] D. Barber *et al.* (LAMP2 Collaboration), Z. Phys. C **7**, 17 (1980).

[14] A. I. Titov, B. Kämpfer, S. Daté, and Y. Ohashi, Phys. Rev. C **74**, 055206 (2006); A. I. Titov, B. Kämpfer, S. Daté, and Y. Ohashi, Phys. Rev. C **72**, 035206 (2005).

[15] C.J. Adams *et al.* Nucl. Phys. B **96**, 54 (1975); T.S. Mast *et al.* Phys. Rev. D **14**, 13 (1976); Particle Data Group, Phys. Lett. B **592**, 1 (2004).

[16] A. Sibirtsev, J. Haidenbauer, S. Krewald, U.-G. Meißner, and A.W. Thomas, Eur. Phys. J. A **31**, 221 (2007).

[17] S.D. Drell, Phys. Rev. Lett. **5**, 278 (1960); S.D. Drell, Rev. Mod. Phys. **33**, 458 (1961).

[18] H. Toki, C. García-Recio, and J. Nieves, Phys. Rev. D **77**, 034001 (2008).

[19] K. Schilling, P. Seyboth, and G. Wolf, Nucl. Phys. **B15**, 397 (1970).

[20] W.-M. Yao *et al.* (Particle Data Group), J. Phys. G **33**, 1 (2006).

[21] S. P. Barrow *et al.* (CLAS Collaboration), Phys. Rev. C **64**, 044601 (2001).

[22] A. D'Angelo, O. Bartalini, V. Bellini, P. Levi Sandri, D. Moricciani, L. Nicoletti and A. Zucchiatti, Nucl. Instr. and Meth. A **455** 1 (2000).

[23] T. Lohse and W. Witzeling, *The Time Projection Chamber*, CERN.

[24] M. Niiyama *et al.* (LEPS Collaboration), Phys. Rev. C **78**, 035202 (2008).

[25] N. Muramatsu, LEPS Technical Note 47.

[26] CERN Program Library Long Writeup W5013 (1993).

[27] J.M. Blatt and V.F. Weisskopf, *Theoretical Nuclear Physics* (John Wiley & Sons, New York, 1952).

[28] Y. Kato, LEPS Technical Note 35.

[29] A.M. Boyarski *et al.*, Phys. Lett. B **34**, 547 (1971).

[30] S.-I. Nam and A. Hosaka, private communications.

[31] T. Hyodo, S. Sarkar, A. Hosaka, and E. Oset, Phys. Rev. C **73**, 035209 (2006).

[32] N. Muramatsu (for the LEPS Collaboration), Prog. Theor. Phys. Supplement **168**, 10 (2007).

[33] T. Nakano *et al.* (LEPS Collaboration), Phys. Rev. Lett. **91**, 012002 (2003); T. Nakano *et al.* (LEPS collaboration), Phys. Rev. C **79**, 025210 (2009).

[34] M. Battaglieri *et al.* (CLAS Collaboration), Phys. Rev. Lett. **96**, 042001 (2006); R. D. Vita *et al.* (CLAS Collaboration), Phys. Rev. D **74**, 032001 (2006).

Appendix A

Differential cross section

In this appendix, the background linearity in the dimension of K^+ polar angle and the value of $d\sigma/d\cos\theta_{K^+}$ from different photon energy ranges, targets and detection modes will be shown. K^+K^- and K^-p detection modes from protons and deuterons and K^+p detection mode from protons will be presented in Sec. A.1, A.3 and A.2 individually.

In Sec. A.1.1, Fig. A.1 shows the background linearity study of 0-30, 30-60, 60-90 and 90-180 degrees in the photon energy of 1.9-2.4 GeV and 0-60 degrees in the photon energy of 1.9-2.2, 2.2-2.4, 1.9-2.06 and 2.06-2.4 GeV from K^+K^- detection mode of LH_2 data. As shown in Fig. A.1, we studied the mass spectra of real data overlaid by estimated backgrounds, $\phi(1020)$ photoproduction, non-resonant $K\bar{K}N$ photoproduction and the sum of individual productions. In the middle and right column of Fig. A.1, the signal-window width dependence of non-linearity and non-linearity factor were studied respectively. A corresponding measurement of the differential cross section were shown in top 2 columns of Fig. A.2. The top-left column of Fig. A.2 shows the signal-window width dependence of differential cross sections, where red- and blue- dash lines indicated values and the range of uncertainty of differential cross section measured by Monte Carlo method. The top-right column of Fig. A.2 listed details of the measurement of differential cross section, number of yield of $\Lambda(1520)$, detector acceptance by Monte Carlo simulation and the differential cross section.

In order to make a comparison with the result of LAMP2 experiment, similar studies were performed in K^+ polar angle of 19-43 degree within the photon energy of 1.9-2.4 GeV, as shown in Sec. A.1.3. The last part of this appendix demonstrated the calculation of differential cross section on LAMP2 experiment.

In the case of K^+K^- (K^+p) detection mode of deuteron (proton) target, no background linearity study was executed. Therefore, the intrinsic side-band subtraction method was applied in it. The signal-window width dependence of results are shown in bottom 2 panel of Fig. A.2 (Fig. A.5-A.12). For K^+K^- detection mode of deuteron target, same angular bins and photon energy as that of proton target are shown. For K^+p detection of proton target, we measured the differential cross sections in K^+ polar angle of 0-30, 30-60, 60-90, 90-180, 0-60 and 19.4-43.2 degrees in photon energy of 1.75-1.9, 1.9-2.05, 2.05-2.2 and 2.2-2.4 GeV under the requirement "$|MMp(\gamma,K^+p)\text{-}M_K| < 0.025$ GeV/c^2", as shown in Fig. A.5-A.8. On the other hand, a cross check for bump structure of differential cross sections was measured in $0.6 < \cos\theta_{K^+} < 0.7$, $0.7 < \cos\theta_{K^+} < 0.8$, $0.8 < \cos\theta_{K^+} < 0.9$ and $0.9 < \cos\theta_{K^+} < 1.0$ in the photon energy of 1.75-1.9, 1.9-2.2 and 2.2-2.4 GeV. 2-dimension signal-window width variations, including 6 kinds of widths for $|MMp(\gamma,K^+)-M_{\Lambda(1520)}|$ and $|MMp(\gamma,K^+p)-M_K|$ individually, were shown as 6×6 panels in one figure simultaneously from Fig.A.9 to A.12.

In the case of the K^-p detection mode of proton and deuteron target, similar studies with

same photon energy slices as that of K^+p detection mode were measured in K^+ polar angle of 90-120, 120-150, 150-180 and 120-180 degrees. Background non-linearity studies for proton (deuteron) were shown in Fig. A.13 and Fig. A.14 (Fig.A.17 and Fig. A.18). The measurement of differential cross sections were presented in Fig. A.15 and Fig. A.16 (Fig. A.19 and Fig. A.20) for proton (deuteron) target.

A.1 K^+K^- detection mode from protons and deuterons

A.1.1 Background non-linearity

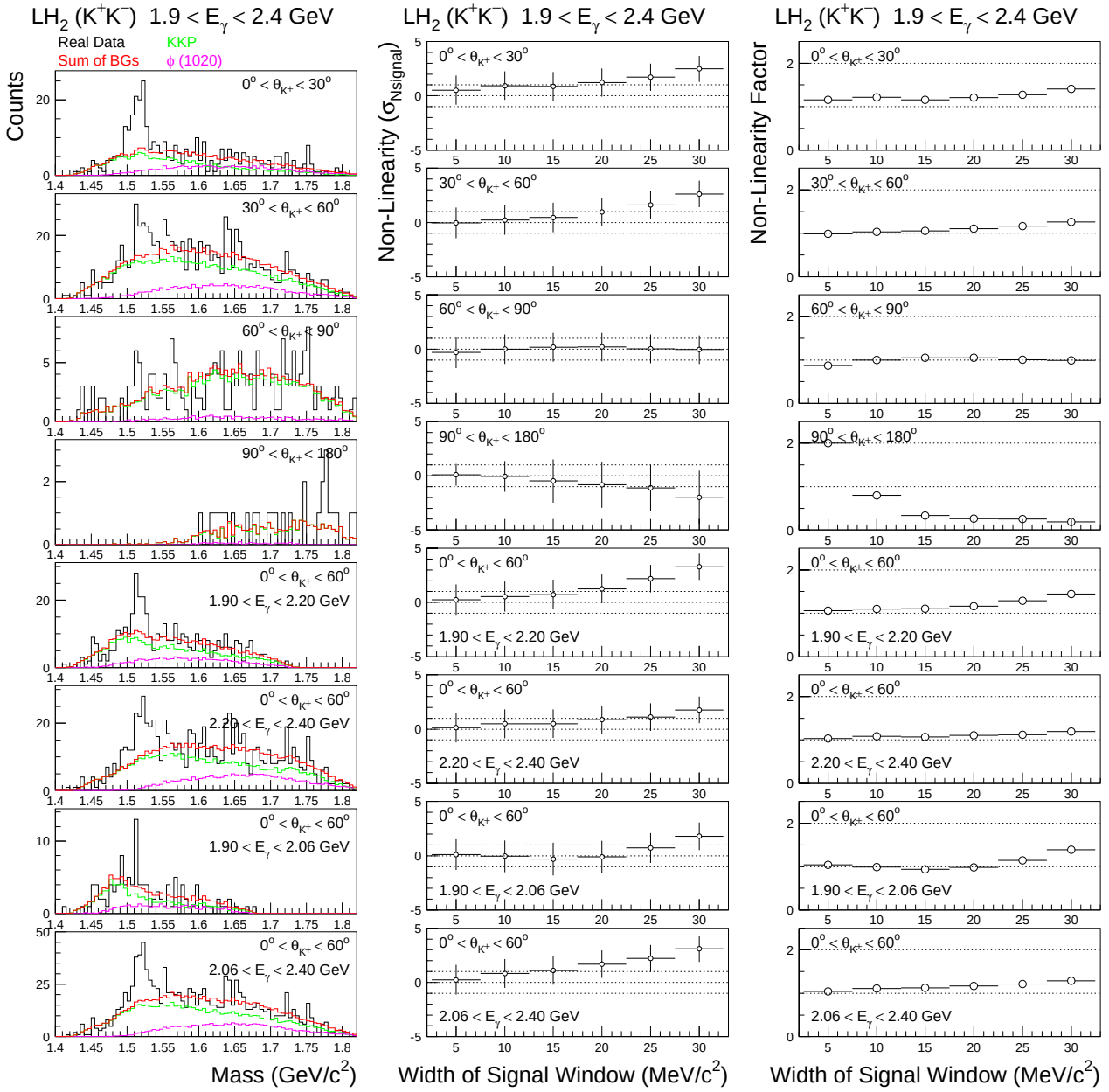

Figure A.1: Background non-linearity studies in different K^+ polar angles within photon energy of 1.9-2.4 GeV from K^+K^- detection mode of LH_2 data are shown in 3 columns respectively, including mass spectra of real data overlaid by that of Monte Carlo simulations, background non-linearities and non-linearity correction factors.

A.1.2 Differential cross section

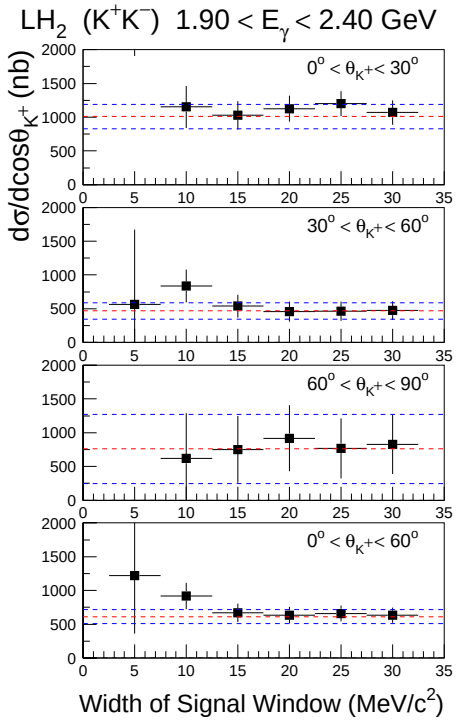

LH$_2$ (K^+K^-) 1.90 < E_γ < 2.40 GeV

K^+ polar angle : 0–30 degree

Width(MeV/c^2)	N_{yield}	Acceptance	dσ/dcosθ
5	60.900± 28.410	0.00165964±0.00005829	3022.980±1114.090
10	61.176± 14.771	0.00308627±0.00007955	1152.250± 312.367
15	70.692± 13.190	0.00407960±0.00009150	1027.820± 211.334
20	87.656± 13.361	0.00457422±0.00009691	1127.020± 191.382
25	103.674± 13.752	0.00494212±0.00010075	1202.160± 182.698
30	105.725± 14.122	0.00512198±0.00010258	1069.400± 180.929

K^+ polar angle : 30–60 degree

Width(MeV/c^2)	N_{yield}	Acceptance	dσ/dcosθ
5	20.017± 41.417	0.00089102±0.00002578	564.493±1104.550
10	63.839± 17.955	0.00176267±0.00003627	834.951± 242.675
15	57.593± 16.633	0.00231695±0.00004159	538.233± 170.904
20	62.943± 16.683	0.00266859±0.00004465	455.755± 148.831
25	76.906± 17.239	0.00289805±0.00004653	461.488± 141.702
30	95.726± 17.909	0.00305152±0.00004775	473.330± 139.930

K^+ polar angle : 60–90 degree

Width(MeV/c^2)	N_{yield}	Acceptance	dσ/dcosθ
5	0.000± 8.795	0.00010387±0.00000754	0.000± 0.000
10	6.184± 6.738	0.00017495±0.00000978	617.582± 670.789
15	10.846± 6.661	0.00023508±0.00001134	751.236± 494.305
20	14.571± 7.286	0.00026023±0.00001193	918.095± 488.978
25	12.606± 7.203	0.00028319±0.00001244	769.999± 443.658
30	13.957± 7.469	0.00029850±0.00001278	826.235± 436.595

K^+ polar angle : 0–60 degree

Width(MeV/c^2)	N_{yield}	Acceptance	dσ/dcosθ
5	0.000± 0.000	0.00000000±0.00000000	1223.370± 861.899
10	0.000± 0.000	0.00000000±0.00000000	919.987± 196.376
15	0.000± 0.000	0.00000000±0.00000000	669.442± 137.325
20	0.000± 0.000	0.00000000±0.00000000	635.654± 120.414
25	0.000± 0.000	0.00000000±0.00000000	659.988± 114.702
30	0.000± 0.000	0.00000000±0.00000000	633.077± 113.326

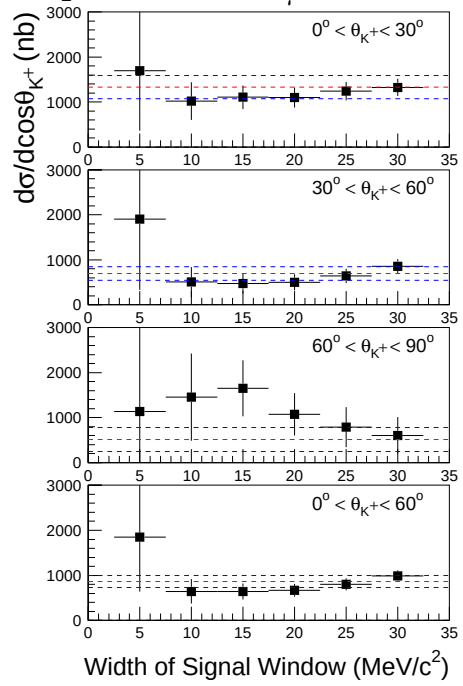

LD$_2$ (K^+K^-) 1.90 < E_γ < 2.40 GeV

K^+ polar angle : 0–30 degree

Width(MeV/c^2)	N_{yield}	Acceptance	dσ/dcosθ
5	52.108± 40.850	0.00108202±0.00004931	1699.400±1334.500
10	57.366± 23.360	0.00198445±0.00006681	1020.090± 416.801
15	86.246± 20.293	0.00274770±0.00007865	1107.630± 262.531
20	99.346± 20.061	0.00318320±0.00008467	1101.320± 224.315
25	124.481± 20.301	0.00353788±0.00008928	1241.610± 204.898
30	144.294± 20.311	0.00384318±0.00009306	1324.900± 189.237

K^+ polar angle : 30–60 degree

Width(MeV/c^2)	N_{yield}	Acceptance	dσ/dcosθ
5	83.652± 68.931	0.00056892±0.00002160	1899.630±1567.000
10	44.618± 29.152	0.00113621±0.00003054	507.338± 331.759
15	55.612± 25.962	0.00152314±0.00003536	471.709± 220.489
20	72.193± 25.358	0.00185269±0.00003901	503.429± 177.153
25	103.269± 25.840	0.00208387±0.00004137	640.247± 160.709
30	147.024± 26.987	0.00221175±0.00004263	858.816± 158.509

K^+ polar angle : 60–90 degree

Width(MeV/c^2)	N_{yield}	Acceptance	dσ/dcosθ
5	7.000± 29.283	0.00005838±0.00000590	1133.910±4744.850
10	17.914± 11.875	0.00011676±0.00000834	1450.920± 967.388
15	27.708± 10.292	0.00015847±0.00000972	1653.610± 622.513
20	21.955± 9.572	0.00019421±0.00001076	1069.110± 469.862
25	17.674± 9.940	0.00021208±0.00001124	788.106± 445.217
30	15.325± 10.277	0.00023949±0.00001195	605.192± 406.964

K^+ polar angle : 0–60 degree

Width(MeV/c^2)	N_{yield}	Acceptance	dσ/dcosθ
5	0.000± 0.000	0.00000000±0.00000000	1845.970±1201.510
10	0.000± 0.000	0.00000000±0.00000000	644.756± 267.306
15	0.000± 0.000	0.00000000±0.00000000	642.136± 176.067
20	0.000± 0.000	0.00000000±0.00000000	663.664± 142.933
25	0.000± 0.000	0.00000000±0.00000000	801.412± 129.824
30	0.000± 0.000	0.00000000±0.00000000	983.727± 126.628

Figure A.2: Measured from K^+K^- detection mode of LH_2 and LD_2 data, the left column shows the signal-window width dependence of differential cross sections in different K^+ polar angles within photon energy of 1.9-2.4 GeV; the right column shows the corresponding numerical tables including number of yields, acceptance and differential cross section $d\sigma/d\cos\theta_{K^+}$. In the bottom of right-column tables, the signal-window dependence of differential cross sections in K^+ polar angle of 0-60 degrees were evaluated by simply summing up the results of K^+ polar angle of 0-30 and 30-60 degrees, instead of a practical measurement.

A.1.3 Background non-linearity and $d\sigma/d\cos\theta_{K^+}$ for $19^o < \theta_{K^+} < 43^o$

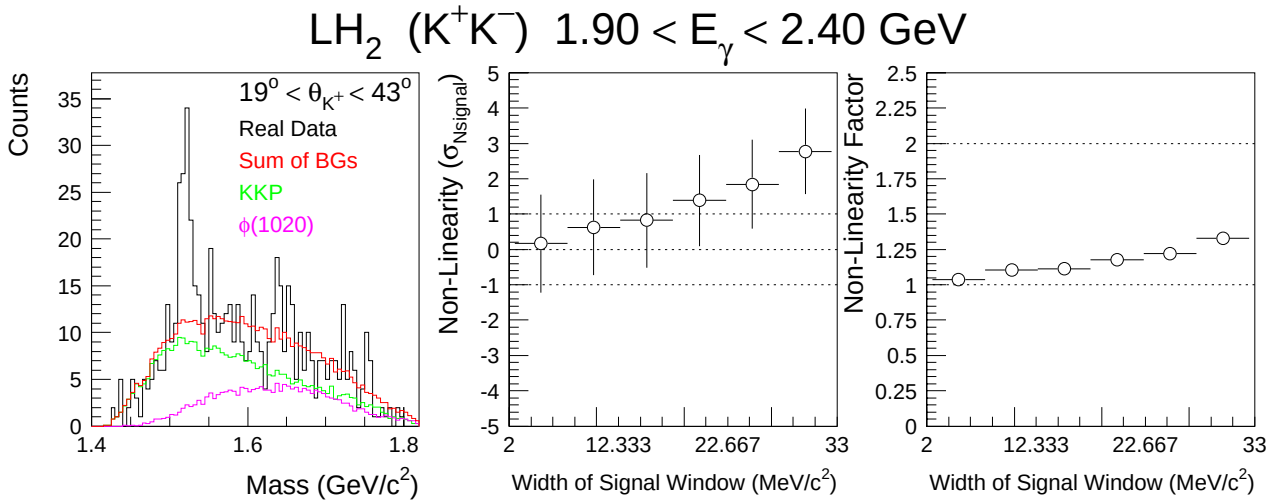

Figure A.3: Background non-linearity studies in K^+ polar angle of 19-43 degrees within photon energy of 1.9-2.4 GeV from K^+K^- detection mode of LH_2 data are shown in 3 columns respectively, including mass spectra of real data overlaid by that of Monte Carlo simulations, background non-linearities and non-linearity correction factors.

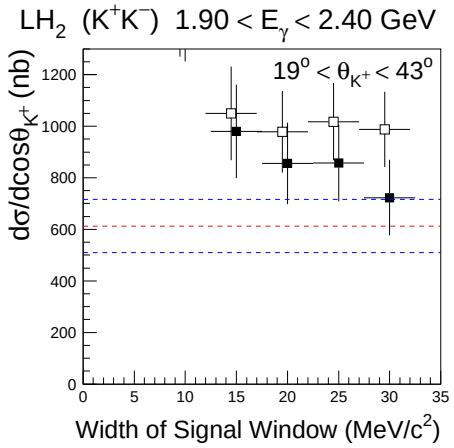

LH$_2$ (K^+K^-) $1.90 < E_\gamma < 2.40$ GeV

K^+ polar angle : 19 – 43 degree

Width(MeV/c^2)	N_{yield}	Acceptance	dσ/dcosθ
5	100.150± 37.207	0.00141399±0.00004247	3071.980±1072.490
10	101.900± 17.789	0.00268531±0.00005857	1523.270± 271.221
15	92.039± 15.764	0.00356173±0.00006748	980.037± 180.898
20	97.903± 15.754	0.00406618±0.00007212	855.975± 158.357
25	110.386± 16.125	0.00440758±0.00007510	857.577± 149.632
30	111.877± 16.471	0.00460120±0.00007674	723.184± 146.360

Figure A.4: Measured from K^+K^- detection mode of LH_2 data, the left column shows the signal-window width dependence of differential cross sections in K^+ polar angle of 19-43 degrees within photon energy of 1.9-2.4 GeV, where hollow- and solid- square indicated the before and after non-linearity correction respectively; the right column shows the corresponding numerical tables including number of yields, acceptance and differential cross section $d\sigma/d\cos\theta_{K^+}$.

A.2 K^+p detection mode from protons

A.2.1 Differential cross section I

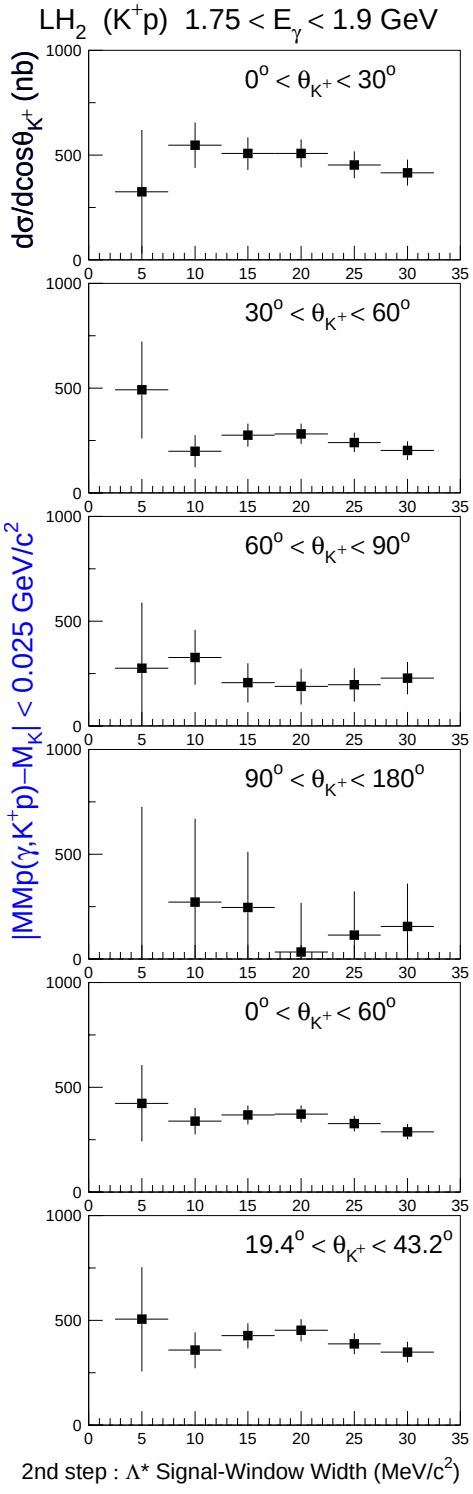

$LH_2(K^+p)$ $1.75 < E_\gamma < 1.9$ GeV

First Side-band Subtraction: $|MMp(\gamma,K^+p)-M_K| < 0.025$ GeV/c^2

K^+ polar angle : 0–30 degree

Width(MeV/c^2)	N_{yield}	Acceptance	dσ/dcosθ
5	36.343± 33.038	0.03320880±0.00034909	324.601± 295.101
10	109.885± 21.840	0.05950590±0.00047321	547.725± 108.947
15	131.915± 20.173	0.07710120±0.00054310	507.479± 77.688
20	149.740± 19.876	0.08743680±0.00058113	507.959± 67.510
25	143.358± 19.886	0.09364520±0.00060312	454.068± 63.055
30	136.607± 20.473	0.09731060±0.00061584	416.387± 62.459

K^+ polar angle : 30–60 degree

Width(MeV/c^2)	N_{yield}	Acceptance	dσ/dcosθ
5	82.786± 38.799	0.01828040±0.00015513	491.790± 230.525
10	60.739± 23.228	0.03300560±0.00020995	199.842± 76.436
15	108.808± 21.583	0.04282060±0.00024027	275.942± 54.758
20	126.108± 21.676	0.04848570±0.00025636	282.448± 48.572
25	115.654± 21.807	0.05198930±0.00026591	241.577± 45.568
30	101.462± 22.160	0.05436540±0.00027222	202.671± 44.277

K^+ polar angle : 60–90 degree

Width(MeV/c^2)	N_{yield}	Acceptance	dσ/dcosθ
5	12.123± 13.803	0.00349725±0.00005775	275.561± 313.773
10	25.223± 10.053	0.00612018±0.00007650	327.612± 130.642
15	20.309± 9.284	0.00782509±0.00008657	206.306± 94.340
20	21.152± 9.511	0.00891798±0.00009247	188.545± 84.797
25	23.762± 9.568	0.00961173±0.00009603	196.514± 79.152
30	29.201± 9.685	0.01013630±0.00009864	229.000± 75.985

K^+ polar angle : 90–180 degree

Width(MeV/c^2)	N_{yield}	Acceptance	dσ/dcosθ
5	-1.660± 6.845	0.00028336±0.00001159	-232.846±-960.089
10	3.459± 5.043	0.00050513±0.00001548	272.204± 396.890
15	4.175± 4.509	0.00067476±0.00001789	245.917± 265.701
20	0.660± 4.526	0.00077048±0.00001911	34.053± 233.453
25	2.484± 4.479	0.00085672±0.00002016	115.254± 207.795
30	3.593± 4.715	0.00091548±0.00002084	155.980± 204.728

K^+ polar angle : 0–60 degree

Width(MeV/c^2)	N_{yield}	Acceptance	dσ/dcosθ
5	118.784± 51.001	0.02226420±0.00014687	424.103± 182.112
10	170.993± 31.903	0.04007740±0.00019877	339.156± 63.301
15	241.210± 29.571	0.05196870±0.00022763	368.955± 45.261
20	276.460± 29.437	0.05888020±0.00024309	373.236± 39.772
25	259.628± 29.540	0.06310550±0.00025216	327.043± 37.233
30	238.552± 30.193	0.06582580±0.00025787	288.076± 36.479

K^+ polar angle : 19.4–43.2 degree

Width(MeV/c^2)	N_{yield}	Acceptance	dσ/dcosθ
5	81.393± 40.090	0.02988130±0.00026091	505.763± 249.152
10	104.128± 24.751	0.05402430±0.00035491	357.882± 85.101
15	160.977± 22.670	0.07003560±0.00040716	426.781± 60.154
20	193.771± 22.582	0.07948570±0.00043567	452.648± 52.810
25	177.720± 22.775	0.08493640±0.00045149	388.511± 49.831
30	166.192± 23.356	0.08853330±0.00046172	348.549± 49.017

Figure A.5: Measured from K^+p detection mode of LH_2 data and under the requirement "$|MMp(\gamma,K^+p)\text{-}M_K| < 0.025$ GeV/c^2", the left column shows the signal-window width dependence of differential cross sections in different K^+ polar angles within photon energy of 1.75-1.9 GeV; the right column shows the corresponding numerical tables including number of yields, acceptance and differential cross section $d\sigma/d\cos\theta_{K^+}$.

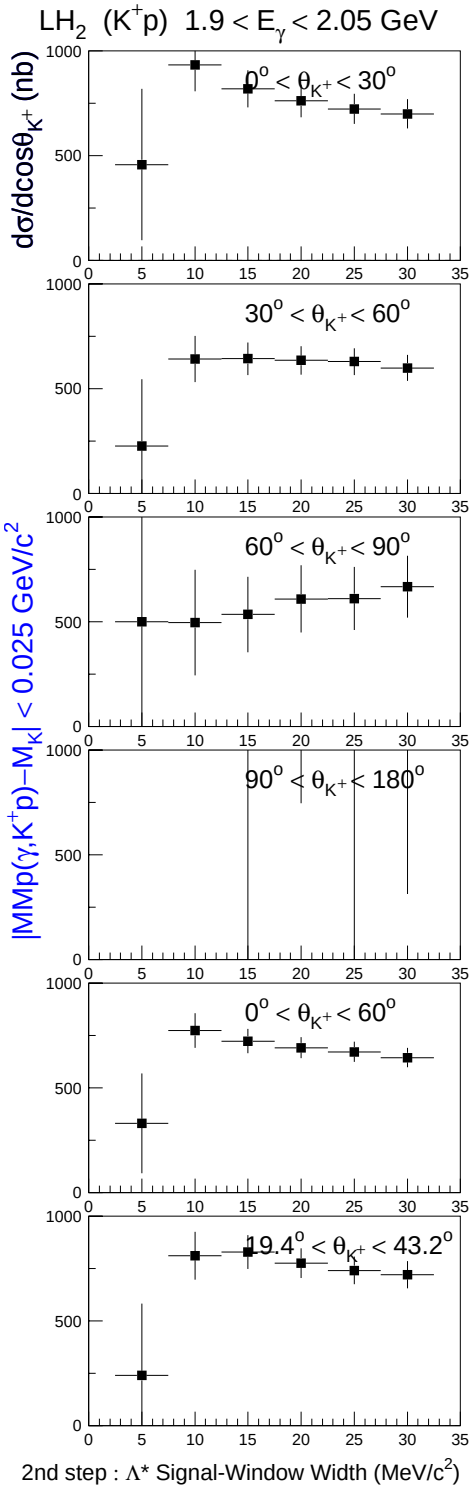

$LH_2(K^+p)$ $1.9 < E_\gamma < 2.05$ GeV

First Side-band Subtraction: $|MMp(\gamma,K^+p)–M_K| < 0.025$ GeV/c^2

K^+ polar angle : 0–30 degree

Width(MeV/c^2)	N_{yield}	Acceptance	dσ/dcosθ
5	65.449± 51.603	0.03632980±0.00034690	457.809± 360.986
10	240.725± 32.261	0.06558290±0.00047263	932.775± 125.188
15	275.417± 29.731	0.08536840±0.00054421	819.860± 88.656
20	290.779± 29.348	0.09709260±0.00058350	761.066± 76.949
25	297.568± 29.659	0.10450800±0.00060742	723.572± 72.241
30	300.387± 30.183	0.10909200±0.00062188	699.735± 70.424

K^+ polar angle : 30–60 degree

Width(MeV/c^2)	N_{yield}	Acceptance	dσ/dcosθ
5	39.939± 55.869	0.01633670±0.00013934	227.458± 318.188
10	203.512± 34.917	0.02950900±0.00018849	641.660± 110.169
15	265.448± 31.911	0.03839650±0.00021593	643.217± 77.410
20	299.695± 31.871	0.04389040±0.00023147	635.301± 67.644
25	319.934± 32.316	0.04725600±0.00024057	629.902± 63.706
30	318.206± 32.934	0.04939830±0.00024621	599.330± 62.102

K^+ polar angle : 60–90 degree

Width(MeV/c^2)	N_{yield}	Acceptance	dσ/dcosθ
5	12.619± 18.928	0.00171703±0.00003843	500.519± 750.867
10	22.571± 11.465	0.00309924±0.00005166	495.998± 252.083
15	31.593± 10.653	0.00402128±0.00005887	535.072± 180.597
20	40.649± 10.699	0.00454670±0.00006262	608.883± 160.485
25	44.123± 10.864	0.00491586±0.00006512	611.281± 150.726
30	50.608± 11.204	0.00516483±0.00006676	667.337± 147.997

K^+ polar angle : 90–180 degree

Width(MeV/c^2)	N_{yield}	Acceptance	dσ/dcosθ
5	0.000± 0.000	0.00000171±0.00000086	0.000± 0.000
10	0.000± 0.000	0.00000171±0.00000086	0.000± 0.000
15	0.415± -0.415	0.00000171±0.00000086	8251.020±9224.920
20	0.366± -0.273	0.00000171±0.00000086	7280.310±6534.250
25	0.152± -0.186	0.00000257±0.00000105	2012.440±2598.070
30	0.266± -0.210	0.00000428±0.00000135	2115.640±1801.400

K^+ polar angle : 0–60 degree

Width(MeV/c^2)	N_{yield}	Acceptance	dσ/dcosθ
5	105.402± 76.055	0.02169200±0.00013775	330.925± 238.795
10	444.567± 47.544	0.03917170±0.00018668	772.940± 82.744
15	541.200± 43.622	0.05097840±0.00021418	723.025± 58.357
20	590.695± 43.329	0.05814110±0.00022951	691.929± 50.828
25	617.714± 43.868	0.06259150±0.00023863	672.129± 47.801
30	618.895± 44.680	0.06538780±0.00024422	644.615± 46.599

K^+ polar angle : 19.4–43.2 degree

Width(MeV/c^2)	N_{yield}	Acceptance	dσ/dcosθ
5	42.608± 60.745	0.02824550±0.00024134	239.972± 342.128
10	262.641± 36.877	0.05152940±0.00032965	810.828± 113.966
15	348.215± 34.115	0.06684740±0.00037819	828.674± 81.322
20	372.341± 33.972	0.07629740±0.00040582	776.341± 70.953
25	383.207± 34.151	0.08226570±0.00042256	741.029± 66.150
30	389.311± 34.697	0.08596390±0.00043269	720.446± 64.312

Figure A.6: Measured from K^+p detection mode of LH_2 data and under the requirement "$|MMp(\gamma,K^+p)\text{-}M_K| < 0.025$ GeV/c^2", the left column shows the signal-window width dependence of differential cross sections in different K^+ polar angles within photon energy of 1.9-2.05 GeV; the right column shows the corresponding numerical tables including number of yields, acceptance and differential cross section $d\sigma/d\cos\theta_{K^+}$.

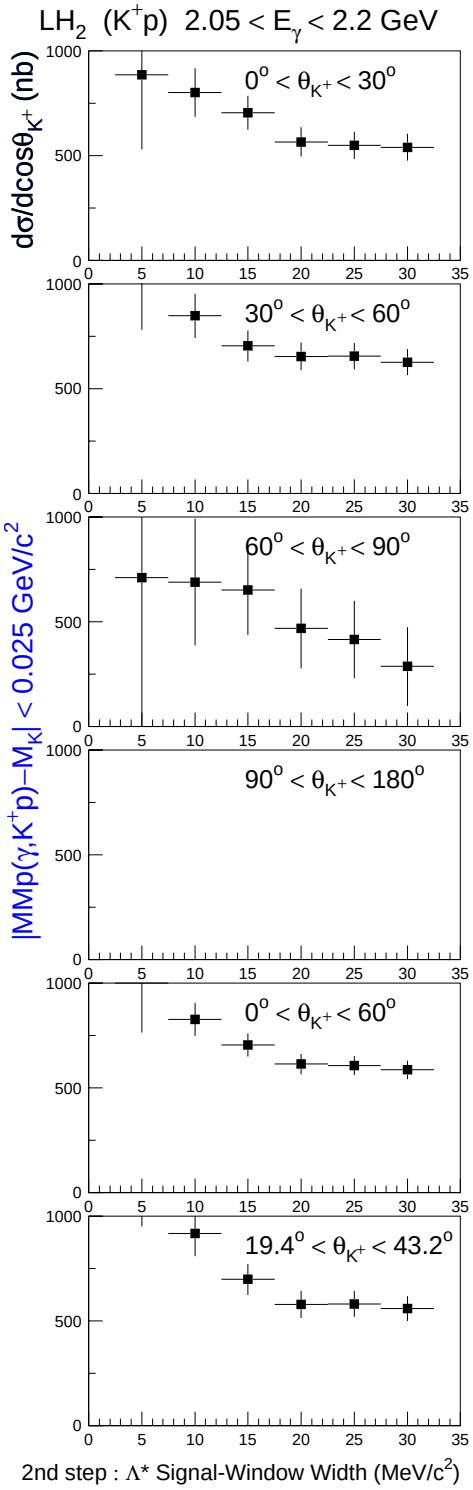

$LH_2(K^+p)$ $2.05 < E_\gamma < 2.2$ GeV

First Side-band Subtraction: $|MMp(\gamma,K^+p)-M_K| < 0.025$ GeV/c^2

K^+ polar angle : 0–30 degree

Width(MeV/c^2)	N_{yield}	Acceptance	dσ/dcosθ
5	142.136± 57.175	0.03541870±0.00032120	885.392± 356.242
10	235.036± 33.941	0.06468200±0.00044015	801.707± 115.900
15	270.837± 30.898	0.08477420±0.00050863	704.868± 80.524
20	249.857± 30.705	0.09742810±0.00054845	565.812± 69.606
25	260.735± 31.098	0.10464100±0.00057025	549.745± 65.637
30	268.211± 31.592	0.10956400±0.00058481	540.097± 63.682

K^+ polar angle : 30–60 degree

Width(MeV/c^2)	N_{yield}	Acceptance	dσ/dcosθ
5	204.690± 58.527	0.01508720±0.00012553	1095.910± 313.487
10	288.687± 35.784	0.02751140±0.00017055	847.626± 105.198
15	312.762± 33.065	0.03588540±0.00019558	704.019± 74.527
20	332.952± 33.296	0.04107570±0.00020977	654.763± 65.564
25	358.014± 34.130	0.04405570±0.00021755	656.426± 62.662
30	356.844± 34.847	0.04596550±0.00022242	627.096± 61.314

K^+ polar angle : 60–90 degree

Width(MeV/c^2)	N_{yield}	Acceptance	dσ/dcosθ
5	11.691± 12.740	0.00097168±0.00002707	711.438± 775.527
10	19.778± 8.630	0.00169479±0.00003576	690.027± 301.444
15	24.411± 7.999	0.00221603±0.00004090	651.345± 213.775
20	19.889± 8.056	0.00250980±0.00004353	468.571± 189.967
25	18.904± 8.428	0.00269057±0.00004508	415.451± 185.345
30	13.746± 9.005	0.00283218±0.00004625	286.986± 188.053

K^+ polar angle : 90–180 degree

Width(MeV/c^2)	N_{yield}	Acceptance	dσ/dcosθ
5	0.000± 0.000	0.00000000±0.00000000	-1000.000± 0.000
10	0.000± 0.000	0.00000000±0.00000000	-1000.000± 0.000
15	0.000± 0.000	0.00000000±0.00000000	-1000.000± 0.000
20	0.000± 0.000	0.00000000±0.00000000	-1000.000± 0.000
25	0.000± 0.000	0.00000000±0.00000000	-1000.000± 0.000
30	0.526± 0.526	0.00000000±0.00000000	-1000.000± 0.000

K^+ polar angle : 0–60 degree

Width(MeV/c^2)	N_{yield}	Acceptance	dσ/dcosθ
5	347.266± 81.773	0.02053220±0.00012565	1000.060± 235.569
10	523.848± 49.312	0.03746620±0.00017113	826.733± 77.916
15	583.597± 45.254	0.04897840±0.00019675	704.543± 54.706
20	582.783± 45.292	0.05616760±0.00021141	613.508± 47.736
25	618.630± 46.171	0.06028130±0.00021944	606.803± 45.342
30	624.875± 47.031	0.06299810±0.00022462	586.495± 44.192

K^+ polar angle : 19.4–43.2 degree

Width(MeV/c^2)	N_{yield}	Acceptance	dσ/dcosθ
5	247.742± 64.632	0.02657170±0.00021908	1287.720± 336.112
10	323.552± 37.734	0.04873760±0.00029989	916.894± 107.080
15	323.868± 34.286	0.06404150±0.00034626	698.467± 74.039
20	307.952± 34.409	0.07353570±0.00037269	578.395± 64.694
25	333.015± 34.917	0.07905340±0.00038741	581.812± 61.070
30	334.207± 35.513	0.08255120±0.00039653	559.154± 59.477

Figure A.7: Measured from K^+p detection mode of LH_2 data and under the requirement "$|MMp(\gamma,K^+p)\text{-}M_K| < 0.025$ GeV/c^2", the left column shows the signal-window width dependence of differential cross sections in different K^+ polar angles within photon energy of 2.05-2.2 GeV; the right column shows the corresponding numerical tables including number of yields, acceptance and differential cross section $d\sigma/d\cos\theta_{K^+}$.

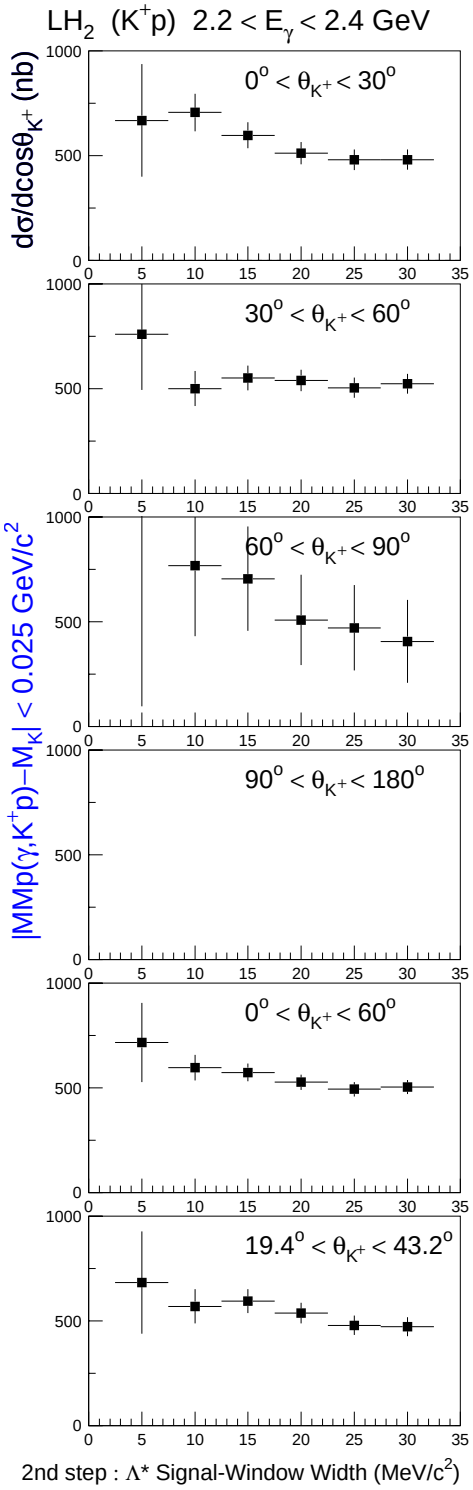

$LH_2(K^+p)$ $2.2 < E_\gamma < 2.4$ GeV

First Side-band Subtraction: $|MMp(\gamma,K^+p)–M_K| < 0.025$ GeV/c^2

K^+ polar angle : 0–30 degree

Width(MeV/c^2)	N_{yield}	Acceptance	dσ/dcosθ
5	160.193± 64.225	0.03452480±0.00025130	668.444± 268.039
10	306.430± 38.993	0.06252170±0.00034272	706.079± 89.933
15	343.234± 35.174	0.08274930±0.00039802	597.556± 61.304
20	339.301± 34.644	0.09540210±0.00042986	512.366± 52.365
25	342.002± 35.319	0.10250700±0.00044702	480.649± 49.682
30	358.133± 36.115	0.10717100±0.00045804	481.416± 48.591

K^+ polar angle : 30–60 degree

Width(MeV/c^2)	N_{yield}	Acceptance	dσ/dcosθ
5	202.851± 70.707	0.01407770±0.00009605	760.015± 264.968
10	245.832± 40.949	0.02588570±0.00013100	500.905± 83.475
15	355.594± 38.076	0.03396240±0.00015064	552.244± 59.183
20	401.045± 37.785	0.03914400±0.00016213	540.388± 50.962
25	402.892± 38.315	0.04207660±0.00016833	505.038± 48.071
30	436.836± 39.231	0.04396750±0.00017223	524.038± 47.107

K^+ polar angle : 60–90 degree

Width(MeV/c^2)	N_{yield}	Acceptance	dσ/dcosθ
5	17.753± 16.058	0.00067408±0.00001788	1016.800± 920.131
10	24.199± 10.579	0.00121733±0.00002404	767.506± 335.866
15	28.757± 10.120	0.00157380±0.00002734	705.466± 248.574
20	23.667± 10.043	0.00179565±0.00002920	508.869± 216.086
25	23.599± 10.215	0.00193218±0.00003029	471.561± 204.258
30	21.397± 10.363	0.00203172±0.00003107	406.617± 197.031

K^+ polar angle : 90–180 degree

Width(MeV/c^2)	N_{yield}	Acceptance	dσ/dcosθ
5	0.000± 0.000	0.00000000±0.00000000	-1000.000± 0.000
10	0.000± 0.000	0.00000000±0.00000000	-1000.000± 0.000
15	0.000± 0.000	0.00000000±0.00000000	-1000.000± 0.000
20	0.000± 0.000	0.00000000±0.00000000	-1000.000± 0.000
25	0.000± 0.000	0.00000000±0.00000000	-1000.000± 0.000
30	0.000± 0.000	0.00000000±0.00000000	-1000.000± 0.000

K^+ polar angle : 0–60 degree

Width(MeV/c^2)	N_{yield}	Acceptance	dσ/dcosθ
5	362.743± 95.478	0.01955060±0.00009713	716.353± 188.586
10	551.688± 56.541	0.03569180±0.00013227	596.778± 61.202
15	698.819± 51.837	0.04702080±0.00015264	573.802± 42.604
20	740.338± 51.262	0.05420210±0.00016445	527.351± 36.550
25	744.884± 52.110	0.05825140±0.00017081	493.708± 34.569
30	794.927± 53.322	0.06088460±0.00017484	504.089± 33.844

K^+ polar angle : 19.4–43.2 degree

Width(MeV/c^2)	N_{yield}	Acceptance	dσ/dcosθ
5	194.158± 69.222	0.02562940±0.00017033	683.196± 243.617
10	293.777± 41.825	0.04650600±0.00023177	569.688± 81.156
15	403.916± 38.497	0.06129870±0.00026797	594.248± 56.697
20	421.300± 38.165	0.07068070±0.00028901	537.550± 48.745
25	403.350± 38.906	0.07597210±0.00030038	478.802± 46.223
30	415.901± 39.933	0.07935190±0.00030747	472.673± 45.421

Figure A.8: Measured from K^+p detection mode of LH_2 data and under the requirement "$|MMp(\gamma,K^+p)\text{-}M_K| < 0.025$ GeV/c^2", the left column shows the signal-window width dependence of differential cross sections in different K^+ polar angles within photon energy of 2.2-2.4 GeV; the right column shows the corresponding numerical tables including number of yields, acceptance and differential cross section $d\sigma/d\cos\theta_{K^+}$.

A.2.2 Differential cross section II

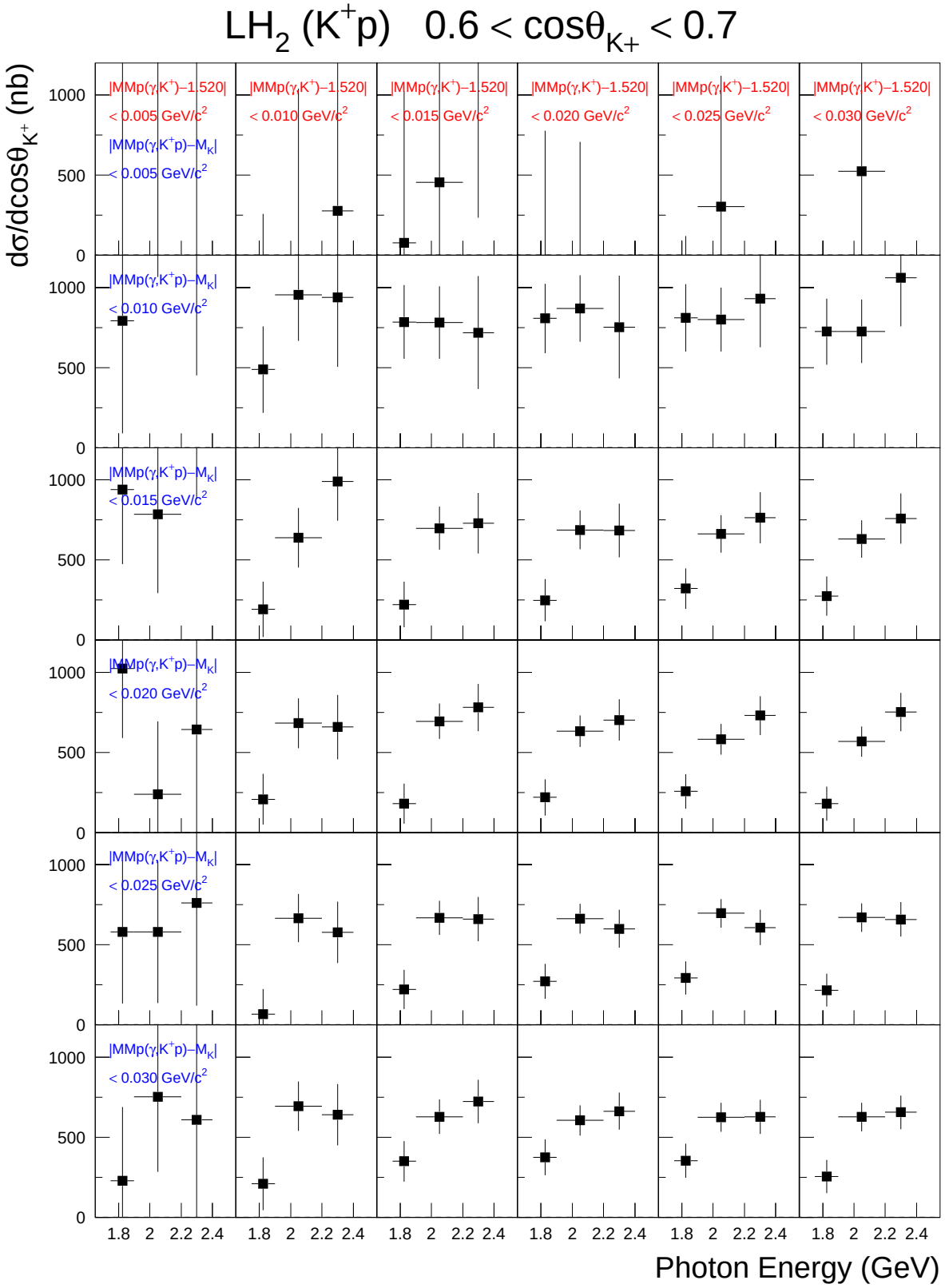

Figure A.9: Measured from K^+p detection mode of LH_2 data, the photon energy dependence of differential cross sections in $0.6 < \cos\theta_{K^+} < 0.7$ are shown in 6×6 2-step side-band subtraction conditions.

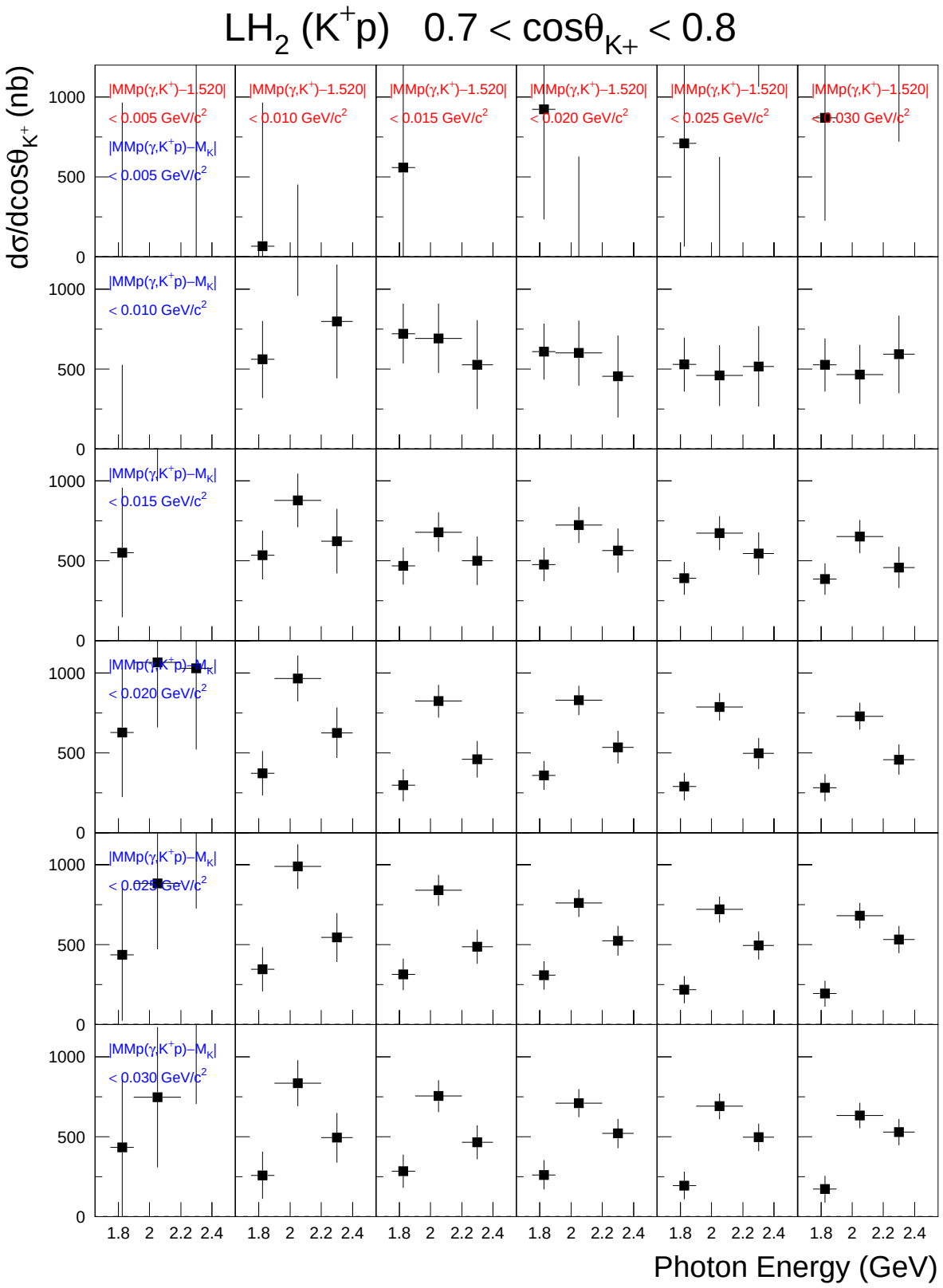

Figure A.10: Measured from K^+p detection mode of LH_2 data, the photon energy dependence of differential cross sections in $0.7 < \cos\theta_{K^+} < 0.8$ are shown in 6×6 2-step side-band subtraction conditions.

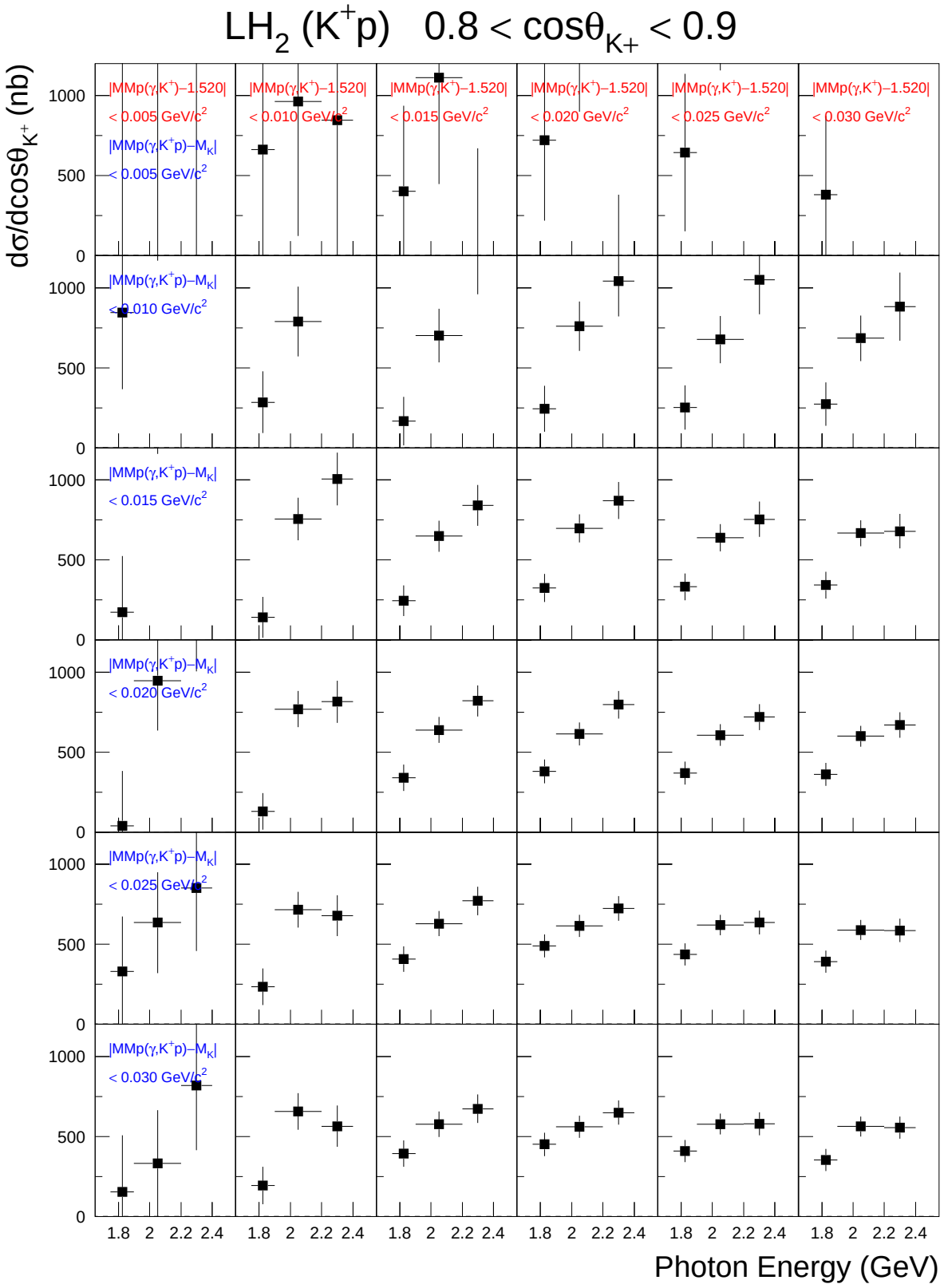

Figure A.11: Measured from K^+p detection mode of LH_2 data, the photon energy dependence of differential cross sections in $0.8 < \cos\theta_{K^+} < 0.9$ are shown in 6×6 2-step side-band subtraction conditions.

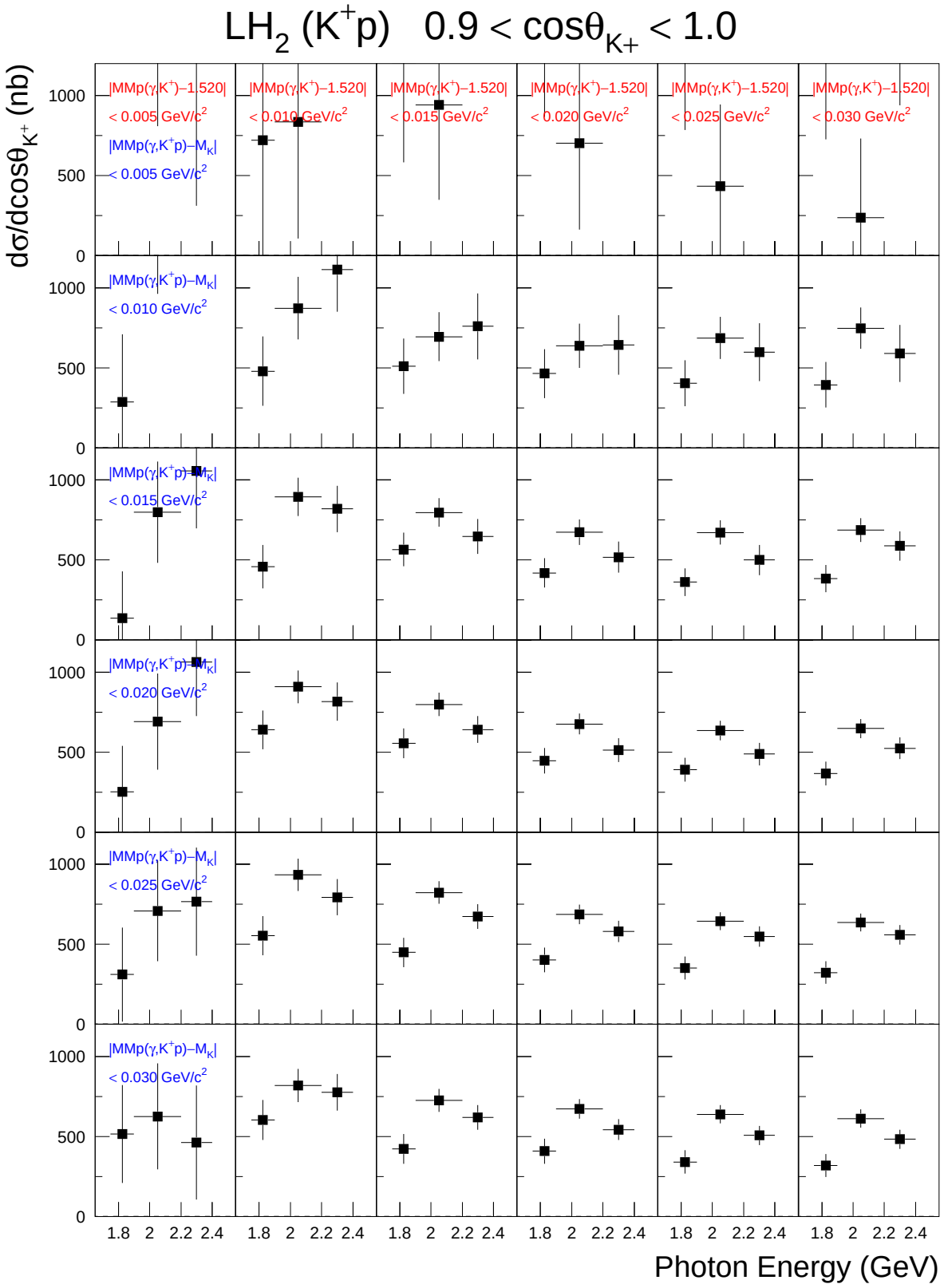

Figure A.12: Measured from K^+p detection mode of LH_2 data, the photon energy dependence of differential cross sections in $0.9 < \cos\theta_{K^+} < 1.0$ are shown in 6×6 2-step side-band subtraction conditions.

A.3 K^-p detection mode from protons

A.3.1 Background non-linearity

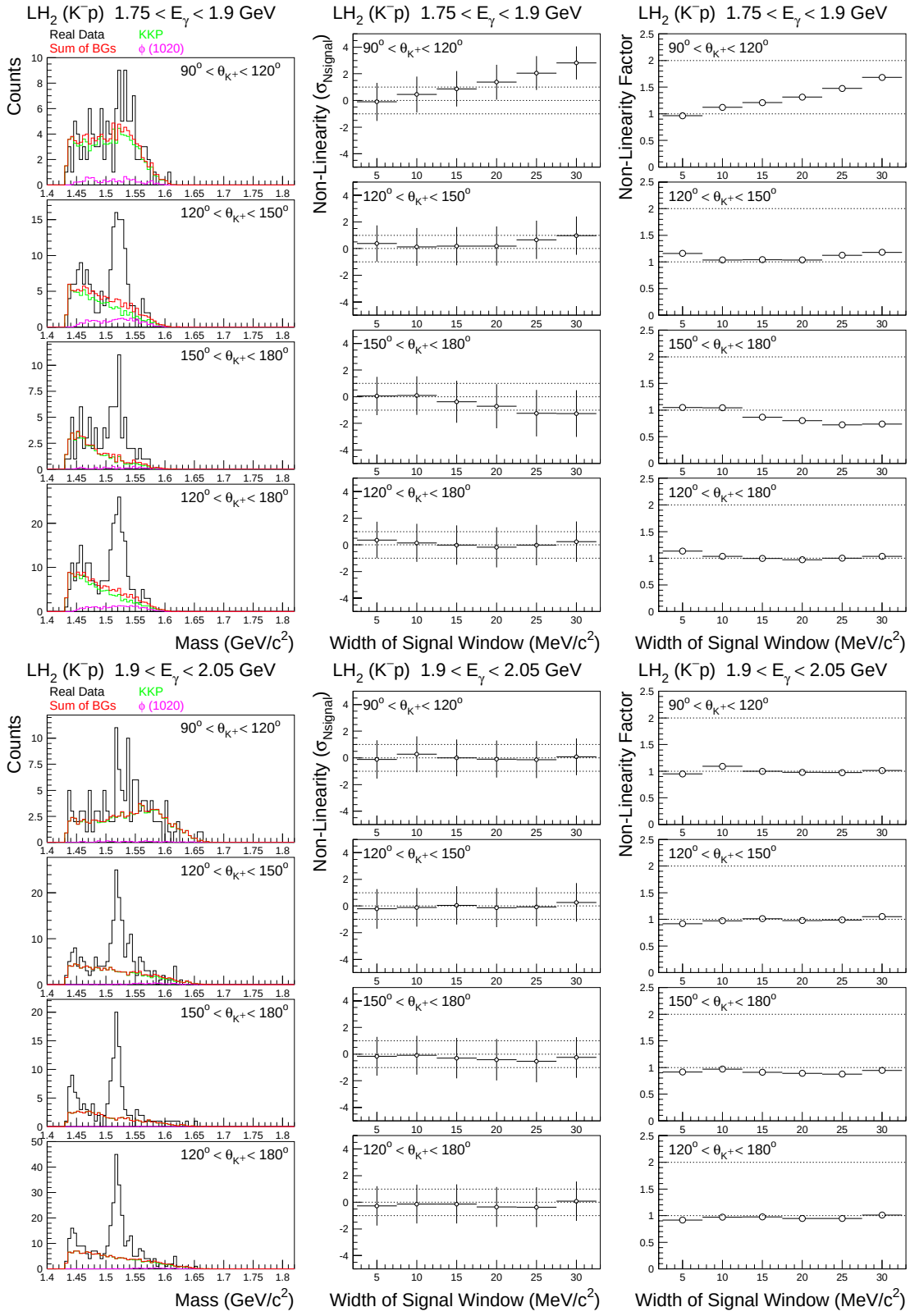

Figure A.13: Background non-linearity studies in different K^+ polar angles within photon energy of 1.75-1.9 GeV and 1.9-2.05 from K^-p detection mode of LH_2 data are shown in 3 columns respectively, including mass spectra of real data overlaid by that of Monte Carlo simulations, background non-linearities and non-linearity correction factors.

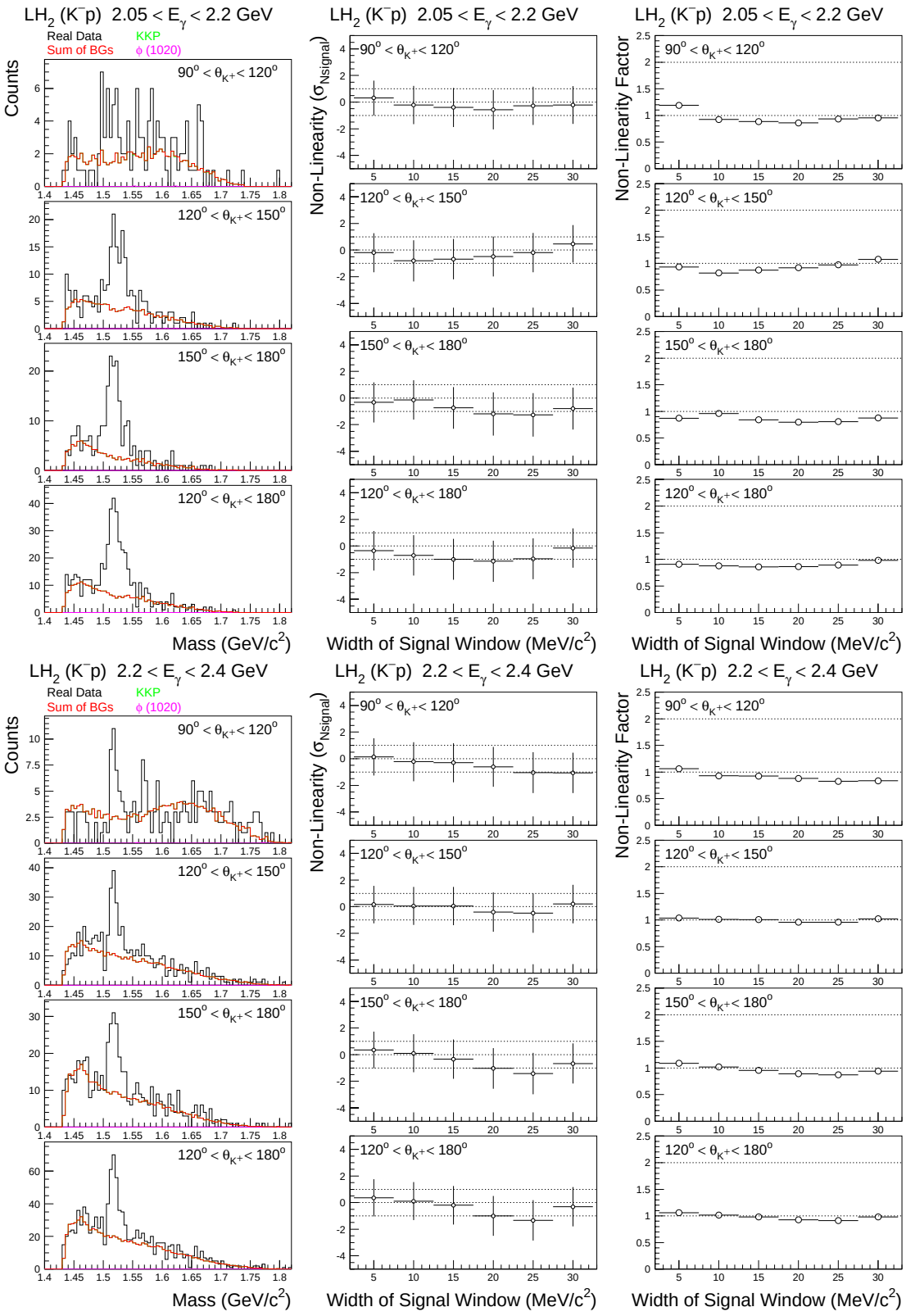

Figure A.14: Background non-linearity studies in different K^+ polar angles within photon energy of 2.05-2.2 GeV and 2.2-2.4 from K^-p detection mode of LH_2 data are shown in 3 columns respectively, including mass spectra of real data overlaid by that of Monte Carlo simulations, background non-linearities and non-linearity correction factors.

A.3.2 Differential cross section

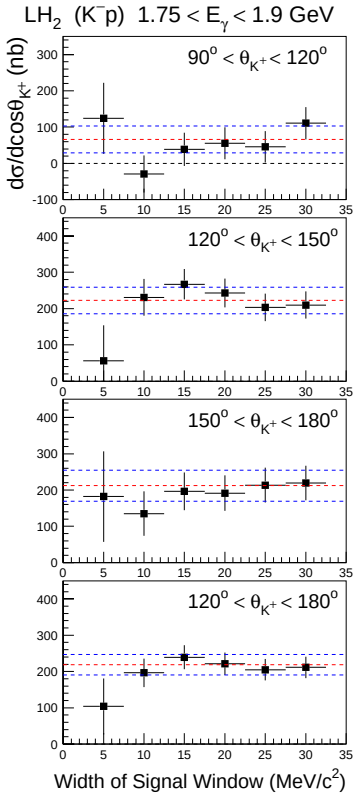

LH$_2$ (K^-p) 1.75 < E_γ < 1.9 GeV

K^+ polar angle : 90–120 degree

Width(MeV/c^2)	N_{yield}	Acceptance	dσ/dcosθ
5	10.551± 8.525	0.00709239±0.00003199	124.320± 97.823
10	-0.646± 7.281	0.01150600±0.00004084	-29.126± -51.501
15	12.125± 7.811	0.01388270±0.00004491	39.011± 45.787
20	19.184± 8.295	0.01525750±0.00004711	55.438± 44.244
25	23.415± 8.614	0.01611900±0.00004845	45.681± 43.491
30	40.184± 9.144	0.01671000±0.00004934	110.602± 44.538

K^+ polar angle : 120–150 degree

Width(MeV/c^2)	N_{yield}	Acceptance	dσ/dcosθ
5	13.558± 12.700	0.01439300±0.00005348	56.001± 98.104
10	49.298± 10.770	0.02351230±0.00006866	230.846± 50.932
15	68.552± 10.748	0.02831640±0.00007552	267.159± 42.207
20	68.481± 10.978	0.03097600±0.00007909	242.841± 39.407
25	63.835± 11.179	0.03270440±0.00008134	203.067± 38.006
30	69.937± 11.385	0.03381230±0.00008275	209.800± 37.440

K^+ polar angle : 150–180 degree

Width(MeV/c^2)	N_{yield}	Acceptance	dσ/dcosθ
5	13.625± 9.129	0.02219170±0.00011019	182.022± 124.927
10	16.666± 7.309	0.03627450±0.00014185	135.126± 61.184
15	26.804± 7.544	0.04377200±0.00015639	196.510± 52.343
20	27.090± 7.701	0.04797090±0.00016405	191.428± 48.749
25	30.517± 7.979	0.05056070±0.00016862	213.356± 47.928
30	32.563± 8.156	0.05223300±0.00017153	219.624± 47.421

K^+ polar angle : 120–180 degree

Width(MeV/c^2)	N_{yield}	Acceptance	dσ/dcosθ
5	27.163± 15.643	0.01648220±0.00004902	103.780± 77.238
10	65.972± 13.017	0.02693120±0.00006298	196.492± 39.337
15	95.343± 13.131	0.03245680±0.00006932	239.254± 32.929
20	95.548± 13.408	0.03552880±0.00007264	221.383± 30.716
25	94.342± 13.734	0.03748800±0.00007468	204.978± 29.817
30	102.489± 14.005	0.03874700±0.00007597	211.458± 29.417

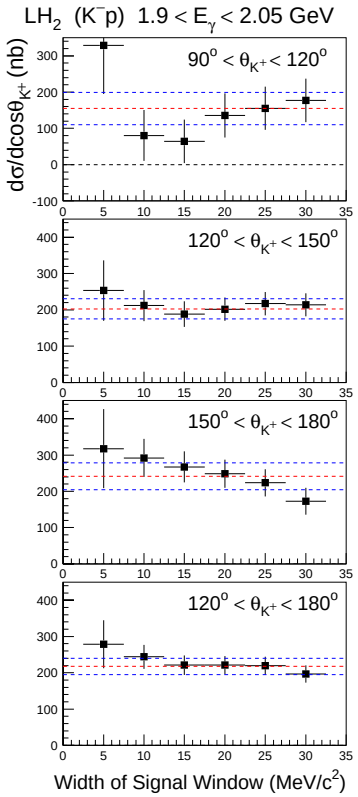

LH$_2$ (K^-p) 1.9 < E_γ < 2.05 GeV

K^+ polar angle : 90–120 degree

Width(MeV/c^2)	N_{yield}	Acceptance	dσ/dcosθ
5	21.912± 8.784	0.00457810±0.00002442	328.282± 133.788
10	10.368± 7.501	0.00743950±0.00003118	80.371± 70.304
15	8.211± 7.692	0.00892896±0.00003418	64.097± 60.066
20	18.518± 8.529	0.00982803±0.00003588	135.555± 60.510
25	22.416± 8.900	0.01043840±0.00003699	155.124± 59.453
30	28.004± 9.359	0.01083760±0.00003769	176.935± 60.215

K^+ polar angle : 120–150 degree

Width(MeV/c^2)	N_{yield}	Acceptance	dσ/dcosθ
5	43.215± 14.212	0.01630660±0.00005415	253.121± 83.021
10	58.488± 11.869	0.02653870±0.00006942	211.708± 42.603
15	63.438± 11.706	0.03193990±0.00007636	188.233± 34.913
20	73.600± 11.933	0.03509850±0.00008017	201.748± 32.388
25	83.983± 12.419	0.03705940±0.00008246	216.949± 31.924
30	87.960± 12.717	0.03832550±0.00008391	213.957± 31.611

K^+ polar angle : 150–180 degree

Width(MeV/c^2)	N_{yield}	Acceptance	dσ/dcosθ
5	36.870± 12.501	0.02983160±0.00012192	317.636± 109.032
10	54.738± 9.830	0.04870540±0.00015721	292.029± 52.516
15	59.888± 9.636	0.05874860±0.00017348	267.092± 42.680
20	60.377± 9.664	0.06444280±0.00018218	248.351± 39.022
25	56.102± 9.838	0.06804670±0.00018753	223.431± 37.617
30	45.155± 9.935	0.07048340±0.00019107	172.753± 36.673

K^+ polar angle : 120–180 degree

Width(MeV/c^2)	N_{yield}	Acceptance	dσ/dcosθ
5	80.036± 18.921	0.01992770±0.00005131	278.963± 66.206
10	113.208± 15.411	0.03247350±0.00006591	244.023± 33.093
15	123.342± 15.162	0.03911750±0.00007257	221.205± 27.028
20	133.981± 15.355	0.04295500±0.00007618	221.074± 24.928
25	140.084± 15.843	0.04535580±0.00007837	219.621± 24.358
30	133.089± 16.137	0.04693530±0.00007979	196.549± 23.974

Figure A.15: Measured from K^-p detection mode of LH_2 data, the left column shows the signal-window width dependence of differential cross sections in different K^+ polar angles within photon energy of 1.75-1.9 and 1.9-2.05 GeV; the right column shows the corresponding numerical tables including number of yields, acceptance and differential cross section $d\sigma/d\cos\theta_{K^+}$.

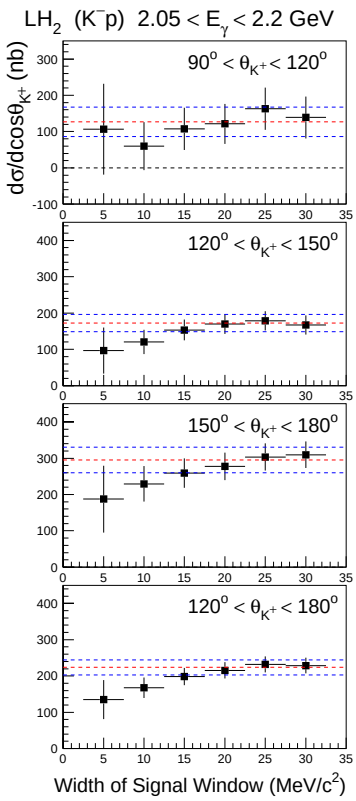

LH$_2$ (K$^-$p) 2.05 < E$_\gamma$ < 2.2 GeV

K$^+$ polar angle : 90–120 degree

Width(MeV/c^2)	N$_{yield}$	Acceptance	dσ/dcosθ
5	7.746± 7.374	0.00356797±0.00002022	106.319± 125.114
10	4.551± 6.337	0.00582781±0.00002587	59.866± 65.823
15	10.540± 6.728	0.00701904±0.00002841	107.198± 58.022
20	12.859± 7.005	0.00772733±0.00002982	121.301± 54.880
25	20.691± 7.853	0.00819725±0.00003072	163.188± 57.995
30	18.249± 8.140	0.00851966±0.00003132	138.867± 57.838

K$^+$ polar angle : 120–150 degree

Width(MeV/c^2)	N$_{yield}$	Acceptance	dσ/dcosθ
5	18.396± 13.589	0.01766110±0.00005291	96.374± 63.632
10	35.642± 11.647	0.02871370±0.00006782	120.162± 33.544
15	60.188± 12.001	0.03474200±0.00007482	153.198± 28.567
20	75.463± 12.524	0.03824290±0.00007863	169.768± 27.085
25	85.885± 12.972	0.04039380±0.00008090	178.339± 26.560
30	88.220± 13.333	0.04183210±0.00008238	167.240± 26.360

K$^+$ polar angle : 150–180 degree

Width(MeV/c^2)	N$_{yield}$	Acceptance	dσ/dcosθ
5	26.136± 14.712	0.03610390±0.00012611	187.332± 92.046
10	58.714± 12.725	0.05894310±0.00016290	229.391± 48.769
15	76.988± 12.669	0.07101400±0.00017982	259.095± 40.301
20	89.218± 13.009	0.07816760±0.00018929	277.534± 37.598
25	103.533± 13.582	0.08253560±0.00019490	303.429± 37.175
30	112.417± 13.773	0.08547340±0.00019861	309.516± 36.404

K$^+$ polar angle : 120–180 degree

Width(MeV/c^2)	N$_{yield}$	Acceptance	dσ/dcosθ
5	44.533± 20.028	0.02260550±0.00005133	134.839± 53.634
10	94.435± 17.259	0.03681800±0.00006596	167.710± 28.378
15	137.171± 17.450	0.04446630±0.00007276	198.424± 23.758
20	164.684± 18.059	0.04894640±0.00007650	215.641± 22.336
25	189.432± 18.782	0.05169180±0.00007872	231.618± 21.998
30	200.661± 19.171	0.05353210±0.00008018	228.585± 21.681

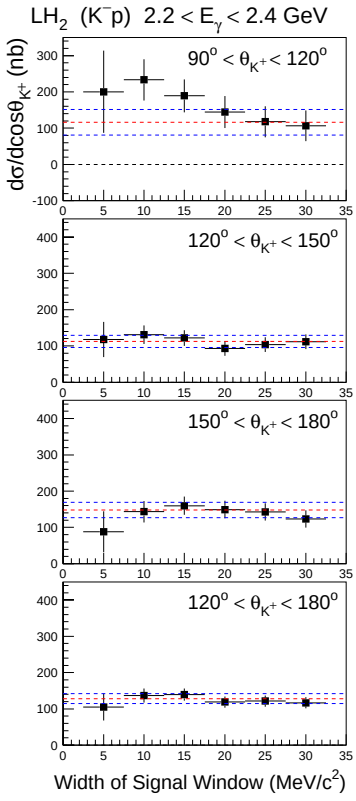

LH$_2$ (K$^-$p) 2.2 < E$_\gamma$ < 2.4 GeV

K$^+$ polar angle : 90–120 degree

Width(MeV/c^2)	N$_{yield}$	Acceptance	dσ/dcosθ
5	16.828± 9.443	0.00328861±0.00001551	200.354± 113.504
10	31.835± 7.769	0.00540054±0.00001990	233.112± 56.871
15	30.786± 7.551	0.00654367±0.00002192	189.101± 45.618
20	23.839± 8.015	0.00719459±0.00002299	144.067± 44.035
25	17.859± 8.225	0.00760656±0.00002364	117.787± 42.744
30	16.001± 8.467	0.00788928±0.00002408	106.773± 42.423

K$^+$ polar angle : 120–150 degree

Width(MeV/c^2)	N$_{yield}$	Acceptance	dσ/dcosθ
5	45.590± 18.276	0.02020820±0.00004532	117.702± 48.838
10	80.334± 15.576	0.03288860±0.00005818	131.188± 25.574
15	90.254± 16.033	0.03979170±0.00006421	121.847± 21.759
20	70.560± 16.519	0.04373460±0.00006744	92.978± 20.397
25	82.692± 17.366	0.04619100±0.00006939	103.338± 20.302
30	101.417± 18.068	0.04790070±0.00007072	111.586± 20.369

K$^+$ polar angle : 150–180 degree

Width(MeV/c^2)	N$_{yield}$	Acceptance	dσ/dcosθ
5	32.004± 17.376	0.04533680±0.00011360	87.977± 56.527
10	72.483± 14.814	0.07375600±0.00014686	143.426± 29.625
15	94.209± 15.303	0.08926240±0.00016272	159.842± 25.286
20	89.783± 16.068	0.09805390±0.00017123	149.067± 24.171
25	85.850± 16.797	0.10360600±0.00017646	142.626± 23.913
30	81.875± 17.367	0.10730100±0.00017988	123.283± 23.873

K$^+$ polar angle : 120–180 degree

Width(MeV/c^2)	N$_{yield}$	Acceptance	dσ/dcosθ
5	77.594± 25.218	0.02693980±0.00004492	105.114± 37.002
10	152.821± 21.496	0.04383640±0.00005778	136.727± 19.384
15	184.474± 22.164	0.05304420±0.00006383	139.246± 16.517
20	160.357± 23.046	0.05828590±0.00006708	118.750± 15.629
25	168.550± 24.161	0.06157180±0.00006905	121.438± 15.511
30	183.292± 25.061	0.06381310±0.00007037	116.857± 15.524

Figure A.16: Measured from K$^-$p detection mode of LH$_2$ data, the left column shows the signal-window width dependence of differential cross sections in different K$^+$ polar angles within photon energy of 2.05-2.2 and 2.2-2.4 GeV; the right column shows the corresponding numerical tables including number of yields, acceptance and differential cross section $d\sigma/d\cos\theta_{K^+}$.

A.4 K^-p detection mode from deuterons

A.4.1 Background non-linearity

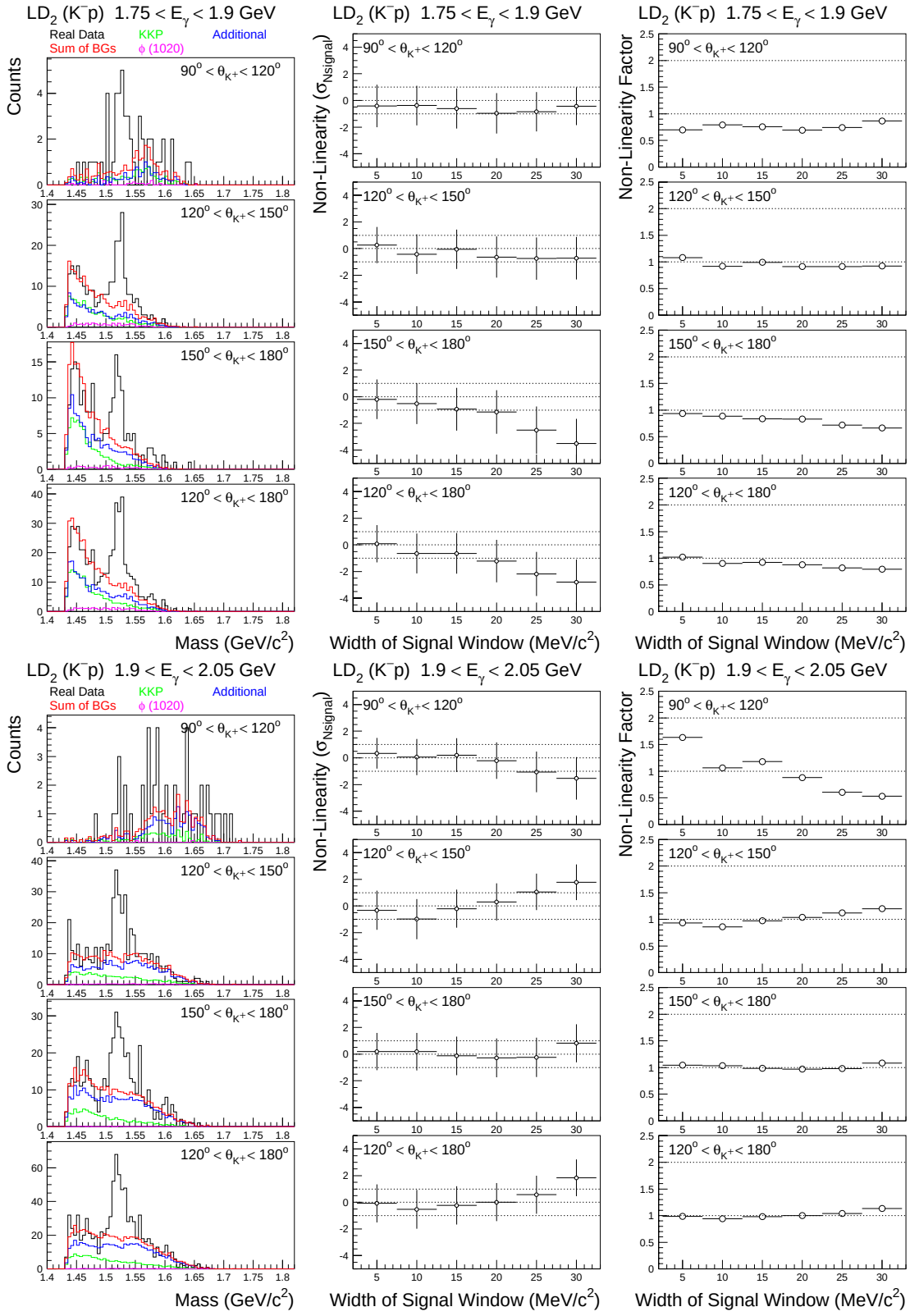

Figure A.17: Background non-linearity studies in different K^+ polar angles within photon energy of 1.75-1.9 GeV and 1.9-2.05 from K^-p detection mode of LD_2 data are shown in 3 columns respectively, including mass spectra of real data overlaid by that of Monte Carlo simulations, background non-linearities and non-linearity correction factors.

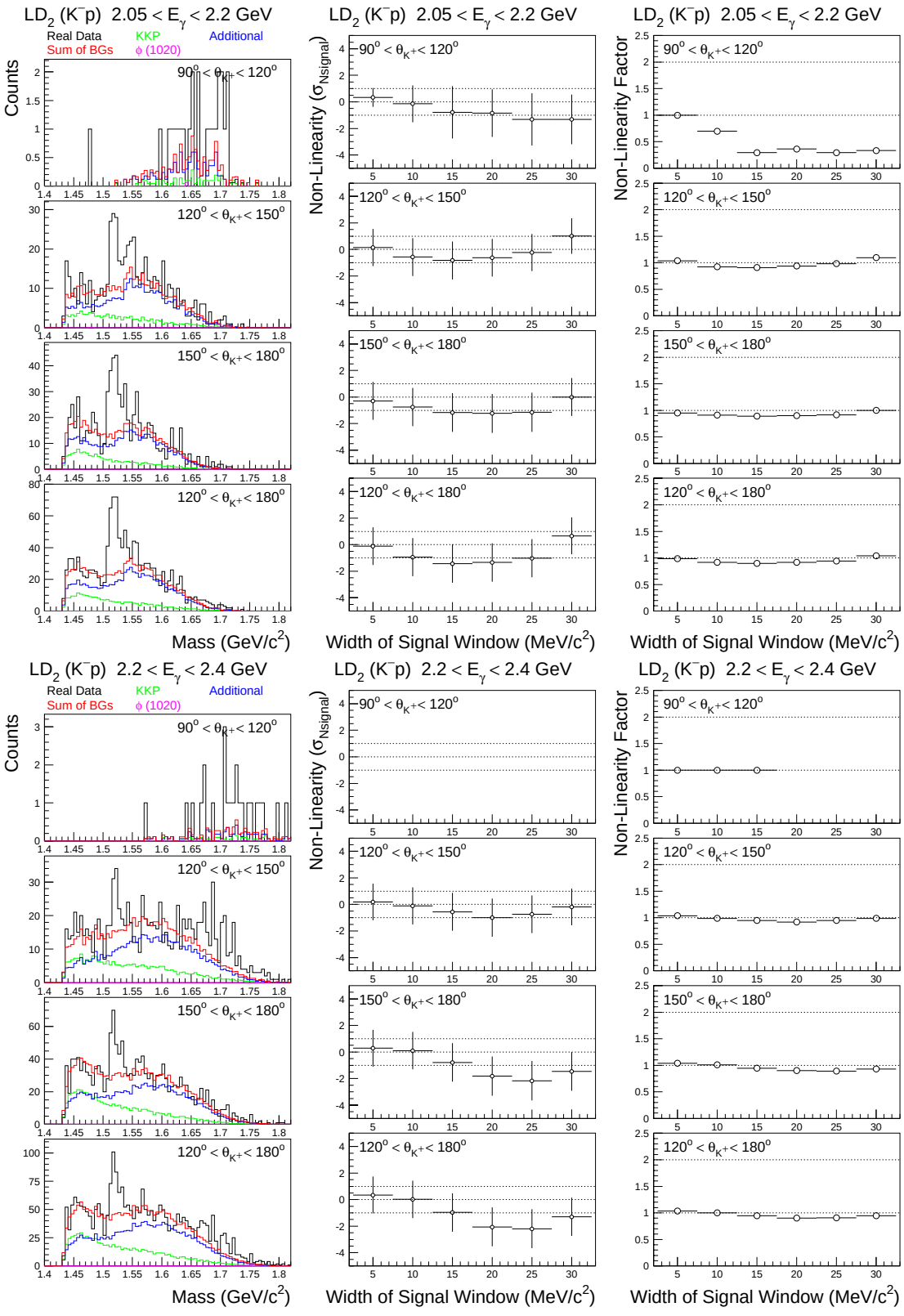

Figure A.18: Background non-linearity studies in different K^+ polar angles within photon energy of 2.05-2.2 GeV and 2.2-2.4 from K^-p detection mode of LD_2 data are shown in 3 columns respectively, including mass spectra of real data overlaid by that of Monte Carlo simulations, background non-linearities and non-linearity correction factors.

A.4.2 Differential cross section

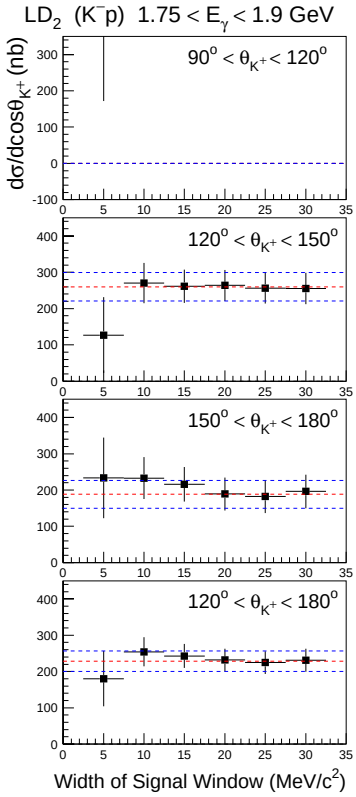

LD$_2$ (K^-p) $1.75 < E_\gamma < 1.9$ GeV

K^+ polar angle : 90–120 degree

Width(MeV/c^2)	N_{yield}	Acceptance	dσ/dcosθ
5	6.797± 6.218	0.00031277±0.00001103	1120.840± 949.387
10	8.933± 5.338	0.00050884±0.00001407	956.789± 501.206
15	9.203± 5.334	0.00061620±0.00001549	873.597± 413.476
20	17.173± 5.889	0.00066678±0.00001611	1388.630± 422.524
25	18.427± 5.986	0.00070334±0.00001655	1390.180± 407.237
30	20.231± 6.070	0.00072902±0.00001685	1397.030± 398.538

K^+ polar angle : 120–150 degree

Width(MeV/c^2)	N_{yield}	Acceptance	dσ/dcosθ
5	21.345± 14.714	0.00916564±0.00007021	126.990± 104.667
10	59.444± 12.671	0.01488840±0.00008974	269.896± 55.509
15	72.108± 12.658	0.01804990±0.00009896	261.726± 45.741
20	75.701± 13.022	0.01973610±0.00010357	263.675± 43.038
25	75.851± 13.655	0.02071250±0.00010615	256.542± 42.997
30	77.671± 14.181	0.02137230±0.00010786	254.958± 43.274

K^+ polar angle : 150–180 degree

Width(MeV/c^2)	N_{yield}	Acceptance	dσ/dcosθ
5	24.080± 11.757	0.01884660±0.00016700	233.097± 111.104
10	38.374± 9.908	0.03063740±0.00021415	232.845± 57.609
15	40.948± 9.851	0.03697280±0.00023598	215.726± 47.460
20	36.729± 10.305	0.04052250±0.00024747	189.178± 45.295
25	28.329± 10.904	0.04269530±0.00025428	182.164± 45.482
30	26.848± 11.406	0.04400830±0.00025832	196.269± 46.155

K^+ polar angle : 120–180 degree

Width(MeV/c^2)	N_{yield}	Acceptance	dσ/dcosθ
5	45.457± 18.829	0.01176440±0.00006812	180.277± 76.388
10	97.820± 16.085	0.01911600±0.00008715	254.111± 40.173
15	113.068± 16.041	0.02312950±0.00009605	242.846± 33.111
20	112.418± 16.606	0.02531600±0.00010060	231.586± 31.315
25	104.113± 17.471	0.02661350±0.00010321	224.748± 31.338
30	104.466± 18.196	0.02744870±0.00010486	231.082± 31.644

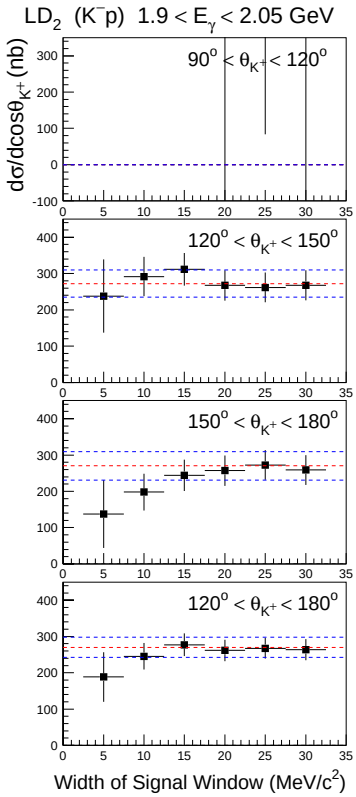

LD$_2$ (K^-p) $1.9 < E_\gamma < 2.05$ GeV

K^+ polar angle : 90–120 degree

Width(MeV/c^2)	N_{yield}	Acceptance	dσ/dcosθ
5	5.400± 4.708	0.00001890±0.00000257	24466.300±9230.110
10	5.833± 3.997	0.00002799±0.00000313	7748.450±5295.060
15	6.512± 3.684	0.00003919±0.00000370	5968.550±3488.150
20	3.214± 3.910	0.00004409±0.00000393	3143.330±3255.200
25	1.197± 4.058	0.00004899±0.00000414	3116.490±3032.980
30	-0.600± 4.200	0.00005039±0.00000420	-398.636±-3051.330

K^+ polar angle : 120–150 degree

Width(MeV/c^2)	N_{yield}	Acceptance	dσ/dcosθ
5	39.383± 18.099	0.00898474±0.00006547	237.976± 100.741
10	78.042± 15.690	0.01456040±0.00008358	291.832± 53.905
15	108.263± 15.908	0.01760070±0.00009203	311.801± 45.224
20	106.584± 16.242	0.01940880±0.00009672	267.224± 41.869
25	118.530± 16.850	0.02055680±0.00009960	261.877± 41.013
30	134.330± 17.639	0.02129250±0.00010140	267.873± 41.452

K^+ polar angle : 150–180 degree

Width(MeV/c^2)	N_{yield}	Acceptance	dσ/dcosθ
5	27.723± 17.074	0.02492990±0.00018094	137.182± 93.550
10	60.387± 14.956	0.04038550±0.00023203	198.077± 50.594
15	86.030± 15.389	0.04871170±0.00025585	244.335± 43.169
20	97.898± 16.197	0.05341430±0.00026851	256.836± 41.434
25	110.178± 16.874	0.05633830±0.00027614	272.589± 40.928
30	119.264± 17.475	0.05829110±0.00028115	258.726± 40.967

K^+ polar angle : 120–180 degree

Width(MeV/c^2)	N_{yield}	Acceptance	dσ/dcosθ
5	67.077± 24.877	0.01328270±0.00006818	188.485± 68.562
10	138.310± 21.668	0.02152140±0.00008714	245.613± 36.866
15	194.179± 22.129	0.02598650±0.00009596	277.231± 31.187
20	204.459± 22.937	0.02857480±0.00010075	261.657± 29.397
25	228.693± 23.846	0.03020160±0.00010366	267.522± 28.917
30	253.569± 24.829	0.03126530±0.00010553	263.336± 29.085

Figure A.19: Measured from K^-p detection mode of LD_2 data, the left column shows the signal-window width dependence of differential cross sections in different K^+ polar angles within photon energy of 1.75-1.9 and 1.9-2.05 GeV; the right column shows the corresponding numerical tables including number of yields, acceptance and differential cross section $d\sigma/d\cos\theta_{K^+}$.

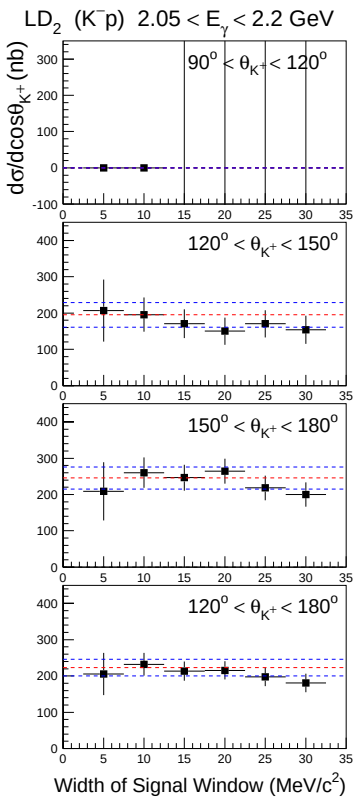

LD_2 (K^-p) $2.05 < E_\gamma < 2.2$ GeV

K^+ polar angle : 90–120 degree

Width(MeV/c^2)	N_{yield}	Acceptance	dσ/dcosθ
5	0.000± 0.000	0.00000123±0.00000062	0.000± 0.000
10	0.000± 0.000	0.00000246±0.00000087	0.000± 0.000
15	-0.583± 0.583	0.00000431±0.00000115	-1145.660±-4463.770
20	-0.500± 0.500	0.00000554±0.00000131	-1052.010±-2953.720
25	-0.529± 0.529	0.00000554±0.00000131	-861.825±-3127.470
30	-1.125± 0.795	0.00000554±0.00000131	-1993.370±-4821.450

K^+ polar angle : 120–150 degree

Width(MeV/c^2)	N_{yield}	Acceptance	dσ/dcosθ
5	41.300± 16.608	0.00845874±0.00005961	207.014± 85.412
10	57.114± 14.772	0.01369030±0.00007603	195.607± 46.942
15	57.402± 14.997	0.01656930±0.00008376	170.671± 39.375
20	56.205± 15.798	0.01825540±0.00008799	149.947± 37.647
25	72.954± 16.741	0.01928670±0.00009049	170.235± 37.763
30	83.927± 17.752	0.01997730±0.00009213	153.843± 38.659

K^+ polar angle : 150–180 degree

Width(MeV/c^2)	N_{yield}	Acceptance	dσ/dcosθ
5	51.444± 21.021	0.03122370±0.00019024	208.826± 79.990
10	105.262± 17.936	0.05056250±0.00024434	260.303± 42.160
15	115.930± 18.663	0.06150320±0.00027089	246.327± 36.063
20	137.861± 19.458	0.06757930±0.00028476	264.154± 34.221
25	116.633± 20.288	0.07134230±0.00029310	218.193± 33.794
30	124.684± 20.799	0.07387130±0.00029860	200.371± 33.459

K^+ polar angle : 120–180 degree

Width(MeV/c^2)	N_{yield}	Acceptance	dσ/dcosθ
5	92.767± 26.779	0.01461400±0.00006713	205.678± 58.351
10	162.364± 23.236	0.02365990±0.00008579	232.000± 31.278
15	173.414± 23.945	0.02871870±0.00009475	213.603± 26.554
20	194.149± 25.066	0.03159180±0.00009952	215.441± 25.269
25	189.605± 26.305	0.03336170±0.00010236	197.346± 25.110
30	208.625± 27.345	0.03454930±0.00010422	180.872± 25.206

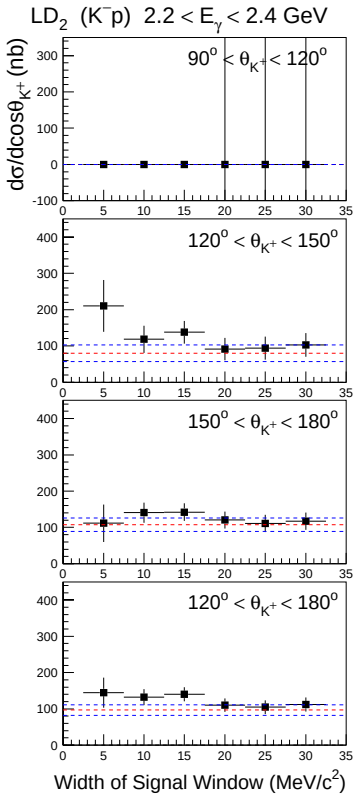

LD_2 (K^-p) $2.2 < E_\gamma < 2.4$ GeV

K^+ polar angle : 90–120 degree

Width(MeV/c^2)	N_{yield}	Acceptance	dσ/dcosθ
5	0.000± 0.000	0.00000039±0.00000028	0.000± 0.000
10	0.000± 0.000	0.00000039±0.00000028	0.000± 0.000
15	0.000± 0.000	0.00000079±0.00000039	0.000± 0.000
20	-0.667± 0.667	0.00000079±0.00000039	0.000±-20126.700
25	-1.000± 1.000	0.00000079±0.00000039	0.000±-30190.000
30	-1.000± 1.000	0.00000079±0.00000039	0.000±-30190.000

K^+ polar angle : 120–150 degree

Width(MeV/c^2)	N_{yield}	Acceptance	dσ/dcosθ
5	53.434± 17.782	0.00727237±0.00004417	210.354± 71.064
10	47.195± 15.176	0.01184960±0.00005651	118.216± 37.219
15	63.070± 15.644	0.01433160±0.00006223	137.609± 31.725
20	38.086± 16.697	0.01572900±0.00006523	91.367± 30.848
25	44.178± 18.111	0.01658720±0.00006702	93.845± 31.729
30	58.286± 19.280	0.01722010±0.00006831	102.716± 32.538

K^+ polar angle : 150–180 degree

Width(MeV/c^2)	N_{yield}	Acceptance	dσ/dcosθ
5	58.269± 24.835	0.03820890±0.00016905	111.434± 51.592
10	111.783± 21.768	0.06243180±0.00021860	140.503± 27.678
15	124.086± 22.960	0.07528240±0.00024149	142.245± 24.210
20	96.678± 24.314	0.08270690±0.00025399	120.272± 23.334
25	83.914± 25.954	0.08739530±0.00026165	110.982± 23.571
30	106.284± 27.399	0.09067320±0.00026692	117.137± 23.985

K^+ polar angle : 120–180 degree

Width(MeV/c^2)	N_{yield}	Acceptance	dσ/dcosθ
5	111.697± 30.545	0.01562330±0.00005555	144.834± 41.590
10	158.981± 26.536	0.02550370±0.00007132	132.350± 22.135
15	187.155± 27.782	0.03078460±0.00007855	140.119± 19.199
20	134.757± 29.494	0.03380890±0.00008244	109.986± 18.558
25	128.091± 31.649	0.03570100±0.00008480	104.783± 18.857
30	164.565± 33.504	0.03704790±0.00008644	111.846± 19.237

Figure A.20: Measured from K^-p detection mode of LD_2 data, the left column shows the signal-window width dependence of differential cross sections in different K^+ polar angles within photon energy of 2.05-2.2 and 2.2-2.4 GeV; the right column shows the corresponding numerical tables including number of yields, acceptance and differential cross section $d\sigma/d\cos\theta_{K^+}$.

A.5 The result of LAMP2 experiment

Table A.1: The data point of LAMP2 experiment

$-t\ (GeV/c)^2$	dt	$\frac{d\sigma}{dt}\ \mu b/\ (GeV/c)^2$	$d\sigma\ (\mu b)$
0.25	0.1	0.76 ± 0.14	0.076 ± 0.014
0.35	0.1	0.69 ± 0.14	0.069 ± 0.014
0.45	0.1	0.45 ± 0.12	0.045 ± 0.012
0.55	0.1	0.29 ± 0.12	0.029 ± 0.012
0.65	0.1	0.12 ± 0.05	0.012 ± 0.005

$$E_\gamma = 3.8 \tag{A.1}$$
$$M_p = 0.93827231 \tag{A.2}$$
$$M_{K^+} = 0.493677 \tag{A.3}$$
$$M_\Lambda = 1.5195 \tag{A.4}$$
$$s \equiv (k_1+k_2)^2 = (k_3+k_4)^2 = m_1^2 + 2E_1E_2 - 2P_1P_2 + m_2^2 = 2E_\gamma M_p + M_p^2 \tag{A.5}$$
$$= 8.01122 \tag{A.6}$$
$$E_{1_{CMS}} = \frac{s+m_1^2-m_2^2}{2\sqrt{s}} = \frac{s-M_p^2}{2\sqrt{s}} = 1.25969 \tag{A.7}$$
$$E_{3_{CMS}} = \frac{s+m_3^2-m_4^2}{2\sqrt{s}} = \frac{s+M_{K^+}^2-M_\Lambda^2}{2\sqrt{s}} = 1.05039 \tag{A.8}$$
$$P_{1_{CMS}} = \sqrt{E_{1_{CMS}}^2 - m_1^2} = E_{1_{CMS}} = 1.25969 \tag{A.9}$$
$$P_{3_{CMS}} = \sqrt{E_{3_{CMS}}^2 - m_3^2} = \sqrt{E_{3_{CMS}}^2 - m_{K^+}^2} = 0.927146 \tag{A.10}$$
$$t \equiv (k_1-k_3)^2 = (k_2-k_4)^2 = m_1^2 + 2E_1E_3 + 2P_1P_3 + m_3^2 \tag{A.11}$$
$$= (E_{1_{CMS}} - E_{3_{CMS}})^2 - (P_{1_{CMS}} - P_{3_{CMS}})^2 - 4P_{1_{CMS}}P_{3_{CMS}}\sin^2\left(\frac{\theta_{CMS}}{2}\right) \tag{A.12}$$
$$= M_{K^+}^2 - 2E_{1_{CMS}}E_{3_{CMS}} + 2P_{1_{CMS}}P_{3_{CMS}}\cos\theta_{CMS} \tag{A.13}$$
$$\cos\theta_{CMS} = \frac{t - M_{K^+}^2 + 2E_{1_{CMS}}E_{3_{CMS}}}{2P_{1_{CMS}}P_{3_{CMS}}} \tag{A.14}$$

Table A.2: The exchange between $-t$ and $\cos\theta_{CMS}$

$-t$ $(GeV/c)^2$	$\cos\theta_{CMS}$	θ_{CMS} (degrees)
0.2	0.942966	19.4442
0.3	0.900155	25.8216
0.4	0.857343	30.9804
0.5	0.814532	35.4589
0.6	0.771720	39.4914
0.7	0.728909	43.2050

From Table A.1 and A.2, the $d\sigma = 0.231 \pm 0.0265518$, the $d\cos\theta = 0.214057$. So, we obtain the result $\frac{d\sigma}{d\cos\theta} = 1.07915 \pm 0.124041$.

A.6 Total cross sections of LEPS results

Table A.3: Total cross sections of LEPS results.

E_γ(GeV)	$\sigma(nb)$
1.825±0.075	378.51±50.51
1.925±0.075	821.68±84.64
2.125±0.075	602.89±101.48
2.300±0.100	587.10±102.94

Appendix B

K^- decay asymmetry in $\Lambda(1520)$ t-channel helicity frame

Relied on the same analysis basis as appendix A, we did the studies of K^- decay asymmetry in $\Lambda(1520)$ t-channel helicity frame. The K^-p, K^+K^- and K^+p detection modes of protons will be presented in Sec. B.1, B.2 and B.3 respectively. Comparisons of photon energy dependence of K^- decay asymmetry were shown in the first part of appendix B.4, where the corresponding energy slices had been listed in Table 4.3.

Similar studies were performed in K^-p and K^+K^- detection modes of protons. It appeared from Fig. B.1 (B.26) that, we studied the $\cos\theta_{K^-}$ slices of mass spectra, non-linearity and non-linearity factor in the photon energy of 1.75-2.4 (1.9-2.4) GeV. The left column of Fig. B.1 (B.26) shows the mass spectra of real data (black) overlaid by the sum of estimated Monte Carlo backgrounds (red). The middle and right columns of Fig. B.1 (B.26) demonstrated the signal-window width dependence of non-linearity and non-linearity factor respectively. The corresponding "Counts", "Acceptance" and "Counts/Acceptance" of K^- polar angle distribution in $\Lambda(1520)$ t-channel helicity frame by side-band and Monte Carlo methods were shown from Fig. B.16 (B.36). In the end, the signal-window width dependence of fraction of helicity-3/2 in photon energy of 1.75-2.4 (1.9-2.4) GeV was shown from Fig. B.21 (B.40) for K^-p (K^+K^-) detection mode of protons. Same analyses with different photon energy were represent in Fig. B.2-B.15 (B.27-B.35) for background linearity, in Fig. B.17-B.20 (B.37-B.39) for K^- polar angle distribution and in Fig. B.22-B.25 (B.41-B.43) for the signal-window width dependence of fraction of helicity-3/2.

In the case of K^+p detection mode of protons, the window dependence of "Counts", "Acceptance" and "Counts/Acceptance" of K^- polar angle distribution by 2-step side-band subtraction method in photon energy of 1.9-2.4 GeV were shown in Fig. B.44-B.46. The energy dependence of "Counts/Acceptance" of K^- polar angle distribution with standard 2-step signal windows in photon energy of 1.75-1.9, 1.9-2.2, 2.2-2.4 and 1.9-2.0 were shown in Fig. B.47.

The photon energy dependence of fraction of helicity-3/2 with 15- and 20- MeV/c^2 signal window from K^-p and K^+K^- detection mode of protons were shown in left and right columns of Fig. B.48 respectively.

B.1 K^-p detection mode from protons

B.1.1 Background non-linearity

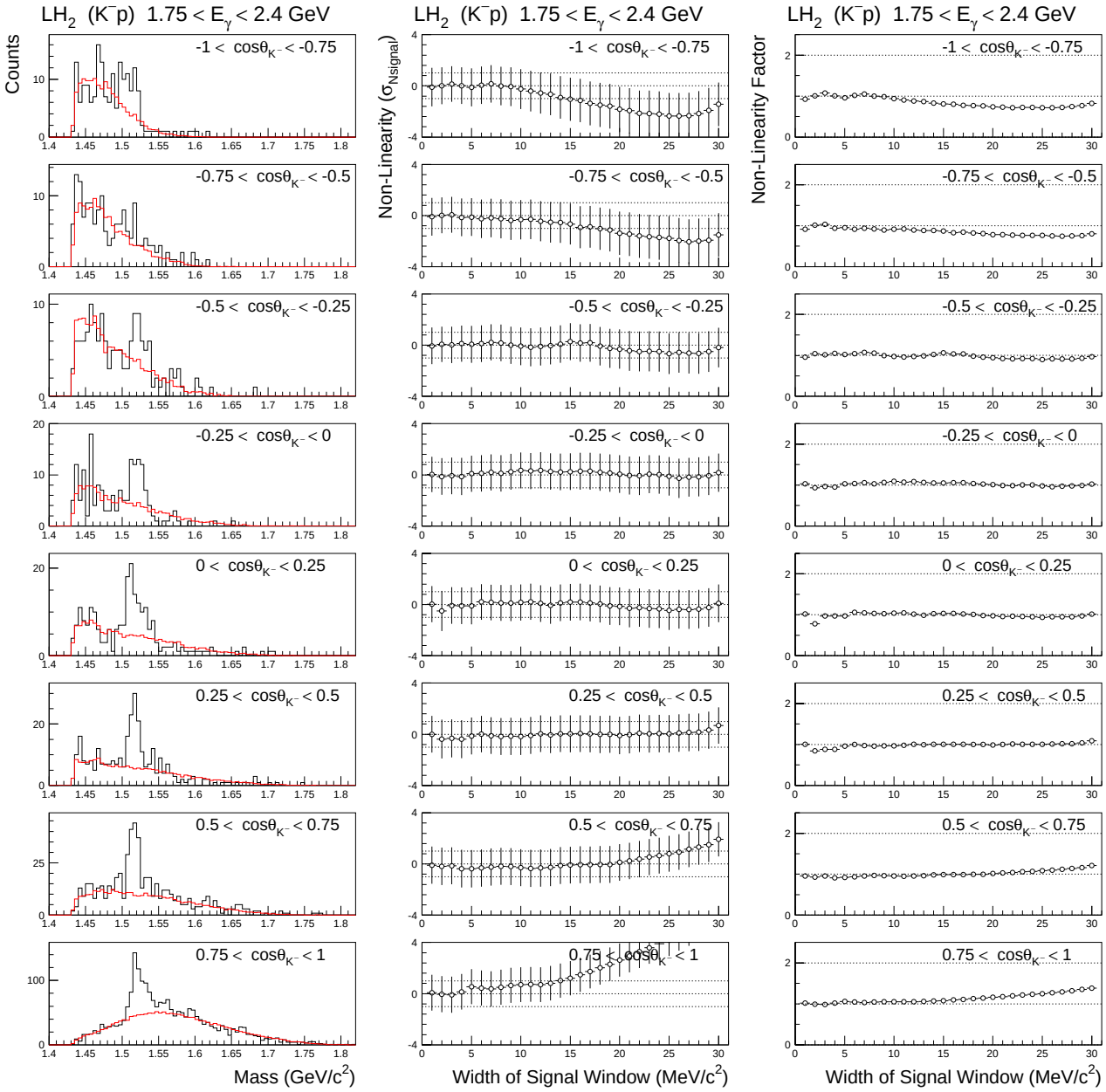

Figure B.1: Background non-linearity studies in different K^- polar angle of $\Lambda(1520)$ helicity frame within photon energy of 1.75-2.4 GeV from K^-p detection mode of protons are shown in 3 columns respectively, including mass spectra of real data overlaid by sum of Monte Carlo simulated background components, background non-linearities and non-linearity correction factors.

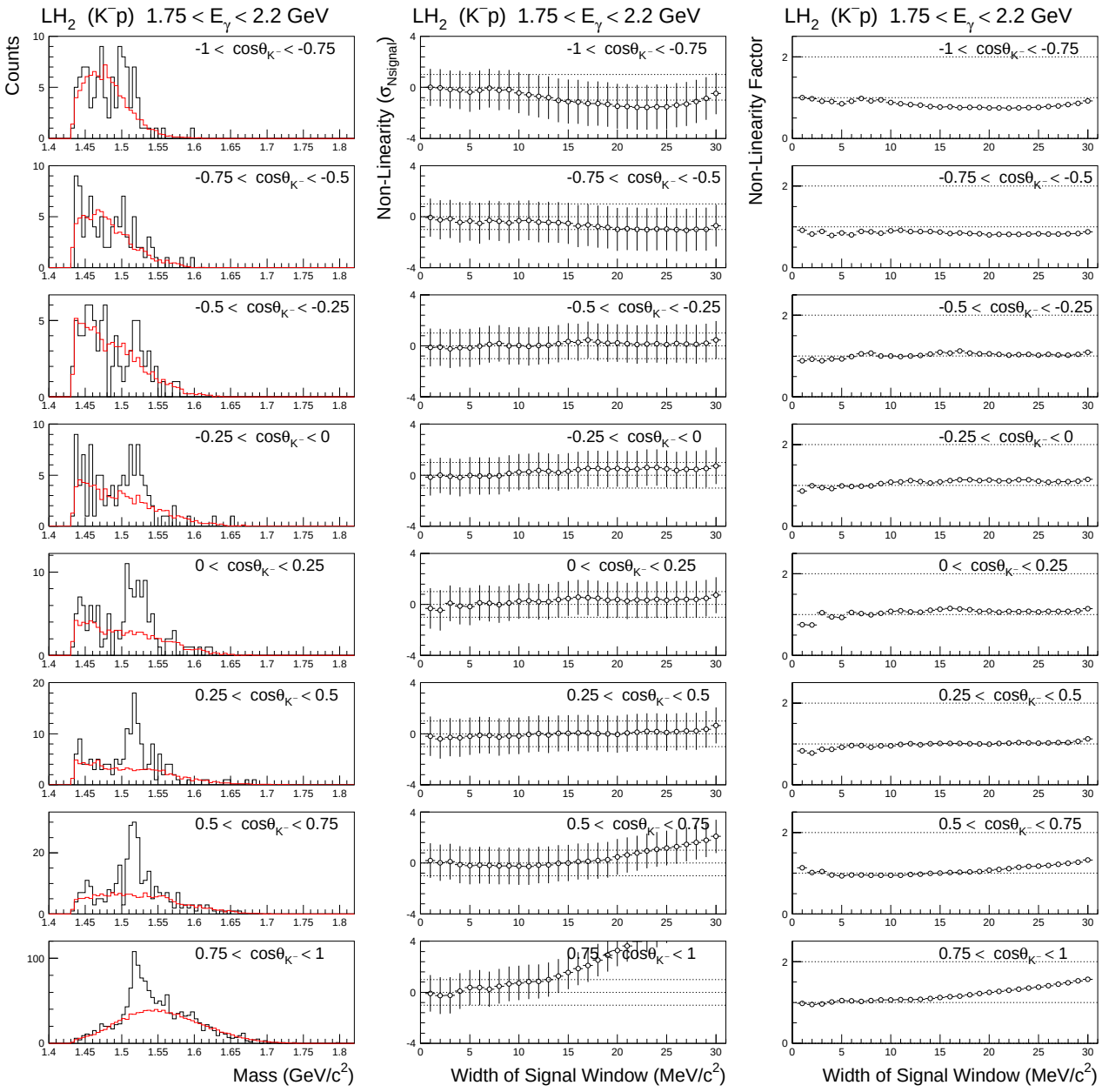

Figure B.2: Background non-linearity studies in different K^- polar angle of $\Lambda(1520)$ helicity frame within photon energy of 1.75-2.2 GeV from K^-p detection mode of protons are shown in 3 columns respectively, including mass spectra of real data overlaid by sum of Monte Carlo simulated background components, background non-linearities and non-linearity correction factors.

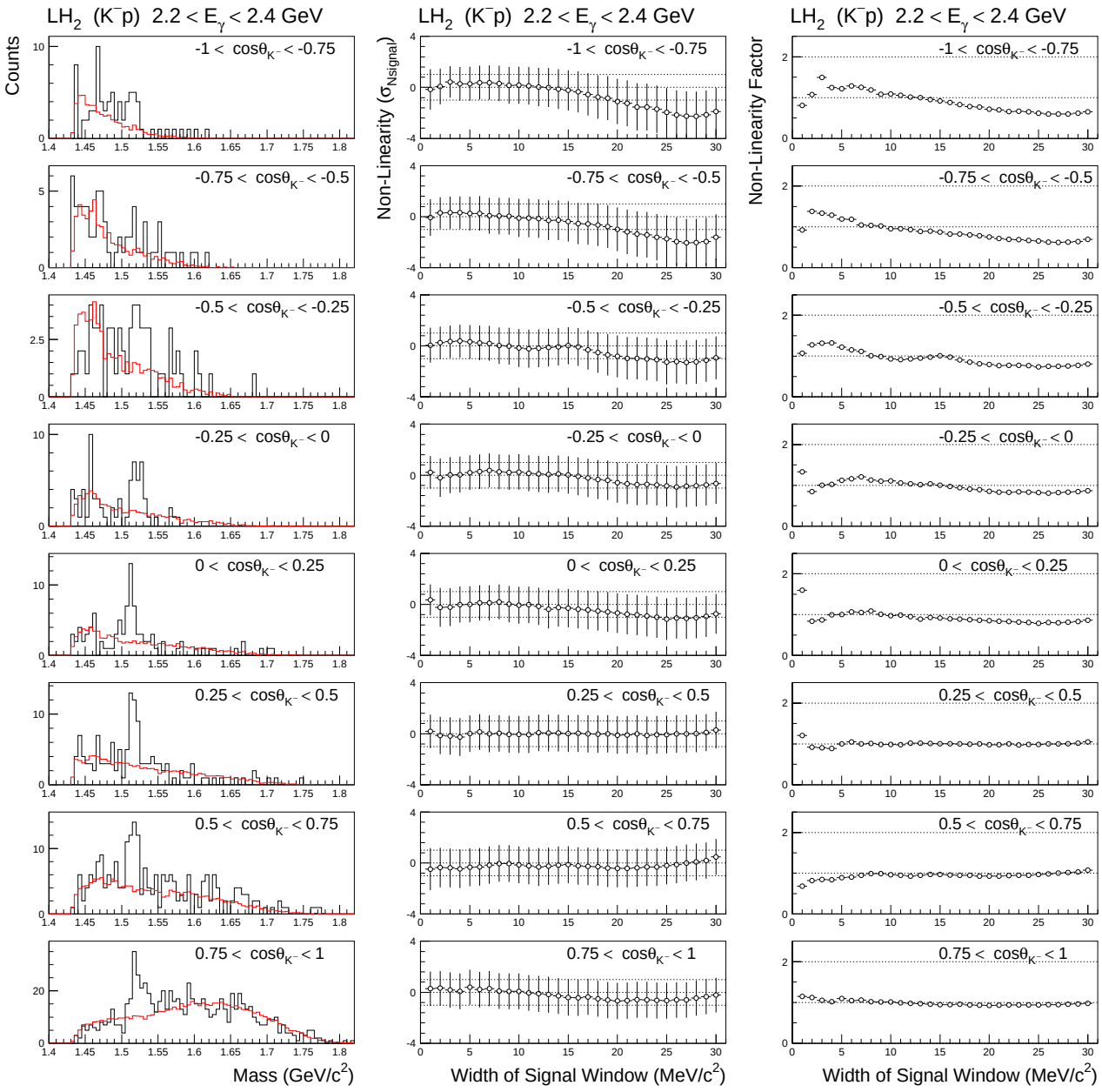

Figure B.3: Background non-linearity studies in different K^- polar angle of $\Lambda(1520)$ helicity frame within photon energy of 2.2-2.4 GeV from K^-p detection mode of protons are shown in 3 columns respectively, including mass spectra of real data overlaid by sum of Monte Carlo simulated background components, background non-linearities and non-linearity correction factors.

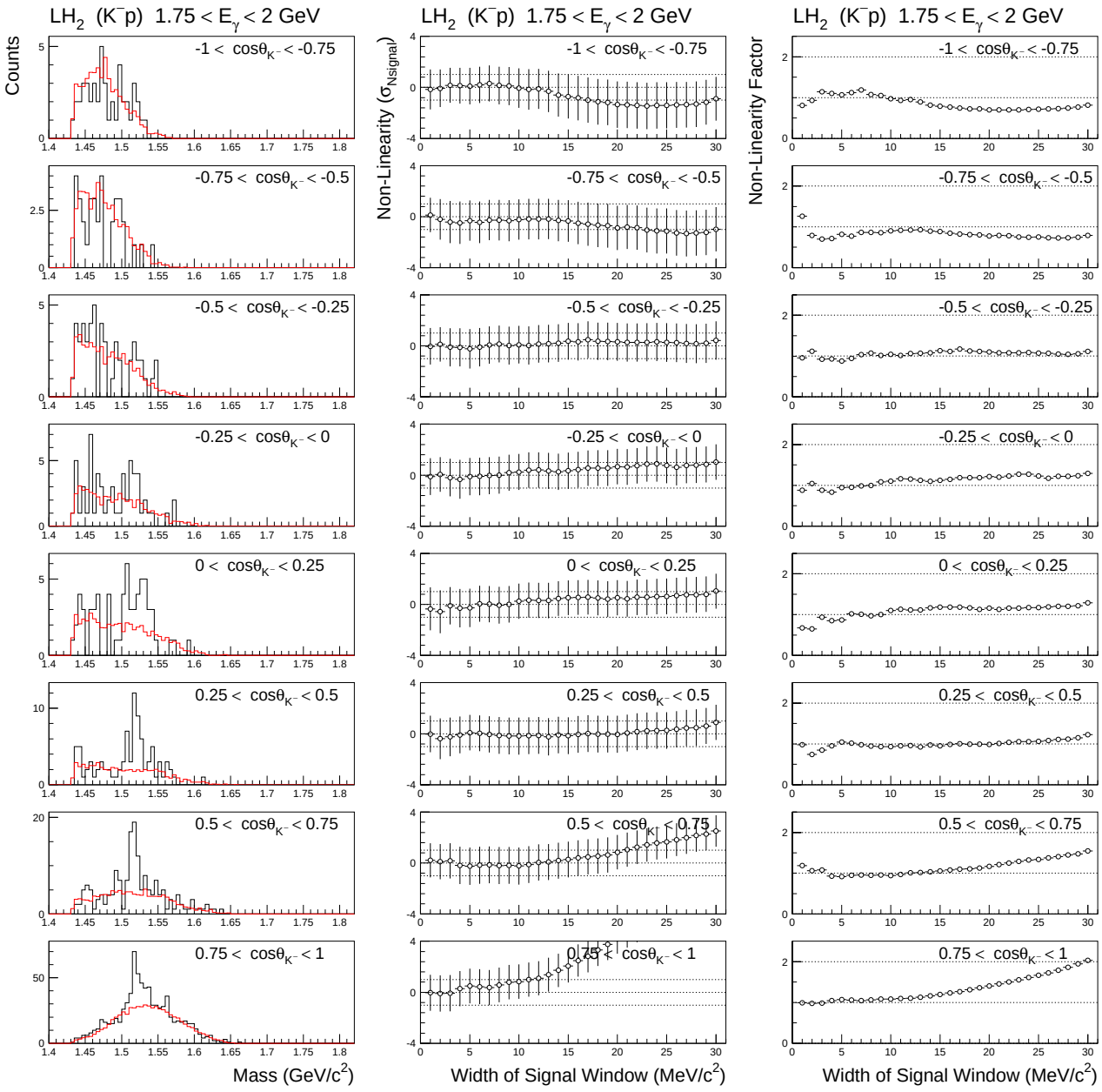

Figure B.4: Background non-linearity studies in different K^- polar angle of $\Lambda(1520)$ helicity frame within photon energy of 1.75-2.0 GeV from K^-p detection mode of protons are shown in 3 columns respectively, including mass spectra of real data overlaid by sum of Monte Carlo simulated background components, background non-linearities and non-linearity correction factors.

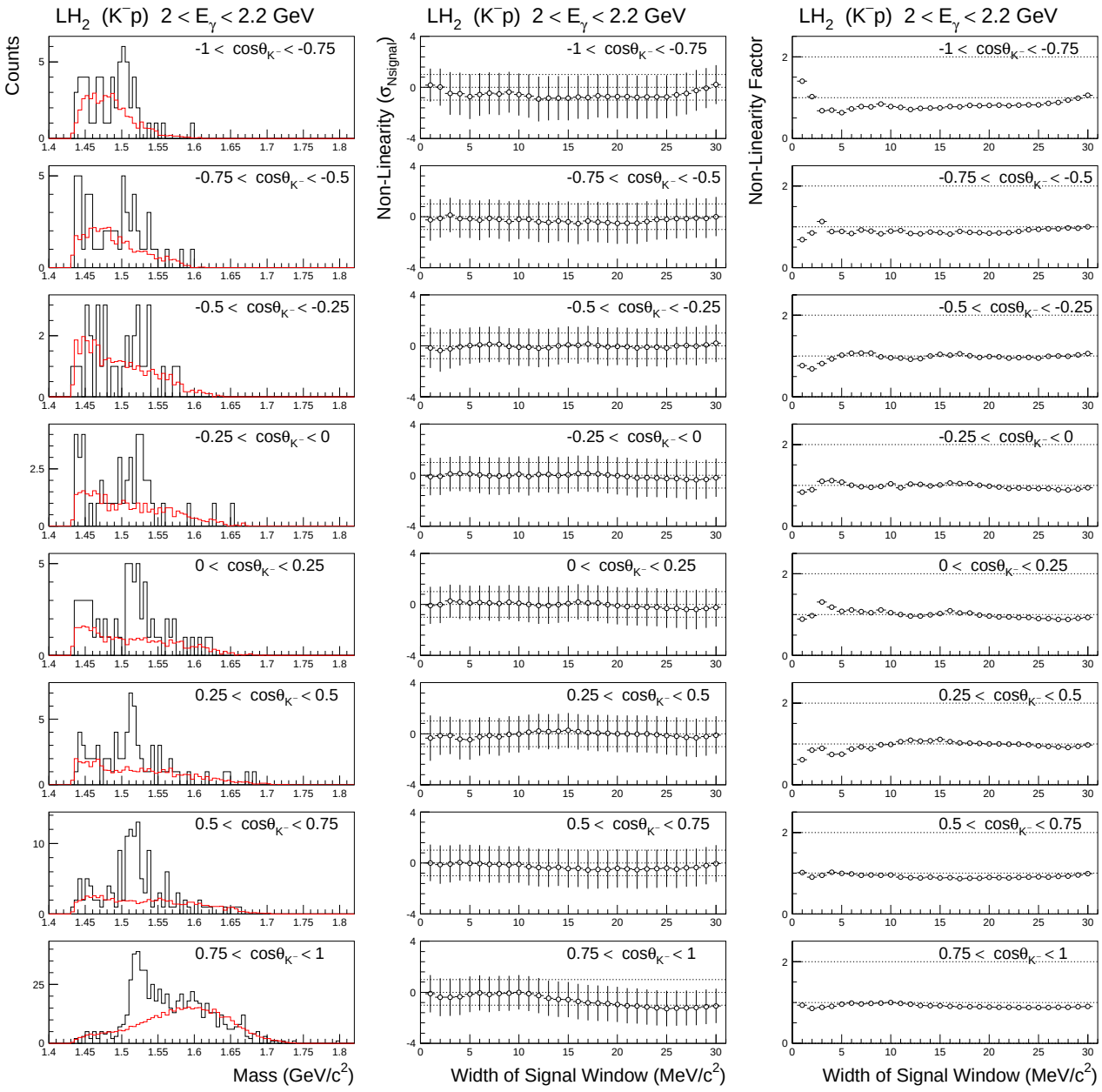

Figure B.5: Background non-linearity studies in different K^- polar angle of $\Lambda(1520)$ helicity frame within photon energy of 2.0-2.2 GeV from K^-p detection mode of protons are shown in 3 columns respectively, including mass spectra of real data overlaid by sum of Monte Carlo simulated background components, background non-linearities and non-linearity correction factors.

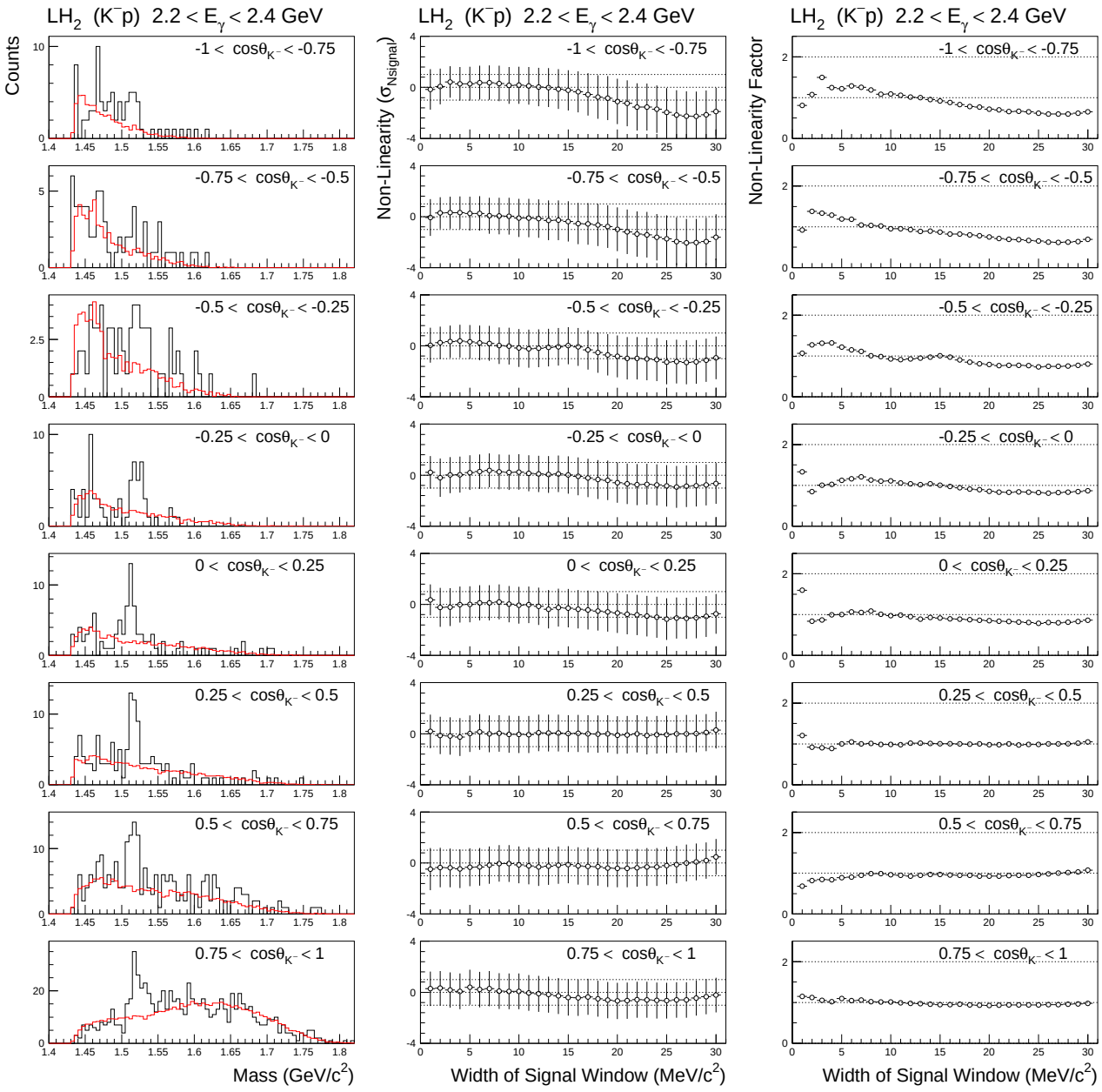

Figure B.6: Background non-linearity studies in different K^- polar angle of $\Lambda(1520)$ helicity frame within photon energy of 2.2-2.4 GeV from K^-p detection mode of protons are shown in 3 columns respectively, including mass spectra of real data overlaid by sum of Monte Carlo simulated background components, background non-linearities and non-linearity correction factors.

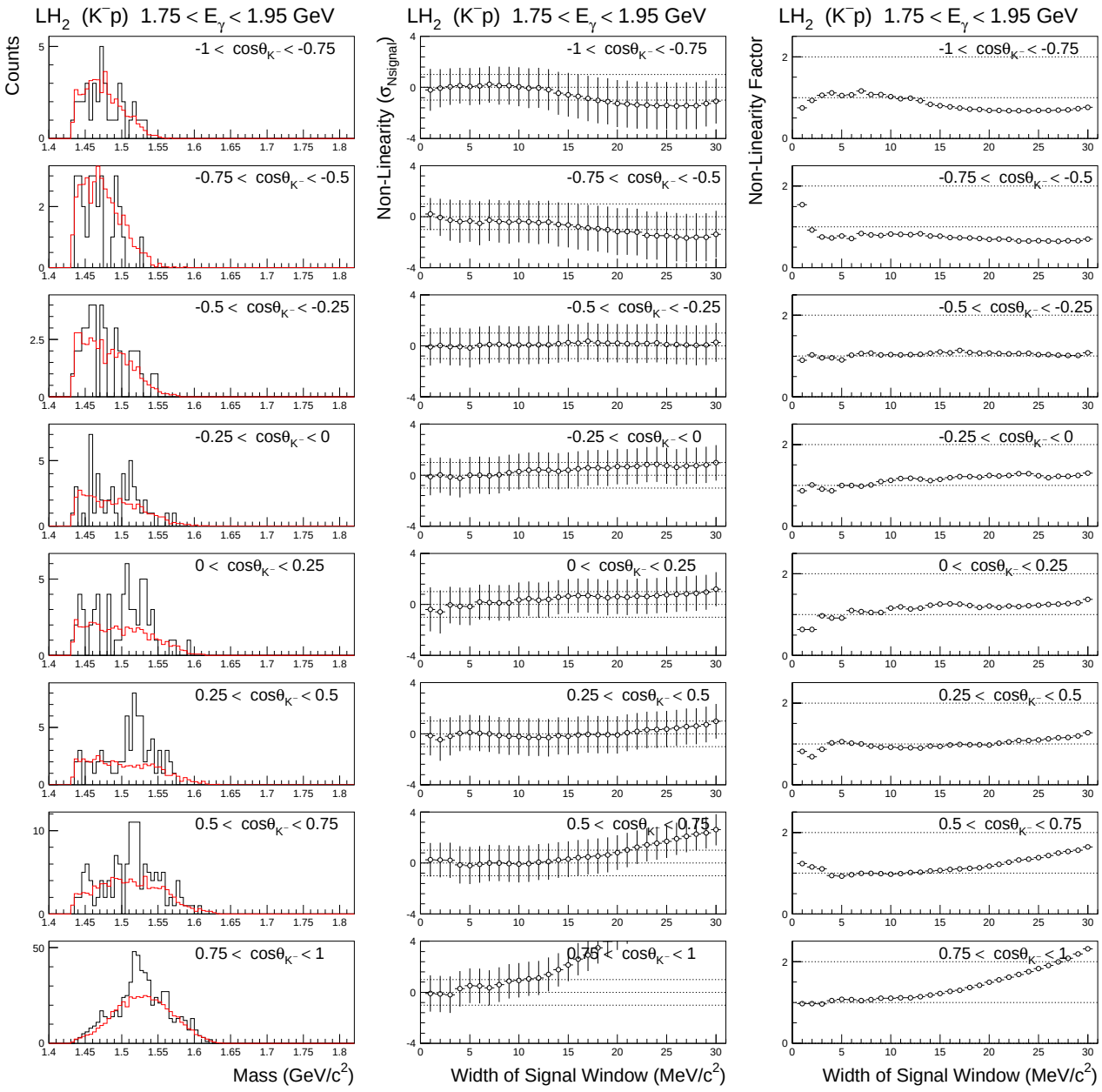

Figure B.7: Background non-linearity studies in different K^- polar angle of $\Lambda(1520)$ helicity frame within photon energy of 1.75-1.95 GeV from K^-p detection mode of protons are shown in 3 columns respectively, including mass spectra of real data overlaid by sum of Monte Carlo simulated background components, background non-linearities and non-linearity correction factors.

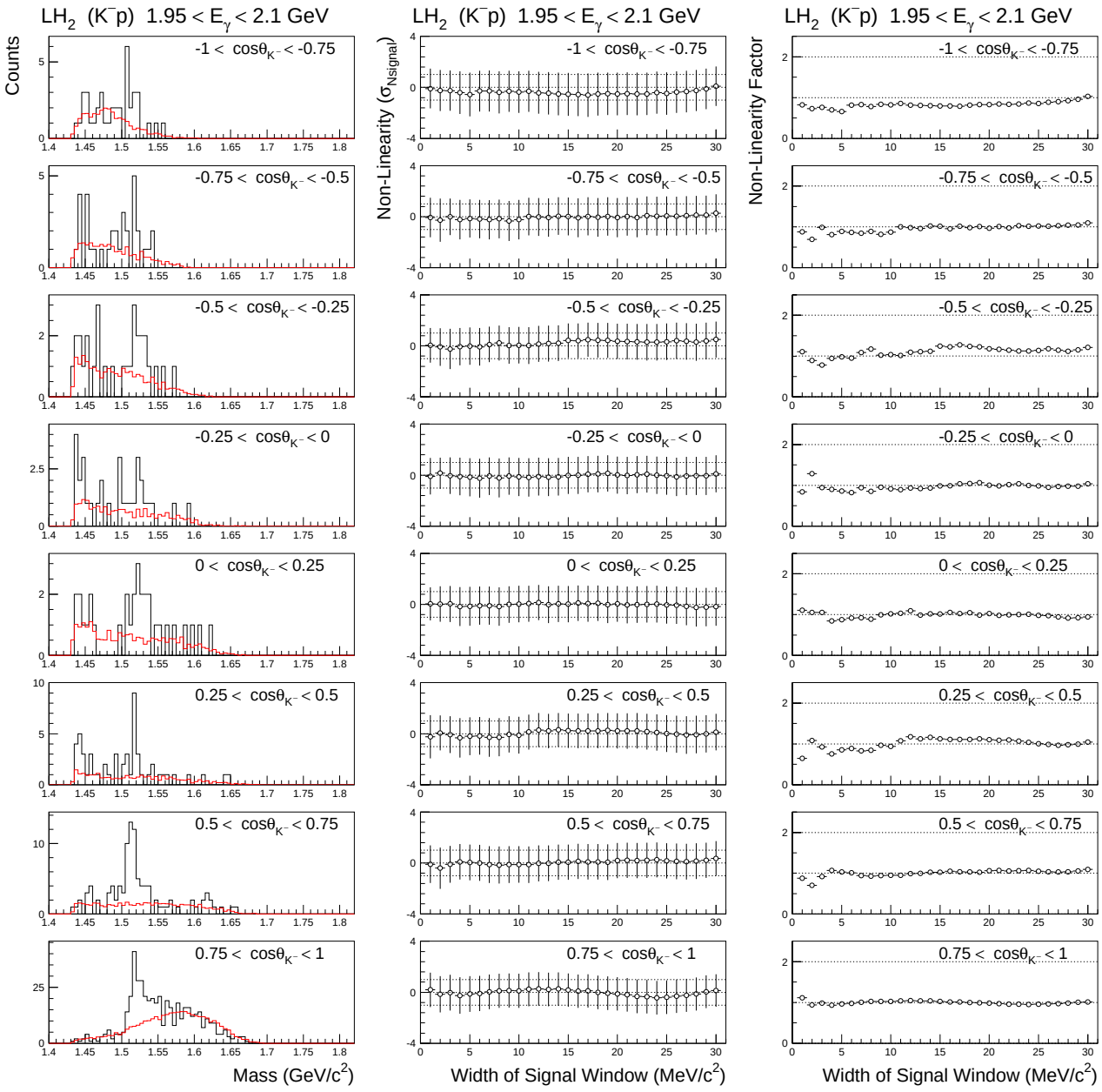

Figure B.8: Background non-linearity studies in different K^- polar angle of $\Lambda(1520)$ helicity frame within photon energy of 1.95-2.1 GeV from K^-p detection mode of protons are shown in 3 columns respectively, including mass spectra of real data overlaid by sum of Monte Carlo simulated background components, background non-linearities and non-linearity correction factors.

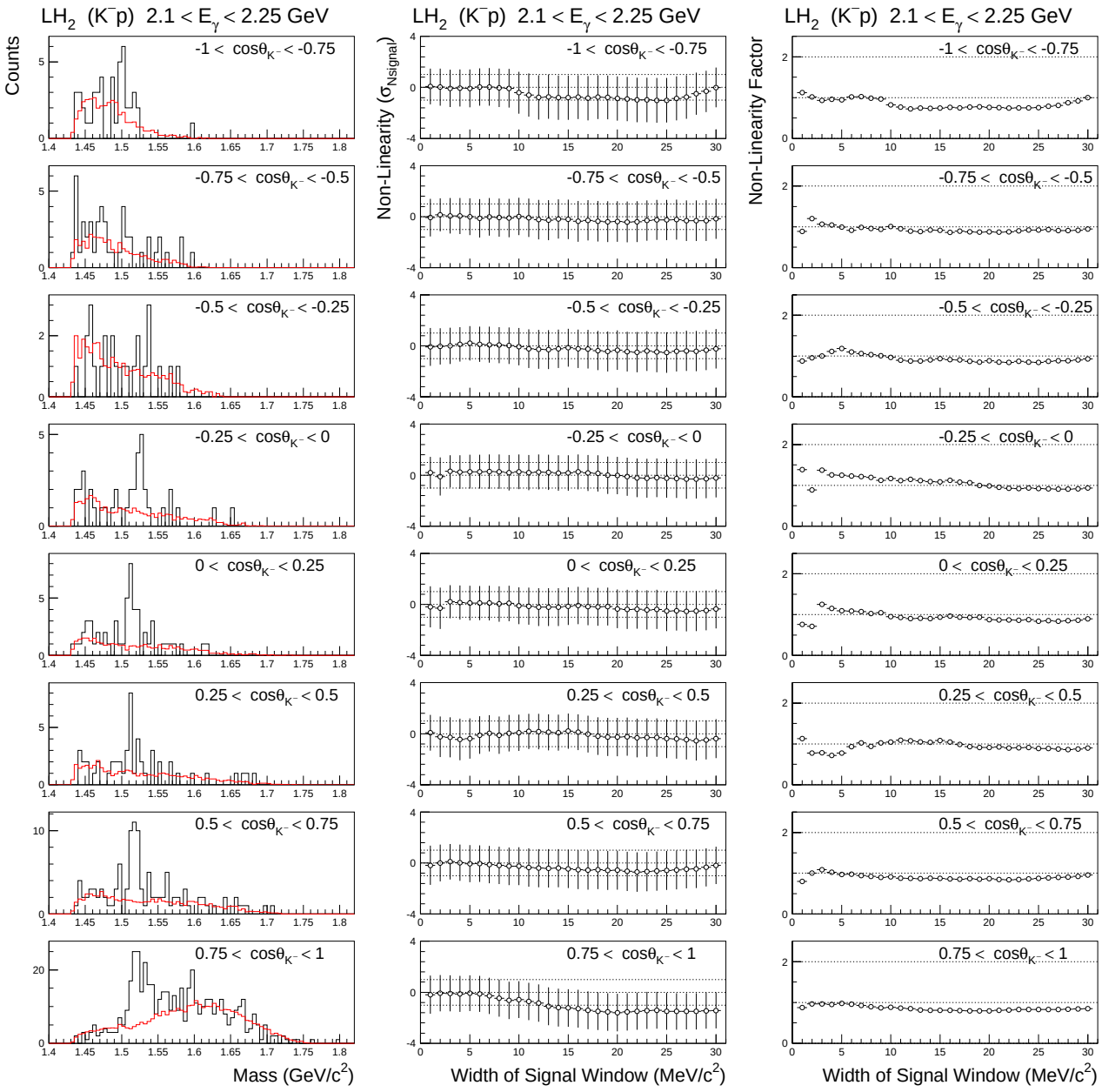

Figure B.9: Background non-linearity studies in different K^- polar angle of $\Lambda(1520)$ helicity frame within photon energy of 2.1-2.25 GeV from K^-p detection mode of protons are shown in 3 columns respectively, including mass spectra of real data overlaid by sum of Monte Carlo simulated background components, background non-linearities and non-linearity correction factors.

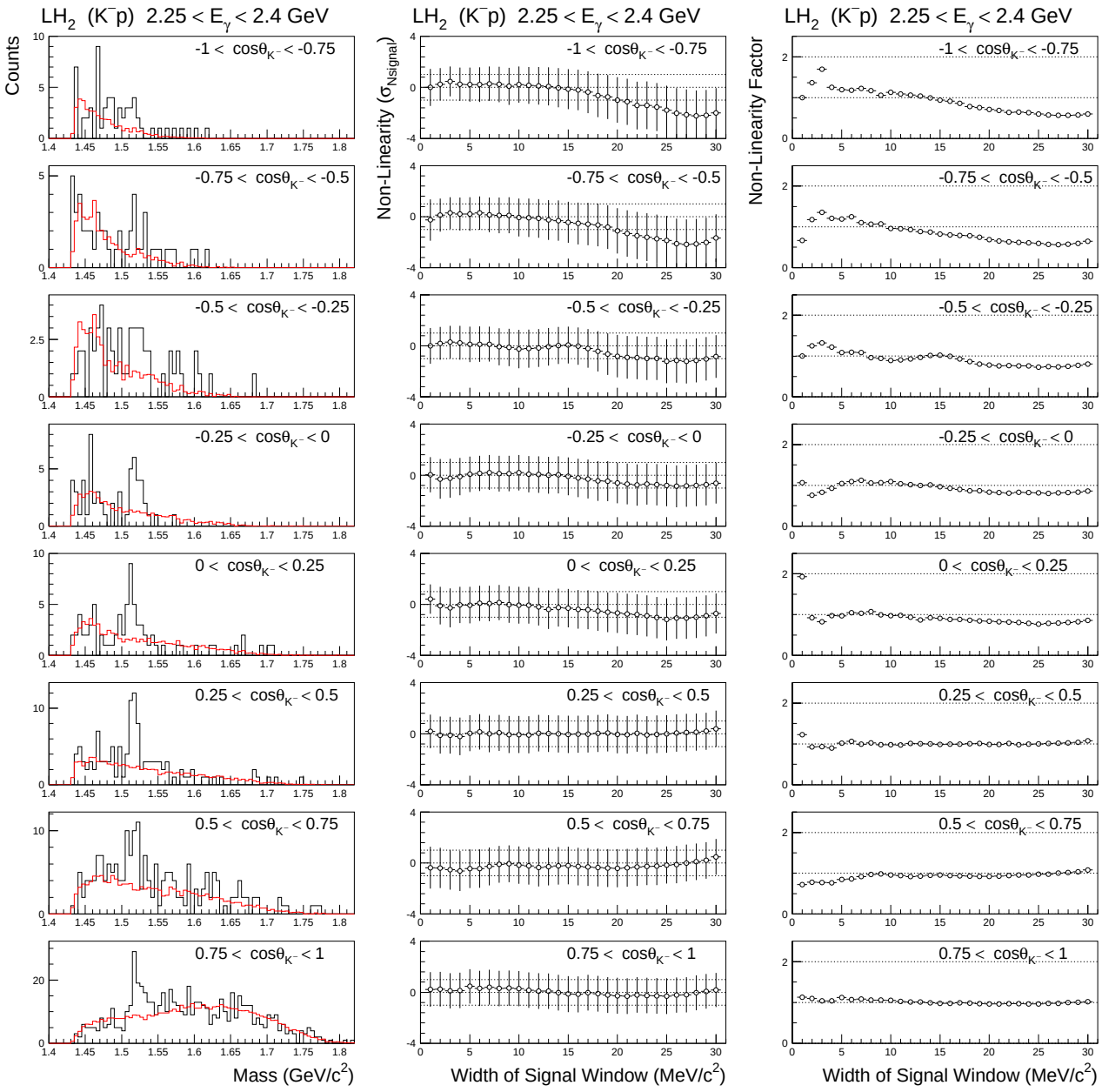

Figure B.10: Background non-linearity studies in different K^- polar angle of $\Lambda(1520)$ helicity frame within photon energy of 2.25-2.4 GeV from K^-p detection mode of protons are shown in 3 columns respectively, including mass spectra of real data overlaid by sum of Monte Carlo simulated background components, background non-linearities and non-linearity correction factors.

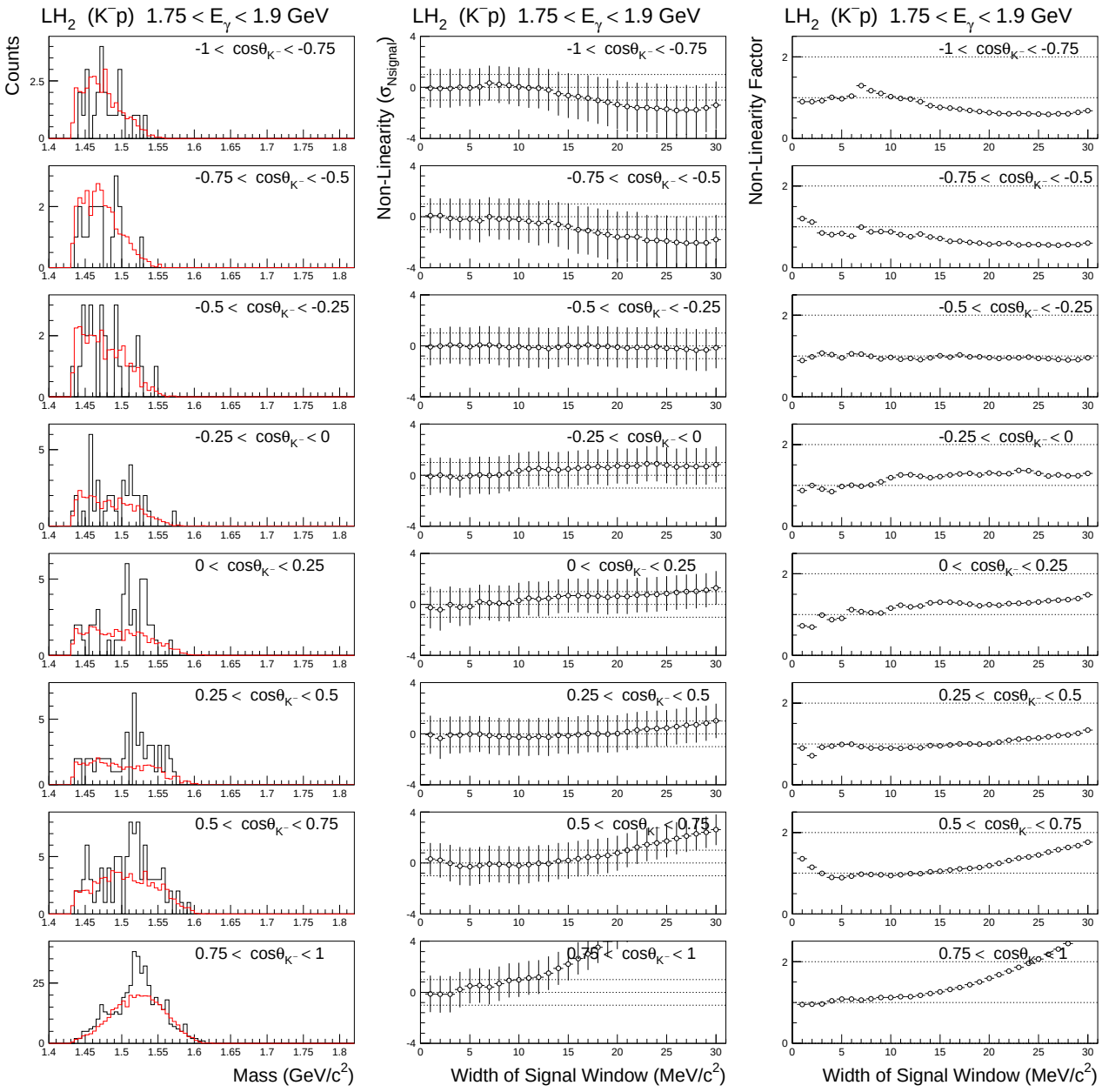

Figure B.11: Background non-linearity studies in different K^- polar angle of $\Lambda(1520)$ helicity frame within photon energy of 1.75-1.9 GeV from K^-p detection mode of protons are shown in 3 columns respectively, including mass spectra of real data overlaid by sum of Monte Carlo simulated background components, background non-linearities and non-linearity correction factors.

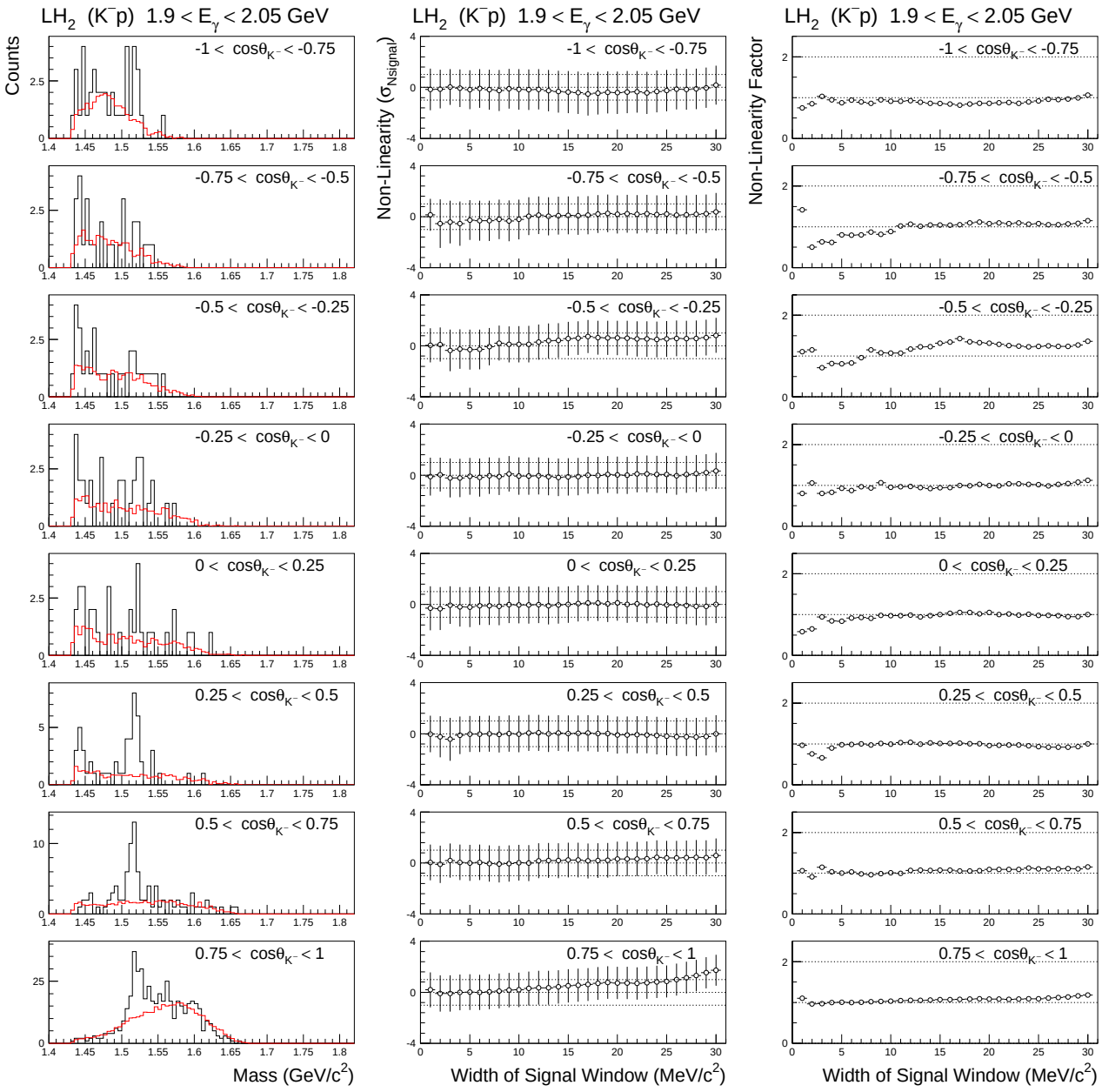

Figure B.12: Background non-linearity studies in different K^- polar angle of $\Lambda(1520)$ helicity frame within photon energy of 1.9-2.05 GeV from K^-p detection mode of protons are shown in 3 columns respectively, including mass spectra of real data overlaid by sum of Monte Carlo simulated background components, background non-linearities and non-linearity correction factors.

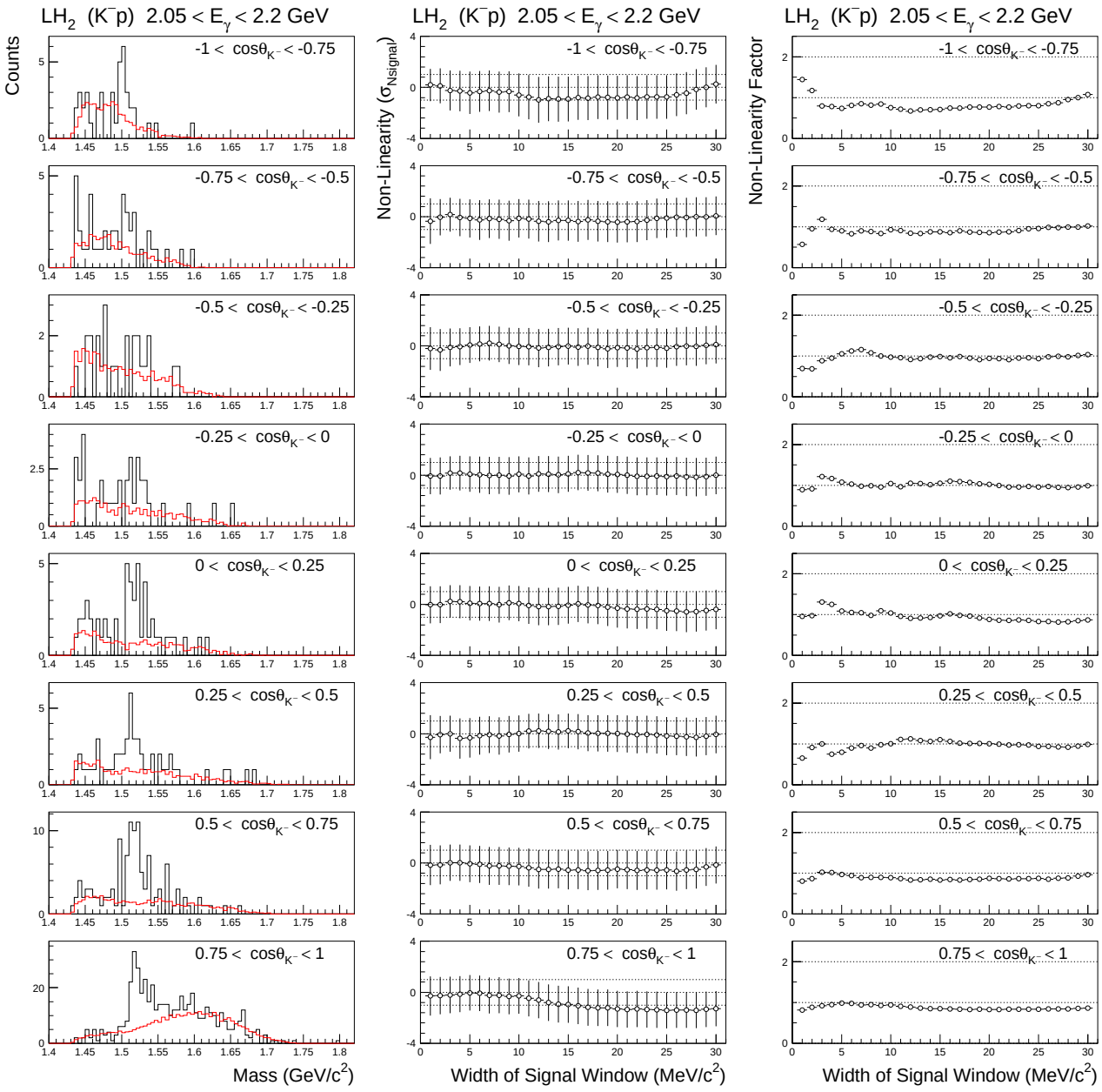

Figure B.13: Background non-linearity studies in different K^- polar angle of $\Lambda(1520)$ helicity frame within photon energy of 2.05-2.2 GeV from K^-p detection mode of protons are shown in 3 columns respectively, including mass spectra of real data overlaid by sum of Monte Carlo simulated background components, background non-linearities and non-linearity correction factors.

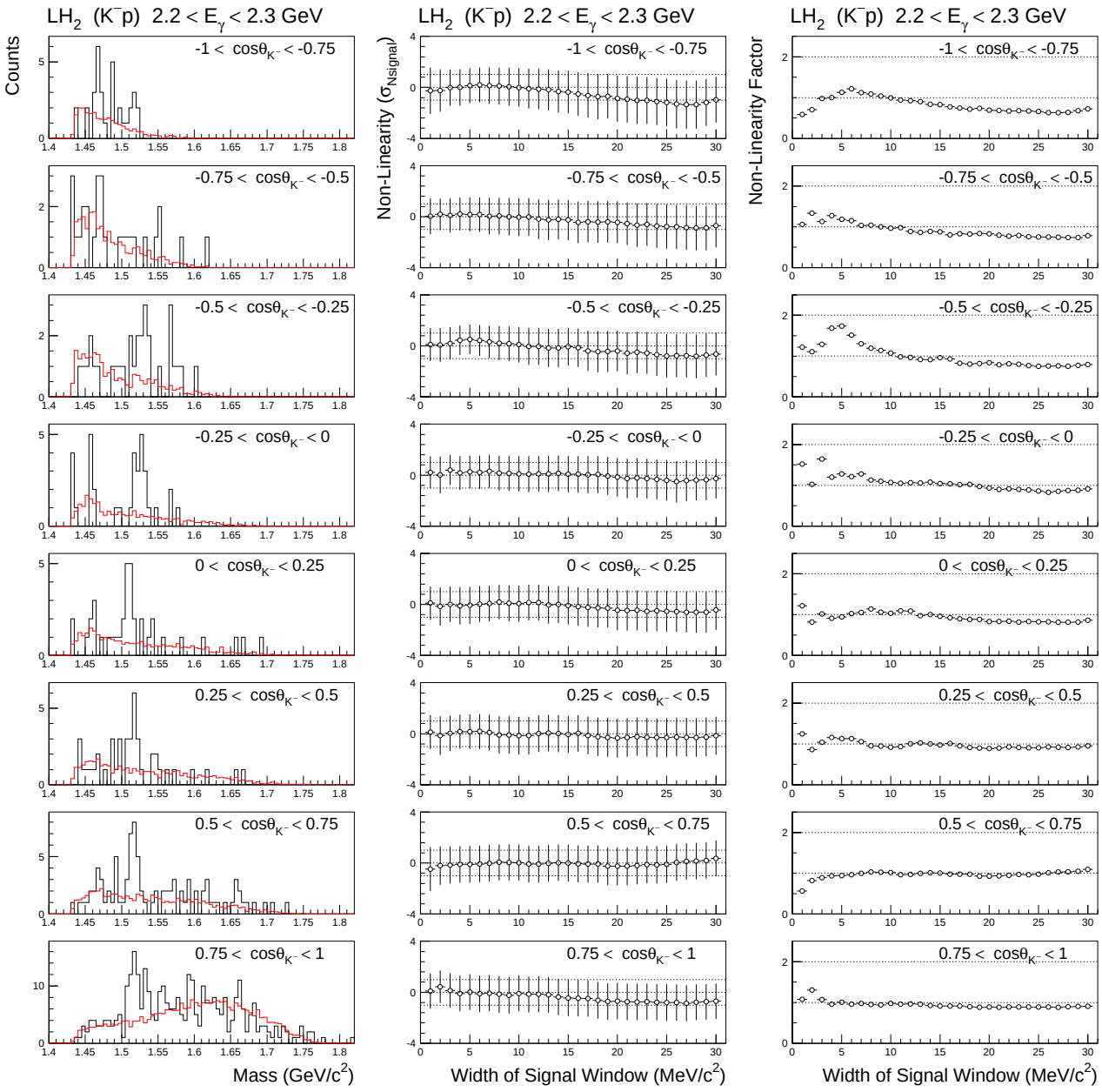

Figure B.14: Background non-linearity studies in different K^- polar angle of $\Lambda(1520)$ helicity frame within photon energy of 2.2-2.3 GeV from K^-p detection mode of protons are shown in 3 columns respectively, including mass spectra of real data overlaid by sum of Monte Carlo simulated background components, background non-linearities and non-linearity correction factors.

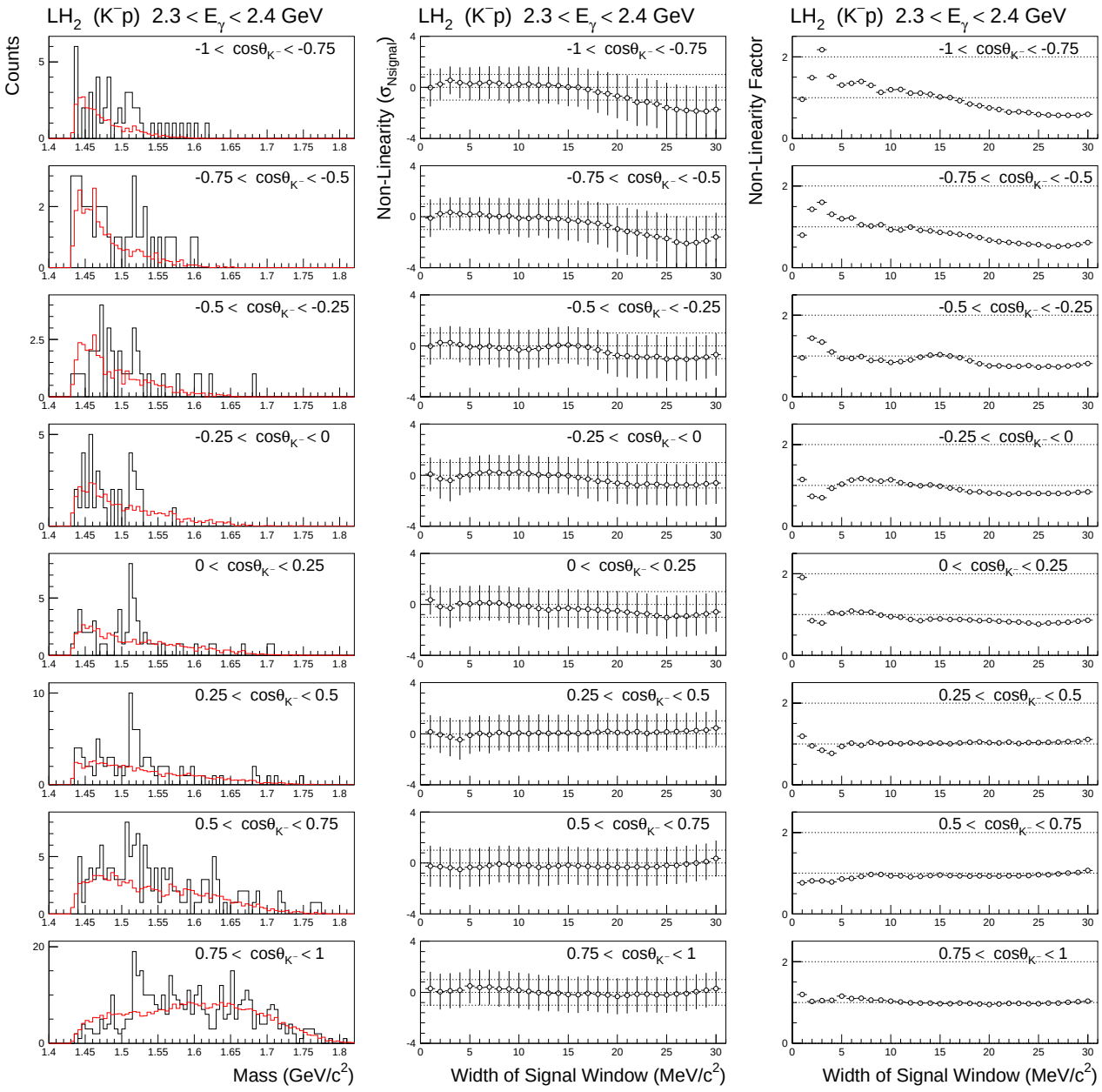

Figure B.15: Background non-linearity studies in different K^- polar angle of $\Lambda(1520)$ helicity frame within photon energy of 2.3-2.4 GeV from K^-p detection mode of protons are shown in 3 columns respectively, including mass spectra of real data overlaid by sum of Monte Carlo simulated background components, background non-linearities and non-linearity correction factors.

B.1.2 K^- polar angle distribution in $\Lambda(1520)$ t-channel helicity frame

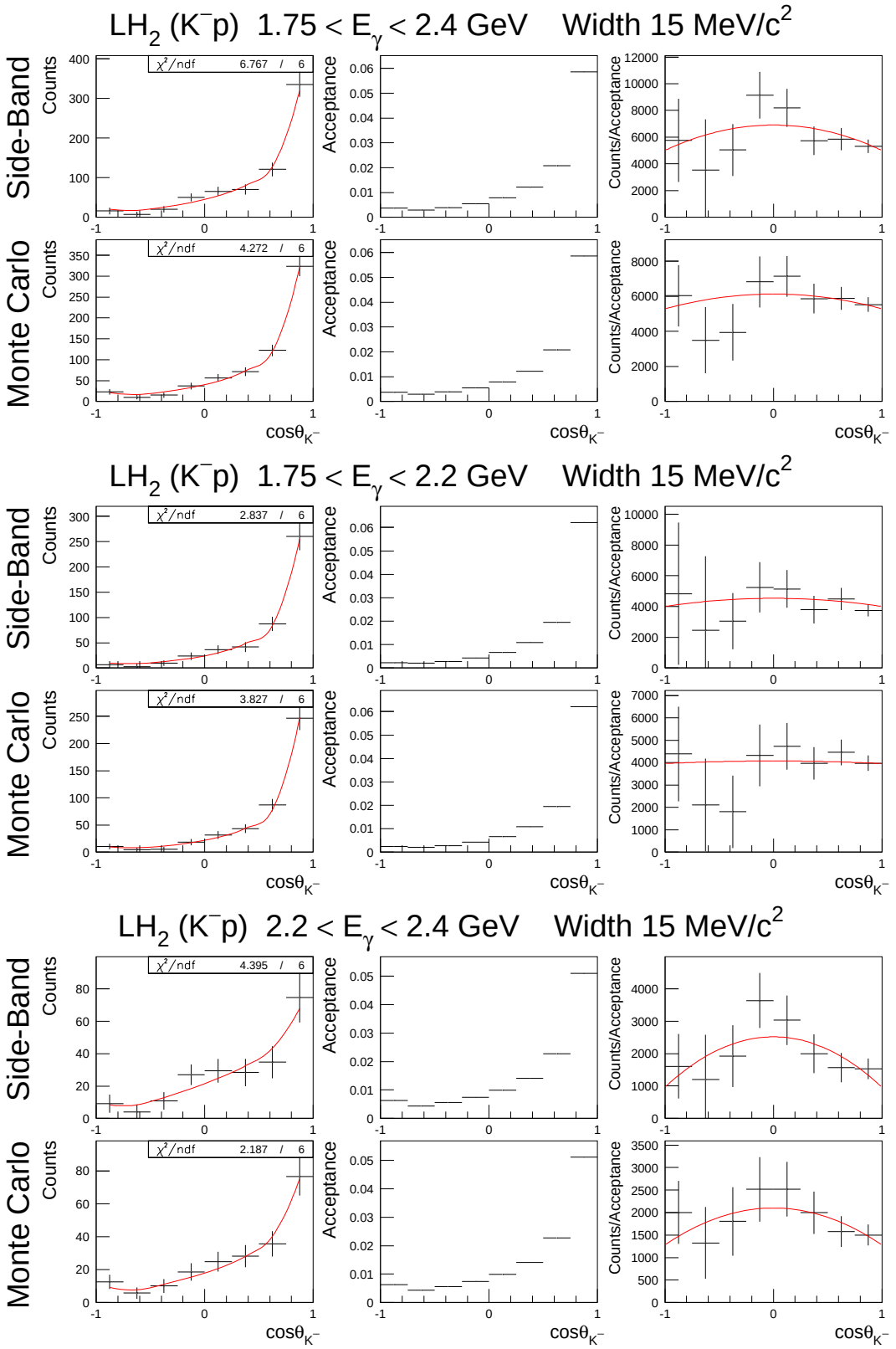

Figure B.16: K^- polar angle distribution in $\Lambda(1520)$ t-channel helicity frame from protons in K^-p detection mode were shown in photon energy of 1.75-2.4, 1.75-2.2 and 2.2-2.4 GeV with 15-MeV/c^2 signal-window width by side-band subtraction and Monte Carlo methods.

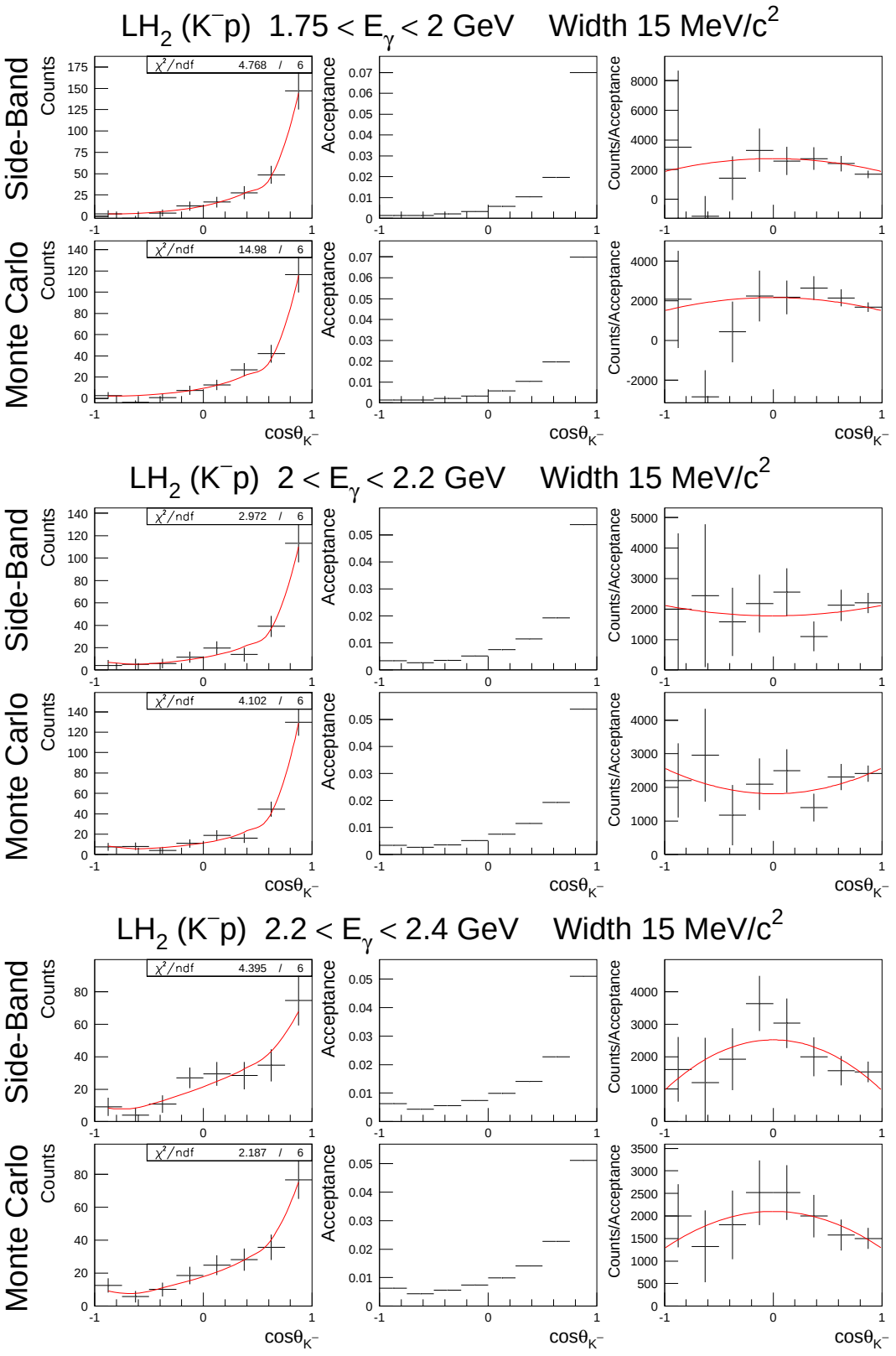

Figure B.17: K^- polar angle distribution in $\Lambda(1520)$ t-channel helicity frame from protons in K^-p detection mode were shown in photon energy of 1.75-2.0, 2.0-2.2 and 2.2-2.4 GeV with 15-MeV/c^2 signal-window width by side-band subtraction and Monte Carlo methods.

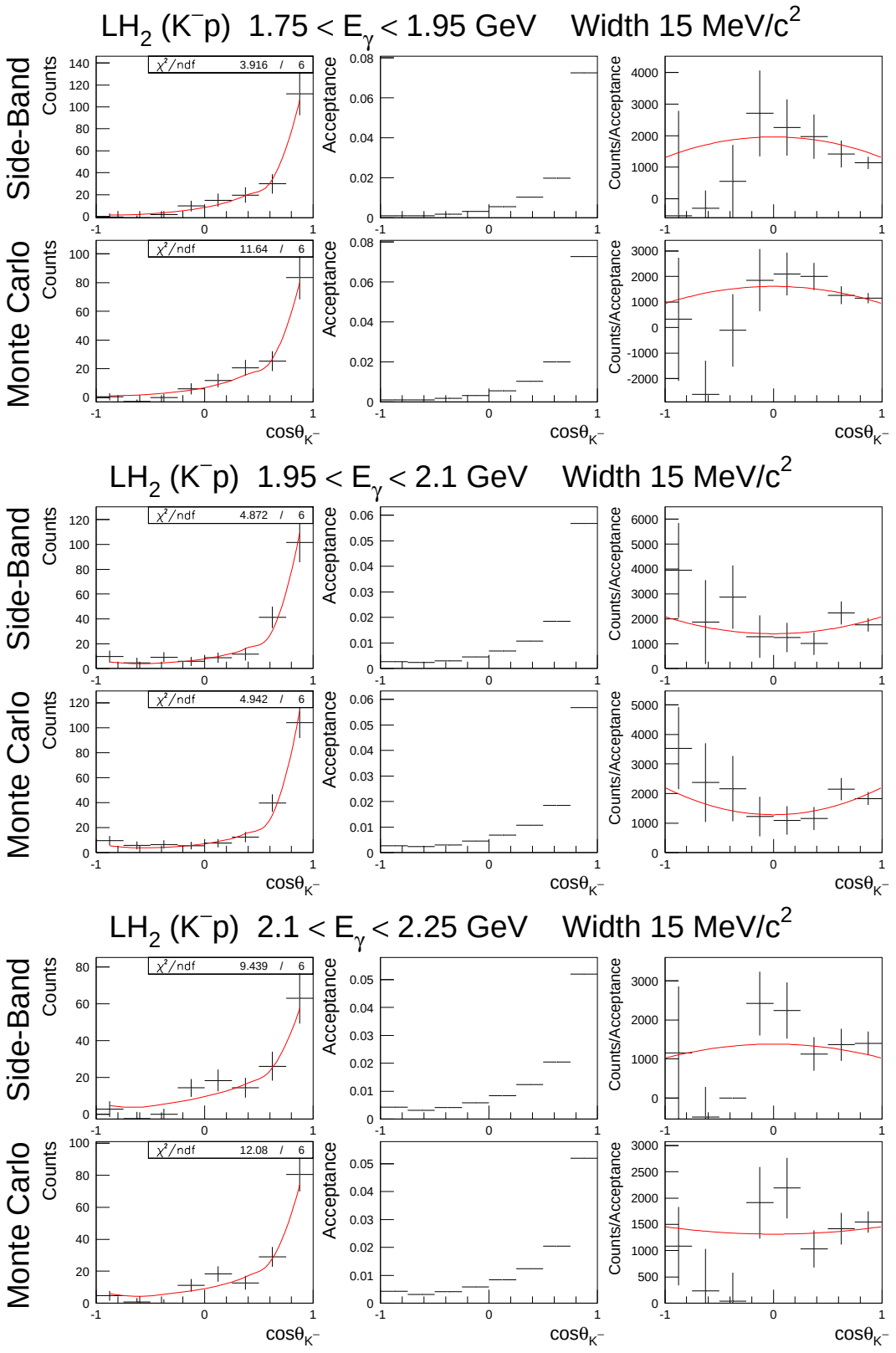

Figure B.18: K^- polar angle distribution in $\Lambda(1520)$ t-channel helicity frame from protons in K^-p detection mode were shown in photon energy of 1.75-1.95, 1.95-2.1 and 2.1-2.25 GeV with 15-MeV/c^2 signal-window width by side-band subtraction and Monte Carlo methods.

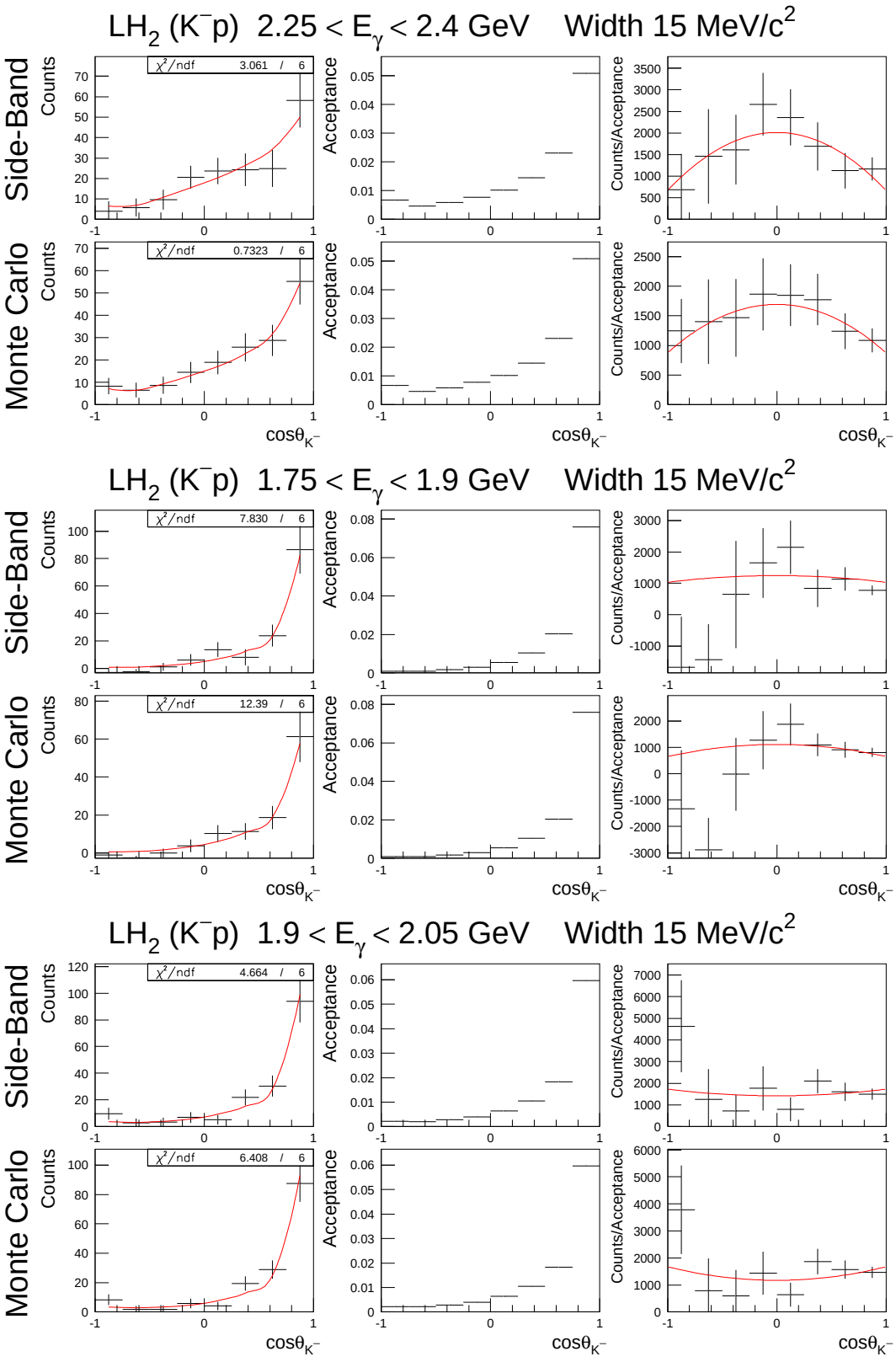

Figure B.19: K^- polar angle distribution in $\Lambda(1520)$ t-channel helicity frame from protons in K^-p detection mode were shown in photon energy of 2.25-2.4, 1.75-1.9 and 1.9-2.05 GeV with 15-MeV/c^2 signal-window width by side-band subtraction and Monte Carlo methods.

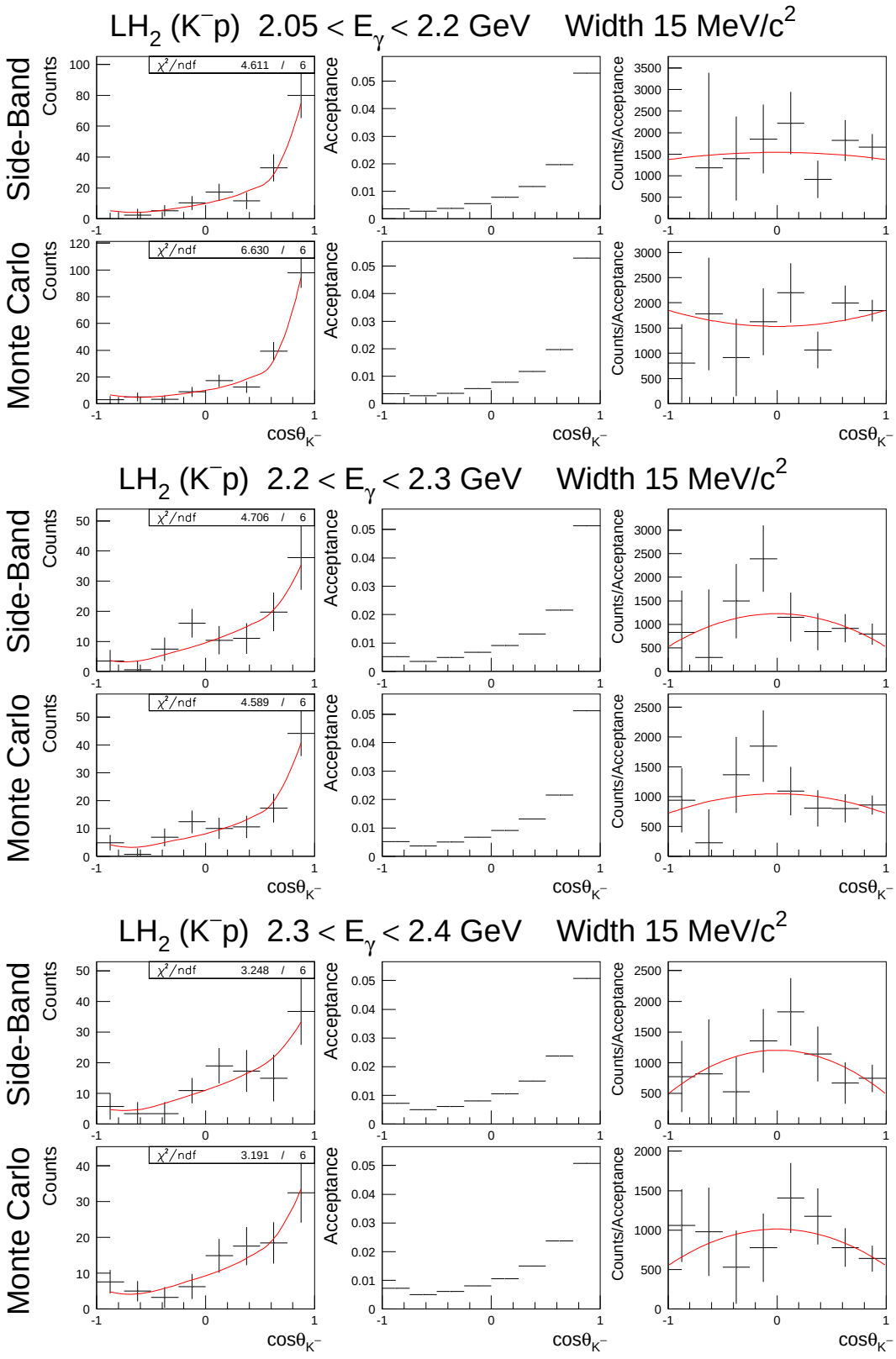

Figure B.20: K^- polar angle distribution in $\Lambda(1520)$ t-channel helicity frame from protons in K^-p detection mode were shown in photon energy of 2.05-2.2, 2.2-2.3 and 2.3-2.4 GeV with 15-MeV/c^2 signal-window width by side-band subtraction and Monte Carlo methods.

B.1.3 Signal-window width dependence of fraction of helicity-3/2

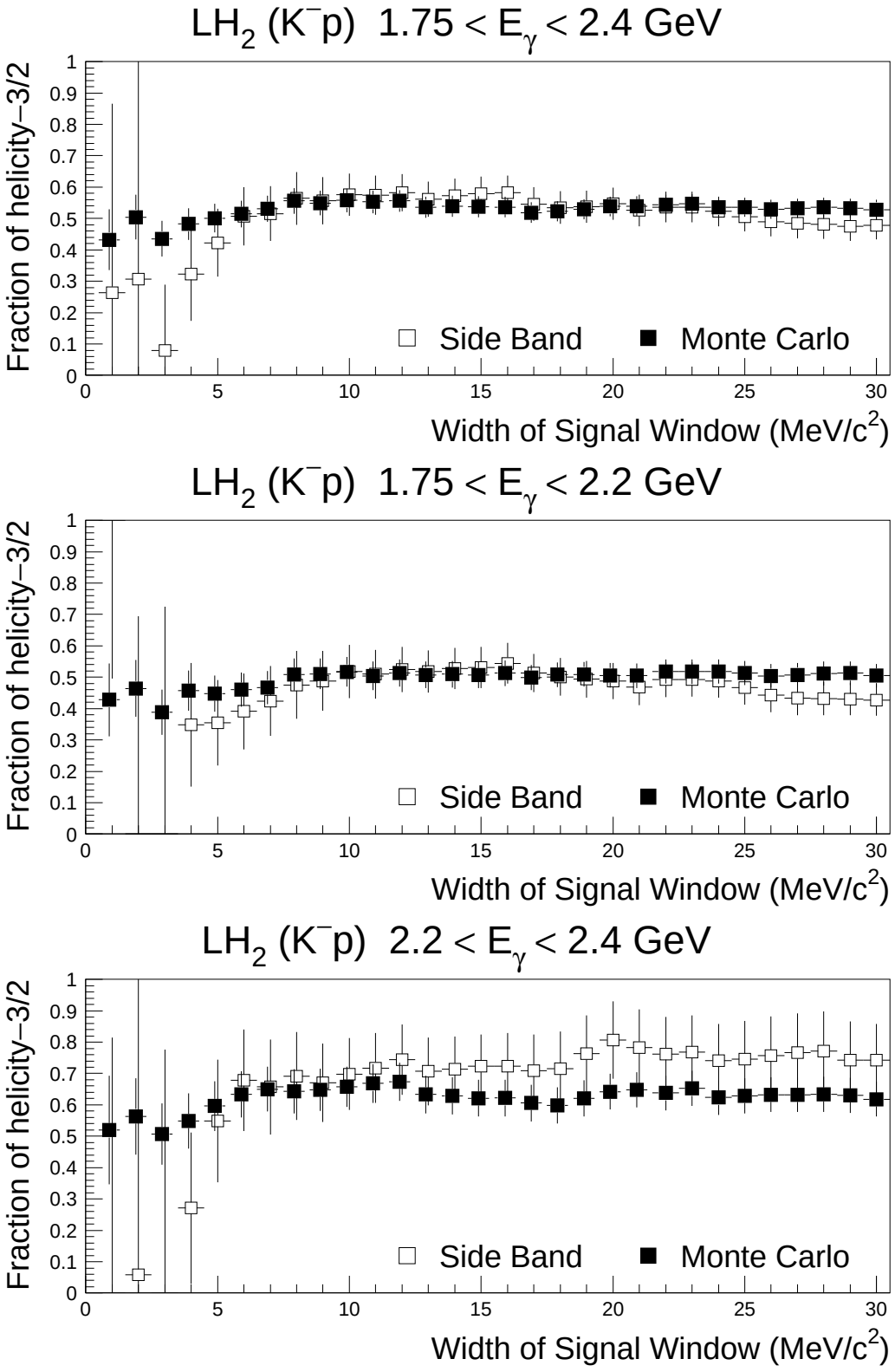

Figure B.21: Signal-window width dependence of fraction of helicity-3/2 from protons in K^-p detection mode in photon energy of 1.75-2.4, 1.75-2.2, 2.2-2.4 GeV were shown from side-band subtraction and Monte Carlo methods respectively.

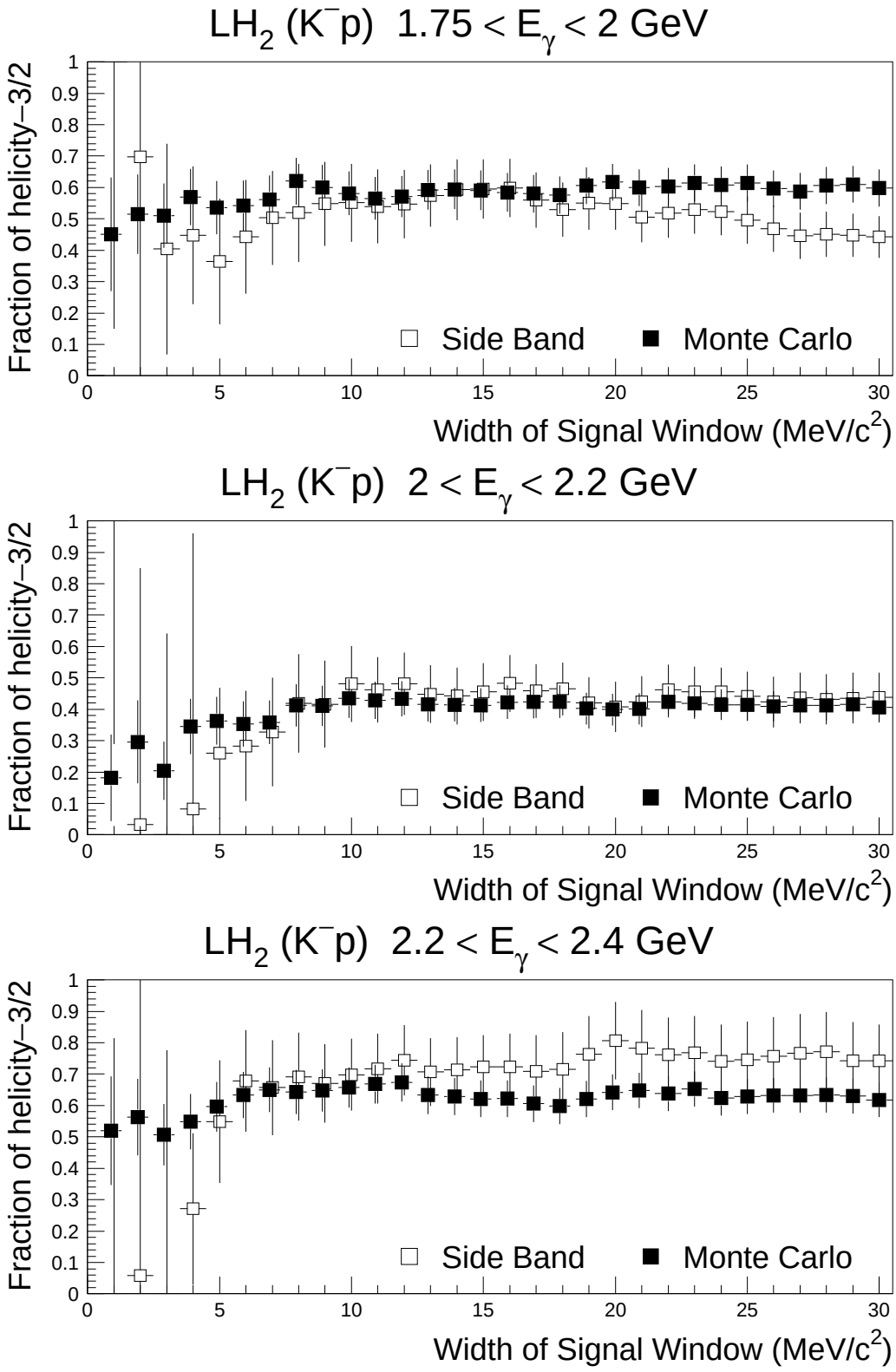

Figure B.22: Signal-window width dependence of fraction of helicity-3/2 from protons in K^-p detection mode in photon energy of 1.75-2.0, 2.0-2.2, 2.2-2.4 GeV were shown from side-band subtraction and Monte Carlo methods respectively.

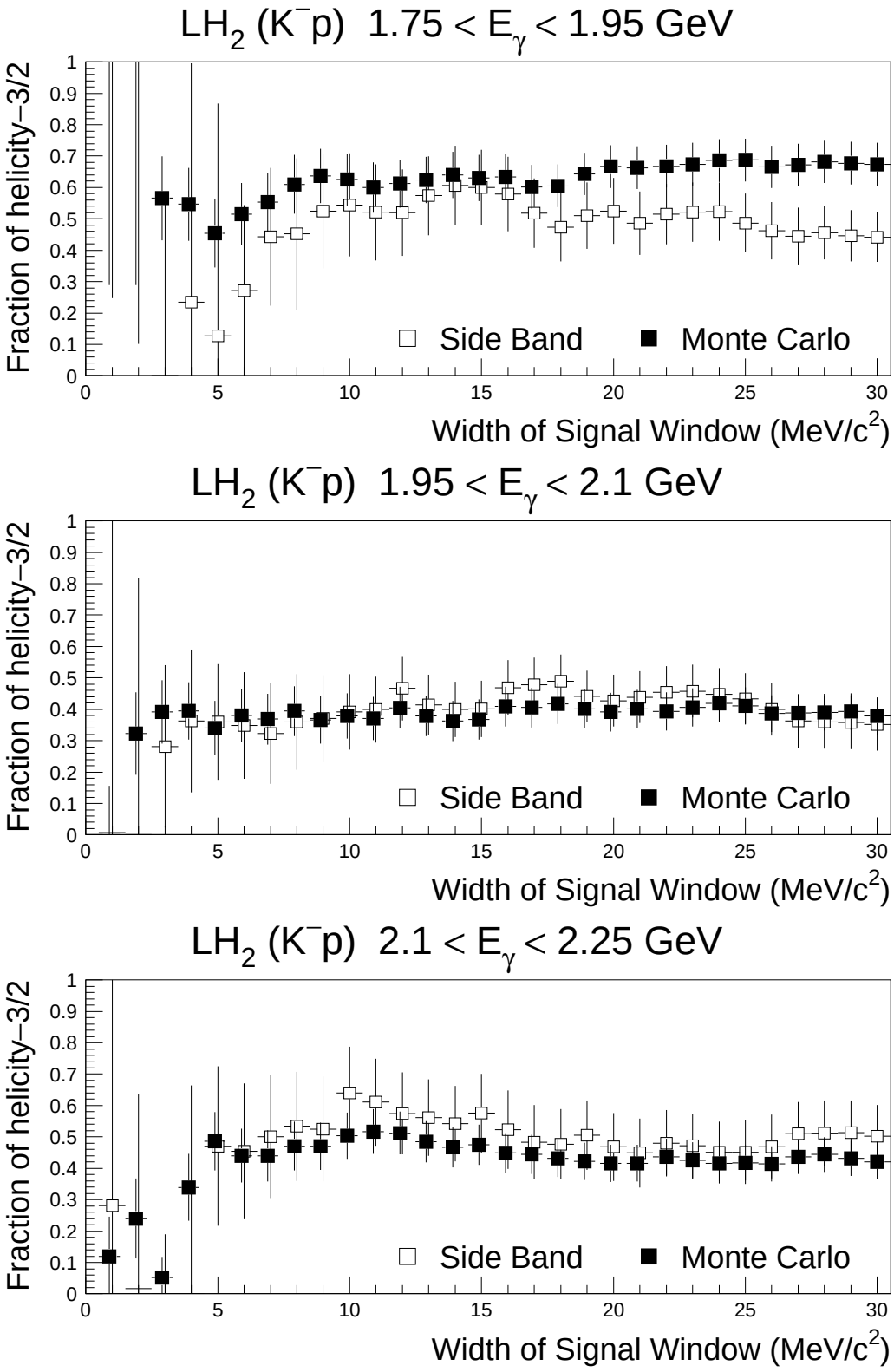

Figure B.23: Signal-window width dependence of fraction of helicity-3/2 from protons in K^-p detection mode in photon energy of 1.75-1.95, 1.95-2.1, 2.1-2.25 GeV were shown from side-band subtraction and Monte Carlo methods respectively.

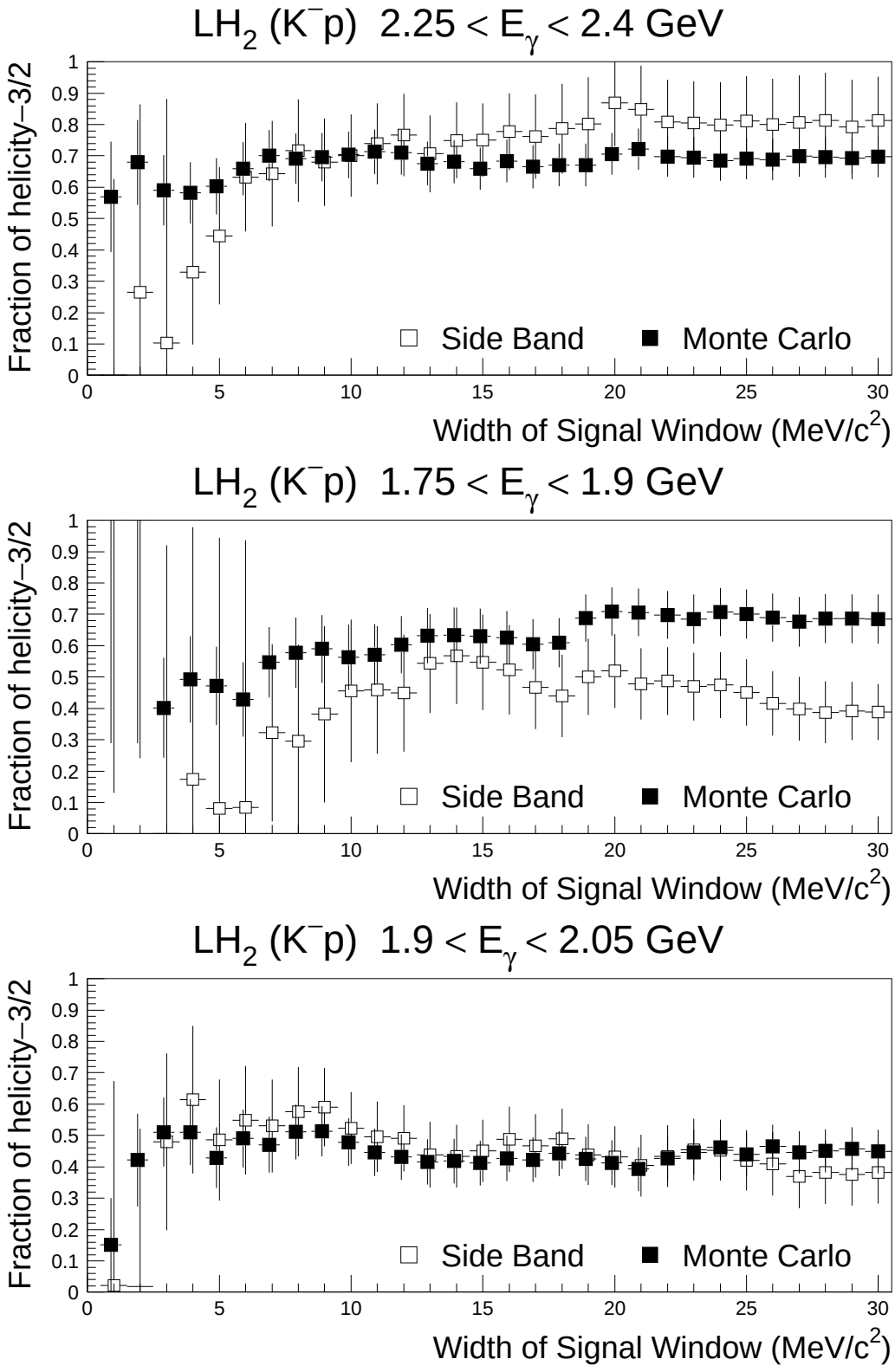

Figure B.24: Signal-window width dependence of fraction of helicity-3/2 from protons in K^-p detection mode in photon energy of 2.25-2.4, 1.75-1.9, 1.9-2.05 GeV were shown from side-band subtraction and Monte Carlo methods respectively.

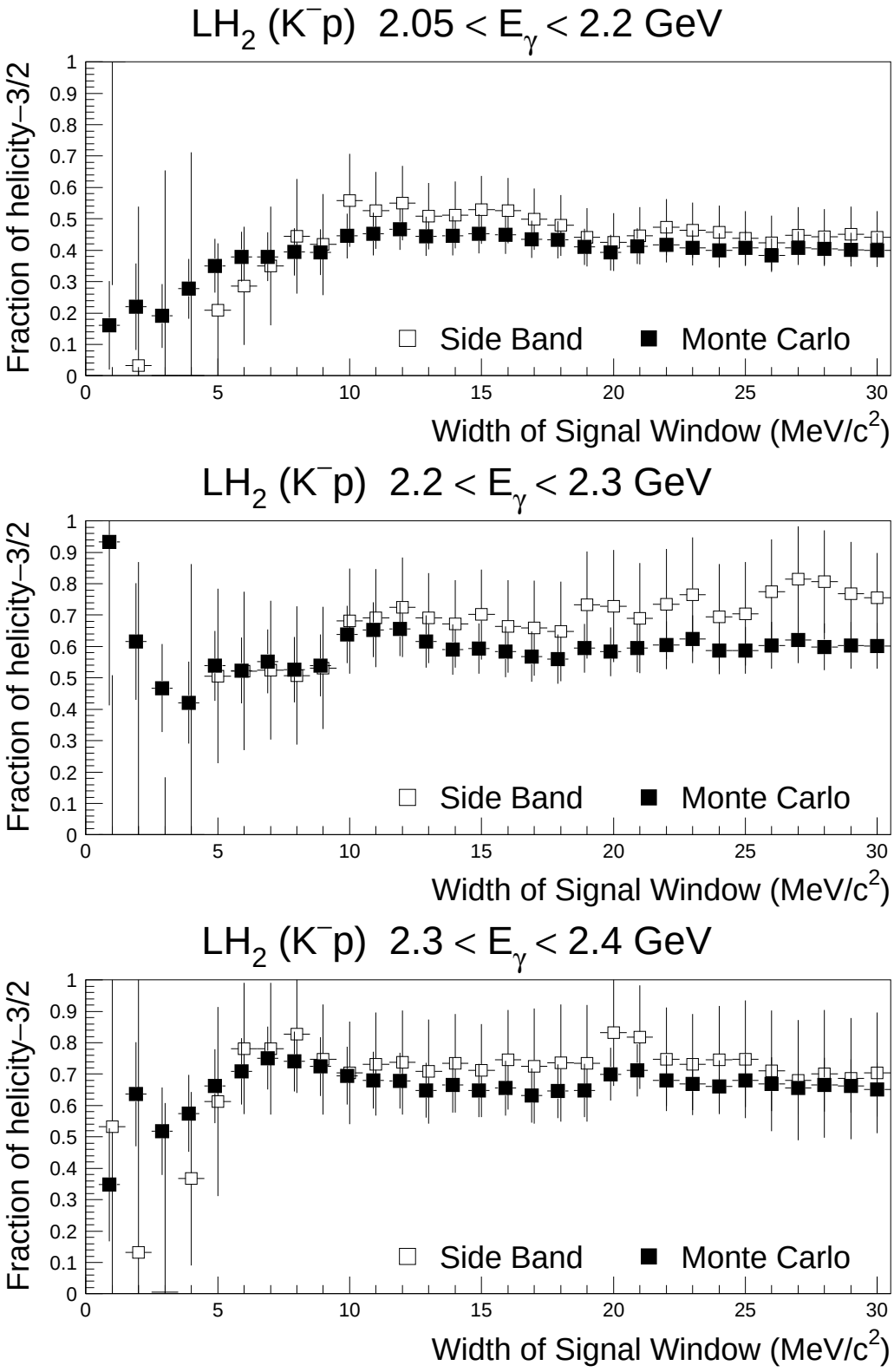

Figure B.25: Signal-window width dependence of fraction of helicity-3/2 from protons in K^-p detection mode in photon energy of 2.05-2.2, 2.2-2.3, 2.3-2.4 GeV were shown from side-band subtraction and Monte Carlo methods respectively.

B.2 K^+K^- detection mode from protons

B.2.1 Background non-linearity

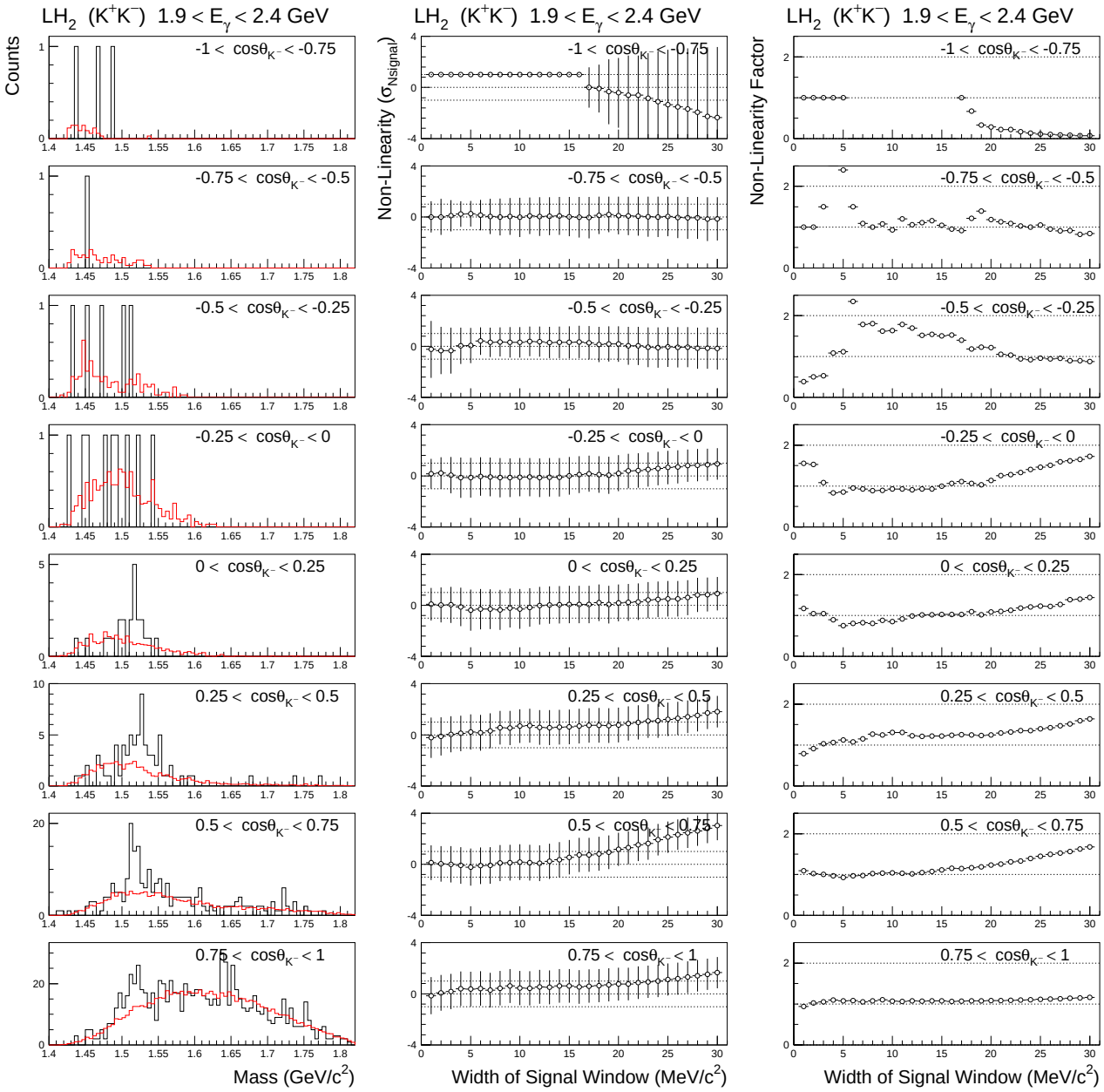

Figure B.26: Background non-linearity studies in different K^- polar angle of $\Lambda(1520)$ helicity frame within photon energy of 1.9-2.4 GeV from K^+K^- detection mode of protons are shown in 3 columns respectively, including mass spectra of real data overlaid by sum of Monte Carlo simulated background components, background non-linearities and non-linearity correction factors.

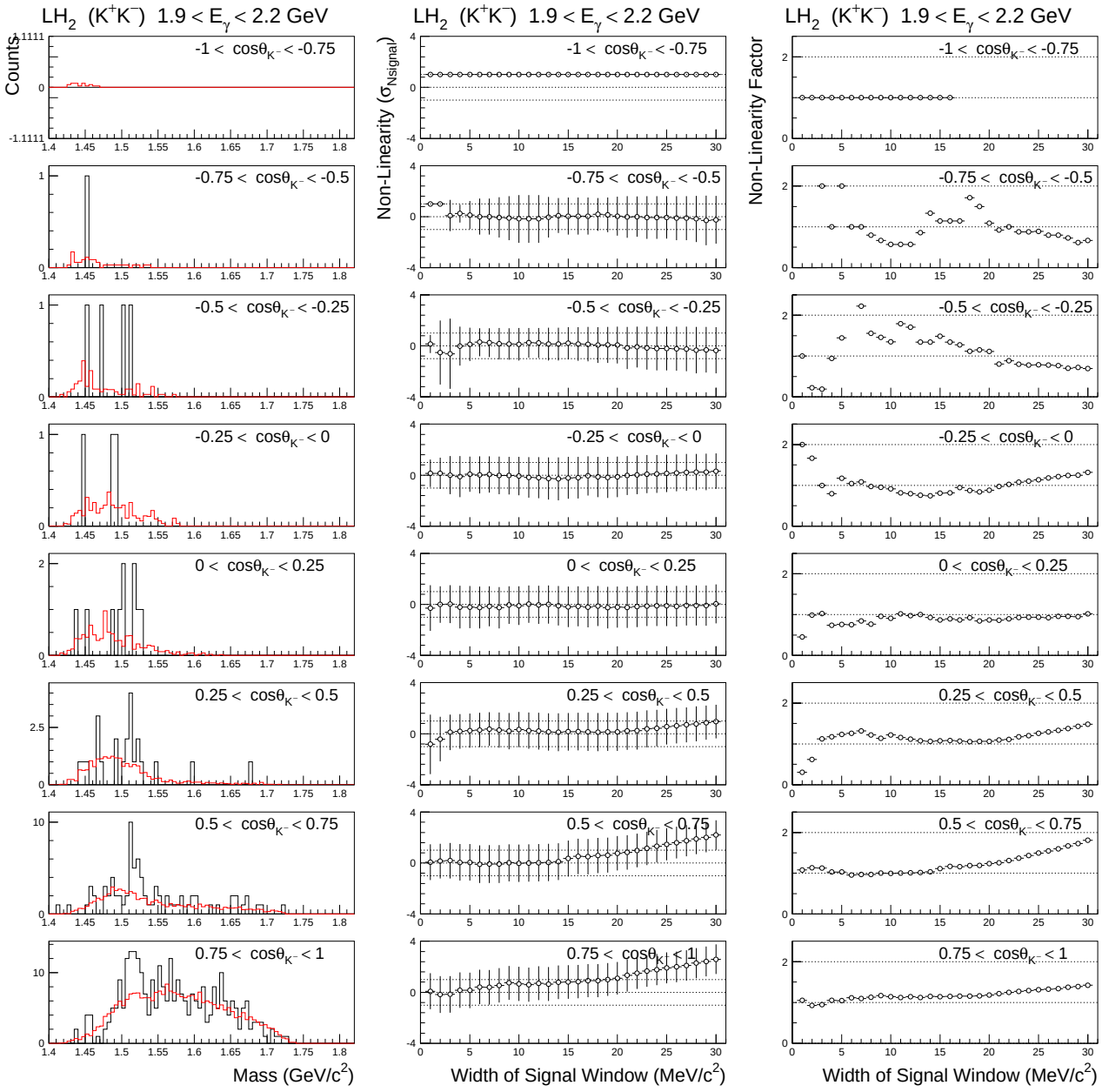

Figure B.27: Background non-linearity studies in different K^- polar angle of $\Lambda(1520)$ helicity frame within photon energy of 1.9-2.2 GeV from K^+K^- detection mode of protons are shown in 3 columns respectively, including mass spectra of real data overlaid by sum of Monte Carlo simulated background components, background non-linearities and non-linearity correction factors.

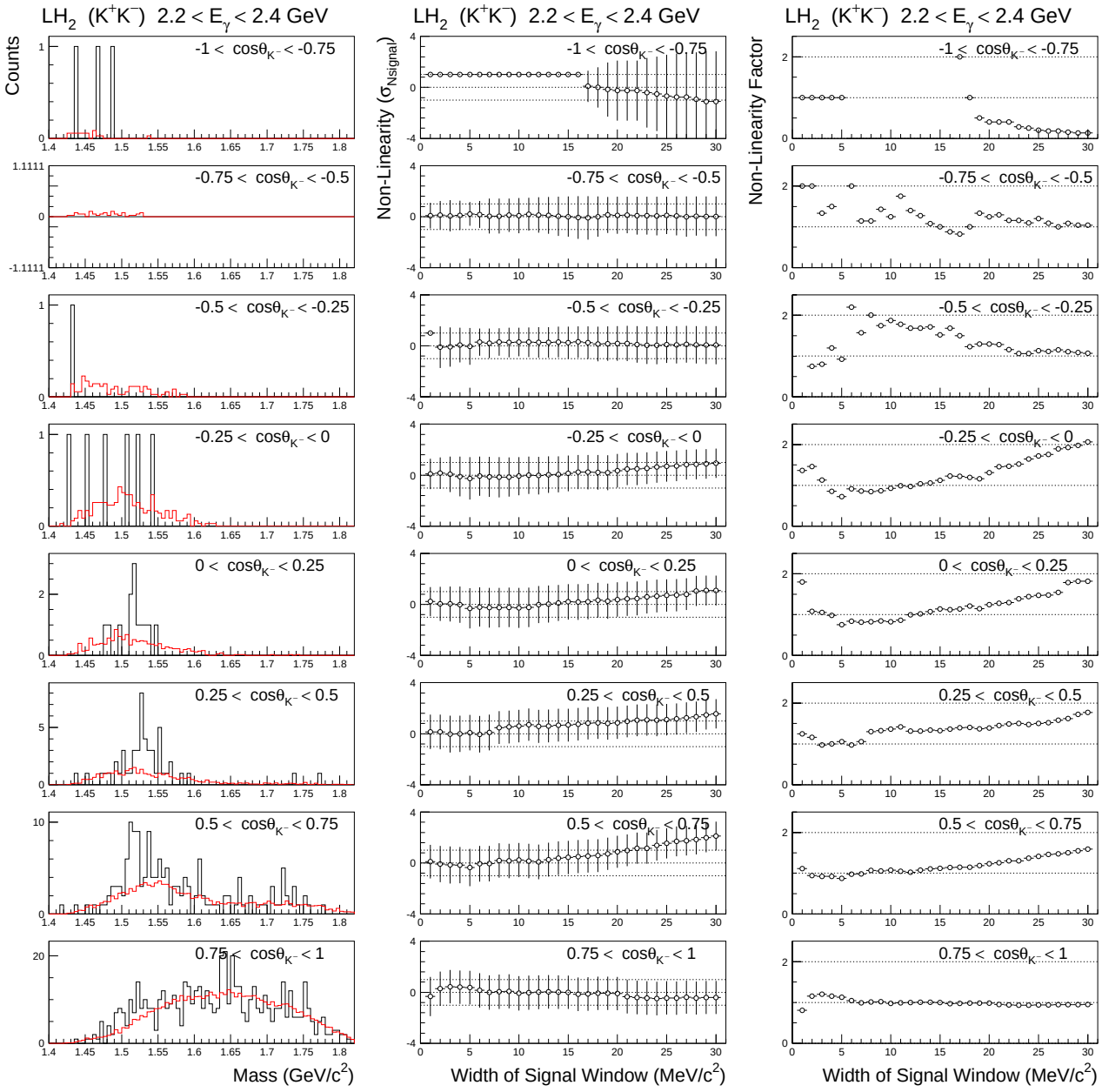

Figure B.28: Background non-linearity studies in different K^- polar angle of $\Lambda(1520)$ helicity frame within photon energy of 2.2-2.4 GeV from K^+K^- detection mode of protons are shown in 3 columns respectively, including mass spectra of real data overlaid by sum of Monte Carlo simulated background components, background non-linearities and non-linearity correction factors.

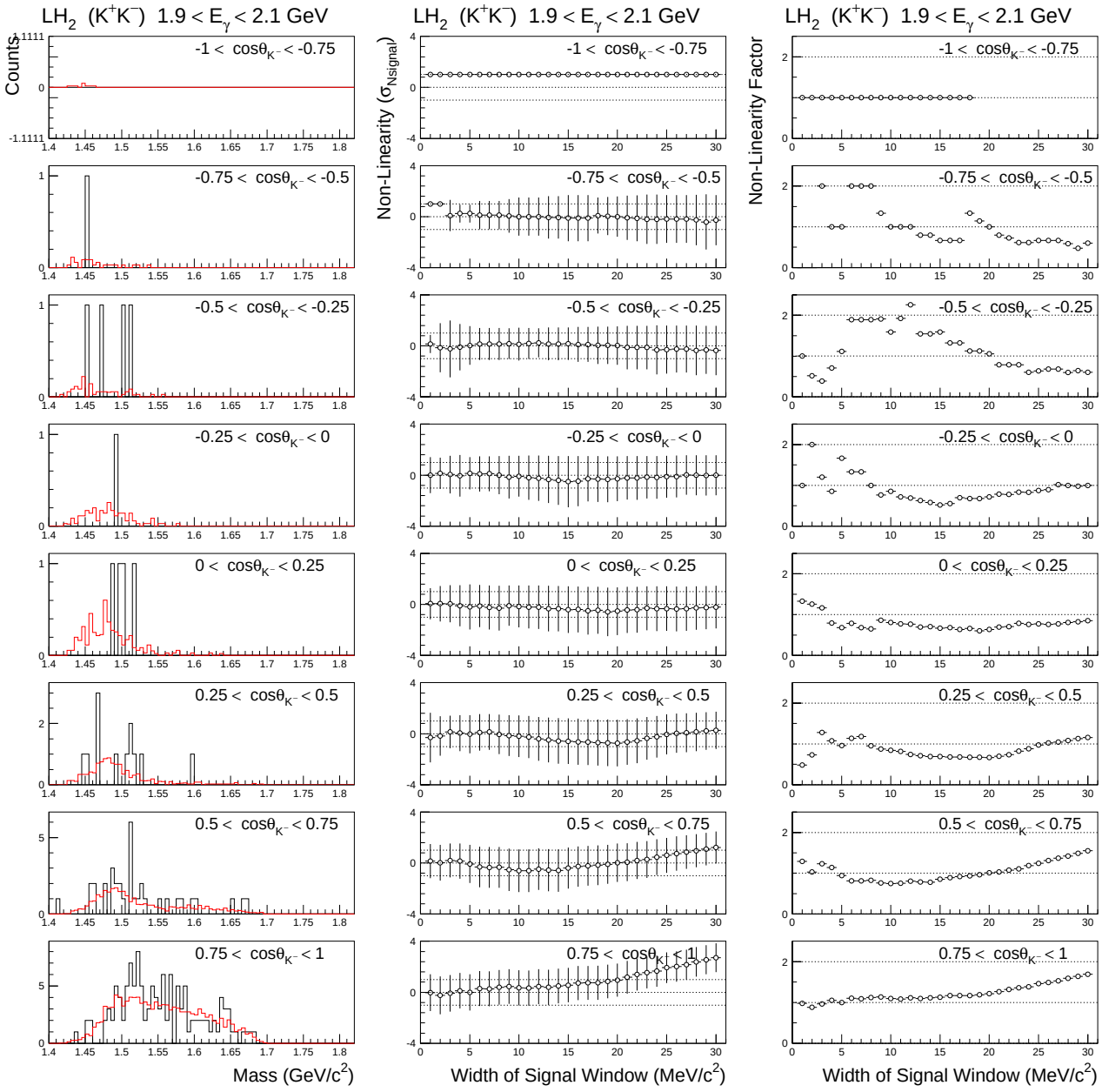

Figure B.29: Background non-linearity studies in different K^- polar angle of $\Lambda(1520)$ helicity frame within photon energy of 1.9-2.1 GeV from K^+K^- detection mode of protons are shown in 3 columns respectively, including mass spectra of real data overlaid by sum of Monte Carlo simulated background components, background non-linearities and non-linearity correction factors.

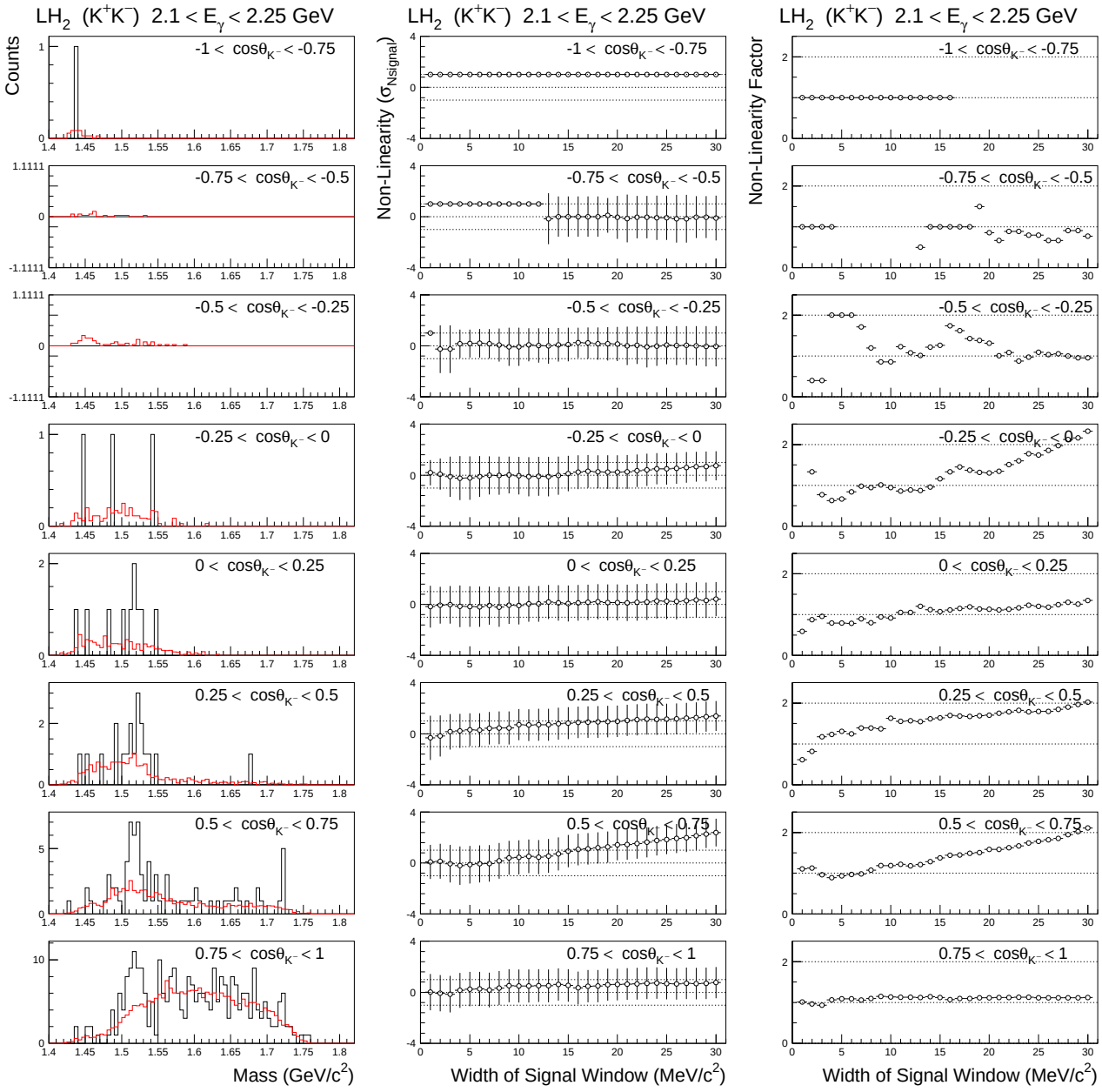

Figure B.30: Background non-linearity studies in different K^- polar angle of $\Lambda(1520)$ helicity frame within photon energy of 2.1-2.25 GeV from K^+K^- detection mode of protons are shown in 3 columns respectively, including mass spectra of real data overlaid by sum of Monte Carlo simulated background components, background non-linearities and non-linearity correction factors.

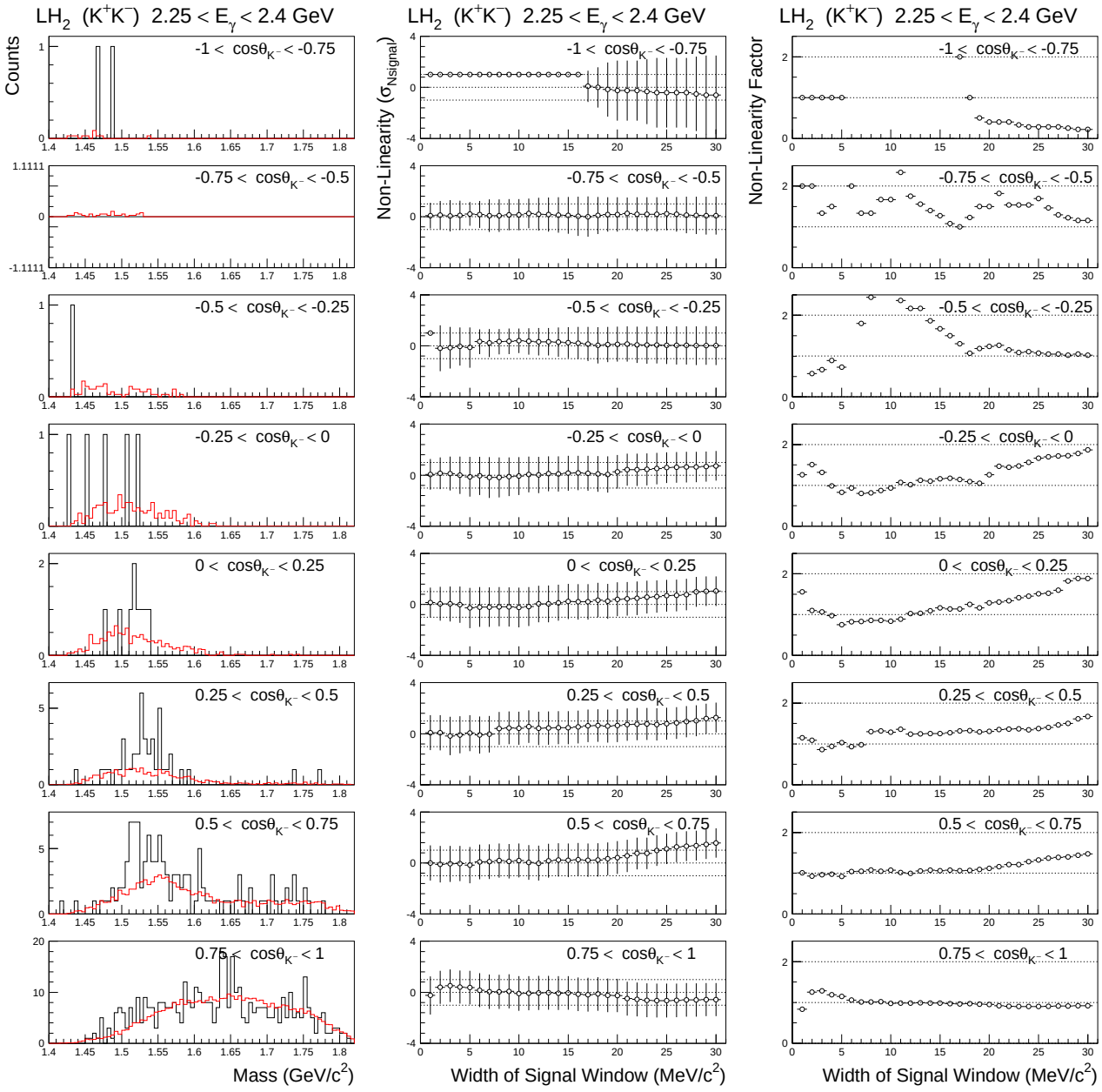

Figure B.31: Background non-linearity studies in different K^- polar angle of $\Lambda(1520)$ helicity frame within photon energy of 2.25-2.4 GeV from K^+K^- detection mode of protons are shown in 3 columns respectively, including mass spectra of real data overlaid by sum of Monte Carlo simulated background components, background non-linearities and non-linearity correction factors.

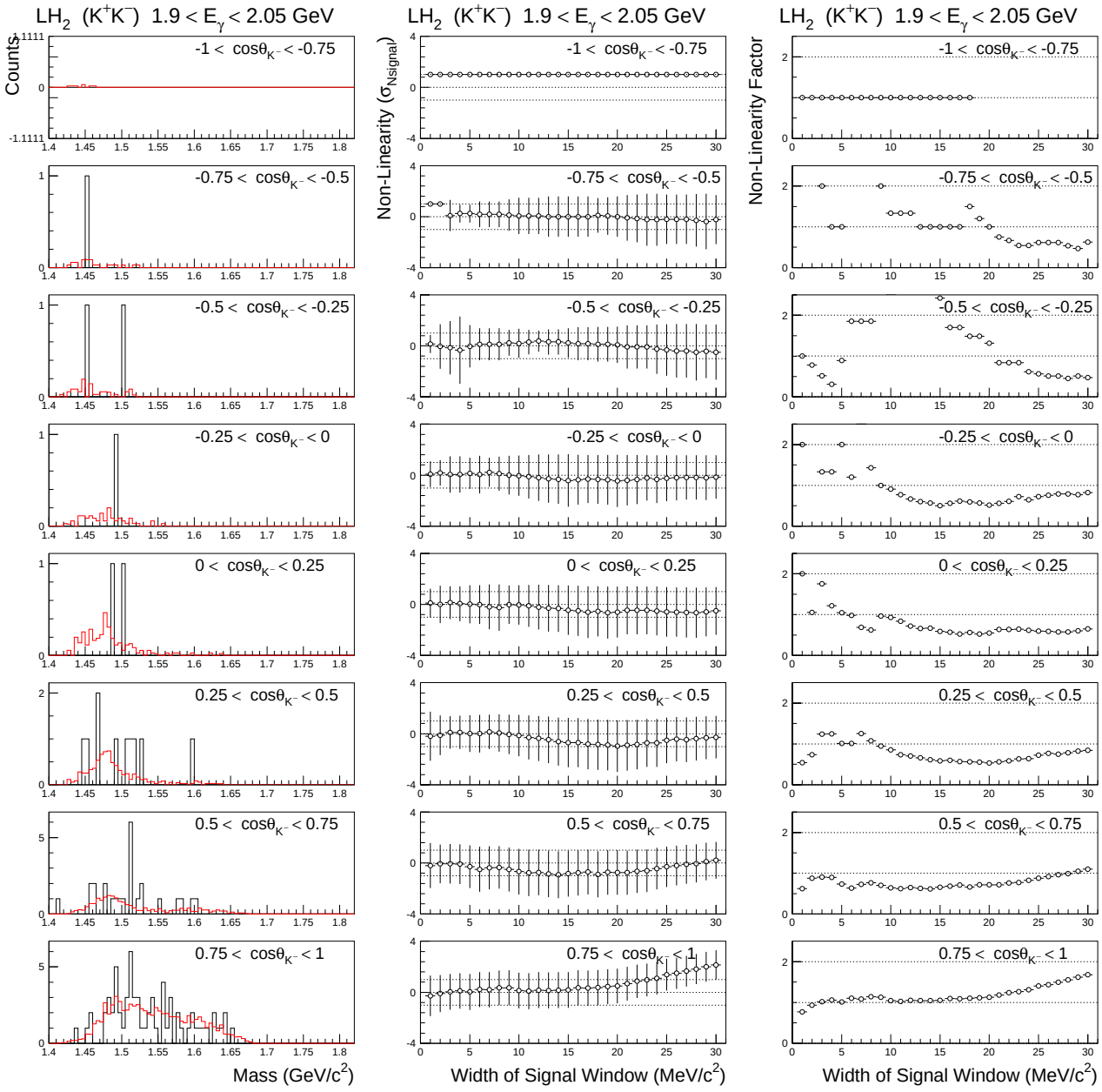

Figure B.32: Background non-linearity studies in different K^- polar angle of $\Lambda(1520)$ helicity frame within photon energy of 1.9-2.05 GeV from K^+K^- detection mode of protons are shown in 3 columns respectively, including mass spectra of real data overlaid by sum of Monte Carlo simulated background components, background non-linearities and non-linearity correction factors.

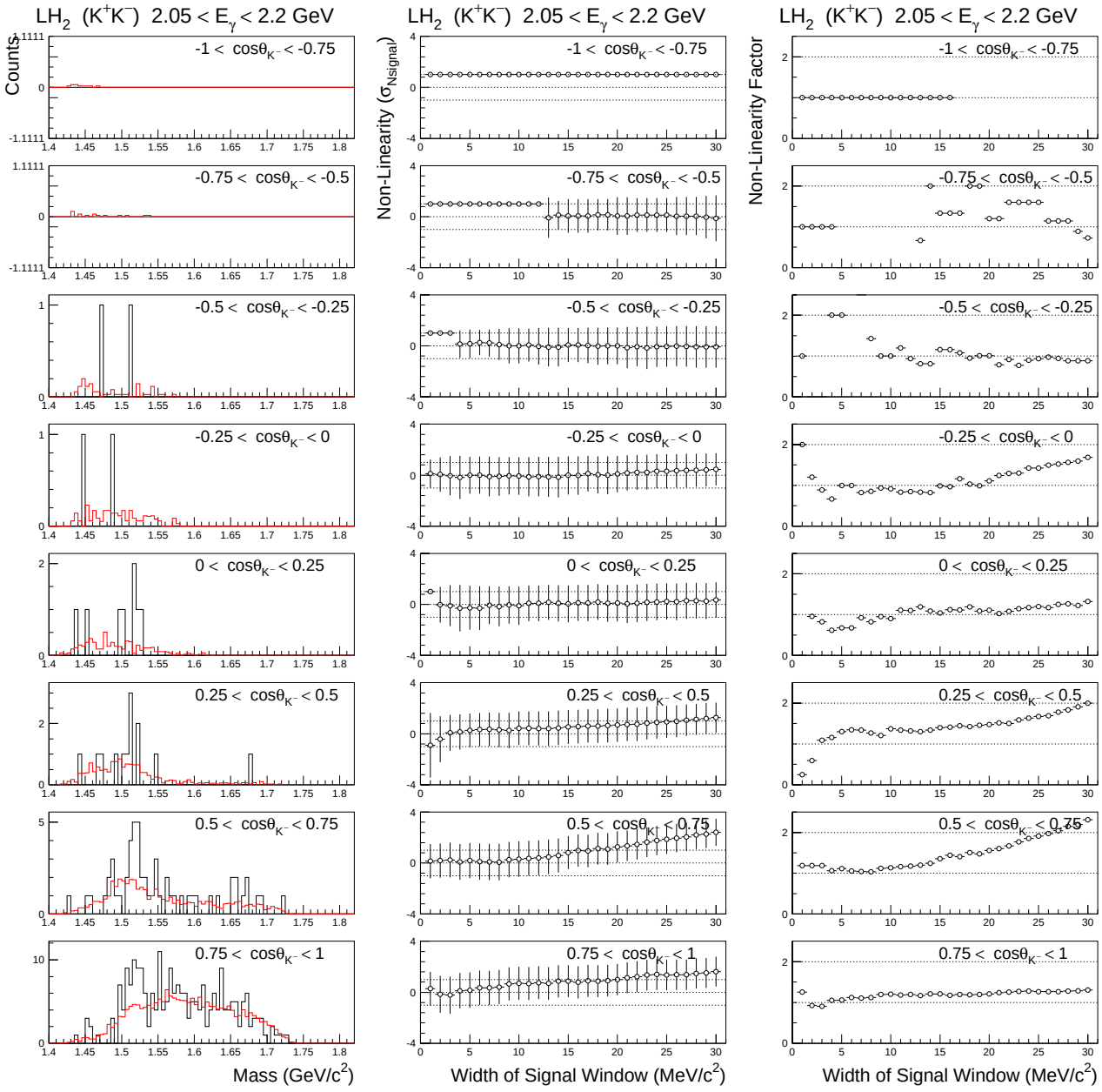

Figure B.33: Background non-linearity studies in different K^- polar angle of $\Lambda(1520)$ helicity frame within photon energy of 2.05-2.2 GeV from K^+K^- detection mode of protons are shown in 3 columns respectively, including mass spectra of real data overlaid by sum of Monte Carlo simulated background components, background non-linearities and non-linearity correction factors.

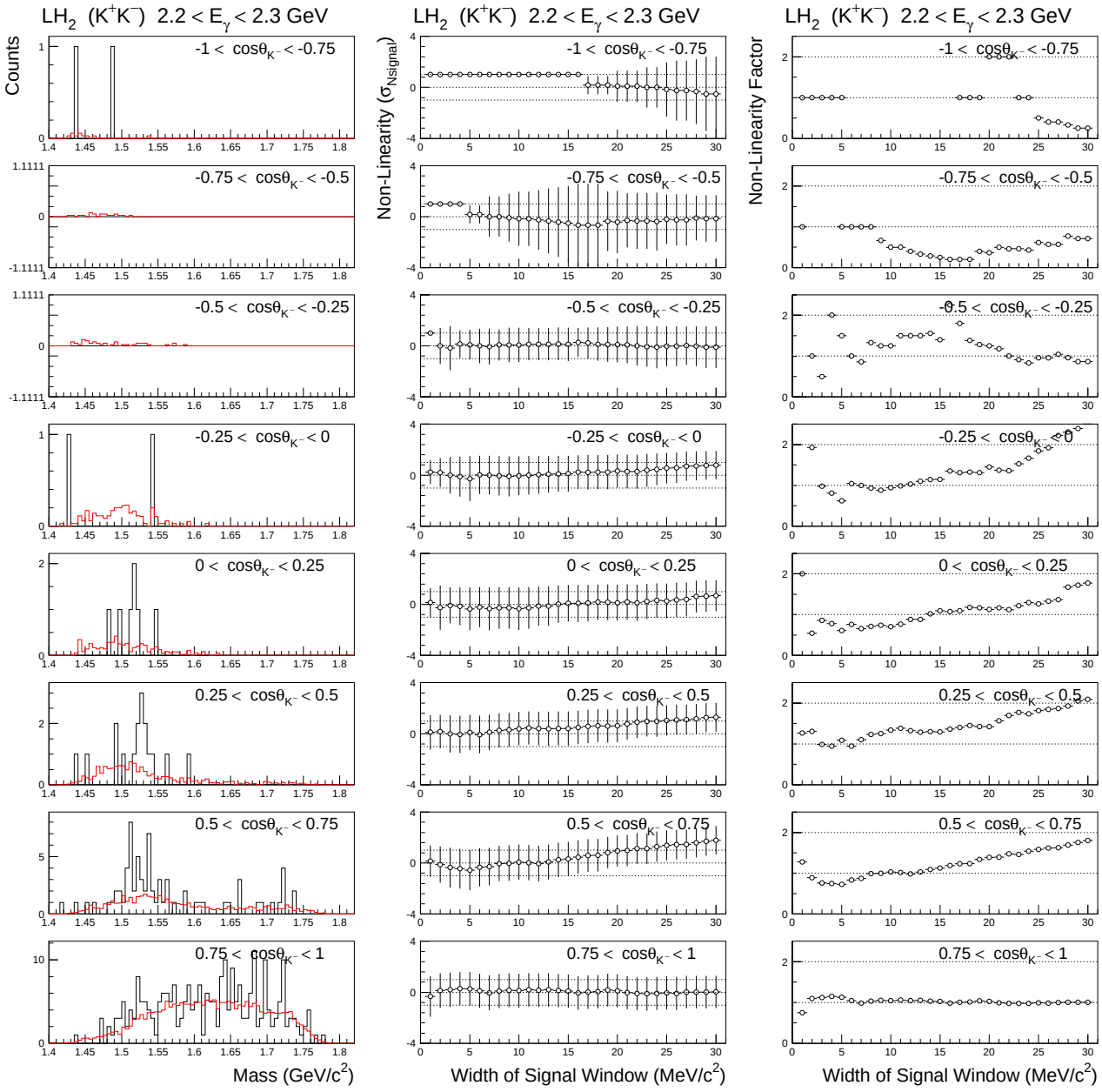

Figure B.34: Background non-linearity studies in different K^- polar angle of $\Lambda(1520)$ helicity frame within photon energy of 2.2-2.3 GeV from K^+K^- detection mode of protons are shown in 3 columns respectively, including mass spectra of real data overlaid by sum of Monte Carlo simulated background components, background non-linearities and non-linearity correction factors.

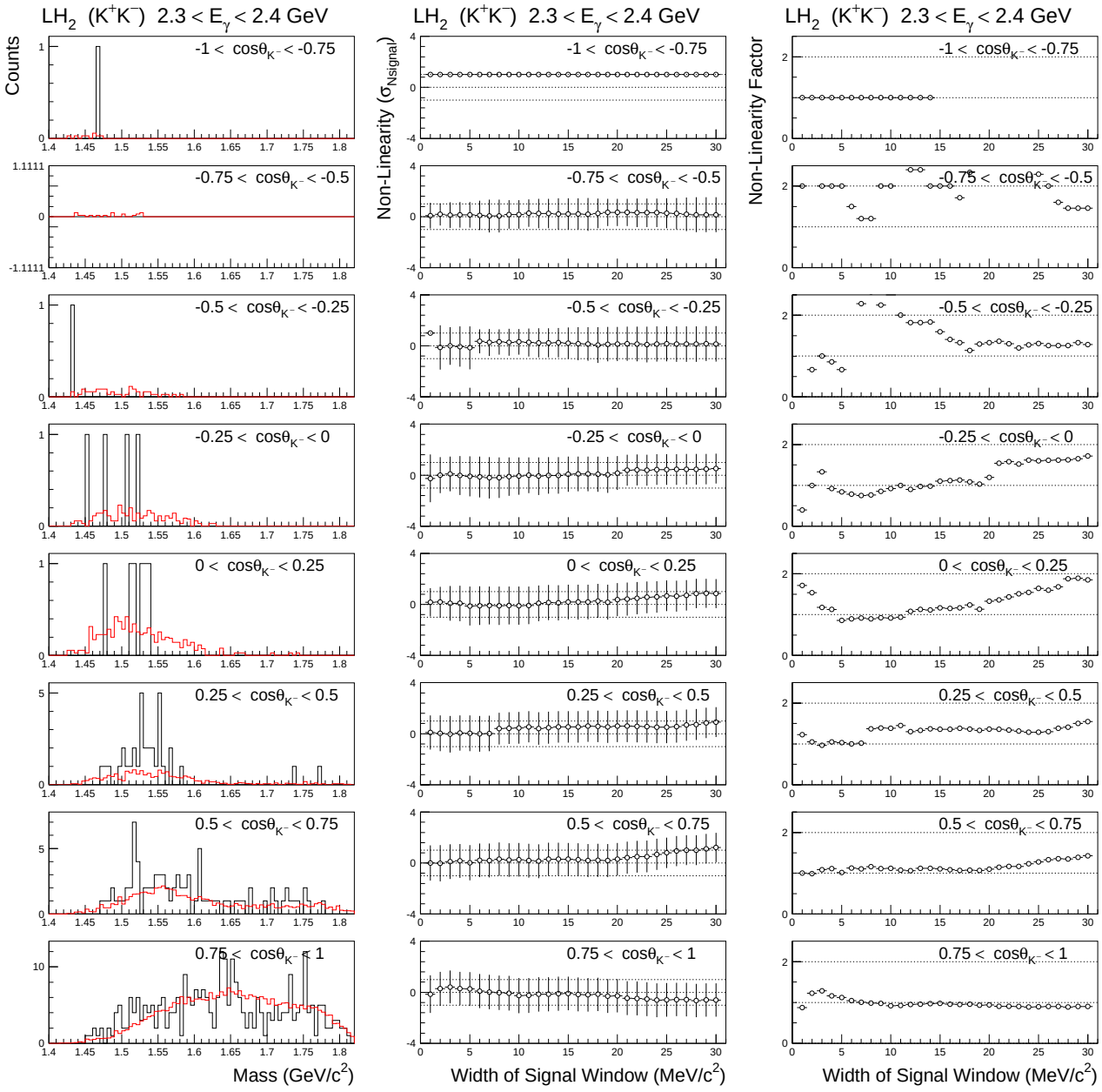

Figure B.35: Background non-linearity studies in different K^- polar angle of $\Lambda(1520)$ helicity frame within photon energy of 2.3-2.4 GeV from K^+K^- detection mode of protons are shown in 3 columns respectively, including mass spectra of real data overlaid by sum of Monte Carlo simulated background components, background non-linearities and non-linearity correction factors.

B.2.2 K^- polar angle distribution in $\Lambda(1520)$ t-channel helicity frame

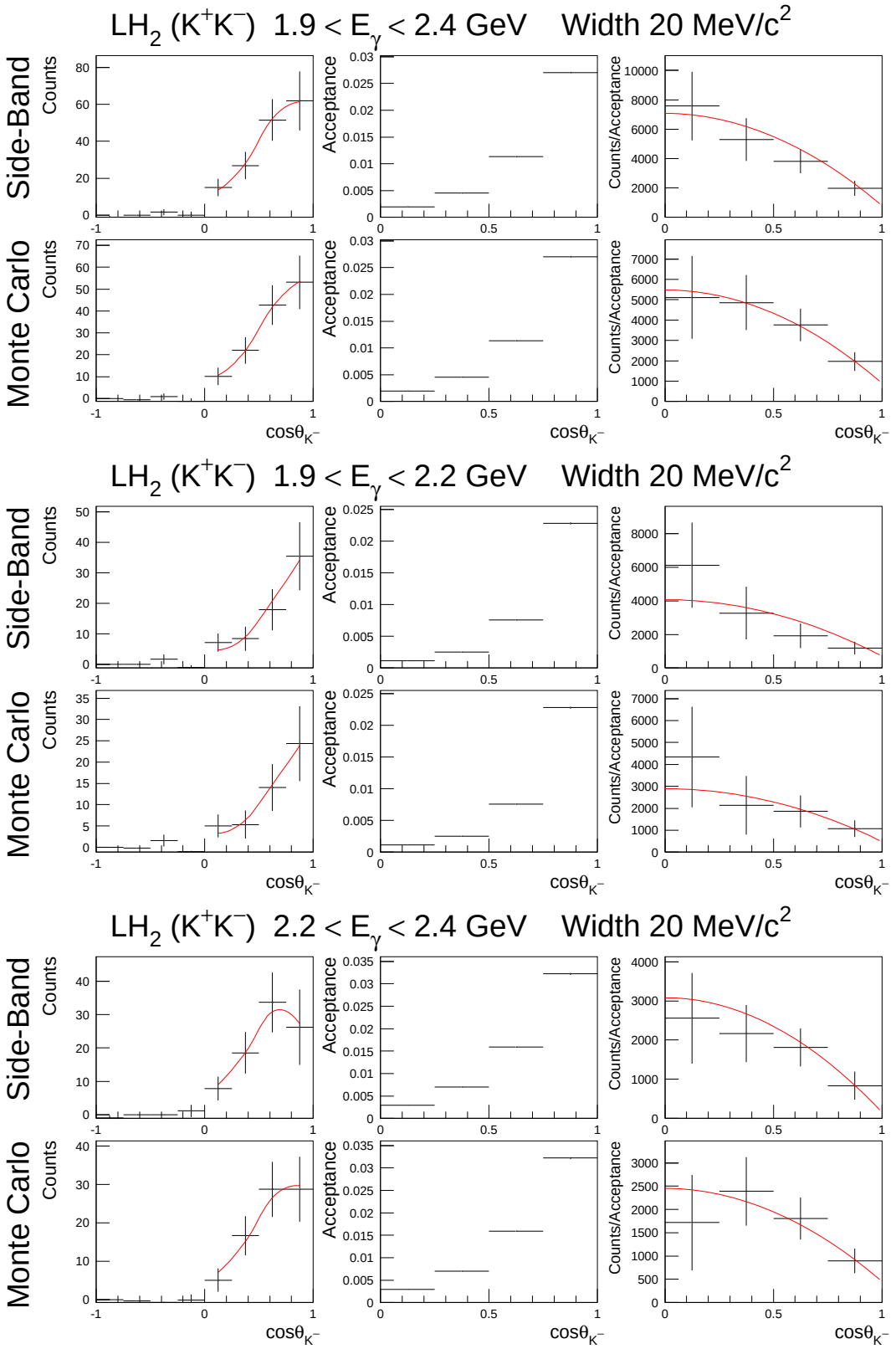

Figure B.36: K^- polar angle distribution in $\Lambda(1520)$ t-channel helicity frame from protons in K^+K^- detection mode were shown in photon energy of 1.9-2.4, 1.9-2.2 and 2.2-2.4 GeV with 20-MeV/c^2 signal-window width by side-band subtraction and Monte Carlo methods.

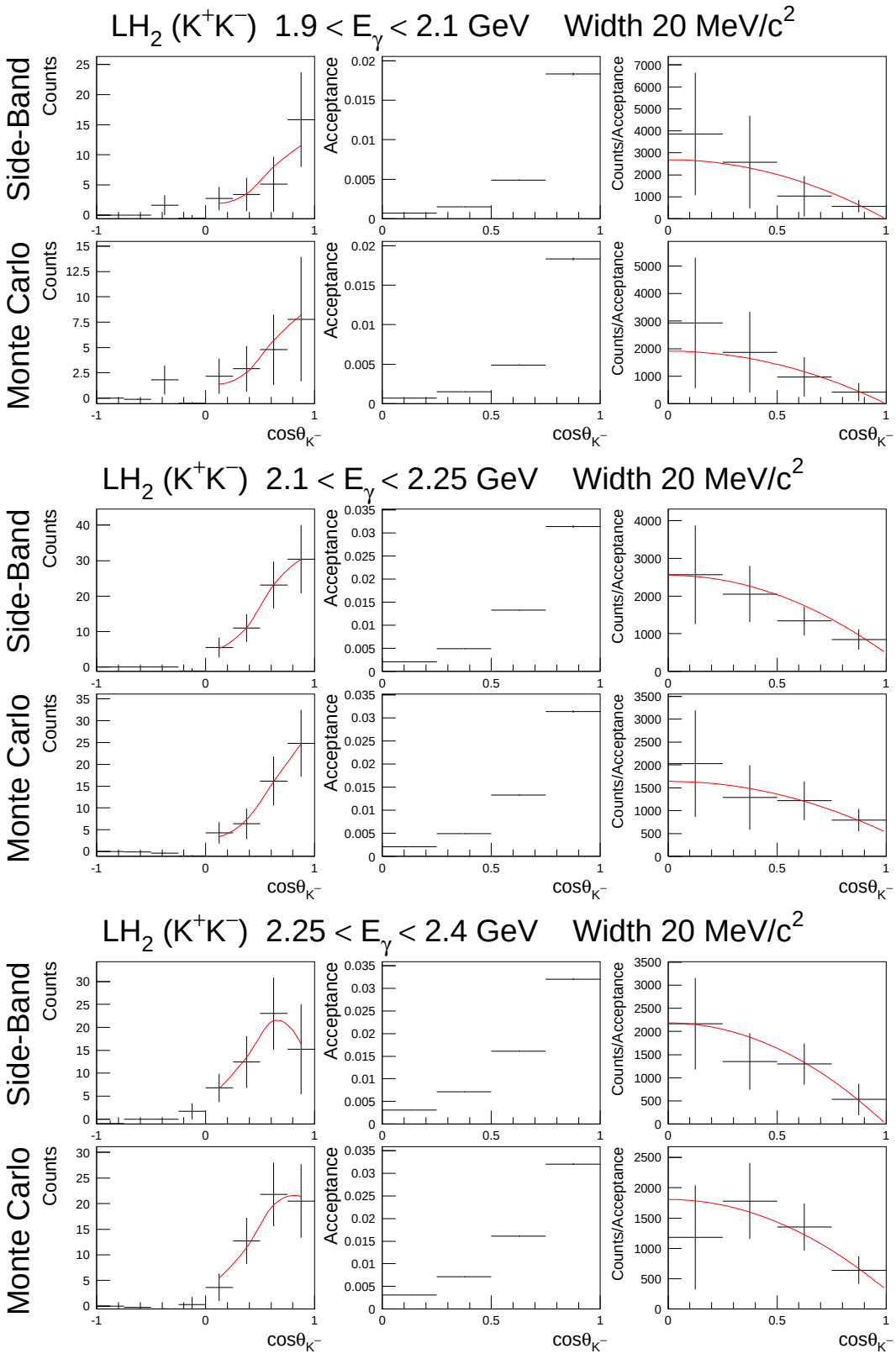

Figure B.37: K^- polar angle distribution in $\Lambda(1520)$ t-channel helicity frame from protons in K^+K^- detection mode were shown in photon energy of 1.9-2.1, 2.1-2.25 and 2.25-2.4 GeV with 20-MeV/c^2 signal-window width by side-band subtraction and Monte Carlo methods.

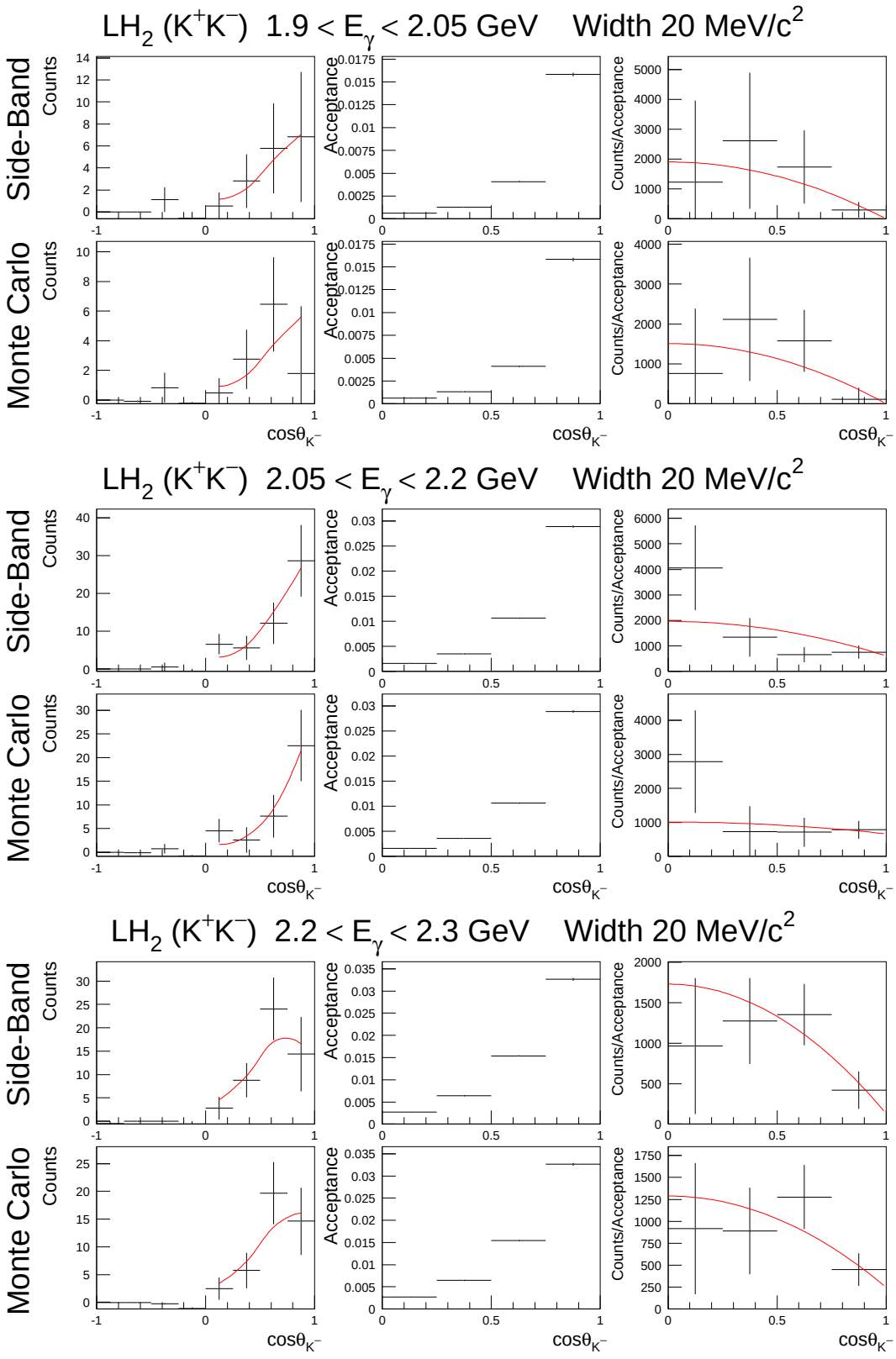

Figure B.38: K^- polar angle distribution in $\Lambda(1520)$ t-channel helicity frame from protons in K^+K^- detection mode were shown in photon energy of 1.9-2.05, 2.05-2.2 and 2.2-2.3 GeV with 20-MeV/c^2 signal-window width by side-band subtraction and Monte Carlo methods.

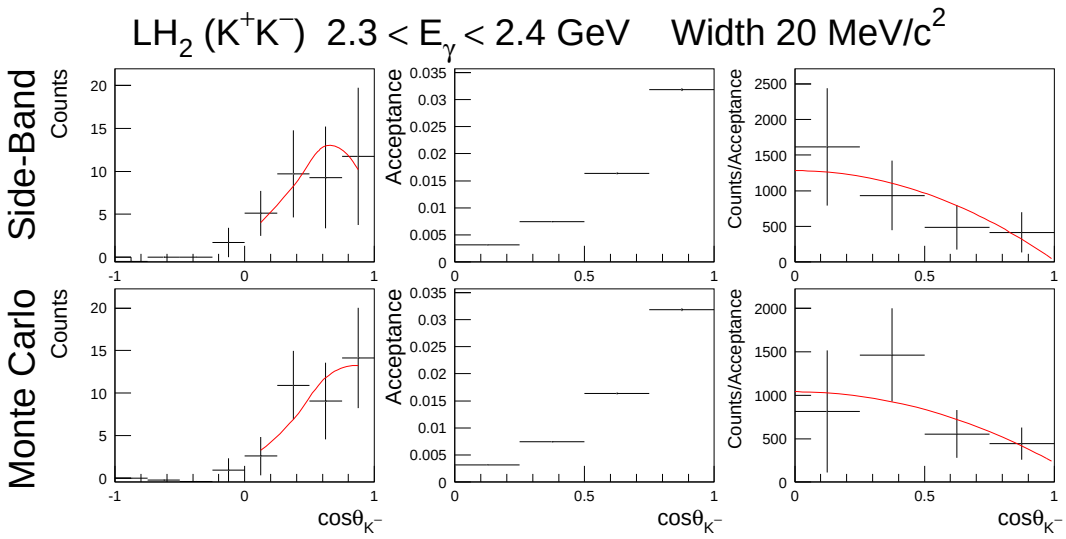

Figure B.39: K^- polar angle distribution in $\Lambda(1520)$ t-channel helicity frame from protons in K^+K^- detection mode were shown in photon energy of 2.3-2.4 GeV with 20-MeV/c^2 signal-window width by side-band subtraction and Monte Carlo methods.

B.2.3 Signal-window width dependence of fraction of helicity-3/2

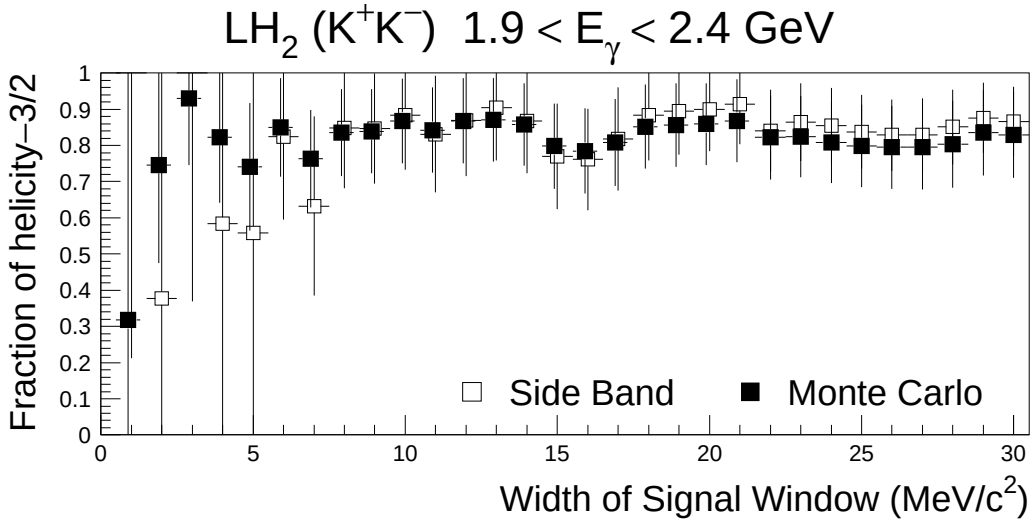

Figure B.40: Signal-window width dependence of fraction of helicity-3/2 from protons in K^+K^- detection mode in photon energy of 1.9-2.4 GeV were shown from side-band subtraction and Monte Carlo methods respectively.

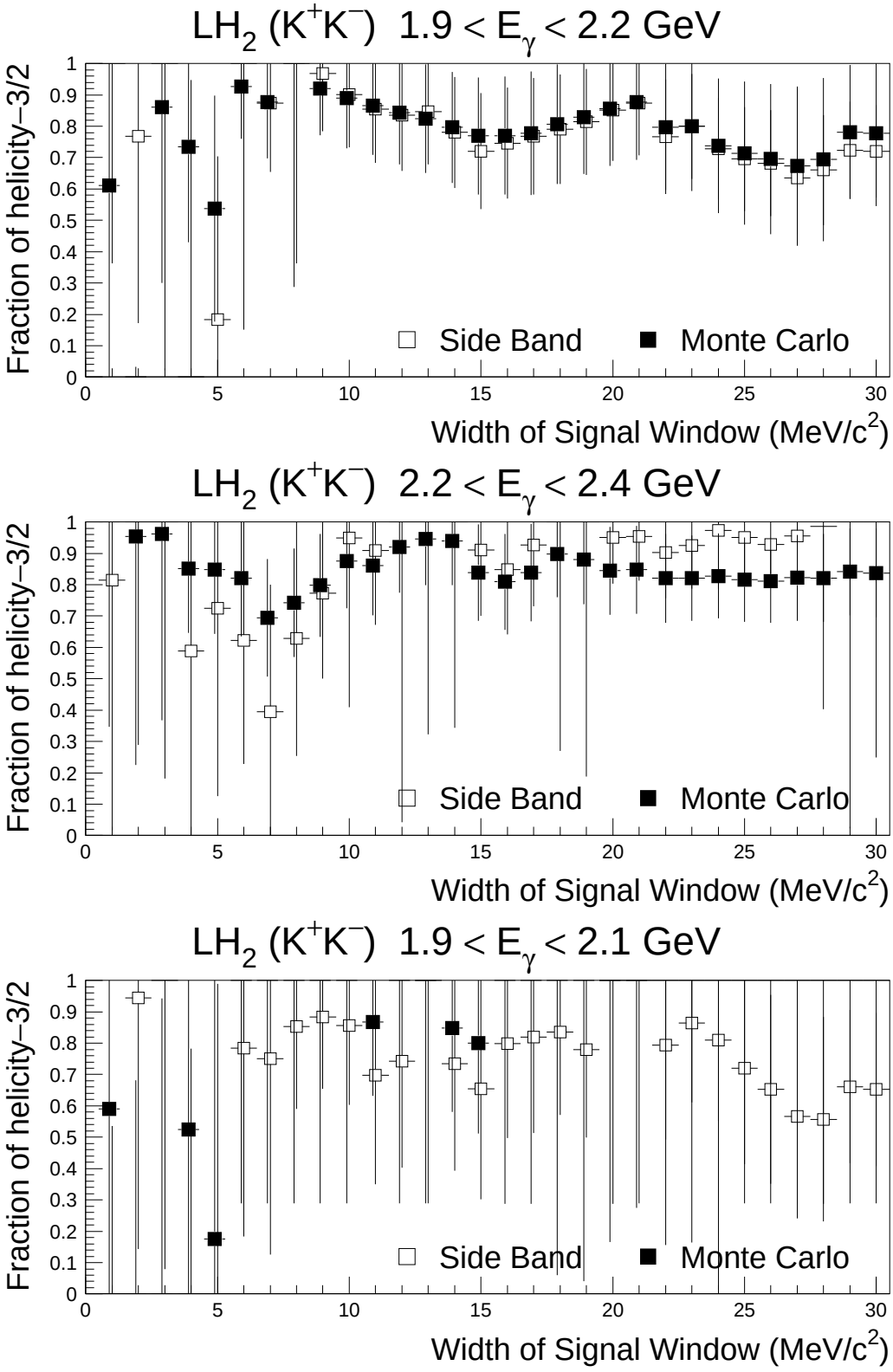

Figure B.41: Signal-window width dependence of fraction of helicity-3/2 from protons in K^+K^- detection mode in photon energy of 1.9-2.2, 2.2-2.4 and 1.9-2.1 GeV were shown from side-band subtraction and Monte Carlo methods respectively.

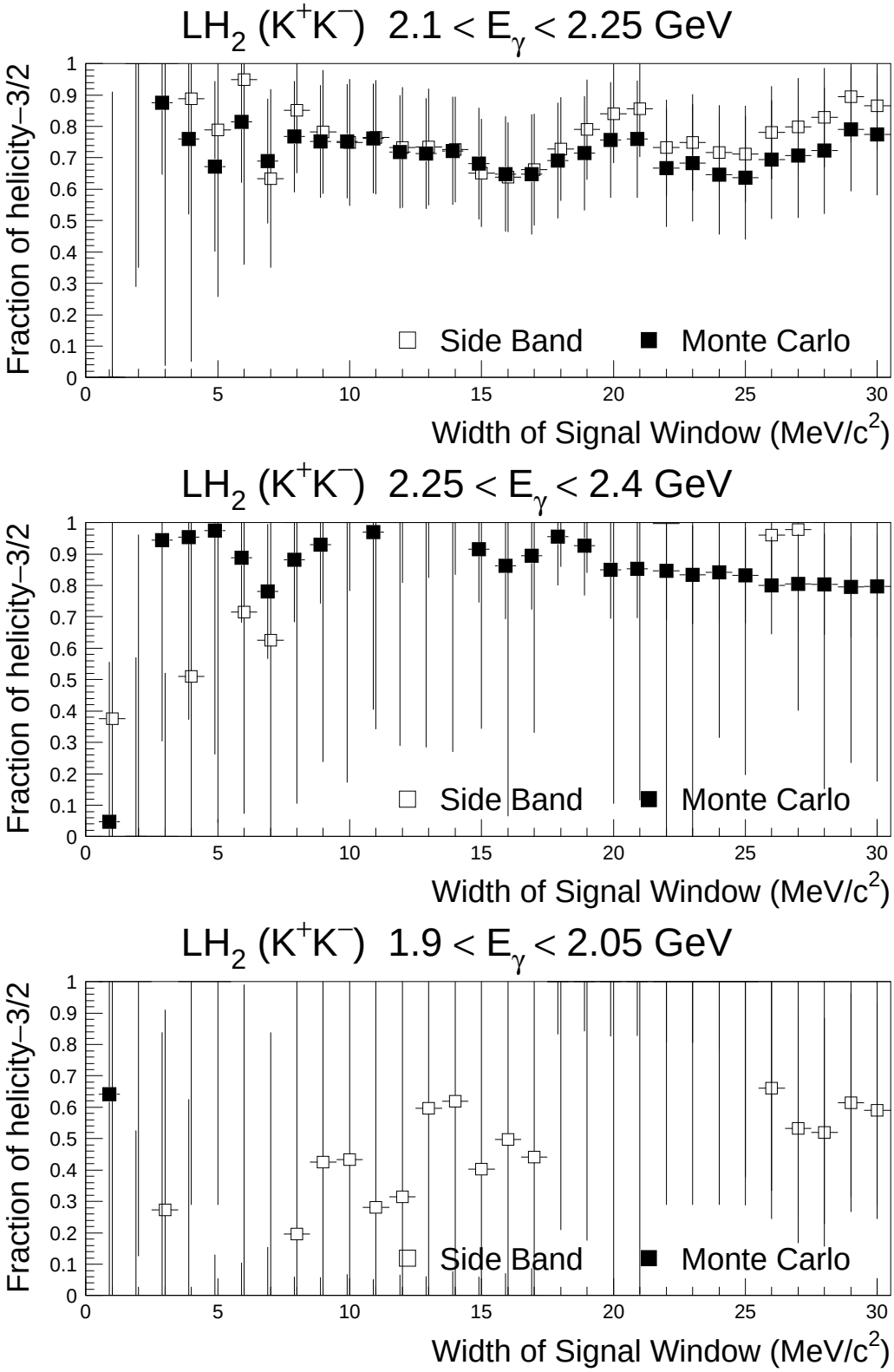

Figure B.42: Signal-window width dependence of fraction of helicity-3/2 from protons in K^+K^- detection mode in photon energy of 2.1-2.25, 2.25-2.4 and 1.9-2.05 GeV were shown from side-band subtraction and Monte Carlo methods respectively.

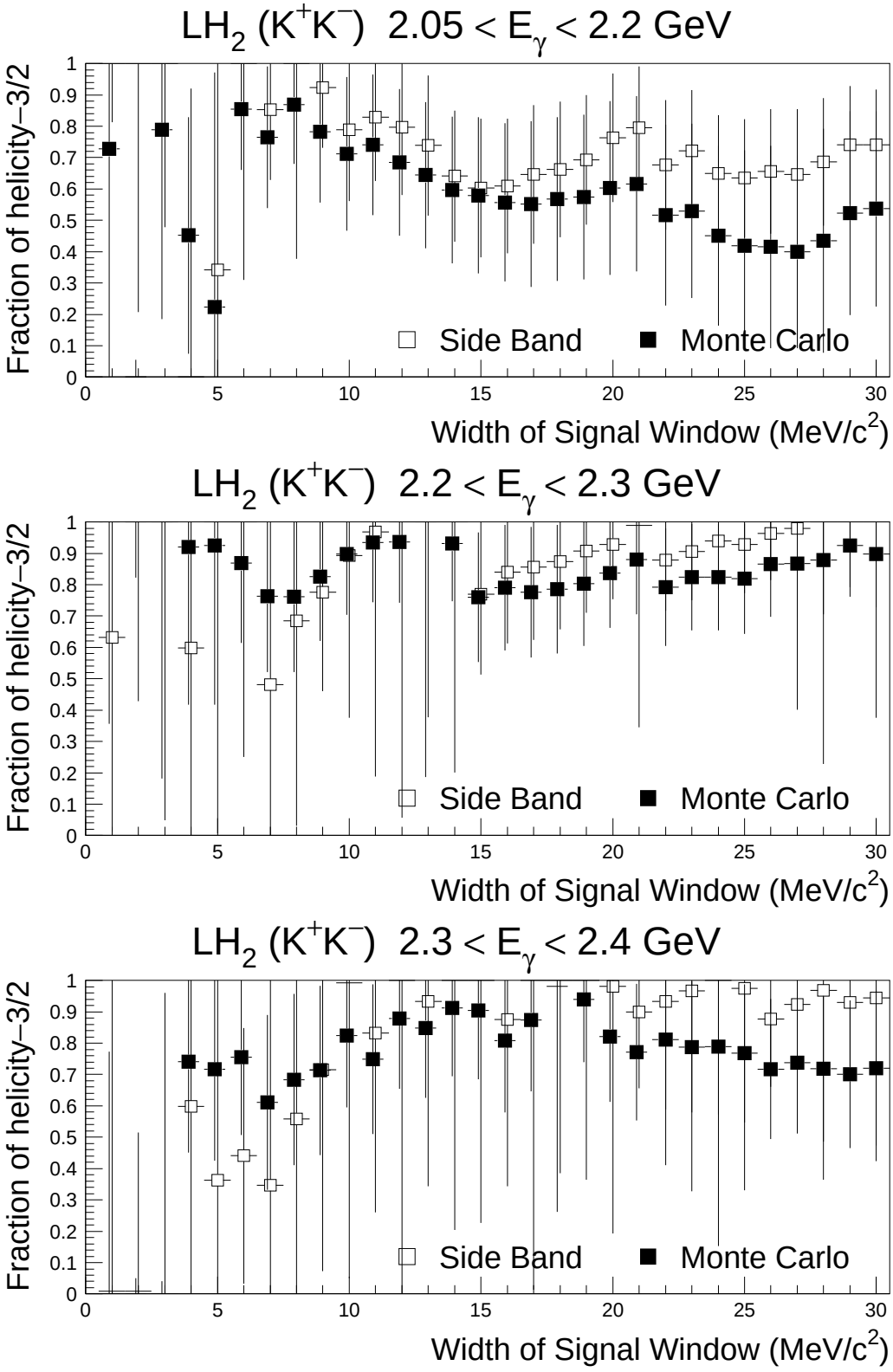

Figure B.43: Signal-window width dependence of fraction of helicity-3/2 from protons in K^+K^- detection mode in photon energy of 2.05-2.2, 2.2-2.3 and 2.3-2.4 GeV were shown from side-band subtraction and Monte Carlo methods respectively.

B.3 K^+p detection mode from protons

B.3.1 Window dependence of K^- polar angle distribution

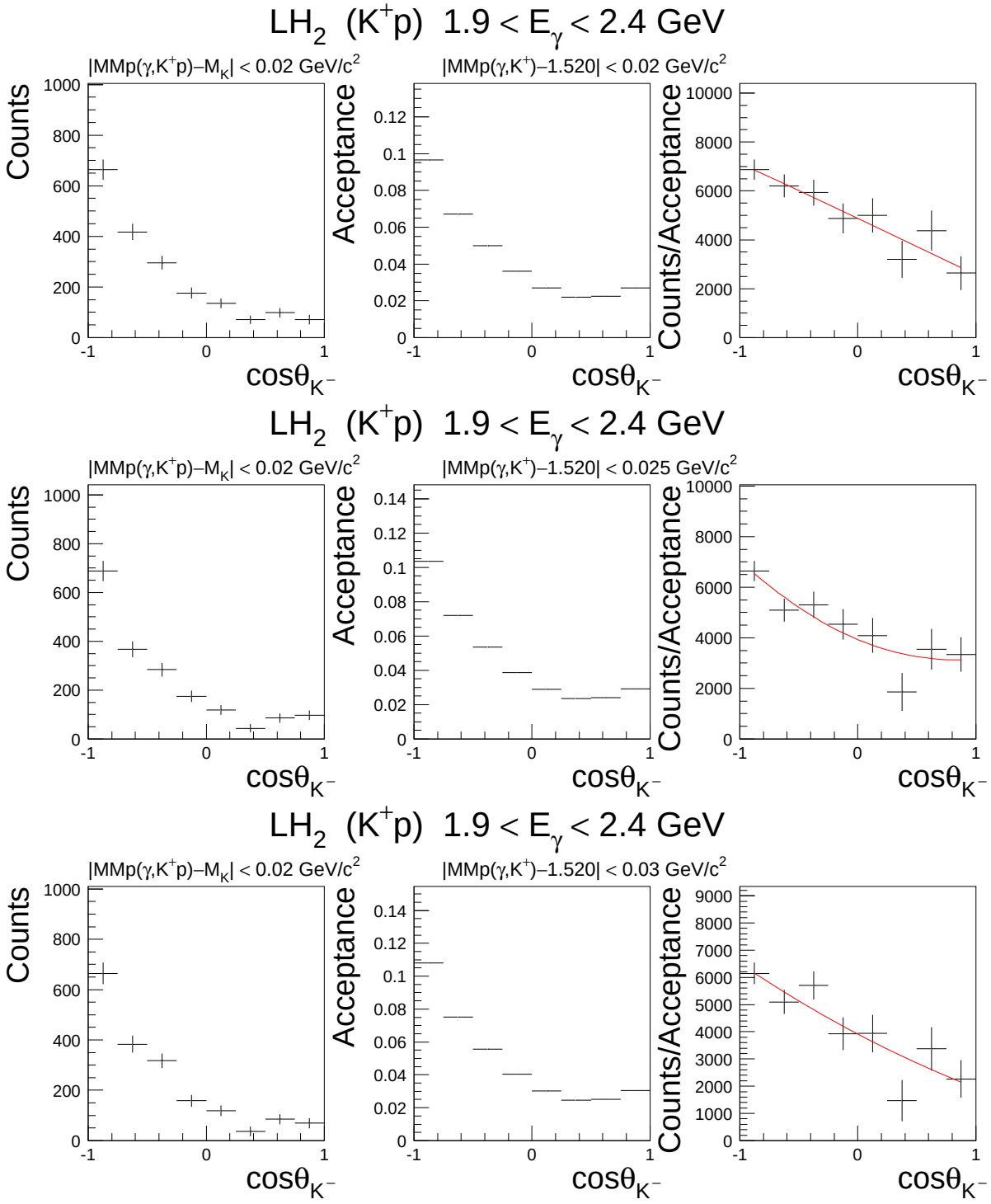

Figure B.44: K^- polar angle distribution in $\Lambda(1520)$ t-channel helicity frame from protons in K^+p detection mode were shown in photon energy of 1.9-2.4 GeV under the requirement $|MMp(\gamma,K^+p)-M_K| < 20$ MeV/c^2 and different $\Lambda(1520)$ signal-window widths by side-band subtraction method.

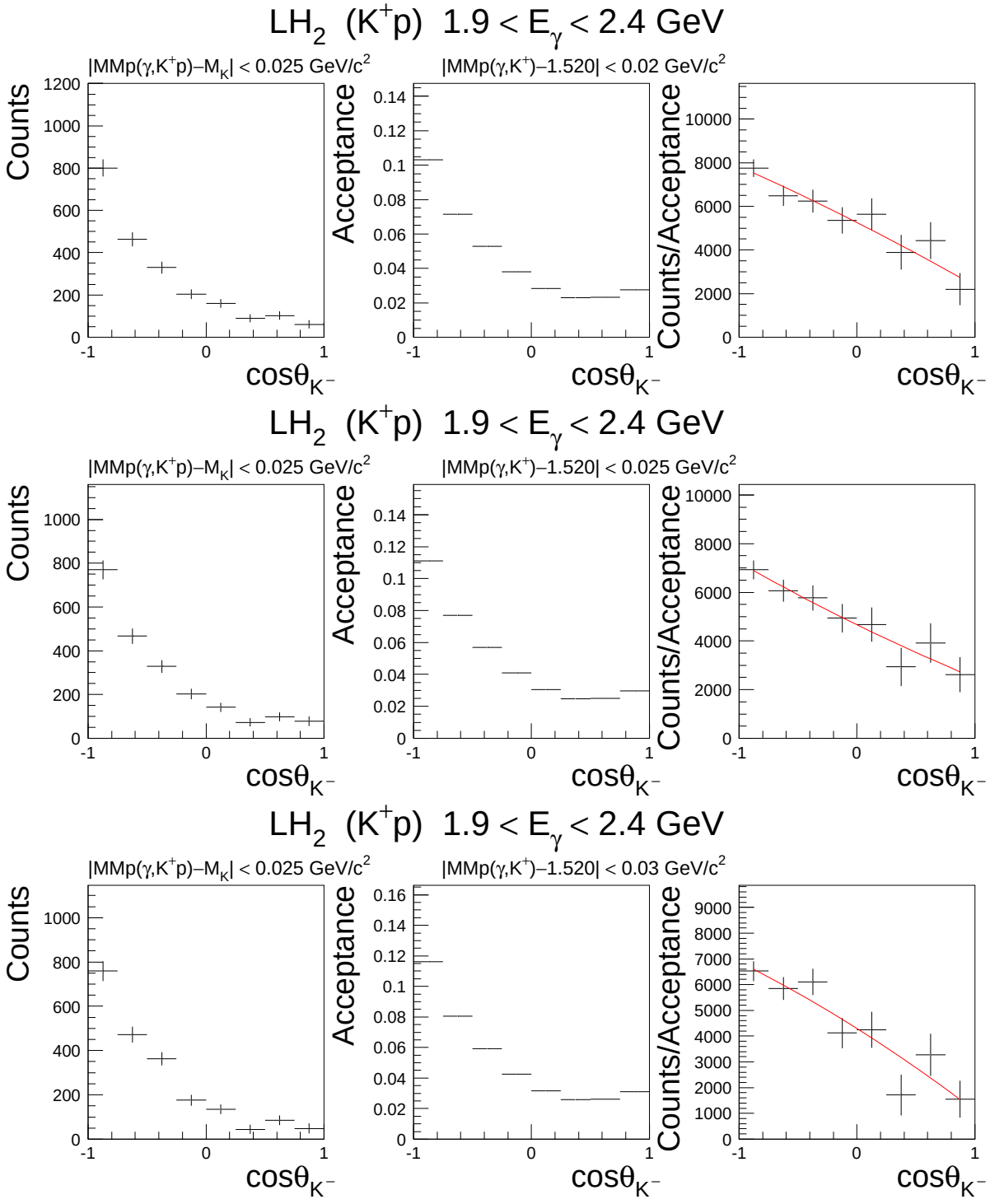

Figure B.45: K^- polar angle distribution in $\Lambda(1520)$ t-channel helicity frame from protons in K^+p detection mode were shown in photon energy of 1.9-2.4 GeV under the requirement $|MMp(\gamma,K^+p)-M_K| < 25$ MeV/c^2 and different $\Lambda(1520)$ signal-window widths by side-band subtraction method.

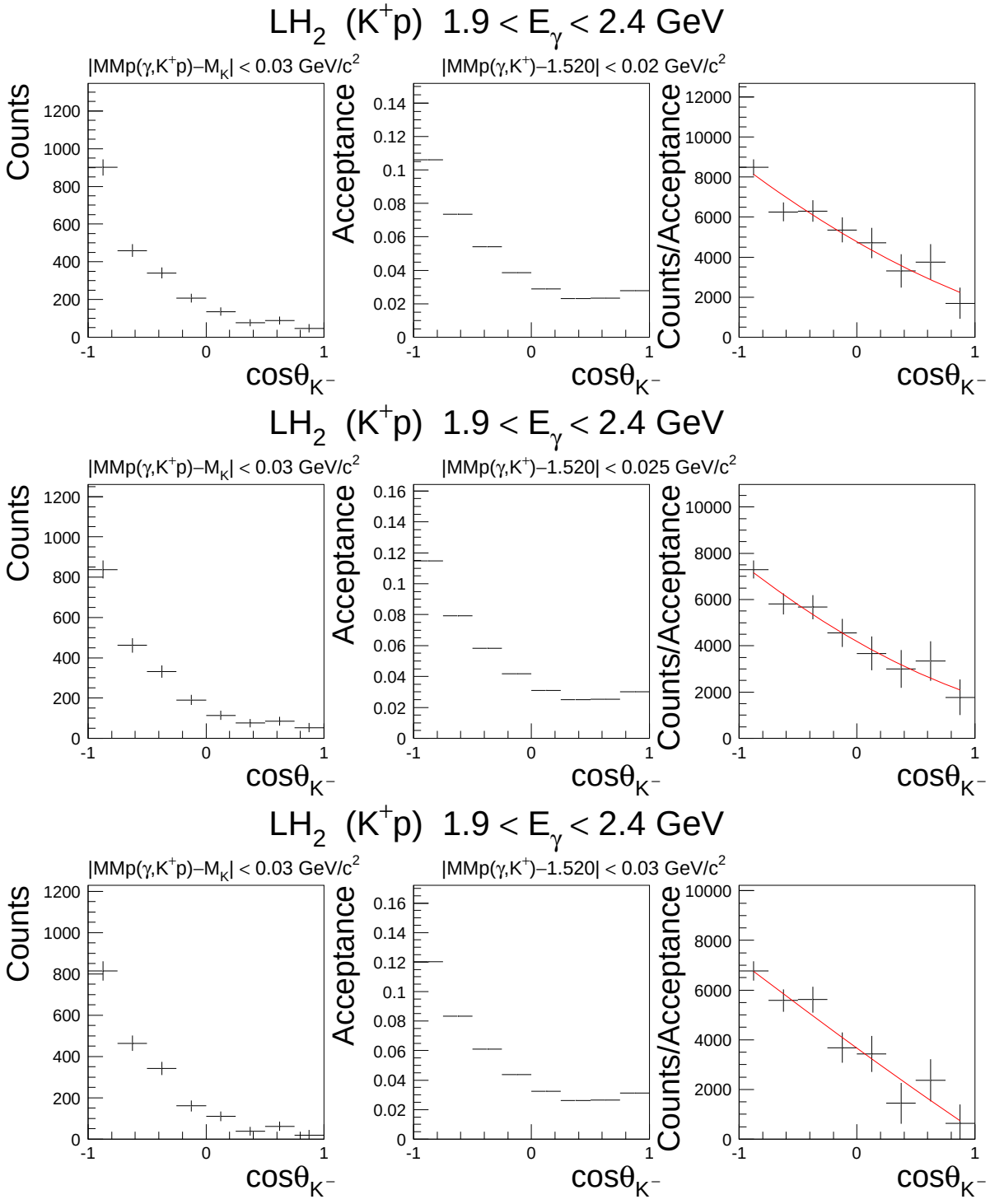

Figure B.46: K^- polar angle distribution in $\Lambda(1520)$ t-channel helicity frame from protons in K^+p detection mode were shown in photon energy of 1.9-2.4 GeV under the requirement $|MMp(\gamma,K^+p)-M_K| < 30$ MeV/c^2 and different $\Lambda(1520)$ signal-window widths by side-band subtraction method.

B.3.2 Energy dependence of K^- polar angle distribution

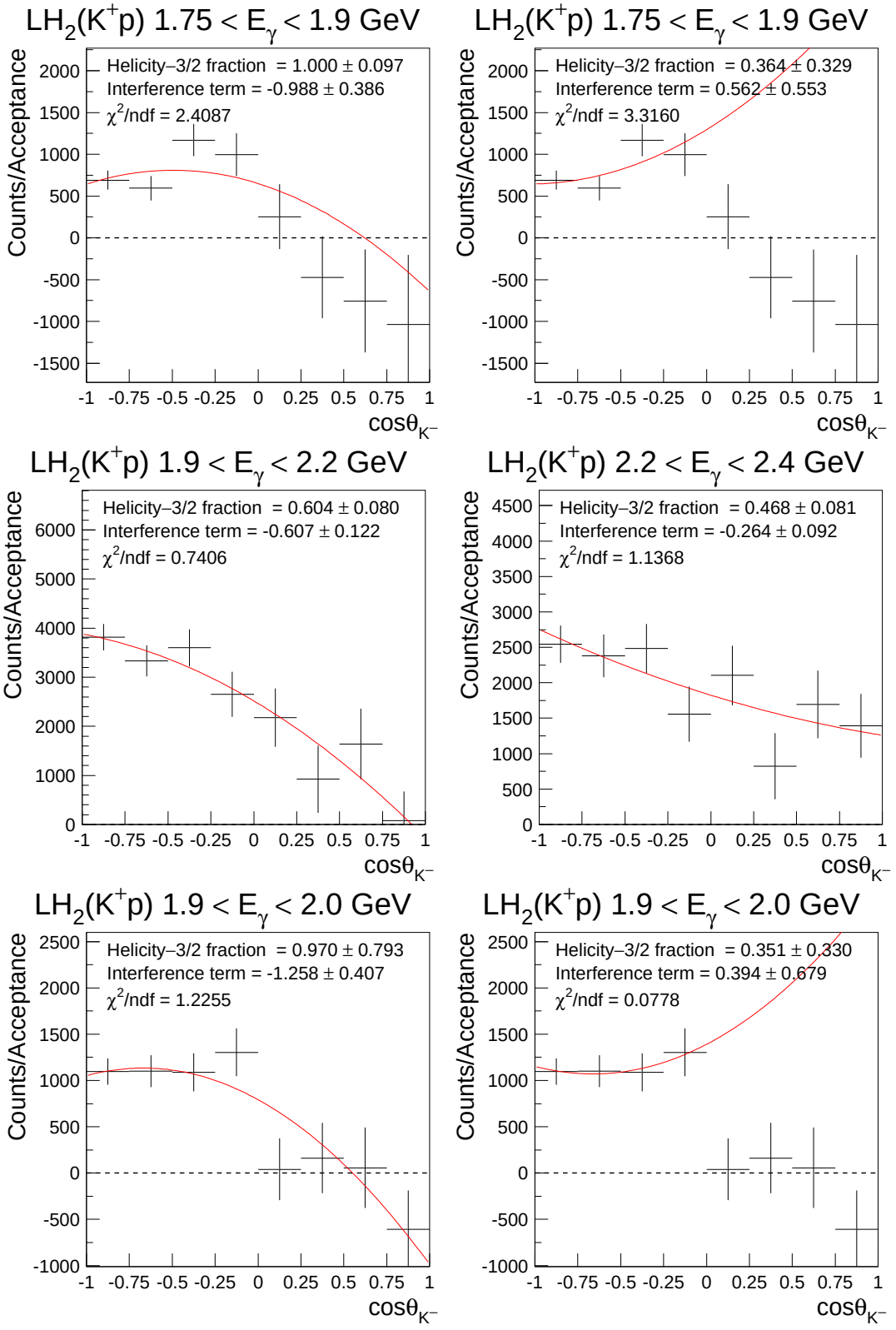

Figure B.47: K^- polar angle distribution in $\Lambda(1520)$ t-channel helicity frame from protons in K^+p detection mode were shown in photon energy of 1.75-1.9, 1.9-2.2, 2.2-2.4 and 1.9-2.0 GeV under the requirements $|\mathrm{MMp}(\gamma,K^+p)-M_K| < 20$ MeV/c^2 and and $|\mathrm{MMp}(\gamma,K^+)-1.520| < 0.030$ GeV/c^2 by side-band subtraction method. In the cases of photon energy of 1.75-1.9 and 1.9-2.0 GeV, negative values happen in the positive region of K^- polar angle. Therefore, two fits with full region (8 bins) and negative region (4 bins, -1.0∼0.0) of K^- polar angle were shown in left and right panels of top and bottom rows respectively.

B.4 Energy dependence of fraction of helicity-3/2

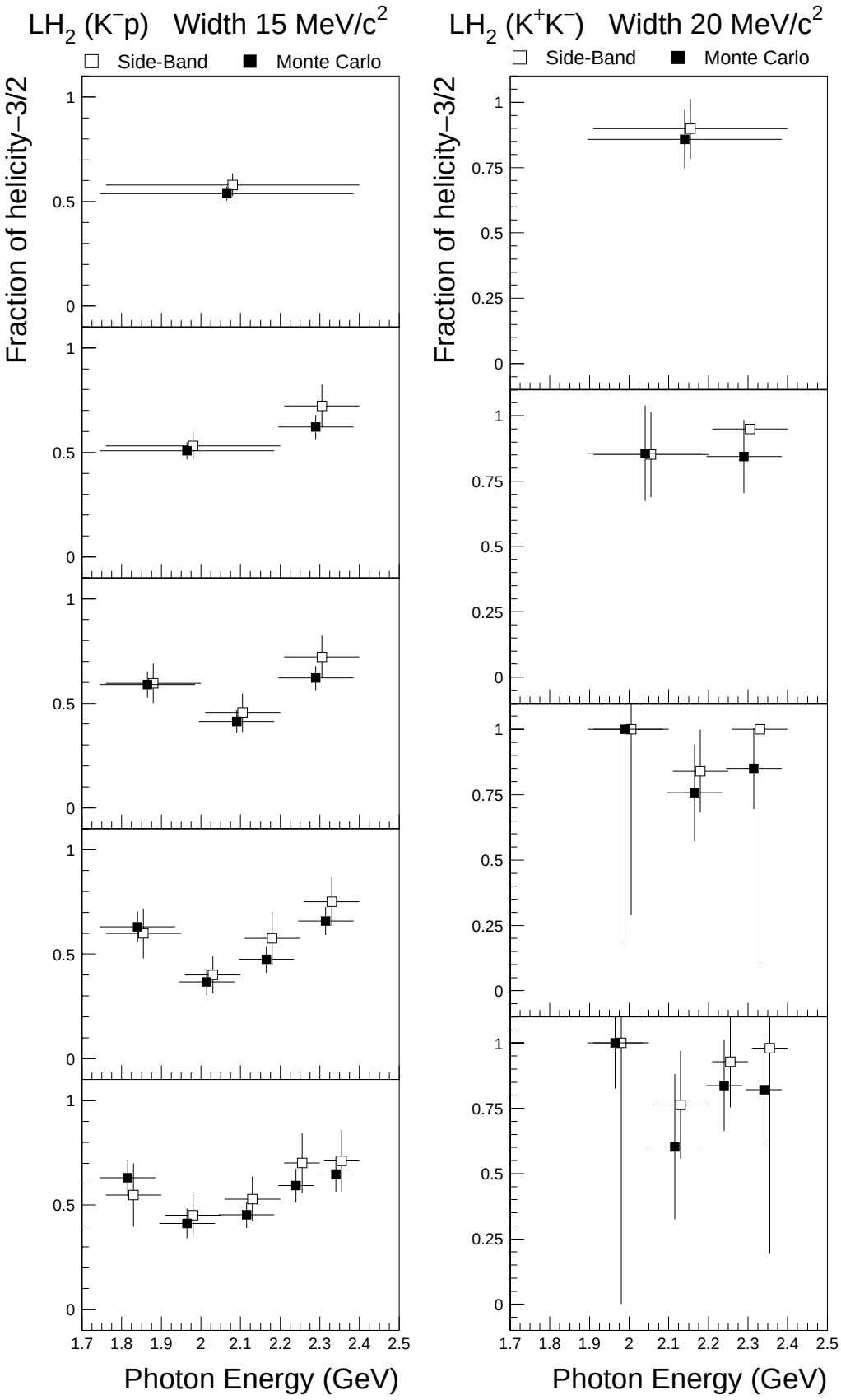

Figure B.48: The comparison of fraction of helicity-3/2 contribution by energy dependence between $LH_2(K^-p)$ and $LH_2(K^+K^-)$ modes at the signal-window widths of the 15 MeV/c^2 and 20 MeV/c^2 respectively.

Appendix C

Photon beam asymmetry

Depending on the 2-step side-band subtraction method, we studied the photon beam asymmetry. In the first part of this appendix C.1, the photon beam asymmetry was measured in K^+p detection mode from protons. In section C.1.1, we studied the width dependence of photon beam asymmetry in photon energy of 1.9-2.4 GeV. As shown in Fig.C.1-C.4, $|MMp(\gamma,K^+p)-M_K|$ and $|MMp(\gamma,K^+)-M_{\Lambda(1520)}|$ are required to be the range of 15-30 MeV/c^2. In section C.1.2, under the standard 2-step side-band subtraction requirement, $|MMp(\gamma,K^+p)-M_K| < 25$ MeV/c^2 and $|MMp(\gamma,K^+p)-M_{\Lambda(1520)}| < 30$ MeV/c^2, we measured the energy dependence of photon beam asymmetry, as shown in Fig. C.5.

Following with the possible bias in beam asymmetry measurement from Monte Carlo simulated ntuples in C.2. Here, we studied the possible bias from different correlations in K^+p and single K^+ detection mode. In the first step, as shown in Fig. C.6, we filtered phase space Monte Carlo ntuples by correlations of "photon polarization and detected K^+" in photon energy of 1.75-2.4, 1.75-1.9, 1.9-2.2 and 2.2-2.4 GeV from protons. For example, in the case of photon energy of 1.75-2.4 GeV, as shown in top-left 3×3 panels of Fig. C.6, the first row shows the distribution of azimuthal angle ϕ for number of vertical events, number of horizontal events and the $(N_v-N_h)/(N_v+N_h)$ from events generator with filtering. After that, events which require the K^+p detected and single K^+ detected are shown in second the three rows respectively. Similar studies with different energy ranges are shown in same figure.

Then, to filter ntuples obtained from first step by the correlations of "photon polarization and detected proton", "detected K^+ and detected proton" and "reversed phase of photon polarization and detected proton", corresponding measurement were shown in Fig. C.7, C.8 and C.9 respectively.

C.1 K^+p detection mode from protons

C.1.1 Width dependence in photon energy of 1.9-2.4 GeV

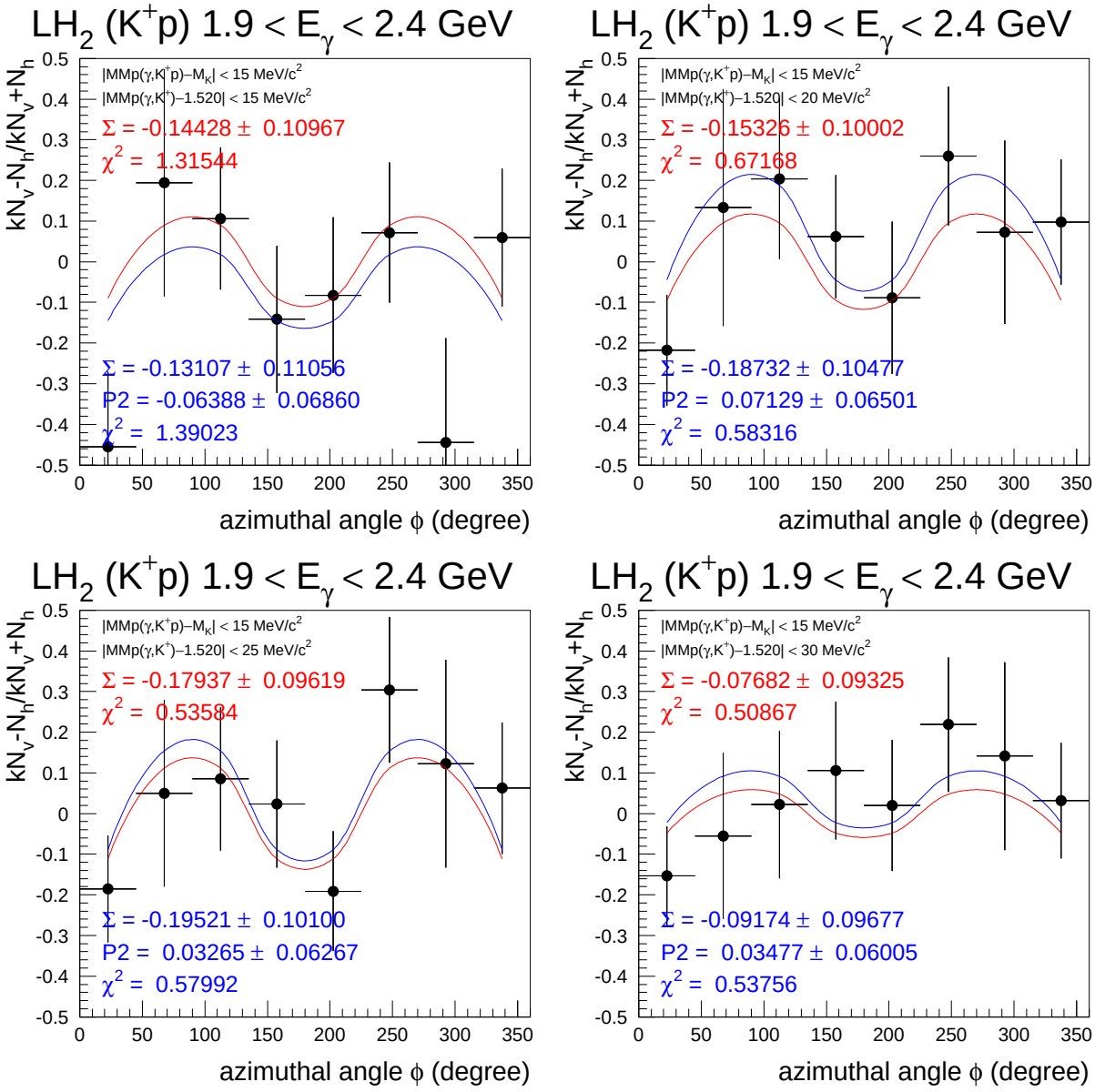

Figure C.1: Photon beam asymmetry were measured in photon energy of 1.9-2.4 GeV under the requirement $|\mathrm{MMp}(\gamma,\mathrm{K^+p})-\mathrm{M}_K| < 15$ MeV/c^2 and different $\Lambda(1520)$ signal-window widths by side-band subtraction method from protons in $\mathrm{K^+p}$ detection mode. Two fits were performed with (blue) and without (red) a vertical offset, P_2.

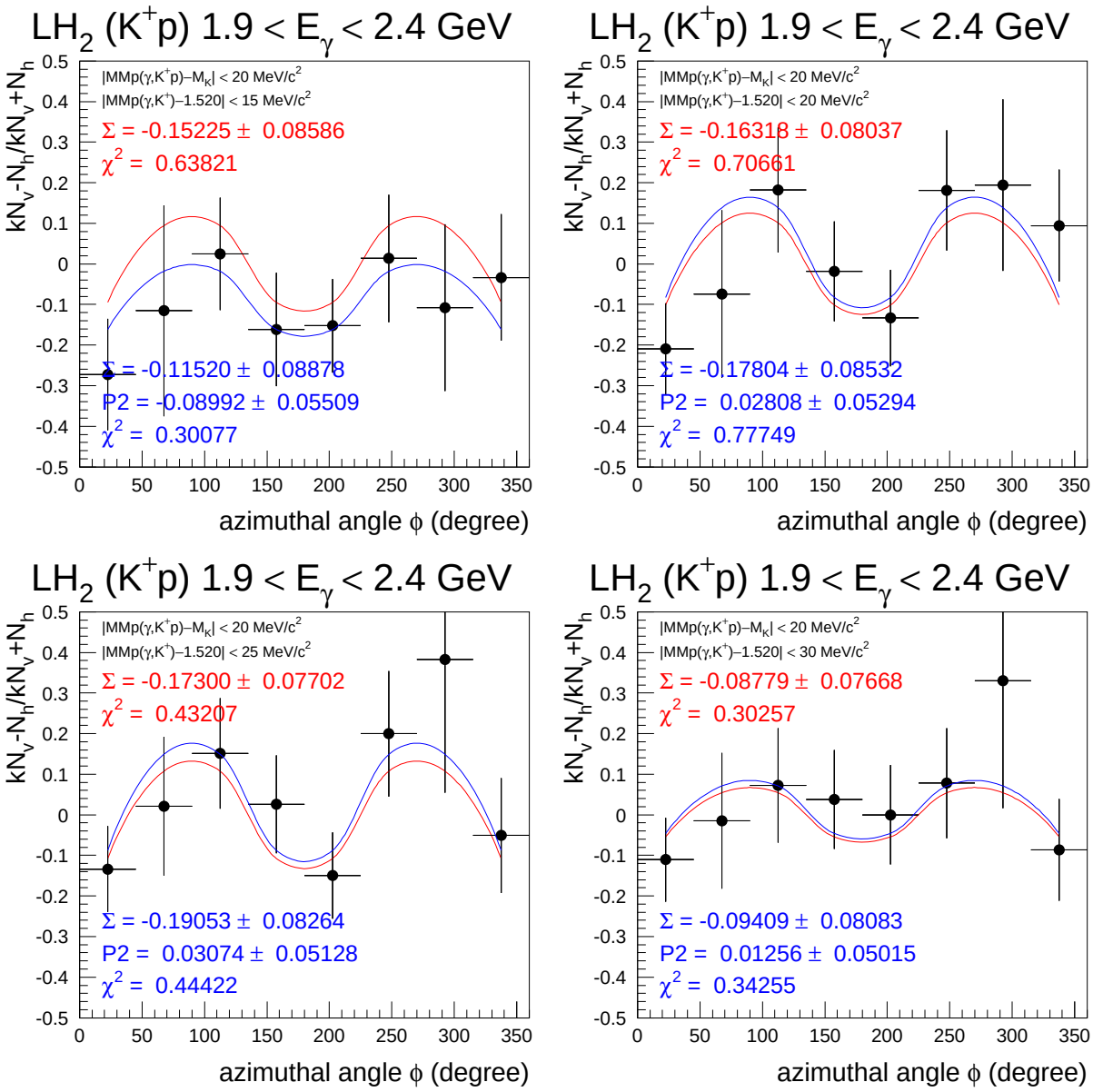

Figure C.2: Photon beam asymmetry were measured in photon energy of 1.9-2.4 GeV under the requirement $|\mathrm{MMp}(\gamma,\mathrm{K^+p})-\mathrm{M}_K| < 20$ MeV/c^2 and different $\Lambda(1520)$ signal-window widths by side-band subtraction method from protons in $\mathrm{K^+p}$ detection mode. Two fits were performed with (blue) and without (red) a vertical offset, P_2.

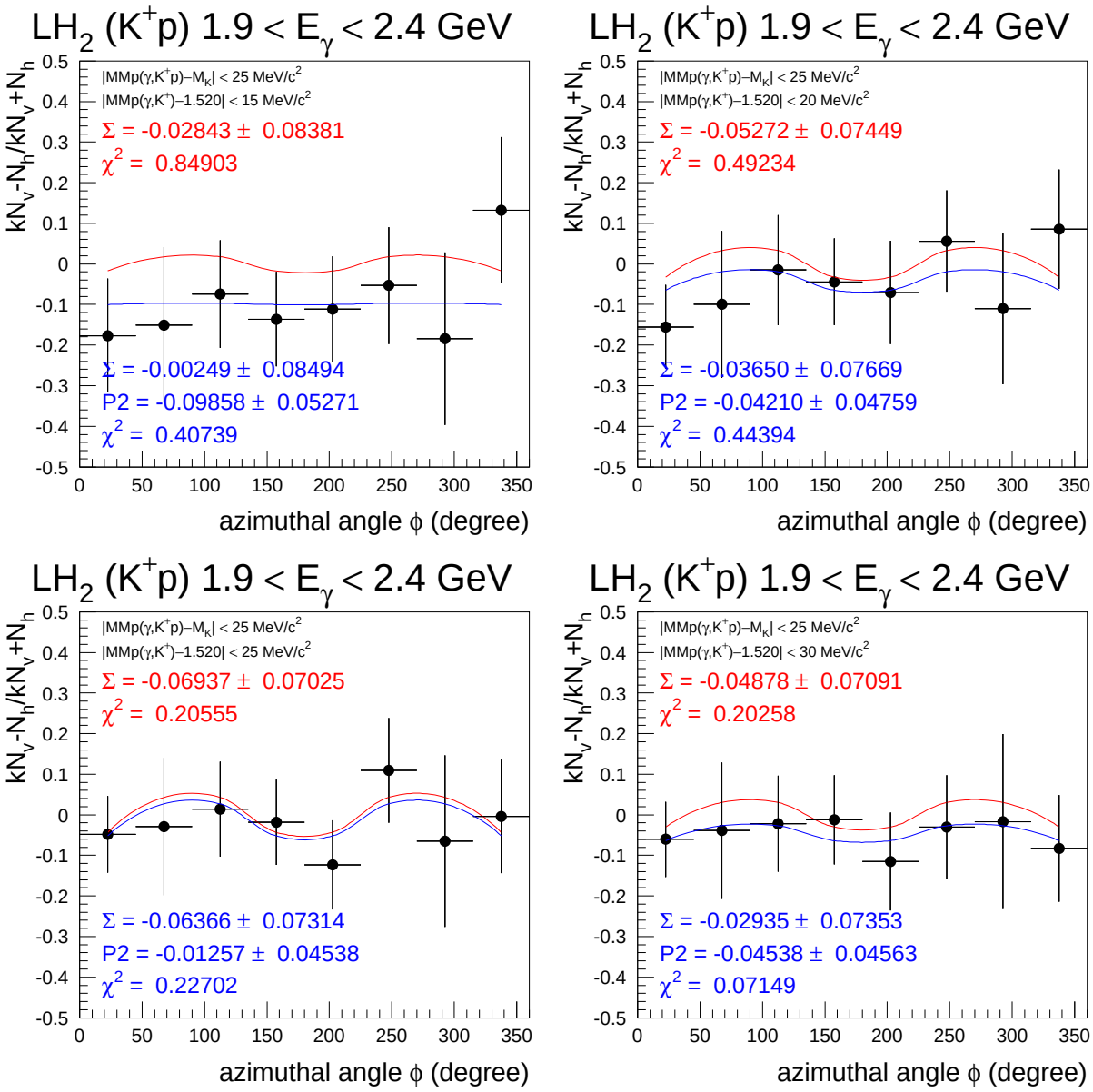

Figure C.3: Photon beam asymmetry were measured in photon energy of 1.9-2.4 GeV under the requirement $|\mathrm{MMp}(\gamma,\mathrm{K^+p})-\mathrm{M}_K| < 25$ MeV/c^2 and different $\Lambda(1520)$ signal-window widths by side-band subtraction method from protons in $\mathrm{K^+p}$ detection mode. Two fits were performed with (blue) and without (red) a vertical offset, P_2.

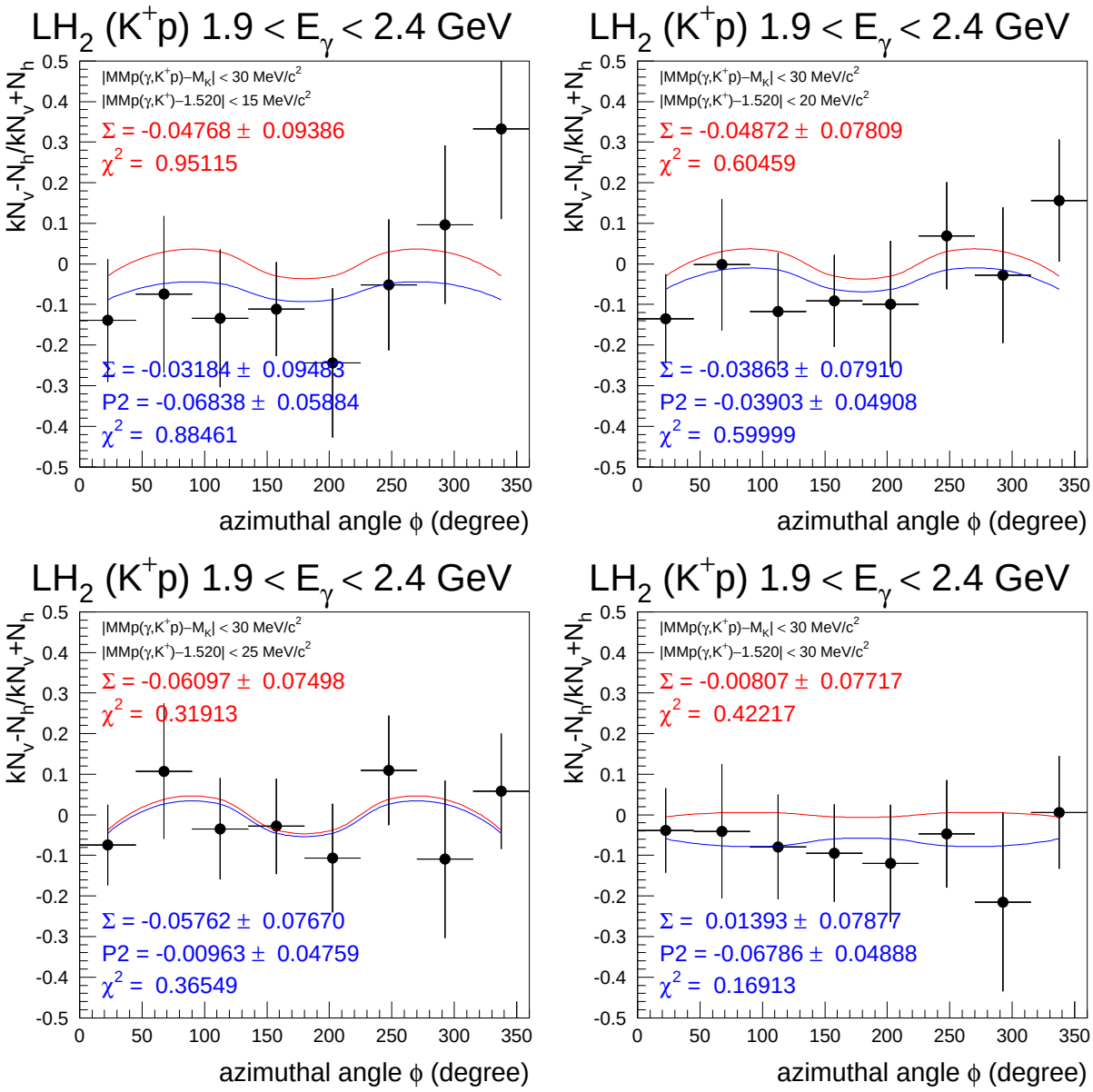

Figure C.4: Photon beam asymmetry were measured in photon energy of 1.9-2.4 GeV under the requirement $|\mathrm{MMp}(\gamma,\mathrm{K^+p})-\mathrm{M}_K| < 30$ MeV/c^2 and different $\Lambda(1520)$ signal-window widths by side-band subtraction method from protons in $\mathrm{K^+p}$ detection mode. Two fits were performed with (blue) and without (red) a vertical offset, P_2.

C.1.2 Energy dependence in standard 2-step side-band widths

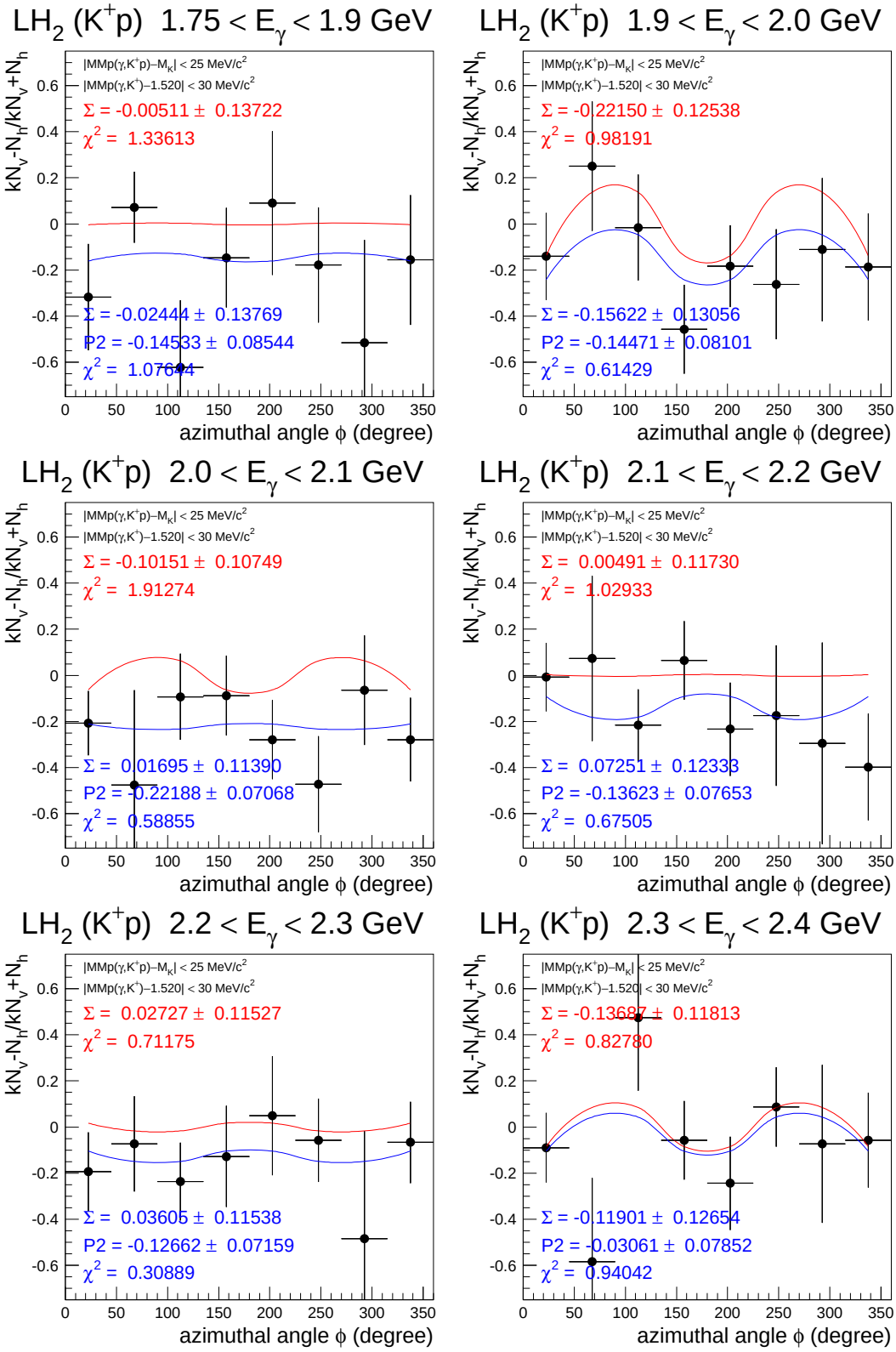

Figure C.5: Photon beam asymmetry were measured in photon energy of 1.75-1.9, 1.9-2.0, 2.0-2.1, 2.1-2.2, 2.2-2.3 and 2.3-2.4 GeV under the requirements $|\mathrm{MMp}(\gamma,\mathrm{K^+p})-\mathrm{M}_K| < 15$ MeV/c^2 and $|\mathrm{MMp}(\gamma,\mathrm{K^+})-1.520| < 0.030$ GeV/c^2 by side-band subtraction method from protons in $\mathrm{K^+p}$ detection mode. Two fits were performed with (blue) and without (red) a vertical offset, P_2.

C.2 Possible bias in beam asymmetry measurement

C.2.1 Filtering between photon polarization and detected K^+

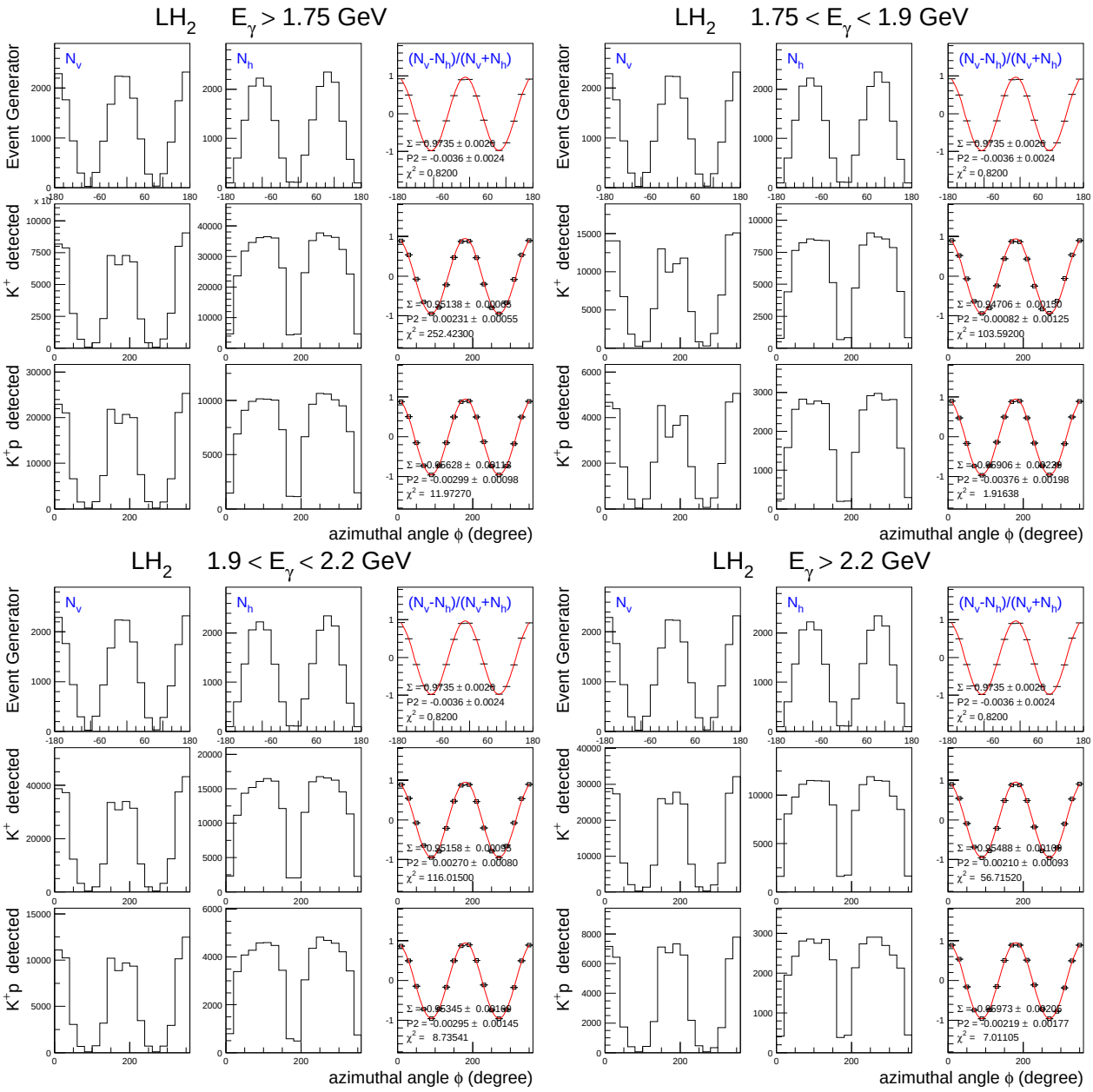

Figure C.6: Distributions of events with vertical and horizontal polarization and the fitted value from $(N_v\text{-}N_h)/(N_v+N_h)$ for three event samples which include event generator, single K^+ detected and K^+p detected in photon energy of 1.75-2.4, 1.75-1.9, 1.9-2.2 and 2.2-2.4 GeV.

C.2.2 Filtering between photon polarization and detected proton

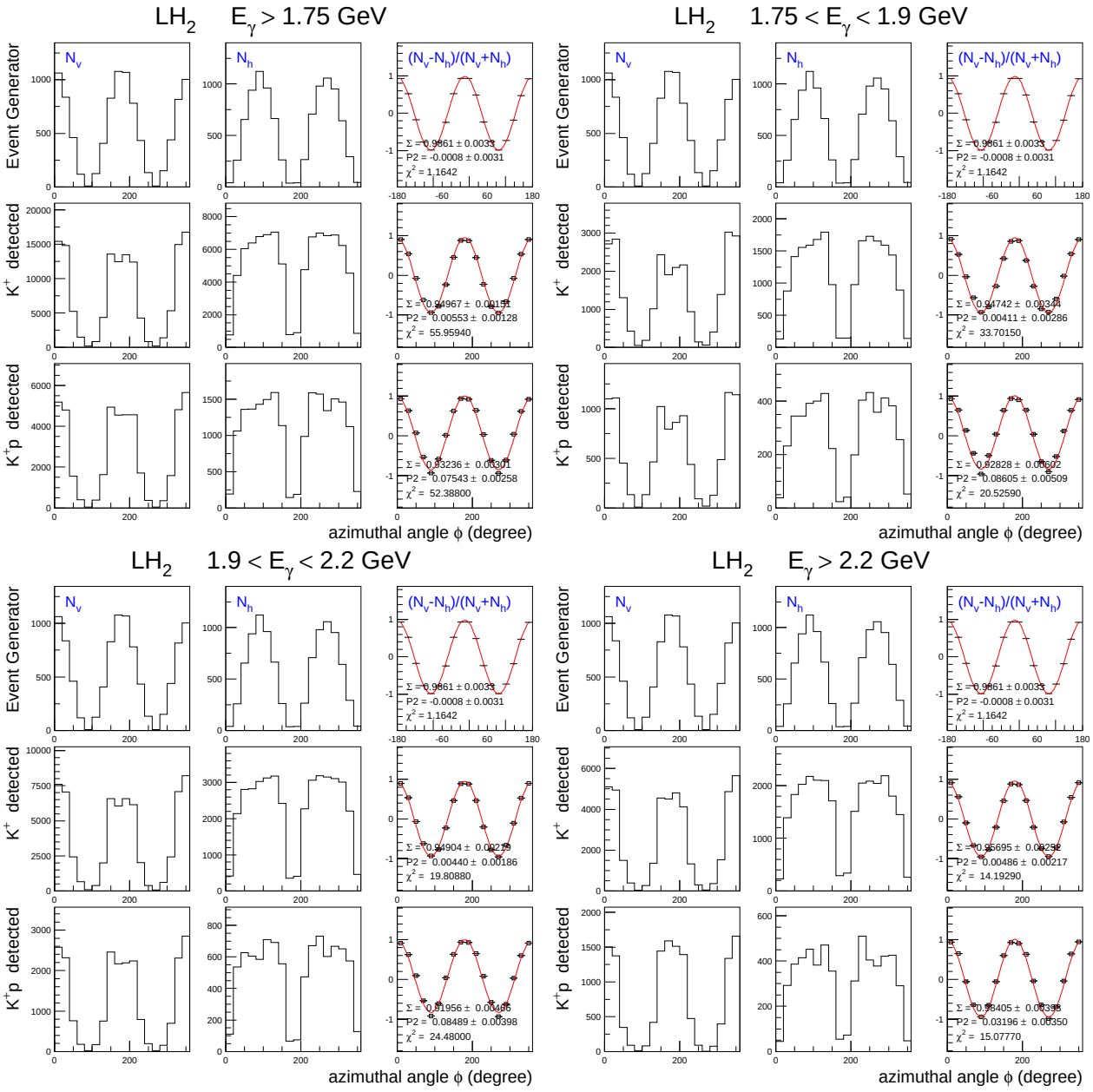

Figure C.7: Distributions of events with vertical and horizontal polarization and the fitted value from $(N_v\text{-}N_h)/(N_v+N_h)$ for three event samples which include event generator, single K^+ detected and K^+p detected in photon energy of 1.75-2.4, 1.75-1.9, 1.9-2.2 and 2.2-2.4 GeV.

C.2.3 Filtering between detected K^+ and detected proton

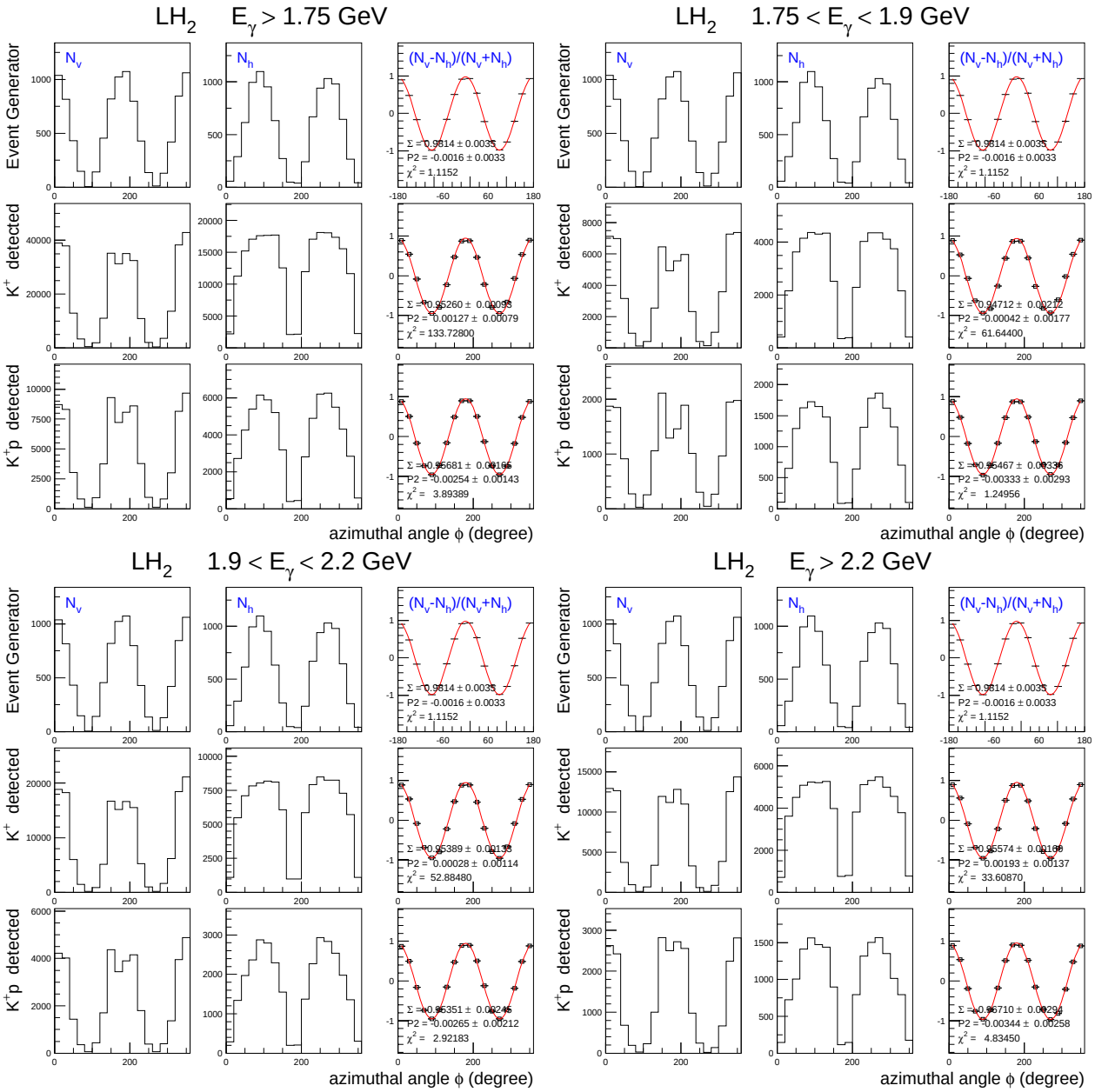

Figure C.8: Distributions of events with vertical and horizontal polarization and the fitted value from $(N_v\text{-}N_h)/(N_v+N_h)$ for three event samples which include event generator, single K^+ detected and K^+p detected in photon energy of 1.75-2.4, 1.75-1.9, 1.9-2.2 and 2.2-2.4 GeV.

C.2.4 Reversed filtering between photon polarization and detected proton

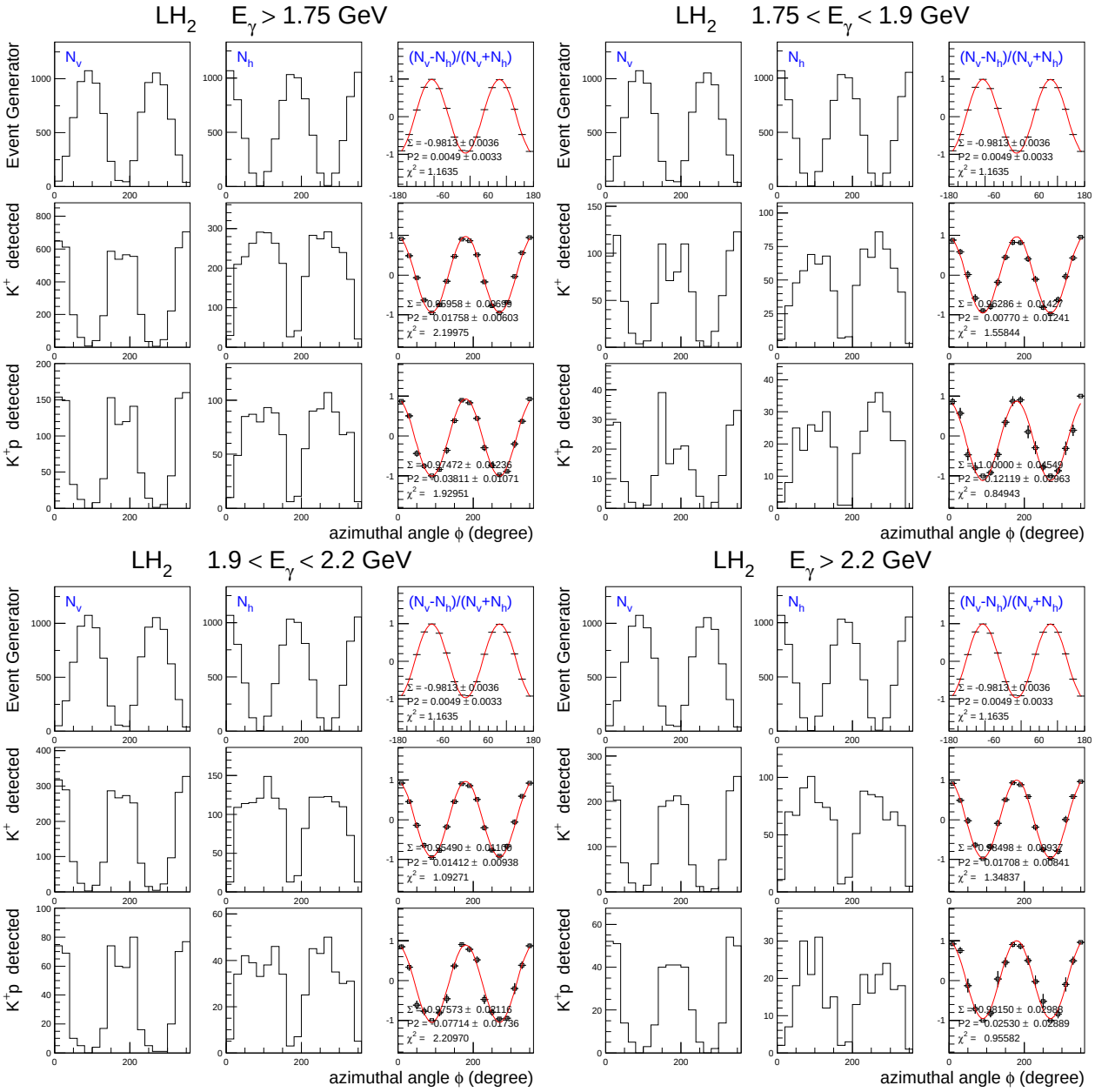

Figure C.9: Distributions of events with vertical and horizontal polarization and the fitted value from $(N_v\text{-}N_h)/(N_v+N_h)$ for three event samples which include event generator, single K^+ detected and K^+p detected in photon energy of 1.75-2.4, 1.75-1.9, 1.9-2.2 and 2.2-2.4 GeV.